ISSN 2518-7198 (Print)
ISSN 2663-5089 (Online)

BULLETIN
OF THE KARAGANDA UNIVERSITY

PHYSICS
Series

№ 2(98)/2020

ISSN 2518-7198 (Print)
ISSN 2663-5089 (Online)
Индексі 74616
Индекс 74616

ҚАРАҒАНДЫ УНИВЕРСИТЕТІНІҢ ХАБАРШЫСЫ

ВЕСТНИК КАРАГАНДИНСКОГО УНИВЕРСИТЕТА

BULLETIN OF THE KARAGANDA UNIVERSITY

ФИЗИКА сериясы

Серия ФИЗИКА

PHYSICS Series

№ 2(98)/2020

Сәуір–мамыр–маусым
30 маусым 2020 ж.
Апрель–май–июнь
30 июня 2020 г.
April–May–June
June, 30th, 2020

1996 жылдан бастап шығады
Издается с 1996 года
Founded in 1996

Жылына 4 рет шығады
Выходит 4 раза в год
Published 4 times a year

Қарағанды, 2020
Караганда, 2020
Karaganda, 2020

Редакцияның мекенжайы: 100024, Қазақстан, Қарағанды қ., Университет к-сі, 28
Тел.: (7212) 77-04-38; факс: (7212) 35-63-98.
E-mail: vestnikku@gmail.com; Сайты: physics-vestnik.ksu.kz/

Редакторлары

Ж.Т. Нурмуханова, С.С. Балкеева, Т. Кохановер

Компьютерде беттеген

В.В. Бутяйкин

Қарағанды университетінің хабаршысы. «Физика» сериясы.

ISSN 2518-7198 (Print). ISSN 2663-5089 (Online).

Меншік иесі: «Академик Е.А. Бөкетов атындағы Қарағанды мемлекеттік университеті» РММ.

Қазақстан Республикасының Мәдениет және ақпарат министрлігімен тіркелген. 23.10.2012 ж. № 13111–Ж тіркеу куәлігі.

Басуға 29.06.2020 ж. қол қойылды. Пішімі 60×84 1/8. Қағазы офсеттік. Көлемі 19,12 б.т. Таралымы 200 дана. Бағасы келісім бойынша. Тапсырыс № 37.

Е.А. Бөкетов атындағы ҚарМУ баспасының баспаханасында басылып шықты.
100012, Қазақстан, Қарағанды қ., Гоголь к-сі, 38. Тел. 51-38-20. E-mail: izd_kargu@mail.ru

Адрес редакции: 100024, Казахстан, г. Караганда, ул. Университетская, 28
Тел.: (7212) 77-04-38; факс: (7212) 35-63-98.
E-mail: vestnikku@gmail.com; Сайт: physics-vestnik.ksu.kz/

Редакторы

Ж.Т. Нурмуханова, С.С. Балкеева, Т. Кохановер

Компьютерная верстка

В.В. Бутяйкин

Вестник Карагандинского университета. Серия «Физика».

ISSN 2518-7198 (Print). ISSN 2663-5089 (Online).

Собственник: РГП «Карагандинский государственный университет имени академика Е.А. Букетова».

Зарегистрирован Министерством культуры и информации Республики Казахстан. Регистрационное свидетельство № 13111–Ж от 23.10.2012 г.

Подписано в печать 29.06.2020 г. Формат 60×84 1/8. Бумага офсетная. Объем 19,12 п.л. Тираж 200 экз. Цена договорная. Заказ № 37.

Отпечатано в типографии издательства КарГУ им. Е.А. Букетова.
100012, Казахстан, г. Караганда, ул. Гоголя, 38, тел.: (7212) 51-38-20. E-mail: izd_kargu@mail.ru

Postal address: 28, University Str., 100024, Karaganda, Kazakhstan
Tel.: (7212) 77-04-38; fax: (7212) 35-63-98.
E-mail: vestnikku@gmail.com; Web-site: physics-vestnik.ksu.kz/

Bulletin of the Karaganda University. «Physics» series.

ISSN 2518-7198 (Print). ISSN 2663-5089 (Online).

Proprietary: RSE «Academician Ye.A. Buketov Karaganda State University».

Registered by the Ministry of Culture and Information of the Republic of Kazakhstan. Registration certificate No. 13111–Zh from 23.10.2012.

Signed in print 29.06.2019. Format 60×84 1/8. Offset paper. Volume 19,12 p.sh. Circulation 200 copies. Price upon request. Order № 37.

Printed in the Ye.A. Buketov Karaganda State University Publishing house.
100012, Kazakhstan, Karaganda, Gogol Str., 38, Tel.: (7212) 51-38-20. E-mail: izd_kargu@mail.ru

МАЗМҰНЫ — СОДЕРЖАНИЕ — CONTENTS

КОНДЕНСАЦИЯЛАНҒАН КҮЙДІҢ ФИЗИКАСЫ
ФИЗИКА КОНДЕНСИРОВАННОГО СОСТОЯНИЯ
PHYSICS OF THE CONDENSED MATTER

ТЕХНИКАЛЫҚ ФИЗИКА
ТЕХНИЧЕСКАЯ ФИЗИКА
TECHNICAL PHYSICS

ЖЫЛУФИЗИКАСЫ ЖӘНЕ ТЕОРИЯЛЫҚ ЖЫЛУТЕХНИКАСЫ
ТЕПЛОФИЗИКА И ТЕОРЕТИЧЕСКАЯ ТЕПЛОТЕХНИКА
THERMOPHYSICS AND THEORETICAL THERMOENGINEERING

АСПАПТАР МЕН ЭКСПЕРИМЕНТ ТЕХНИКАСЫ
ПРИБОРЫ И МЕТОДЫ ЭКСПЕРИМЕНТА
INSTRUMENTS AND EXPERIMENTAL TECHNIQUES

ФИЗИКАНЫ ОҚЫТУ ӘДІСТЕМЕСІ
МЕТОДИКА ПРЕПОДАВАНИЯ ФИЗИКИ
METHODS OF TEACHING PHYSICS

DOI 10.31489/2020Ph2/7-17

UDC 621.793:621.785.532

A.S. Rudenkov[1], A.V. Rogachev[1], S.M. Zavadski[2], D.A. Golosov[2],
P.A. Luchnikov[3], G.Yu. Dalskaya[3], A.N. Vtoruchina[4]

[1]Francisk Skorina Gomel State University, Gomel, Belarus;
[2]Belarusian State University of Informatics and Radioelectronics, Minsk, Belarus;
[3]MIREA – Russian Technological University, Moscow, Russia;
[4]National Research Tomsk Polytechnic University, Tomsk, Russia
(E-mail: xamdex@gmail.com)

Nitrided Silicon-Carbon Coatings Structure and Properties

The paper considers structural and physicomechanical properties of silicon-carbon coatings deposited from a gaseous medium in doping with nitrogen ions. The analysis of the coatings by X-ray photoelectron spectroscopy shows that nitriding of silicon-carbon coatings promotes the formation of silicon nitride and compounds such as CN_x and $Si_xO_yN_z$. A 1.5–2-fold increase in the content of sp^2-hybridized carbon and silicon carbide atoms is found to prevent silicon oxidation. Thermal annealing of the resulting silicon-carbon coatings increases the content of the graphite phase and silicon oxide.It is shown that doping of the working gas with nitrogen ($Ar_{57\,\%} + N_{43\,\%}$) leads to the formation of a more finely dispersed structure as compared to that when using argon only. During thermal annealing in air, the decreased carbon concentration and increased oxygen concentration can be observed due to silicon and carbon oxidation followed by desorption of carbon and oxygen compounds. In addition, annealing leads to nitrogen desorption from the coating. Nitriding of silicon-carbon coatings increases the dispersion of their structure, and heat-resistant compounds CN_x, Si_3N_4 improve heat resistance and thermal stability of coatings, and increase microhardness and friction coefficient in friction units.

*Keywords***:** carbon coatings, nitriding, silicon, phase composition, ion beam sputtering, Raman spectroscopy, XPS, microhardness, friction coefficient.

Introduction

In the general case, the properties of carbon coatings and their dependence on the synthesis parameters are determined by the polymorphism of the structural configurations of carbon in both crystalline and amorphous states [1–5]. Ion nitriding of nanosized carbon-based coatings is an effective technological technique that allows controlling their phase structure during the deposition process [6, 7]. Silicon alloying is one of the most effective methods for increasing the heat resistance of carbon coatings [8]. Thus, the study of chemical interaction processes which occur during the deposition of silicon-carbon coatings by ion-beam sputtering of a silicon carbide target using a mixture of nitrogen and argon as a working gas and which lead to the formation of solid carbide and nitride phases is a vital task. Solving this problem will allow us to develop effective technological methods for the formation of coatings that will be characterized by high heat resistance properties.

The aim of this article is to study the influence of nitriding on the structure and mechanical properties of silicon-carbon coatings deposited by ion-beam sputtering of a silicon carbide target during the formation process and subsequent thermal treatment.

Samples and research methods

Silicon-carbon coatings were formed by ion beam sputtering of a silicon carbide target. The power of the ion source was 738 W ($I_{of\ discharge}$=164 mA, $U_{of\ discharge}$ = 4,5 kV, $I_{of\ target}$= 174 mA), the coating thickness was (270±10) nm. Nitrogen was brought in the working gas for coating nitriding. The volume content of argon was 57 %, and the nitrogen content was about 43 %. The coatings were being annealed in the air at a temperature of 600 °C and 700 °C for 30 minutes.

Silicon-carbon coatings morphology was studied by atomic force microscopy method (AFM) in the modes of topography measuring and phase contrast using a Solver Pro device manufactured by NT-MDT (Moscow, Russia). Sections of 4x4 μm^2 in size were scanned. The coatings chemical structure was determined by X-ray photoelectron spectroscopy (XPS) method. The measurements were carried out using a PHI Quantera device when the substance was excited with aluminum Kα-radiation with quantum energy of 1486.6 eV and a total power of 250 W. The error in determining the concentration of elements was ± 1 atom per cent. The hydrophobic properties of silicon-carbon coatings were determined by measuring the limiting wetting angle and by calculating the surface energy and its components. The microhardness of silicon-carbon coatings was measured by Knupp method using a DM-8 microhardness tester (AFFRI, Italy). The indenter load was 490 mN. Tribotechnical tests were carried out according to the «sphere-plane» scheme under load of 980 mN, the average indenter movement speed was 0.017 m/s.

Results and Their Discussion

It is given that the size of individual structural features (grains) of silicon-carbon coatings is larger and the grain which was carried out in the presence of nitrogen and argon in the working gas structure. When the annealing temperature of nitrided silicon-carbon coatings is increased, the average height of individual structural features is decreased and their average diameter is slightly decreased as well as the coating dispersion is increased. Annealing of non-nitrided coatings is also accompanied by a decrease in the average height of grains (by 4.7 times) but it occurs in combination with an increase in their average diameter and a decrease in dispersion. Most likely, this is due to graphite clusters merging.

The comparative analysis (Table 1) of non-nitrided and nitrided silicon-carbon coatings elemental structure showed that when nitrogen is brought into the working gas, the concentration of silicon and carbon is slightly lower in comparison with non-nitrided coatings. The influence of annealing in the air on the elemental structure of both types of coatings is similar: there is a decrease in carbon concentration and an increase in oxygen concentration; it is due to silicon and carbon oxidation that is followed by desorption of carbon and oxygen compounds. It was shown that annealing leads to nitrogen desorption, its content decreases by 4 times. Apparently, nitrogen remains in a bound state in the form of CN_x or Si_3N_4 compounds after annealing. These compounds are characterized by high heat resistance [9–11].

Table 1

Chemical structure of non-nitrided and nitrided silicon-carbon coatings

Coating	Temperature, °C	Working gas	Concentration of elements, at. %			
			C	Si	O	N
C+Si	–	$Ar_{100\ \%}$	40.3	25.7	34.0	0.0
		$Ar_{57\ \%}+N_{43\ \%}$	37.1	23.2	31.5	8.6
	600	$Ar_{100\ \%}$	22.3	25.7	52.0	0.0
		$Ar_{57\ \%}+N_{43\ \%}$	22.5	23.2	51.3	3.0
	700	$Ar_{100\ \%}$	20.2	25.7	54.1	0.0
		$Ar_{57\ \%}+N_{43\ \%}$	17.3	23.2	57.4	2.1

In general, the following two-phase carbon peak model is distinguished: phase 1 corresponds to the sp^2 matrix, which includes sp^3-hybridized carbon atoms, and is determined by the D-peak between 1300 cm^{-1} and 1500 cm^{-1}; phase 2 means sp^2 clusters and is determined by G-peak about 1580 cm^{-1} [9]. The analysis of the width of these peaks, changes in their position and intensity ratios gives an idea of the degree of carbon-based coatings ordering, the number and size of clusters with sp^2 bonds.

It is well-known [12], that the ratio of the intensities of the D- and G-peaks is in inverse proportion to the size of the sp^2 clusters: $\frac{I_D}{I_G} = \frac{c(\lambda)}{L_a}$, (1)

where I_D and I_G are the intensities of the correspondent peaks; L_a is the size of graphite grains (nm); $c(\lambda)$ is the proportionality coefficient depending on the wavelength of the exciting radiation (nm).

Table 2

Influence of annealing temperature and working gas structure on the morphological features of silicon-carbon coatings

Coating	Annealing temperature, °C	Working gas	Average height, nm	Rms, nm	Average diameter of grains, nm
C+Si	–	$Ar_{100\,\%}$	5.0	0.6	44
		$Ar_{57\,\%}+N_{43\,\%}$	11.0	0.4	57
	600	$Ar_{100\,\%}$	4.0	1.8	140
		$Ar_{57\,\%}+N_{43\,\%}$	3.9	0.3	53
	700	$Ar_{100\,\%}$	3.7	2.3	166
		$Ar_{57\,\%}+N_{43\,\%}$	2.3	0.5	51

Taking into account the ratio (1), the analysis of Raman spectroscopy results (Table 3) shows that the size of sp^2 clusters in nitrided silicon-carbon coatings is larger than in non-nitrided ones. This conclusion is confirmed by the results of atomic force microscopy (Table 2).

Table 3

Statistical analysis of Raman spectroscopy results

Coating	Working gas	D-peak		G-peak		I_D/I_G
		Position, cm^{-1}	Width, cm^{-1}	Position, cm^{-1}	Width, cm^{-1}	
C+Si	$Ar_{100\,\%}$	1408.9	117.0	1487.3	117.9	1.78
	$Ar_{57\,\%}+N_{43\,\%}$	1427.7	166.9	1513.9	153.2	1.36

The Raman spectra of nitrided silicon-carbon coatings exposed to thermal treatment in the air could not be reliably analyzed due to the high noise level. It is well-known that the coatings based on nitride or silicon oxide and containing silicon clusters have luminescent properties [13]. After thermal treatment the carbon concentration decreases almost by 2 times and the carbon input to the Raman spectrum does not exceed the silicon input and its components, which leads to an increase in the luminescence influence, causing distortion of the spectra. This phenomenon indirectly confirms the presence of SiN_x compounds in the coating, which are characterized by stronger luminescent properties than silicon oxide. It is confirmed by Raman spectroscopy results since the level of distortion in the case of annealing of non-nitrided samples of silicon-carbon coatings is not so significant. The mathematical processing of the above spectra confirms the presence of D- and G-peaks. But they can't be compared with the spectra of non-nitrided silicon-carbon coatings. In addition, the peak was detected at the level of 2250 cm^{-1}. This peak can correspond to the compound of CN_x type or simply be an overton of D- and G- peaks.

The detailed analysis of the results of XPS of silicon-carbon coatings formed by ion-beam sputtering of silicon carbide was given by us earlier in the article [8].

There are several methods for the C1s peak decomposition of XPS of nitrogen-containing carbon coatings. In [14] the C1s peak is decomposed into four components: Csp^2 ~ 284.5 eV, Csp^2–N ~ 286.6 eV, Csp^3–N ~ 287.3 eV and C=O ~ 290 eV. The author of [15] mean C–N and C=N bonds by components with a binding energy of 285÷286 eV and 287 eV, respectively, and they compare 288 eV to β-C_3N_4. The authors of [16] divide the C1s peak into three and correlate the component with a binding energy of 285–286 eV with sp^3-hybridized carbon atoms and C — N, C = N. Due to such an ambiguity in the determination of CN_x bonds and a low nitrogen concentration in the coating the Csp^3 compound of the C1s peak is combined with the component related to the C — N, C = N bonds.

C–Si with binding energy ~ 283.6 eV [17] Csp^2 ~ 284.4 eV, Csp^3 and CN_x ~ 285.5 eV, C–O ~ 286.5 eV [8] were identified in the C1s peak of nitrided silicon-carbon coatings (Fig. 1).

In addition to the above specified components of the Si2p peak, nitrided silicon-carbon coatings are characterized by the presence of a component near 101.7 ÷ 102 eV (Fig. 2), which corresponds to the Si N bond (Si_3N_4) [18]. The values of Si-N binding energy are close to values of C–Si–O binding energy (101.7 eV) [19], therefore, these components were combined into one during the decomposition of Si2p peak.

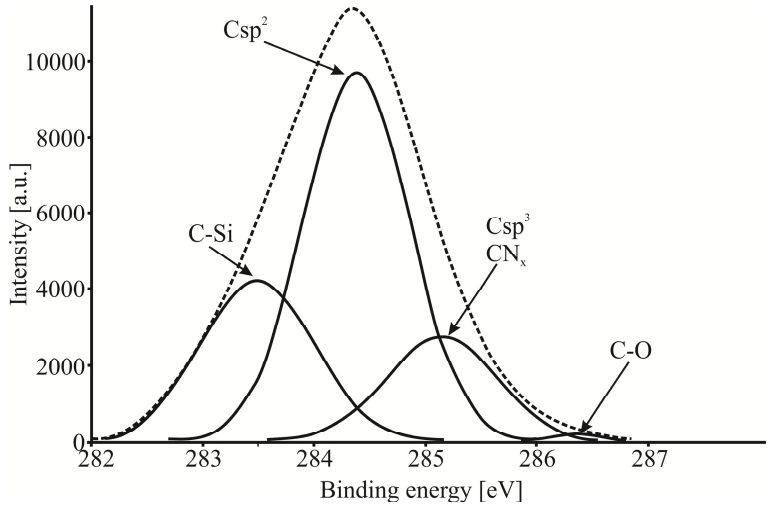

Figure 1. C1s peak of XPS of nitrided silicon-carbon coatings

In addition, during the decomposition of the Si2p peak the nitrided silicon-carbon coatings are characterized by the occurrence of a component with the binding energy of 102.4÷102.8 eV corresponding to the O — Si — N bond [20].

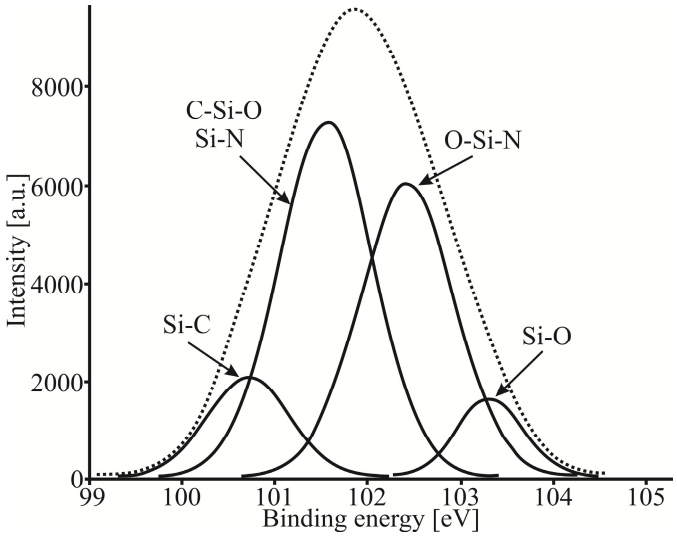

Figure 2. Si2p peak of XPS of nitrided silicon-carbon coatings

Making Si-N bonds during the formation of silicon-carbon coatings using a gas mixture of $Ar_{57\,\%}$ + $N_{43\,\%}$ is also confirmed by analysis of the N1s peak. Bond N-Si in the N1s peak is detected near 397÷398 eV [19, 20], bond of nitrogen atoms with sp^2- hybridized carbon atoms is determined at the level of 399 eV, and with sp^3-hybridized — near 399.9 eV [21]. Bond Si-O-N is determined close to 400 eV [22], these components of N1s peak were combined due to their proximity to N-Csp^2. The decomposition of the N1s peak was made as follows (Fig. 3): N-Si with binding energy 397.6 eV, N-Csp^3~398.7 eV, N-Csp^2+Si-O-N ~399.9 eV.

Thus, the XPS analysis of nitrided silicon-carbon coatings shows that bringing nitrogen into the working gas structure ($Ar_{57\,\%}$+$N_{43\,\%}$) at ion sputtering of the SiC target leads to the formation of silicon nitride and compounds of CN_x and $Si_xO_yN_z$ type. According to the relative input of the integral areas, nitrogen, the component of the N1s peak of XPS, is mainly associated with sp^3- hybridized carbon atoms.

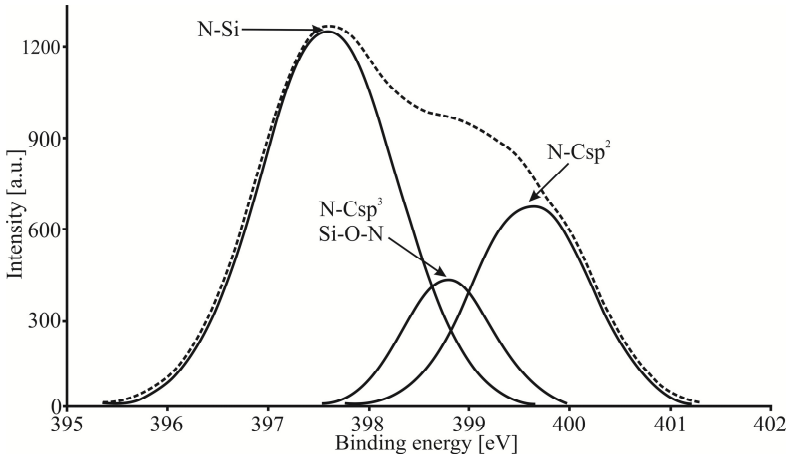

Figure 3. N1s peak of XPS of nitrided silicon-carbon coatings after annealing at 600 °C

If silicon-carbon coatings are formed by bringing nitrogen into the working gas structure, the proportions of the integral area of Csp^2 component of the C1s peak and Si-C component of the Si2p peak is higher, and Si-O component of the Si2p peak are lower than when the coatings are not nitrided (Fig. 4).

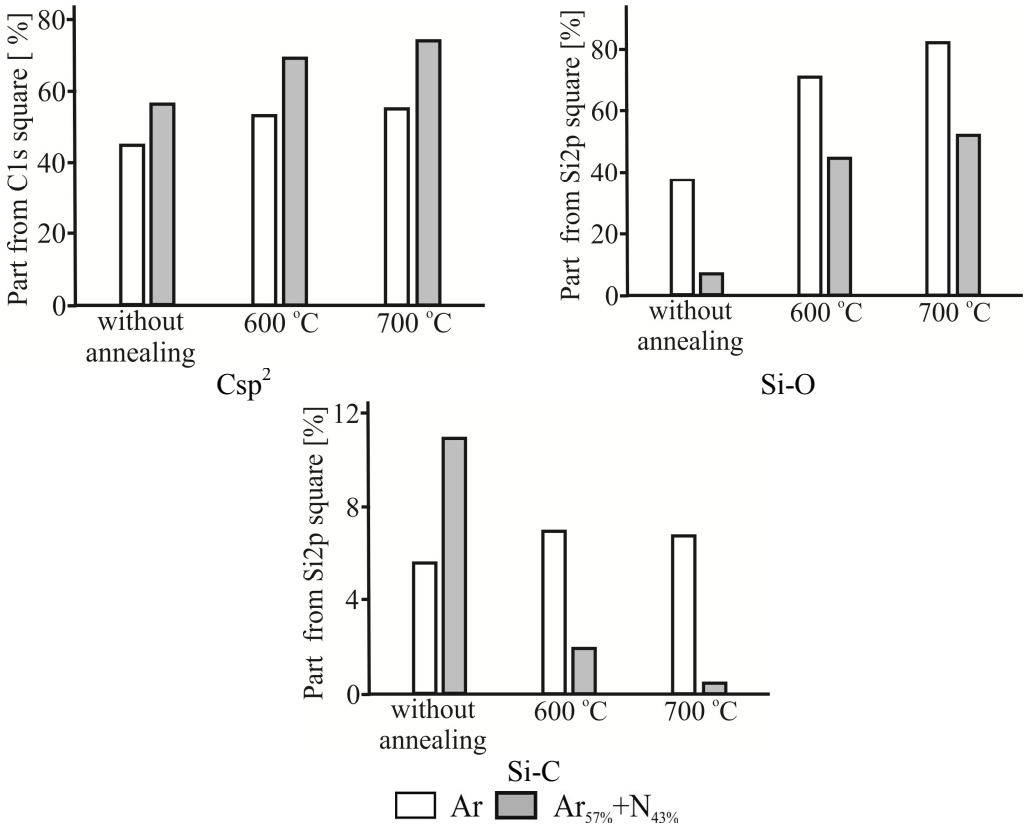

Figure 4. Influence of annealing temperature and nitrogen presence in the working gas on the silicon-carbon coatings structure

Thus, bringing nitrogen into the working gas structure ($Ar_{57\,\%} + N_{43\,\%}$) during the formation of silicon-carbon coatings by ion sputtering of silicon carbide contributes to an increase in the content of sp^2- hybridized carbon atoms and silicon carbide in addition to the formation of silicon nitride and compounds of the CN_x and $Si_xO_yN_z$ type. It also prevents from silicon oxidation.

High-temperature annealing of both non-nitrided and nitrided silicon-carbon coatings leads to an increase in the content of the graphite phase and silicon oxide. Nitrided silicon-carbon coatings annealing

causes intense destruction of silicon carbide, while non-nitrided coatings are characterized by a slight increase in the content of silicon carbide after annealing. Apparently the following happens: annealing causes nitrogen desorption (its content decreases by 4 times (Table 2)), the coating becomes less dense, due to which the oxidation becomes more intense, silicon carbide is destroyed and there occurs the further interaction of silicon and carbon atoms with oxygen and the subsequent desorption of oxygen and carbon compounds. Non-nitrided coatings are probably denser or contain more free silicon atoms, which interact with carbon during annealing, by comparison with the nitrided coatings free silicon atoms interact with nitrogen at the deposition stage.

If the annealing temperature is increased to 700 °C, the proportion of the integral area of N-Si and N-Csp^3 components of the N1s peak of XPS (Fig. 5) is decreased, and at the same time the proportion of integral area of the component which correlates with N-Csp^2 and Si-O-N simultaneously is increased.

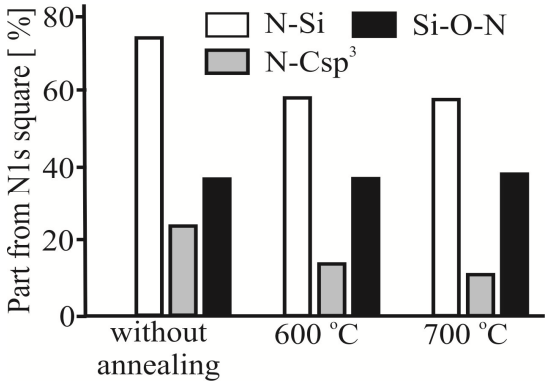

Figure 5. Influence of annealing temperature on the content of N-Si, N-Csp^3 and Si-O-N bonds of nitride silicon-carbon coatings

This increase is explained primarily by the annealing of the $sp^3 \rightarrow sp^2$ phase transitions (Fig. 4), since the increase in the proportion of the integral area of Csp^2 component of the C1s peak is more significant than the change in the proportion of the integral area of Si-O-N component of the Si2p peak (Fig. 5).

We found that heat treatment of non-nitrided silicon-carbon coatings leads to an increase in their surface energy by almost 1.9 times.

After annealing at a temperature of 600°C, the surface energy of silicon-carbon coatings increases, mainly due to an increase in its polar component, which is explained by the $sp^3 \rightarrow sp^2$ phase transition, as well as the formation of strongly polar bonds. With a further increase in the annealing temperature to 700°C, the Si-O-C bonds are destroyed and more stable C-O and Si-O bonds are formed, which leads to a decrease in the polar component of surface energy.

It was found out if nitrogen is brought into the working gas structure at the silicon-carbon coatings deposition by silicon-carbide ion sputtering, the contact angle decreases, and therefore the surface energy decreases (Fig. 6, a, b).

The values of the dispersion component of the surface energy are determined, first of all, by the surface morphology. The dispersion component of nitrided silicon-carbon coatings is higher than that of non-nitrided ones (Fig. 6, c). This is due to their high dispersion structure. The dispersion component of nitrided silicon-carbon coatings changes less significantly after annealing than that of non-nitrided ones. It is completely consistent with the previously obtained results of the analysis of atomic force microscopy data (the surface morphology parameters of nitrided silicon-carbon coatings are practically unchanged).

The values of the polar component of surface energy (Fig. 6, d) of nitrided silicon-carbon coatings are lower than that of non-nitrided coatings. It is explained by a lower content of silicon oxide, since bringing nitrogen into the working gas structure helps to reduce the intensity of oxidizing processes.

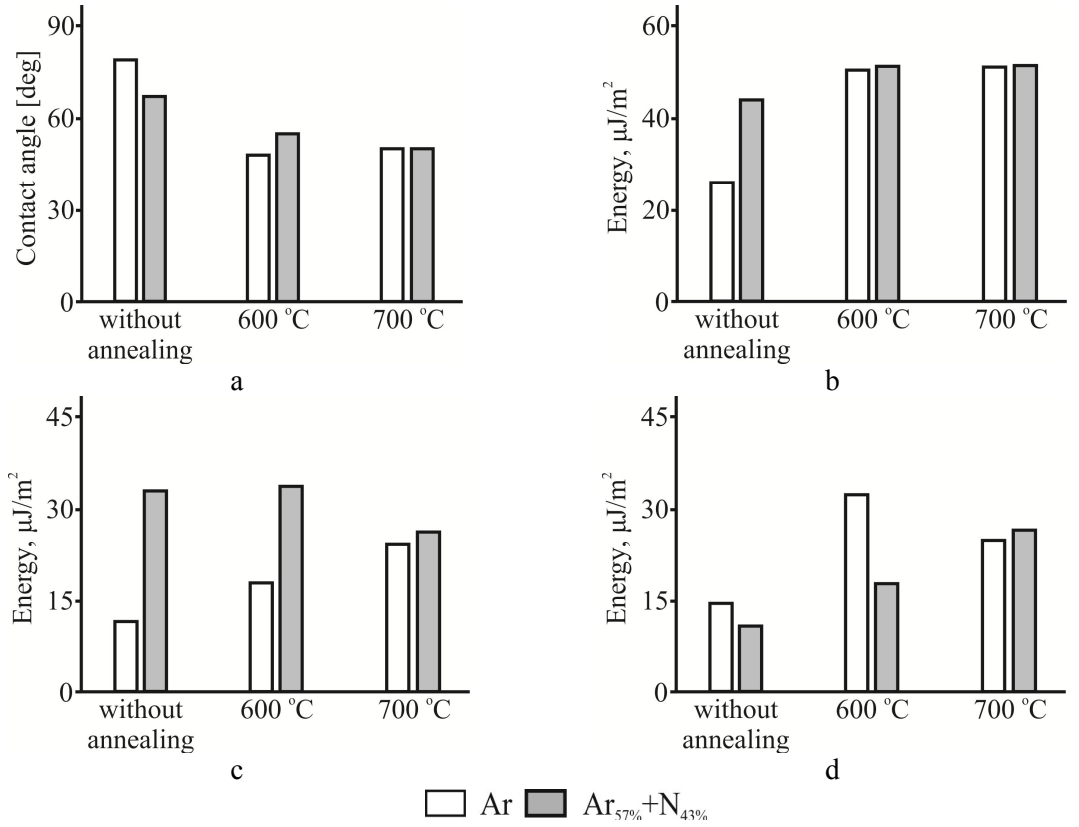

Figure 6. Contact angle (a), total surface energy (b), its dispersion (c) and polar (d) components which characterize the hydrophobic properties of nitrided and non-nitrided silicon-carbon coatings

The total surface energy after annealing in the air raises due to an increase in the polar component both as applied to nitrided and non-nitrided coatings. It is caused by the $sp^3 \rightarrow sp^2$ phase transition, as well as the formation of strongly polar bonds.

Table 4

Influence of thermal treatment parameters on microhardness H_k of nitrided and non-nitrided silicon-carbon coatings and coefficient of volume wear of the counterbody j when interacting with such coatings.

Coating	T, °C	Working gas	H_k, GPa	$j \times 10^{-17}$, $m^3/(N \cdot m)$
C+Si	–	$Ar_{100\,\%}$	13.34±0.25	332±17.3
		$Ar_{57\,\%}+N_{43\,\%}$	10.68±0.15	252±15.1
	600	$Ar_{100\,\%}$	12.05±0.27	185±16.9
		$Ar_{57\,\%}+N_{43\,\%}$	10.86±0.17	302±14.7
	700	$Ar_{100\,\%}$	11.59±0.22	167±14.3
		$Ar_{57\,\%}+N_{43\,\%}$	10.36±0.28	426±15.3

Experimental studies of the microhardness H_k of silicon-carbon coatings (Table 4) showed that it is 10.63 ± 0.2 GPa in nitrided films and 2.7 GPa higher in non-nitrided H_k, i.e. is 12.33 ± 0.2 GPa. This fact is apparently caused by a higher content of sp^2-hybridized carbon atoms in the carbon coating. (Fig. 4).

High-temperature annealing of such coatings, unlike non-nitrided ones, does not cause significant changes in microhardness. It is due to the presence of CN_x and Si_3N_4 compounds in the coating structure, which are characterized by high heat resistance. In addition, according to the Hall-Petch law, a change in microhardness can be caused by a change in the size of sp^2 clusters. According to the previously cited data of atomic force microscopy (Table 1), in the case of nitrided silicon-carbon coatings, the average diameter of individual structural formations varies slightly.

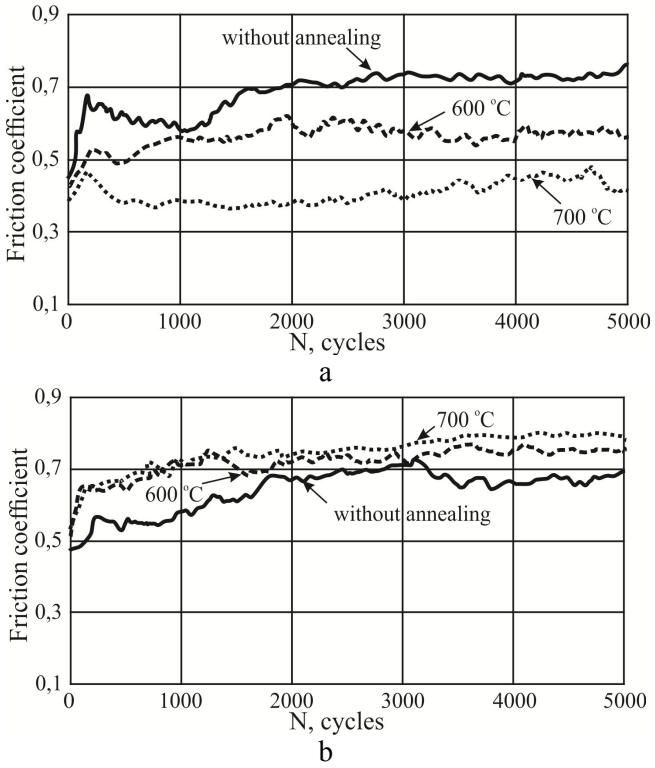

Figure 7. Influence of heat treatment on kinetic dependences of friction coefficient of non-nitrided (a) and nitrided (b) silicon-carbon coatings

In fact, the microhardness, friction, and wear of carbon-based coatings largely depend on the sp^2 / sp^3 ratio of hybridized carbon atoms [23–25]. The surface roughness of carbon coatings can also lead to an increase in the friction and wear coefficients during counterbody motion [23]. In addition to surface roughness, a high degree of chemical and/or adhesive interaction in the slip plane can also adversely affect the coefficient of friction.

On the one hand, the increase in surface energy recorded by us after annealing should contribute to an increase in the adhesive component of the friction force. The main source of adhesive interaction in the case of carbon-based coatings is covalent bonds or free σ-bonds of carbon atoms [2]. This type of bond can cause a very strong adhesive interaction and increase the friction coefficient, especially in the case of non-hydrogenated carbon coatings containing a high number of sp^3-hybridized carbon atoms [26–28].

However, according to the XPS data, the heat treatment of silicon-carbon coatings increases the graphite content, which plays the role of a solid lubricant and helps to reduce the friction coefficient. The high coefficient of friction before heat treatment is explained by the presence of solid phases based on silicon carbide and uneven surface wear during friction [29].

The abrasive action of silicon carbide also explains the higher coefficient of volumetric wear of the counterbody when interacting with the surface of silicon-carbon coatings not subjected to heat treatment.

It was found that silicon-carbon coatings nitriding contributes to the thermal stability of the friction coefficient (Figure 7, b). However, if the friction coefficient of nitrided silicon-carbon coatings does not change significantly, then the coefficient of volume wear of the counterbody when interacting with such coatings raises by increasing annealing temperature. It is explained by the highly dispersed structure of nitrided coatings and the abrasive action of heat-resistant solid interstitial phases based on CN_x and Si_3N_4 compounds present in their composition.

Conclusion

It was shown that bringing nitrogen into the working gas structure ($Ar_{57\,\%}$ + $N_{43\,\%}$) leads to the formation of a highly dispersed structure than using only argon. The influence of annealing in the air on the elemental structure of nitrided and non-nitrided coatings is similar: there is a decrease in carbon concentration and an increase in oxygen concentration. It is due to silicon and carbon oxidation which is followed by carbon and oxygen compounds desorption. It was shown that annealing leads to nitrogen desorption, its content

decreases by 4 times. Apparently, after annealing nitrogen remains only in the bound state in the form of CN_x or Si_3N_4 compounds, which are characterized by high heat resistance.

The analysis of XPS results shows that in addition to the formation of silicon nitride silicon-carbon coatings nitriding contributes to the formation of compounds of the CN_x and $Si_xO_yN_z$ type and increases the content of sp^2-hybridized carbon atoms by 1.25 times, and silicon carbide by almost 2 times. It also prevents from silicon oxidation. High-temperature annealing of both non-nitrided and nitrided silicon-carbon coatings leads to an increase in the content of the graphite phase and silicon oxide. It was shown if the annealing temperature is increased to 700 °C, the proportion of the integral area of N-Si and N-Csp^3 components of the N1s peak of XPS is decreased, and at the same time the proportion of integral area of the component which correlates with N-Csp^2 and Si-O-N simultaneously is increased. This increase is explained primarily by the annealing of the $sp^3 \rightarrow sp^2$ phase transitions, since the increase in the proportion of the integral area of Csp^2 component of the C1s peak is more significant than the change in the proportion of the integral area of Si-O-N component of the Si2p peak.

Silicon-carbon coatings annealing increases the thermal stability of their mechanical properties: the microhardness and friction coefficient during annealing do not change significantly in contrast to non-nitrided coatings. It is due to the presence of heat-resistant compounds CN_x and Si_3N_4 in the coating structure.

Acknowledgments

The research was produced with the financial support of the Belarusian Republican Foundation for Fundamental Research (contract No. T18M-005).

The study was supported by the Ministry of Science and Higher Education of Russia (project/application No. FSFZ-2020–0022).

References

1 Zhumabekov, A.Zh., Ibrayev, N.Kh., Seliverstova, E.V., & Kamalova, G.B. (2019). Preparation and study of electrophysical and optical propertiesof TiO_2-GO nanocomposite material. *Bulletin of the University of Karaganda-Physics, 2 (94),* 54–60, DOI: 10.31489/2019Ph2/54–60

2 Donnet, C. (1998). Recent progress on the tribology of doped diamond-like and carbon alloy coatings: a review. *Surf. Coat. Technol,* 100–101, 180–186, DOI:10.1016/S0257–8972(97)00611–7.

3 Zhumabekov, A.Zh., Ibrayev, N.Kh., Seliverstova, E.V., & Kamalova, G.B. (2019). Preparation and study of electrophysical and optical propertiesof TiO_2-GO nanocomposite material. *Bulletin of the University of Karaganda-Physics, 2 (94),* 54–60, DOI:10.31489/2019Ph2/54–60

4 Chu, P.K. (2006). Characterization of amorphous and nanocrystalline carbon films. *Mater. Chem. Phys, 96,* 253–277, DOI:10.1016/j.matchemphys.2005.07.048.

5 Voevodin, A.A., & Zabinski, J.S. (1998). Superhard, functionally gradient, nanolayered and nanocomposite diamond-like carbon coatings for wear protection. *Diam. Relat. Mater, 7,* 463–467, DOI:10.1016/S0925–9635(97)00214–8.

6 Miao, Yi Ming, Piliptsou, D.G., Rudenkov, A.S., Rogachev, A.V., Xiaohong Jiang, Sun Dongping, Chaus, A.S., & Balmakou, A. (2017). Structure, mechanical and tribological properties of Ti-doped amorphous carbon films simultaneously deposited by magnetron sputtering and pulse cathodic arc. *Diam. Relat. Mater, 77,* 1–9, DOI: 10.1016/j.diamond.2017.05.010

7 Piliptsou, D.G, Rudenkov, A.S., Rogachev, A.V., Xiaohong, Jiang, Lychnikov, P.A., & Emel'yanov, V.A. (2017). XPS study of the structure of nitrogen doped a-C film. *IOP Conf. Ser.: Mater. Sci. Eng,* 168, DOI:10.1088/1757–899X/168/1/012103.

8 Rudenkov, A.S., Rogachev, A.V., Kupo, A.N., Luchnikov, P.A., & Chicherina, N. (2019). The phase composition and structure of silicon-carbon coatings. *Materials Science Forum, 970,* 283–289, DOI: 10.4028/www.scientific.net/MSF.970.283

9 Raveh, A. (2007). Thermal stability of nanostructured superhard coatings: a review. *Surf. Coat. Technol, 201,* 6136–6142, DOI:10.1016/j.surfcoat.2006.08.131.

10 Cloutier, M. (2014). Long-term stability of hydrogenated DLC coatings: Effects of aging on the structural, chemical and mechanical properties. *Diam. Relat. Mater, 48,* 65–72, DOI: 10.1016/j.diamond.2014.07.002.

11 Ferrari, A.C. (2002). Determination of bonding in diamond-like carbon by Raman spectroscopy. *Diam. Relat. Mater, 11,* 1053–1061, DOI:10.1016/S0925–9635(01)00730–0.

12 Shuleiko, D.V., Zabotnov, S.V., Zhigunov, D.M., Zelenina, A.A., Kamenskih, I.A., & Kashkarov, P.K. (2017). Photoluminescence of amorphous and crystalline silicon nanoclusters in silicon nitride and oxide superlattices. *Semiconductors, 51,* 196–202. DOI: 10.1134/S1063782617020208.

13 Li, H. (2004). Zhang The study of bonding composition of CN_x film by thermal degradation method. *Carbon, 42,* 537–545, DOI: 10.1016/j.carbon.2003.12.036.

14 Quirós, C. (2000). Bonding and morphology study of carbon nitride films obtained by dual ion beam sputtering. *Journal of Vacuum Science and Technology A, 18,* 515–523, DOI:10.1116/1.582218.

15 Ronning, C. (1998). Carbon nitride deposited using energetic species: a reviews on XPS studies. *Physical Review B, 58,* 2207–2215, DOI:10.1103/PhysRevB.58.2207.

16 Lubwama, M. (2012). Characteristics and tribological performance of DLC and Si-DLC films deposited on nitrile rubber. *Surf. Coat. Technology, 206,* 4585–4593, DOI: 10.1016/j.surfcoat.2012.05.015.

17 Kusunoki, I., & Igari, Y. (1992). XPS study of a SiC film produced on St(100) by reaction with a C_2H_2 beam, *Applied Surface Science, 59,* 95–104, DOI: 10.1016/0169–4332(92)90293–7.

18 Castanho Mello, S., & Moreno, R. (1998). Characterization of Si_3N_4 powders in aqueous dispersions. *Cerâmica, 44,* 287–288, DOI: 10.1590/S0366–69131998000400006.

19 Nguen, V.L. (2015). N-doped polymer-derived Si(N)OC: The role of the N-containing precursor. *Journal of Materials Research, 30,* 770–781, DOI: 10.1557/jmr.2015.44.

20 Trusso, S., Vasi, C., & Neri, F. (1999). CNx thin films grown by pulsed laser deposition: Raman, infrared and X-ray photoelectron spectroscopy study. *Thin Solid Films, 335–356,* 219–222, DOI: 10.1016/S0040–6090(99)00503–9.

21 Surzhikov, A.P., Peshev, V.V., Pritulov, A.M., & Gyngazov, S.A. (1999). Grain-boundary diffusion of oxygen in polycrystalline ferrites. *Russian Physics Journal, 42,* 490–495, DOI: 10.1007/BF02508222.

22 Chang J.P. (2000). Profiling nitrogen in ultrathin silicon oxynitrides with angle-resolved x-ray photoelectron spectroscopy. *Journal of Applied Physics, 87,* 4449–4455, DOI: 10.1063/1.373090.

23 Donnet, C. (1999). Diamond-like carbon based functionally gradient coatings for space tribology, *Surf. Coat. Technology, 120, 548–*554, DOI:10.1016/S0257–8972(99)00432–6.

24 Evaristo, M., Polcar, T., & Cavaleiro, A (2014). Tribological behavior of W-alloyed carbon based coat-ings in dry and lubricated sliding contact. *Lubrication Science, 26,* 428–439, DOI: 10.1002/ls.1259.

25 Luchnikov, P.A. (2018). Defect formation in fluoropolymer films at their condensation from a gas phase. *IOP Conf. Ser.: Mater. Sci. Eng, 289,* DOI: 10.1088/1757–899X/289/1/012037.

26 Wang, L.L., Wang, R.Y., Yan, S.J., Zhang, R., Yang, B., Zhang, Z.D., Huang, Z.H., & Fu, D.J. (2013). Structure and properties of Mo-containing diamond-like carbon films produced by ion source assisted cathodic arc ion-plating, *Applied Surface Science, 286,* 109–114, DOI: 10.1016/j.apsusc.2013.09.029.

27 Shi, W.L., Wei, X.T., Zhang, W., Wang, Z.G., Dong, C. H., & Li, S. (2017). Developments and applications of diamond-like carbon. *Applied Mechanics and Materials, 864,* 14–24, DOI: 10.4028/www.scientific.net/AMM.864.14.

28 Surzhikov, A.P., Lysenko, E.N., Malyshev, A.V., Vlasov, V.A., Suslyaev, V.I., Zhuravlev, V.A., Korovin, E.Y., & Dotsenko, O.A. (2014). Study of the radio-wave absorbing properties of a lithium-zinc ferrite based composite. *Russian Physics Journal, 57,* 621 — 626.

29 Surzhikov, A., Frangulyan, T., & Ghyngazov, S. (2014). A thermoanalysis of phase transformations and linear shrinkage kinetics of ceramics made from ultrafine plasmochemical $ZrO_2(Y)$-Al_2O_3powders. *Journal of Thermal Analysis and Calorimetry, 115,* 1439–1445 DOI: 10.1007/s10973–013–3455-y

А.С. Руденков, А.В. Рогачев, С.М. Завадский, Д.А. Голосов,
П.А. Лучников, Г.Ю. Дальская, А.Н. Вторушина

Нитридті кремний-көміртек жабындарының құрылымы және қасиеттері

Мақалада азот иондарымен легирлеу кезінде газ тәріздес ортадан алынған кремний-көміртекті жабындардың құрылымдық және физика-механикалық қасиеттері қарастырылған. Рентгендік фотоэлектронды спектроскопия көмегімен жабындарды талдау кремний-көміртекті жабындарды нитриттеу кремний нитридінің және CN_x және $Si_xO_yN_z$ сияқты қосылыстардың түзілуіне ықпал ететіндігін көрсетеді. Sp2-гибридтендірілген көміртек атомдары мен кремний карбиді мөлшерінің 1,5–2 есе артуы кремнийдің тотығуына жол бермейді. Алынған кремний-көміртекті жабындарды термиялық жағу графит фазасы мен кремний оксидінің құрамын арттырады. Азотпен ($Ar_{57\,\%}$ + $N_{43\,\%}$) жұмыс жасайтын газды легирлеу тек аргонды қолданумен салыстырғанда ұсақ дисперсті құрылымның пайда болуына әкелетіні көрсетілген. Ауаны термиялық жағу кезінде кремний мен көміртектің тотығуынан көміртегі мен оттегі қосылыстарының десорбциясының нәтижесінде көміртектің төмен концентрациясы және оттегінің жоғарылауы байқалған. Сонымен қатар, балқыту жабыннан азоттың десорбциясына әкеледі. Кремний-көміртекті жабындарды нитрлеу олардың құрылымының дисперсиясын жоғарылатады, ал CN_X, Si_3N_4 ыстыққа төзімді қосылыстар жабындардың жылуға төзімділігі мен жылуға төзімділігін жақсартады, сонымен қатар үйкеліс бөліктеріндегі микроқаттылық пен үйкеліс коэффициентін арттырады.

Кілт сөздер: көміртекті жабындар, азоттандыру, кремний, фазалық құрам, ион сәулесінің шашырауы, комбинациялық шашырау спектроскопиясы, XPS, микроқаттылық, үйкеліс коэффициенті.

А.С. Руденков, А.В. Рогачев, С.М. Завадский, Д.А. Голосов,
П.А. Лучников, Г.Ю. Дальская, А.Н. Вторушина

Структура и свойства нитридных кремниево-углеродных покрытий

В статье рассмотрены структурные и физико-механические свойства кремний-углеродных покрытий, нанесенных из газовой среды при легировании ионами азота. Анализ покрытий методом рентгеновской фотоэлектронной спектроскопии показывает, что азотирование кремний-углеродных покрытий способствует образованию нитрида кремния и таких соединений, как CN_x и $Si_xO_yN_z$. Установлено, что увеличение содержания sp2-гибридизованных атомов углерода и карбида кремния в 1,5–2 раза предотвращает окисление кремния. Термический отжиг полученных кремний-углеродных покрытий увеличивает содержание графитовой фазы и оксида кремния. Показано, что легирование рабочего газа азотом ($Ar_{57\,\%}$ + $N_{43\,\%}$) приводит к образованию более мелкодисперсной структуры по сравнению с использованием только аргона. Во время термического отжига на воздухе можно наблюдать пониженную концентрацию углерода и повышенную концентрацию кислорода из-за окисления кремния и углерода с последующей десорбцией соединений углерода и кислорода. Кроме того, отжиг приводит к десорбции азота с покрытия. Азотирование кремний-углеродных покрытий увеличивает дисперсию их структуры, а термостойкие соединения CN_x, Si_3N_4 улучшают термостойкость покрытий и повышают микротвердость, а также коэффициент трения в узлах трения.

Ключевые слова: углеродные покрытия, азотирование, кремний, фазовый состав, ионно-лучевое распыление, спектроскопия комбинационного рассеяния, XPS, микротвердость, коэффициент трения.

DOI 10.31489/2020Ph2/18-23

UDC 538.958, 54.057, 541.145

A.Zh. Zhumabekov, A.E. Sadykova, E.V. Seliverstova

Institute of Molecular Nanophotonics, Buketov Karaganda state University, Kazakhstan
(E-mail: almar89-89@mail.ru)

Synthesis and study of photoelectrical properties of planar ensembles based on TiO_2 and graphene oxide

In this paper, planar structures of various configurations based on TiO_2 and graphene oxide are synthesized. Using SEM, it is shown that graphene oxide forms an insular film both on the surface and under the TiO_2 layer during deposition. As well as SEM images show that TiO_2 nanoparticles on the surface of graphene oxide are distributed as evenly as on the surface of FTO glass. The absorption spectra of synthesized films are a combination of the absorption curves of the original components. In this case, there is a shift of the absorption band of the planar structure nanocomposite to the longwave region. It is shown that in planar ensembles, the photoelectrochemical activity of films is higher only for the first lighting cycle. Research shows that the amount of graphene oxide affects not only the optical and photoelectrochemical properties, but also the electrical parameters. The latter, in turn, show that the resistance decreases by 1.3 times in the planar structure of graphene oxide with 30 layers. It was found that in planar structures of nanocomposite materials, the location of graphene oxide also affects the overall properties of the material. Research shows that the best indicators of photoinduced current generation are registered for the FTO/GO/TiO_2 structure. Thus, a nanocomposite material in a planar structure based on TiO_2 and graphene oxide depends on the architecture of the location and deposited volume of graphene oxide.

Keywords: semiconductors, graphene oxide, TiO_2, planar structure, SEM image, photoinduced current, impedance spectra, photocatalysis.

Introduction

Titanium dioxide (TiO_2) is one of the most affordable photocatalysts due to its physicochemical properties. This semiconductor is distinguished by its strong oxidizing ability, non-toxicity, high chemical stability, photoconversion efficiency and photostability. Currently, it is a very attractive material for photocatalysis, photovoltaics, and optoelectronics. [1–3].

Graphene and its derivatives are very popular due to their electronic, mechanical, thermal and optical characteristics [4–6]. Graphene has found application in nanoelectronics, chemical and biochemical sensing, photocells and in photocatalysis [7–9].

Currently, graphene oxide (GO) is a very promising material for the development of hybrid structures that can combine the properties of both GO and nanosized particles of metal oxide. Hydrothermal synthesis is often used to create these structures. The resulting materials have higher photoelectric, photoelectrochemical, and catalytic properties [10–13] compared to the initial semiconductor.

When used in photocatalytic cells, semiconductor nanoparticles easily form agglomerates in which the generation and transport of charge carriers to the pick-off electrodes decreases. When using graphene oxide, TiO_2 nanoparticles are uniformly distributed over the surface of graphene «sheets» and easily form chemical bonds along the folds of their folds or other defects. The result is a material with improved photocatalytic and photodetecting parameters [14].

In this paper, we propose a method for preparation of planar nanocomposite material based on films of graphene oxide and TiO_2. It is assumed that the addition of graphene oxide to the TiO_2 will improve the photoelectrochemical properties of the semiconductor, which can be used to increase the efficiency of the photocatalyst based on it.

Experiment

To prepare a material with a planar structure, single-layer graphene oxide (GO, Cheaptubes) and TiO_2 (d>21 nm, anatase, 99.7 %, Sigma Aldrich), deionized water (purified using the AquaMax water treatment system), ethanol (anhydrous) were used. The films were deposited on the surface of glass substrates coated with a FTO conductive layer (Fluorine doped tin oxide coated glass slide, ~ 7Ω / sq, Sigma Aldrich).

Graphene oxide films were prepared by airbrushing from water-isopropanol dispersion. The preparation of the GO water-isopropanol dispersion was performed as follows: 4 mg of graphene oxide was mixed with

1.8 ml of isopropanol (C_3H_8O) and 0.4 ml of deionized water. The resulting mixture was sonicated for 2 hours. For film deposition, a graphic airbrush was used, the nozzle diameter of which was equal to 0.2 mm. The resulting films were dried at 80 °C in an oven for at least 3 hours to completely remove the solvent.

TiO_2 semiconductor films were deposited on the surface of FTO substrates by spin-coating method from ethanol-based paste at a substrate rotation speed of 3000 rpm.

To create a planar structure, 2 types of samples were prepared. In the first type, the GO film was sprayed directly onto the FTO surface, and a semiconductor film was deposited over it. In the second type, thin films of graphene oxide were deposited on top of a TiO_2 film. The thickness of the graphene oxide films was different — 2 and 30 layers. The prepared samples of the first type (FTO/GO/TiO_2 structure) with 2 layers of graphene oxide are denoted as 1a, and with 30 layers as 1b. Samples of the second type (FTO/TiO_2/GO structure) with 2 layers of graphene oxide marked as 2a and with 30 layers — as 2b. Next, the obtained films were annealed in an Ar inert atmosphere at 450 °C.

The surface morphology of the obtained composite materials was investigated using a Tescan Mira-3 (Tescan) scanning electron microscope (SEM).

The optical properties of the films were recorded using a Cary-300 spectrophotometer (Agilent). To measure the optical characteristics of the film, they were deposited on quartz substrates. To study the kinetics of transport and recombination of charge carriers, the samples were illuminated with a xenon lamp with a radiation power of 100 mW/cm^2 (Cell Tester Model#CTAAA, Photo Emission Tech. Inc., USA) in a standard two electrode cell. Z–500PRO impedance meter (Elins) was used for this purpose. The amplitude of the applied signal was 25 mV, and the frequency was varied from 1 MHz to 100 MHz. Platinum films deposited by the electrochemical method from an ethanol solution of H_2PtCl_6 onto glass substrates with a conductive layer of FTO were used as counter electrode. The electrodes were glued together. Meltonix polymer film was used as a gasket between the working and counter electrode in the cell. Iodolyte was used as the electrolyte. The area of the illuminated area was equal to 0.16 cm^2. In all samples, the electrolyte volume in the cells, as well as the thickness and area of the films were the same. The measured impedance spectra were analyzed using the EIS analyzer program. The equivalent electrical circuit of the electrochemical cell used for analysis was shown in ref. [15].

The transition photocurrent characteristics of the obtained materials were studied by recording the photocurrent in a standard three electrode photoelectrochemical cell with a quartz window on a P–30J potentiostat-galvanostat (Elins). Ag/AgCl electrode was used as a reference. The radiation source was served a diode lamp with a power of 35 mW/cm^2. The studied samples were deposited by centrifugation on the surface of substrates with FTO, which were connected to the working electrode. A platinum electrode was connected to the negative potential. The measurements were carried out in an electrolyte of 0.1 M NaOH.

Results and its discussion

During the study of the structural characteristics of the synthesized samples by using of SEM (Figure 1), it was found that in planar structures, as in samples of pure TiO_2, titanium dioxide particles are aggregated.

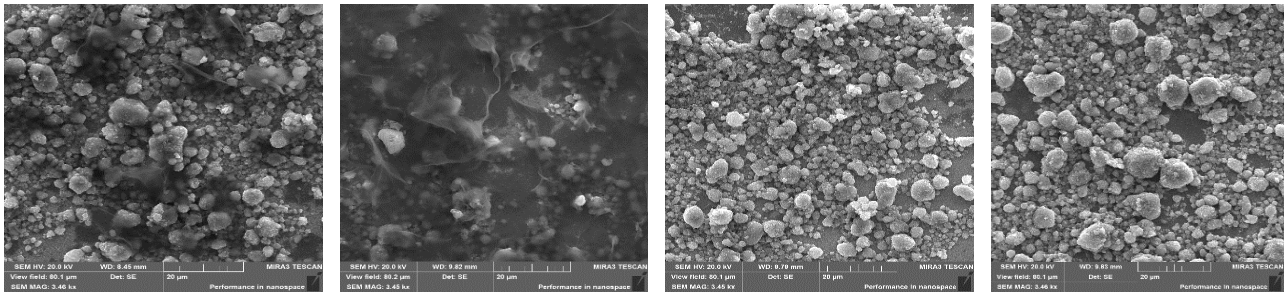

1a 1b 2a 2b

Figure 1. SEM image of planar structures

From SEM images of films 1a and 2a, in which the thickness of the graphene oxide films was equal to 2 layers, it can be seen that GO is deposited in the form of an island film. In the film with 30 layer of GO, graphene oxide almost completely covers the substrate. At the same time, «folds» and «wrinkles» that are formed during the deposition of graphene oxide are clearly distinguishable on the surface of TiO_2.

The data, obtained under study of optical characteristics, are shown in Figure 2. It is known that the absorption spectrum of TiO_2 appears in the UV region of the spectrum at about 380 nm. Graphene oxide also absorbs in the UV range; its absorption spectrum reaches a maximum at 230 nm. In this case, GO films are almost transparent in the wavelength range from 400 to 800 nm [16, 17].

In the planar structures of GO/TiO_2 and TiO_2/GO the absorption band of the semiconductor broadens to the visible spectral range up to 510 nm (Figure 2). It is also seen that the nanocomposite actively absorbs light in the UV region of the spectrum. Previously, it was shown in refs. [12, 18] that the semiconductor band gap changes in the nanocomposites. This contributes to a wider spectral sensitivity of nanocomposite materials, as well as improving their photoelectrochemical properties.

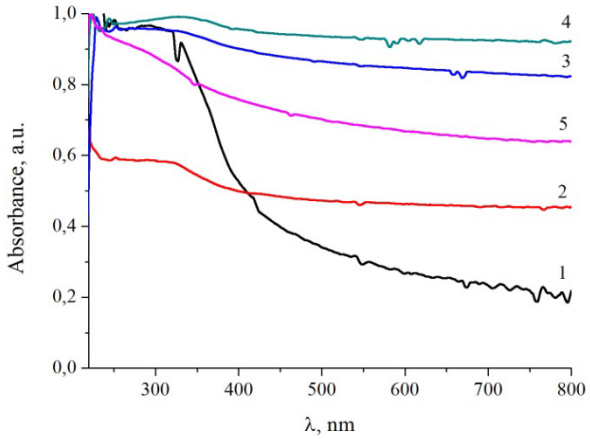

Figure 2. Normalized absorption spectra of films of: 1 — TiO_2; 2 — 1a, 3 — 1b, 4 — 2a, 5 — 2b

Next, the photoelectric characteristics of TiO_2 and planar structures were studied, with the help of which their photocatalytic activity can be estimated. The photoinduced current values was measured for 20 seconds when the light was turned on and off cyclically.

The photocurrent of a TiO_2 — based film was equal to ~23 μA (Figure 3a). When sample 1b was irradiated, the photocurrent was increased of 1.5 times. Also, a high photocurrent generation for the first switching cycle was recorded for films 1a, where the film thickness of graphene oxide was 2 layers. Thinner films generate a little less current. At the same time, for samples where graphene oxide was deposited on top of the conductive layer, the parameters were lower on 10 %.

Since the efficiency of the photocatalytic splitting of water into molecular oxygen and hydrogen will directly depend on the number of photoinduced electrons, it can be assumed that when using planar structures based on TiO_2 and graphene oxide, hydrogen generation will be higher compared to other similar nanocomposites.

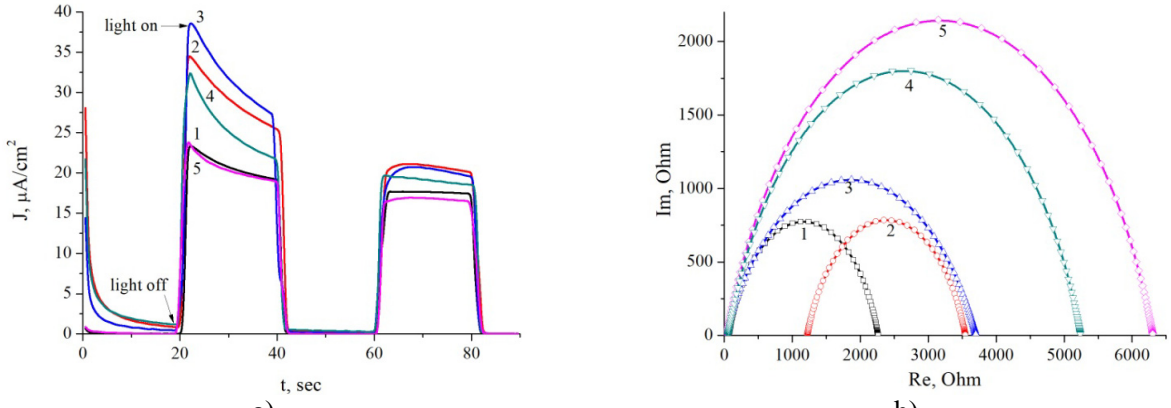

Figure 3. Transient characteristics of the photocurrent (a) and impedance spectra in the Nyquist plot (b) of films: 1 — TiO_2; 2 — 1a, 3 — 1b, 4 — 2a, 5 — 2b.

It should be noted that lower photocurrent generation for thinner graphene oxide films is related to their structure. As was shown earlier in [19], thin GO films are inhomogeneous, which leads to large values of the transport resistance of charge carriers. Nevertheless, it can be unequivocally stated that the presence of graphene oxide in the planar structure leads to an increase in the photocatalytic activity of semiconductor coatings. It is much more efficient when graphene oxide is located under a TiO_2 layer.

Further, the electrophysical characteristics of planar structures and nanocomposite material were studied. The impedance spectra in the Nyquist coordinates based on the films are presented in Figure 3b. Based on the obtained impedance spectra, the main electric transport properties of the films were calculated. Parameters, such as R_k — charge-transfer resistance related to recombination of electron, R_w — electron transport resistance in TiO_2-GO, k_{eff} — effective rate constant for recombination and τ_{eff} — effective lifetime of electrons [20] were obtained.

Figure 3b shows that the diameter of the hodograph of a TiO_2 film is smaller than that of most other films. This means that the studied samples have a smaller amount of charge transfer resistance. The addition of graphene oxide makes it possible results in lower the resistance values R_k and R_w of semiconductor samples.

Table 1 shows the values of the electrophysical parameters of the TiO_2 film and planar structures. Using the EIS — analyzer software package, R_k and R_w w are calculated, and k_{eff} — is determined by the maximum of the hodograph arc according to the formula $\omega_{max} = k_{eff}$. The film thickness was determined using a TESCAN Mira3 scanning electron microscope.

Table 1

The value of the electrophysical parameters of TiO_2 films and planar structures

Sample	k_{eff}, s^{-1}	τ_{eff}, ms	R_k, Ohm	R_w, Ohm
TiO_2	13.895	72	2194.0	69.3
1a	5,1795	193	2327,9	1221,8
1b	3,7276	268	3693,7	11,8
2a	2,6827	373	6274,8	30,8
2b	2,6827	373	5185,2	54,8

In the sample 1a, the charge transfer resistance is R_k = 2327.9 Ohms and is the smallest value among planar structures were obtained. But R_w in this film is equal to 1221.8 Ohms, which means that the resistance to electronic transport in the film is very large compared to other samples. With an increase in the number of graphene oxide layers to 30, the charge transfer resistance also increases by 1.6 times. Nevertheless, this sample characterizes the best electrophysical parameters compared to other planar structures.

When the GO film was deposited onto TiO_2surface, the resistance of both charge transfer and electron transport of such a structure were also increased. In sample 2a, R_k = 6274.8 Ohms and in 1.7 times more than in sample 1b. Also in sample 2b, the value of the charge transfer resistance is R_k = 5185.2 Ohms, which is in 1.4 times higher than the value for the more optimal sample 1b. Thus, it was shown that the architecture of a planar nanocomposite (the location of GO on the surface or under TiO_2) affects its electrophysical parameters. At the same time, improved properties show samples where GO films are deposited between TiO_2 and FTO. However, when graphene oxide is added to TiO_2 in planar structures, the electrophysical characteristics do not decreases with respect to resistance. This is due to the high resistance values of graphene oxide itself.

Conclusion

Samples based on graphene oxide and TiO_2 were prepared in the form of a planar structure and their photoelectric and electrophysical characteristics were studied. SEM studies have shown that graphene oxide forms an island film during deposition, both on the surface and under the TiO2 layer. SEM images clearly show graphene oxide sheets. Measurements of the optical characteristics of the synthesized material showed that the absorption spectrum of planar structures corresponds to the spectra of the starting components. In this case, a slight shift of the absorption band of the nanocomposite to the long-wavelength region was observed. The transient characteristics of the photocurrents of planar structures show an increase in the photoinduced current only for the first illumination cycle, and in the future the photocurrent decreases. Studies of the impedance spectra showed that the addition of graphene oxide in the form of a planar structure does not contribute to a decrease in the resistance of semiconductor films due to the high resistance value of graphene oxide itself.

The results can be used for development of photocatalytic materials for the UV and visible spectral ranges, as well as relevant in areas requiring photodegradation of organic compounds.

Acknowledgment

This work had been performed within the framework of the research grant AP05132443 and BR05236691, funded by the Ministry of Education and Science of the Republic of Kazakhstan.

References

1 Fujishima, A., & Honda, K. (1972). Electrochemical photolysis of water at a semiconductor electrode. *Nature*, *238*, 37–38. DOI: 10.1038/238037a0

2 Gadgil, T., Ibrayev, N., & Nuraje, N. (2016). Photocatalytic Water Oxidation, in: Heterogeneous photocatalysis: from fundamentals to green applications, series: Green Chemistry and Sustainable Technology. *Springer*, 33–61. DOI: 10.1007/978–3-662–48719–8_2

3 Shen, Sh., Kronawitter, C., & Kiriakidis, G. (2017). An overview of photocatalytic materials. Journ*al of Materiomics*., *3*, 1–2. DOI: 10.1016/j.jmat.2016.12.004

4 Geim, A.K., & Novoselov, K.S. (2007). The Rise of Graphene. *Nature Materials*, *6*, 183–191. DOI: 10.1038/nmat1849

5 Allen, M.J., Tung, V.C., & Kaner, R.B. (2010). Honeycomb Carbon: A Review of Graphene. *Chem. Rev.*, *110*, *1*, 132–145. DOI: 10.1021/cr900070d

6 Bunch, J.S., van der Zande, A.M., Verbridge, S.S., Frank, I.W., Tanenbaum, D.M., & Parpia, J.M., et al. (2007). Electronmechanical Resonators from Graphene Sheets. *Science*. *315*, 490–493. DOI: 10.1126/science.1136836

7 Ozer, L.Y., Garlisi, C., Oladipo, H., Pagliaro, M., Sharief, S.A., & Yusuf, A., et al. (2017). Inorganic Semiconductors-Graphene Composites in Photo (electro) catalysis: Synthetic Strategies, Interaction Mechanisms and Applications. *J. Photochem. and Photobiol. C: Photochem. Rev.*, *33*, 132–164. DOI: 10.1016/j.jphotochemrev.2017.06.003

8 Dubey, P.K., Tripathi, P., Tiwari, R.S., Sinha, A.S.K., & Srivastava, O.N. (2014). Synthesis of reduced graphene oxide-TiO_2 nanoparticle composite systems and its application in hydrogen production. *Int. J. Hydrogen energy*., *39*, 16282–16289. DOI: 10.1016/j.ijhydene.2014.03.104

9 Li, Q., Guo, B.D., Yu, J.G., Ran, J.R., Zhang, B.H., & Yan, H.J., et al. (2011). Highly efficient visible-light-driven photocatalytic hydrogen production of CdS-cluster-decorated graphene nanosheets. *J. Am. Chem. Soc., 133*, 10878–10884. DOI: 10.1021/ja2025454

10 Zhumabekov, A.Zh., Ibrayev, N.Kh., Seliverstova, E.V., & Kamalova, G.B. (2019). Preparation and study of electrophysical and optical properties of TiO_2-GO nanocomposite material. *Bull. of the Univ. of Karag.-Phys.*, *94*, *2*, 54–63. DOI: 10.31489/2019Ph2/54–60

11 Zhumabekov, A.Zh., Seliverstova, E.V., & Ibrayev, N.Kh. (2019). Investigation of photocatalytic activity of TiO_2–GO nanocomposite. *Eur. Phys. Tech. J.*, *16*, *1,* 42–46.

12 Ibrayev, N., Zhumabekov, A., Ghyngazov, S., & Lysenko, E. (2019). Synthesis and study of the properties of nanocomposite materials TiO_2-GO and TiO_2-rGO. *Materials Research Express*, *6,* 1–11. DOI: 10.1088/2053–1591/ab51a3

13 Ibrayev, N., Seliverstova, E., & Zhumabekov, A. (2018). Preparation of graphene nanostructured films for photovoltaics. *IOP Conf. Series: Materials Science and Engineering.*, *447*. DOI: 10.1088/1757–899X/447/1/012068

14 Woan, K., Pyrgiotakis, G., & Sigmund, W. (2009). Photocatalytic carbon-nanotube-TiO_2 composites. *Advanced Materials, 21*, 2233–2229. DOI: 10.1002/adma.200802738

15 Zhang, B., Wang, D., & Hou, Y. (2013). Facet-Dependent Catalytic Activity of Platinum Nanocrystals for Triiodide Reduction in Dye-Sensitized Solar Cells. *Sci. Rep.*, *3*, 1836–1843. DOI: 10.1038/srep01836

16 Stankovich, S., Dikin, D.A., Piner, R.D., Kohlhaas, K.A., Kleinhammes, A., & Jia, Y., et al. (2007). Synthesis of graphene-based nanosheets via chemical reduction of exfoliated graphite oxide. *Carbon*, *45*, 1558–1565. DOI: 10.1016/j.carbon.2007.02.034

17 Lambert, T.N., Luhrs, C.C., Chavez, C.A., Wakeland, S., Brumbach, M.T., & Alam, T.M. (2010). Graphite oxide as a precursor for the synthesis of disordered graphenes using the aerosol-through-plasma method. *Carbon*, *48*, 4081–4089. DOI: 10.1016/j.carbon.2010.07.015

18 Zhumabekov, A.Zh., Ibrayev, N.Kh., & Seliverstova, E.V. (2020). Photoelectric properties of a nanocomposite derived from reduced graphene oxide and TiO_2. *Theoretical and Experimental Chemistry*. *55*, *6*, 398–406. DOI: 10.1007/s11237–020–09632–8

19 Dzhanabekova, R.Kh., Seliverstova, E.V., Zhumabekov, A.Zh., & Ibrayev, N.Kh. (2019). Fabricating and Examining of Langmuir Films of Reduced Graphene Oxide. *Rus. Jour. of Phys. Chem. A.*, *93*, *2*, 338–342. DOI: 10.1134/S0036024419020092

20 Adachi, M., Murata, Y., Takao, J., & Jinting, J. (2004). Highly efficient dye–sensitized solar cells with a titania thin–film electrode composed of a network structure of single–crystal–like TiO_2 nanowires made by the «oriented attachment» mechanism. *J. Am. Chem. Soc.*, *126*, 14943–14949. DOI: 10.1021/jp061693u

А.Ж. Жумабеков, А.Е. Садыкова, Е.В. Селиверстова

TiO_2 және графен оксиді негізіндегі планарлық ансамбльдердің фотоэлектрлік қасиеттерін зерттеу және синтездеу

Мақалада TiO_2 және графен оксиді негізінде әртүрлі конфигурациялы планарлы құрылымдар синтезделген. СЭМ көмегімен графен оксиді тозаңдағанда TiO_2 қабатының астында аралдық пленканы түзеді. Сондай-ақ, графен оксиді бетінде TiO_2 нанобөлшектері FTO шыны бетінде біркелкі бөлінген. Синтезделген пленкалардың сіңіру спектрлері бастапқы компоненттердің сіңіру қисықтарының комбинациясын білдіреді. Бұл ретте жоспарлы құрылымның нанокомпозит жұту жолағының ұзын толқынды аймаққа ауысуы байқалған. Планарлық ансамбльдерде пленкалардың фотоэлектрохимиялық белсенділігі жарықтандырудың бірінші циклі үшін ғана жоғары екендігі көрсетілген. Зерттеу нәтижесі көрсеткендей, графен оксидінің саны оптикалық және фотоэлектрохимиялық қасиеттерге ғана емес, сонымен қатар электр параметрлеріне де әсер етеді. Соңғылары өз кезегінде, 30 қабатты графен оксидінің жоспарлы құрылымында 1,3 есе кедергінің азайғанын көрсетті. Нанокомпозитті материалдардың планарлы құрылымдарында графен оксидінің орналасуы да материалдың жалпы қасиеттеріне әсер ететіні анықталған. FTO/GO/TiO_2 құрылымы үшін фотоиндуцирленген ток генерациясының ең жақсы көрсеткіштері тіркелгенін көрсеткен. Осылайша, TiO_2 және графен оксиді негізіндегі планарлық құрылымдағы нанокомпозиттік материал орналасу архитектурасына және графен оксиді жағылған көлеміне байланысты.

Кілт сөздер: жартылай өткізгіштер, графен оксиді, TiO_2, планарлық құрылым, СЭМ суреті, фотоиндуцирленген ток, импеданс спектрі, фотокатализ.

А.Ж. Жумабеков, А.Е. Садыкова, Е.В. Селиверстова

Синтез и исследование фотоэлектрических свойств планарных ансамблей на основе TiO_2 и оксида графена

В статье синтезированы планарные структуры различной конфигурации на основе TiO_2 и оксида графена. При помощи СЭМ показано, что при напылении оксид графена формирует островковую пленку как на поверхности, так и под слоем TiO_2. А также СЭМ-изображения показывают, что наночастицы TiO_2 на поверхности оксида графена распределены так же равномерно, как и на поверхности FTO стекла. Спектры поглощения синтезированных пленок представляют комбинацию кривых поглощения исходных компонентов. При этом наблюдается сдвиг полосы поглощения нанокомпозита планарной структуры в длинноволновую область. Показано, что в планарных ансамблях фотоэлектрохимическая активность пленок выше только для первого цикла освещения. По результатам исследования видно, что количество оксида графена влияет не только на оптические и фотоэлектрохимические свойства, но и на электрические параметры. Последние, в свою очередь, показывают, что происходит уменьшение сопротивления в 1,3 раза в планарной структуре оксида графена с 30-м слоем. Установлено, что в планарных структурах нанокомпозитных материалов расположение оксида графена также влияет на общие свойства материала. Определено, что для структуры FTO/GO/TiO_2 зарегистрированы наилучшие показатели генерации фотоиндуцированного тока. Таким образом, можно заключить, что нанокомпозитный материал в планарной структуре на основе TiO_2 и оксида графена зависит от архитектуры расположения и нанесенного объема оксид графена.

Ключевые слова: полупроводники, оксид графена, TiO_2, планарная структура, СЭМ-изображение, фотоиндуцированный ток, импеданс-спектры, фотокатализ.

DOI 10.31489/2020Ph2/24-31

UDC 535.8, 535.015, 543.4

R.Kh. Dzhanabekova, M.S.Kim, N.Kh. Ibrayev

Institute of Molecular Nanophotonics, Ye.A. Buketov Karaganda State University, Kazakhstan
(E-mail: rumiya_j@mail.ru)

Detection of polycyclic aromatic hydrocarbons by surface enhanced Raman scattering on colloidal silver substrates

The present work reports on the possibility of polycyclic aromatic hydrocarbons (PAHs) detection by surface enhanced Raman scattering (SERS) on substrates coated with colloidal silver stabilized with cetyltrimethylammonium bromide (CTAB). It was shown that cetyltrimethylammonium bromide acts not only as a stabilizer of metal nanoparticles, but also as modifying agent that promotes the concentration of hydrophobic PAH molecules near the amplified electromagnetic field of plasmon silver nanoparticles. Anthracene and pyrene were used as model analytes. To determine the sensitivity of the prepared SERS active coating, ethanol solutions of the analyzed substances with concentrations in the range of $2 \cdot 10^{-4}$ — 10^{-6} mol/L were used. The lowest concentrations of solutions for which anthracene and pyrene are found on the tested substrates were equal to $2.5 \cdot 10^{-6}$ M and $5 \cdot 10^{-5}$ M, respectively. These results indicate that substrates are more sensitive to anthracene than to pyrene. The work also shows that various PAH molecules can be detected by characteristic peaks in a complex mixture without preliminary separation of the components.

Keywords: surface-enhanced Raman scattering, polycyclic aromatic hydrocarbons, anthracene, pyrene, silver nanoparticles, cetyltrimethylammonium bromide, SERS sensor, plasmon particles.

Introduction

Polycyclic aromatic hydrocarbons (PAHs) are strong environmental pollutants. PAHs are mainly formed and evolved during oil refining, mineral oil and coal combustion. In addition, PAHs are formed during smoking, during high-temperature processing of food products. Most organic pollutants have carcinogenic and mutagenic properties. Although PAHs are released into the environment in relatively small quantities, they are quite resistant to external influences and can accumulate in soil and water to dangerous concentrations [1–3].

Currently, chromatographic methods, such as liquid chromatography with fluorescence methods and gas chromatography in combination with mass spectroscopy, are used to detect PAHs [1–4]. Chromatography methods have high sensitivity and reproducibility, however, the analysis requires long and complex sample preparation.

A promising alternative to chromatographic methods for PAHs deterction is surface-enhanced Raman spectroscopy (SERS). SERS is based on a giant amplification of the electromagnetic field induced by noble metal nanoparticles as a result of plasmon resonance. An increase in the electromagnetic field at distances up to several tens of nanometers from nanoparticles significantly increases the changes in the polarization of the electron cloud and, therefore, the Raman signal [5–7]. The work of [8] demonstrated that the maximum gain can reach values of 10^{10}–10^{11}. The maximum signal amplification is facilitated by a combination of long-range electromagnetic and short-range chemical amplifications [5, 6, 9].

It is well known [9] that SERS active molecules usually exhibit good affinity for metals, which leads to their approaching to the surface. And most of the currently available developments and commercial SERS sensors are focused precisely on such analytes. At the same time, there are a number of organic compounds containing hydrophobic molecules with low affinity for metals that not adsorbed on the active surface of «traditional» SERS substrates and cannot be determined by this method. PAHs belong to this category of unconventional analytes.

Recently, researchers have made significant efforts to develop methods to facilitate the use of SERS in the detection of unconventional analytes. For these purposes, metal nanostructures are modified with substances that promote the adsorption of hydrophobic molecules near the plasmonic nanoparticles. Alkylthiols [10, 11], calixarenes [12, 13], and cyclodextrins [14, 15] are quite successfully used as modifiers.

In the present work, the possibility of using silver nanoparticles (Ag NPs) in the complex with cetyltrimethylammonium bromide (CTAB) for the determination of PAHs by the SERS method was studied. CTAB is a cationic surfactant that is often used for the controlled synthesis of silver and gold nanoparticles

as a stabilizing agent [16–18]. At the same time, CTAB was used to modify plasmon nanoparticles to determine PAHs only in very few studies [19, 20].

A feature of the presented work is the use of a simple, one-step method for producing Ag NPs stabilized by CTAB as a SERS sensor for detection individual and mixed PAHs.

Experimental

Synthesis of colloidal silver particles. Silver nanoparticles were obtained by the reduction of silver nitrate with sodium borohydride. Cetyltrimethylammonium bromide was used to stabilize the nanoparticles. The preparation of silver nanoparticles was performed according to the technique proposed in [18]. The synthesis was carried out in a 50 ml beaker, with continuous sonication. CTAB (0.22 g) and silver nitrate (0.085 g) were successively dissolved in 10 ml of deionized water. After 10 minutes of sonication, 2.5 ml of a freshly prepared sodium borohydride solution (0.04 g) was droped. After the addition of the reducing agent, the solution was kept in an ultrasonic bath for another 20 minutes.

Preparation of analyte solutions. Anthracene and pyrene were used as model PAHs. Stock solutions of anthracene and pyrene in ethanol with a concentration of 10^{-3} mol/L were prepared. The studied solutions with PAH concentrations in the range of $2 \cdot 10^{-4}$–10^{-6} mol/L were prepared immediately before measurements by successive dilution of the stock solution.

Preparation of SERS-active substrates. Silica glasses were used as the basis for SERS-active substrates. 15 μl of silver hydrosol was deposited on glass and distributed over the surface with a glass rod. The prepared film was dried at room temperature in air.

Measurements. The absorption spectrum of the synthesized silver hydrosol was measured on a Cary 300 spectrophotometer (Agilent). The sizes of the nanoparticles were determined by dynamic light scattering using the Zetasizer NanoS (Malvern) system. To measure the absorption spectrum and sizes of Ag NPs, the initial solution was previously diluted 150 times.

The Raman spectra of the samples were measured on a Confotec MR 520 scanning laser Raman spectrometer. A laser with λ=532 nm radiation was used to excite Raman spectra. The laser power on the sample was 2.2 mW, and the spectral accumulation time was 10 s. To measure the Raman spectra, 5 μl of the corresponding PAH solution were dropped onto the surface of the prepared substrates; the drop was dried under natural conditions. Spectra were recorded on each sample from 7 points; the obtained data were averaged. For more convenient visualization, the spectra in the presented graphs are spaced relative to each other.

Results and discussion

Silver nanoparticles obtained by the borohydride method in the presence of CTAB form stable aquasols [18]. The absorption spectrum of the synthesized aquazole in the visible region with a maximum at 417 nm (Figure 1) indicates the formation of plasmon silver nanoparticles [21]. The study of Ag NPs by the method of dynamic light scattering showed the presence in the solution of particles ranging in size from 1 to 18 nm.

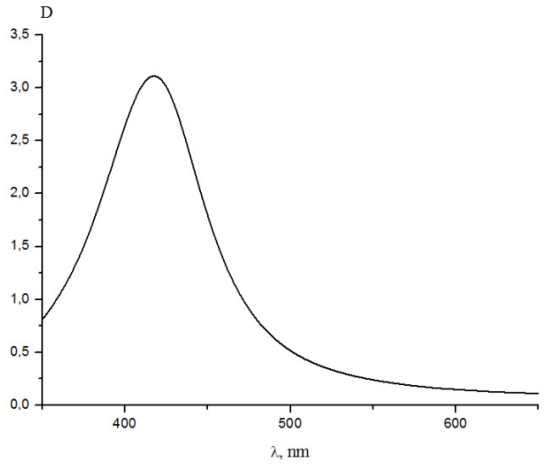

Figure 1. Absorption spectrum of Ag NPs solution

CTAB is a cationic surfactant that, on the one hand, plays the role of a stabilizer to prevent aggregation of silver nanoparticles. On the other hand, the presence of a long hydrocarbon tail contributes to the solubilization of hydrophobic molecules, as a result of which PAH molecules are concentrated and held near metal nanoparticles. Thus, the analyte molecules find themselves in the zone of the amplified electromagnetic field of the plasmon particles.

Figure 2 shows the Raman spectrum of crystalline anthracene and the SERS spectra of the substrate (AgNPs — CTAB) and $2 \cdot 10^{-4}$ M anthracene solution on the substrate.

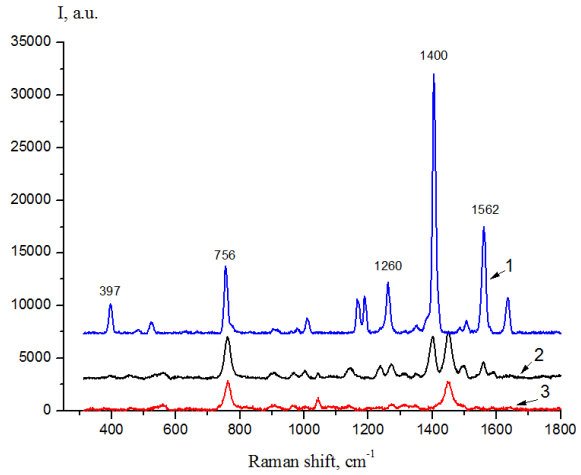

Figure 2. Raman spectrum of crystalline anthracene (1), SERS spectra of the $2 \cdot 10^{-4}$ M anthracene solution on the substrate (2) and the substrate (3)

The SERS spectrum of the substrate is characterized by two main Raman bands at 760 and 1450 cm^{-1}, which belong to the CTAB [19, 20]. The obtained Raman spectrum of crystalline anthracene has characteristic bands of medium and high intensity at 397, 756, 1260, 1400, and 1562 cm^{-1}. In the SERS spectrum of $2 \cdot 10^{-4}$ M anthracene solution on the substrate, bands belonging to both anthracene (397, 1260, 1400 and 1562 cm^{-1}) and CTAB (760, 1450 cm^{-1}) are clearly observed. The Raman band of anthracene at 756 cm^{-1} coincides with the CTAB Raman band at 760 cm^{-1} and cannot be used for analytical purposes.

The SERS spectrum obtained for $2 \cdot 10^{-4}$ M pyrene solution on the substrate is shown in Figure 3. The Raman spectrum of crystalline pyrene and the SERS spectrum of the substrate are also presented for comparison. The Raman spectrum of crystalline pyrene is characterized by frequency shifts at 406, 594, 1242, 1408, 1597, and 1630 cm^{-1}. In the SERS spectra of the pyrene solution, the bands at 406, 1242, 1408, 1597, and 1630 cm^{-1}, which belong to the pyrene, and the bands at 760 and 1450 cm^{-1}, which belong to the substrate, are most clearly observed.

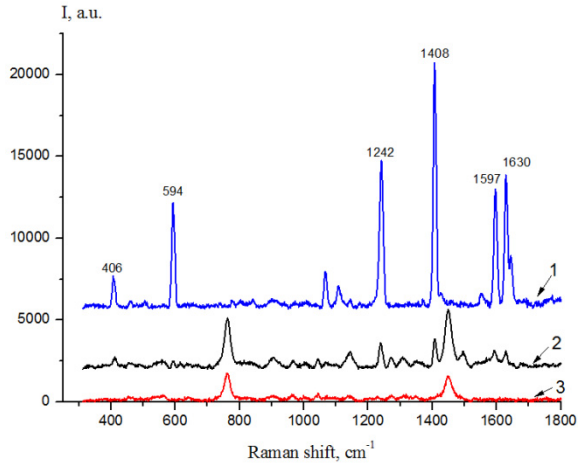

Figure 3. Raman spectrum of crystalline pyrene (1), SERS spectra of the $2 \cdot 10^{-4}$ M pyrene solution on the substrate (2) and the substrate (3)

To determine the minimum concentration of PAHs on the test coating, we measured the SERS spectra of solutions in the concentration range of $2 \cdot 10^{-4}$–10^{-6} mol/L. SERS spectra of anthracene and pyrene with different concentrations are shown in Figures 4 and 5.

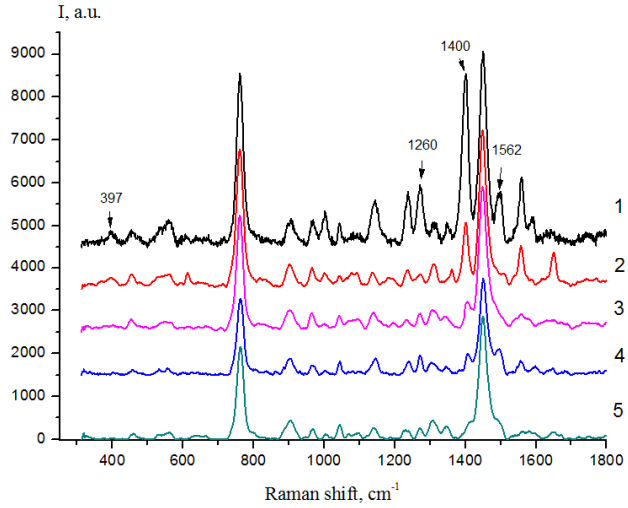

Figure 4. SERS spectra of anthracene solutions with different concentration, mol/L:
1– $2 \cdot 10^{-4}$, 2 — $5 \cdot 10^{-5}$, 3 — $5 \cdot 10^{-6}$, 4 — $2.5 \cdot 10^{-6}$, 5 — 10^{-6}

To determine the content of anthracene, an intense Raman scattering band at 1400 cm^{-1} was used. As can be seen from Figure 4, this band is clearly observed in the SERS spectra of anthracene for solutions of $2 \cdot 10^{-4}$– $2.5 \cdot 10^{-6}$ mol/L. In the SERS spectrum of anthracene with a concentration of 10^{-6} mol/L, the characteristic band at 1400 cm^{-1} is practically not detected. Thus, $2.5 \cdot 10^{-6}$ mol/L is the lowest concentration of the solution in which anthracene is found on the tested substrates.

Figure 5 shows the SERS spectra of different concentrations of pyrene. To detect pyrene, several Raman bands can be used as analytical: at 1242, 1408, 1597, and 1630 cm^{-1}. It can be seen from the obtained spectra that for solutions with concentration of $5 \cdot 10^{-6}$ mol/L and lower, characteristic peaks of pyrene are practically not detected. The minimum detectable pyrene concentration in the solution was $5 \cdot 10^{-5}$ mol/L.

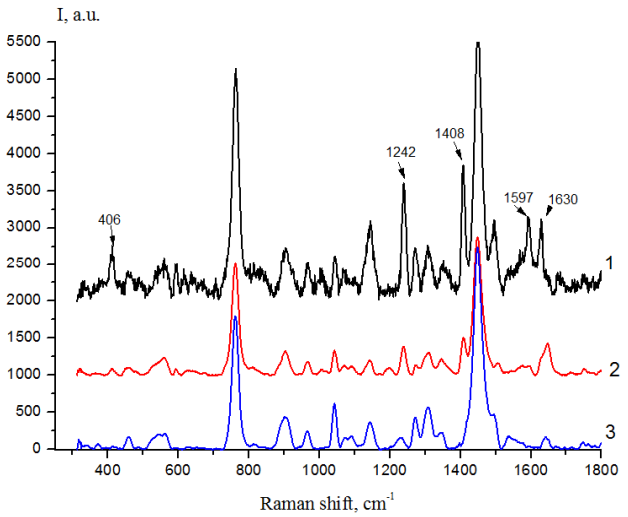

Figure 5. SERS spectra of pyrene solutions with different concentration, mol/L:
1– $2 \cdot 10^{-4}$, 2 — $5 \cdot 10^{-5}$, 3 — $5 \cdot 10^{-6}$

The results obtained indicate that the coating based on Ag NPs with CTAB is more sensitive to anthracene.

The identification of PAHs was also carried out in a complex system that simultaneously contains anthracene and pyrene. Figure 6 presents the SERS spectrum obtained for solution containing 10^{-4} mol/L anthracene and 10^{-4} mol/L pyrene.

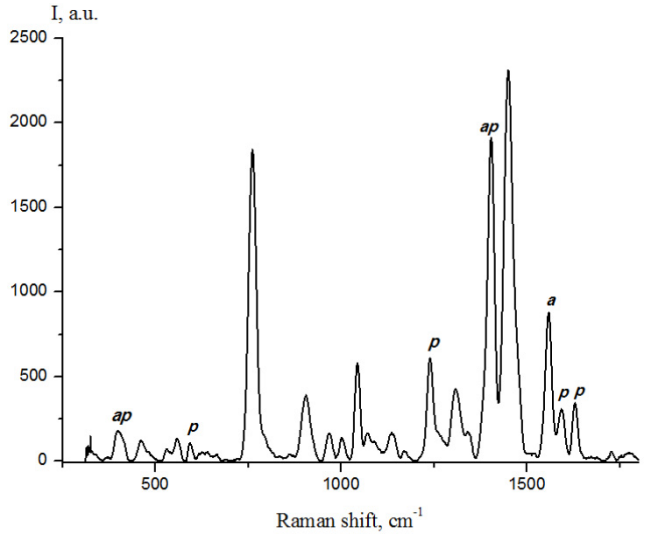

Figure 6. SERS spectrum of mixed solution of anthracene and pyrene

The anthracene bands in the figure are indicated by the letter ***a***, and the pyrene bands are indicated by the letter ***p***. The anthracene bands at 397 and 1400 cm^{-1} overlap with the pyrene bands at 406 and 1408 cm^{-1} and, therefore, cannot be used for identification in this mixture. However, the main peaks of individual PAHs are well distinguishable. Thus, the tested SERS coating can be used to identify PAHs in complex systems without prior separation of components.

Conclusion

It was shown that colloidal silver nanoparticles stabilized by CTAB can be used to obtain the SERS active substrate. In the resulting system, CTAB acts not only a stabilizer of silver nanoparticles, but also a modifier that promotes the concentration and holding of PAH molecules near the surface of plasmon particles. The maximum concentration of solutions in which anthracene and pyrene were detected are equal to $2.5 \cdot 10^{-6}$ M and $5 \cdot 10^{-5}$ M, respectively. With further optimization, the prepared substrates can be used as sensors both in determining individual PAHs and in the simultaneous detection of individual components in complex mixtures.

This work was carried out as part of the research project BR05236691, funded by the Ministry of Education and Science of the Republic of Kazakhstan.

References

1 Другов Ю.С. Экологическая аналитическая химия / Ю.С. Другов. — М.: Москва, 2000. — 432 с.

2 Другов Ю.С. Методы анализа загрязнений воздуха / Ю.С. Другов, А.В. Беликов, Г.А. Дьякова, В.М. Тульчинский. — М.: Химия, 1984. — 384 с.

3 Plaza-Bolanos P. Polycyclic aromatic hydrocarbons in food and beverages. Analytical methods and trends / P. Plaza-Bolanos, A.G. Frenich, J.L.M. Vidal // J. Chromatogr. A. — 2010. — Vol. 1217. — P. 6303–6326.

4 Moret S. Polycyclic aromatic hydrocarbons in edible fats and oils: occurrence and analytical methods. / S. Moret, L.S. Conte // J. Chromatogr. A — 2000. — Vol. 882. — P. 245–253.

5 Moskovits M. Surface-enhanced spectroscopy / M. Moskovits // Rev. Mod. Phys. — 1985. — Vol. 57. — P. 783–826.

6 Etchegoin L.R., Principles of Surface-Enhanced Raman Spectroscopy and Related Plasmonic Effects / L.R. Etchegoin. — Amsterdam: Elsevier Science, 2008. — 633 p.

7 Гигантское комбинационное рассеяние / под ред. Р. Ченга, Т. Фуртака. — М.: Мир, 1984. — 408 с.

8 Etchegoin P.G. A perspective on single molecule SERS: current status and future challenges / P.G. Etchegoin, E.C. Le Ru // Phys. Chem. Chem. Phys. — 2008. — Vol. 10. — P. 6079–6089.

9 Поверхностно-усиленная рамановская спектроскопия (SERS): аналитические, биофизические и биомедицинские приложения / под ред. С.М. Шлюкера. — М.: Техносфера, 2017. — 328 с.

10 Gu X. SERS detection of polycyclic aromatic hydrocarbons on a bowl-shaped silver cavity substrate / X. Gu, Sh. Tian, Q. Zhou, J. Adkins, Zh. Gu, X. Li et al. // RSC Adv. — 2013. — Vol. 3. — P. 25989–25996.

11 Jones C.L. Partition layer-modified substrates for reversible surface-enhanced Raman scattering detection of polycyclic aromatic hydrocarbons / C.L. Jones, K.C. Bantz, C.L. Haynes // Anal. Bioanal. Chem. — 2009. — Vol. 394. — P. 303–311.

12 Guerrini L. Functionalization of Ag Nanoparticles with Dithiocarbamate Calix [4] arene As an Effective Supramolecular Host for the Surface-Enhanced Raman Scattering Detection of Polycyclic Aromatic Hydrocarbons / L. Guerrini, J.V. Garcia-Ramos, C. Domingo, S. Sanchez-Cortes // Langmuir. — 2006. — Vol. 22. — P. 10924–10926.

13 Shi X. Trace analysis of polycyclic aromatic hydrocarbons using calixarene layered gold colloid film as substrates for surface ‑ enhanced Raman scattering / X. Shi, Y.-H. Kwon, J.Ma, R. Zheng, C. Wang, H.D. Kronfeldt // J. Raman Spectrosc. — 2013. — Vol. 44. — P. 41–46.

14 Xie Y. Sensing of polycyclic aromatic hydrocarbons with cyclodextrin inclusion complexes on silver nanoparticles by surface-enhanced Raman scattering / Y. Xie, X. Wang, X. Han, X. Xue, W. Ji, Z. Qi et al. // Analyst. — 2010. — Vol. 135. — P. 1389–1394.

15 Xie Y. Selective SERS detection of each polycyclic aromatic hydrocarbon (PAH) in a mixture of five kinds of PAHs. / Y. Xie, X. Wang, X. Han, W. Song, W. Ruan, J. Liu, B. Zhao, Y. Ozaki // J. Raman Spectrosc. — 2011, Vol. 42. — P. 945–950.

16 Богатырев В.А. Методы синтеза наночастиц с плазмонным резонансом: учеб. пос. / В.А. Богатырев, Л.А. Дымкан, Н.Г. Хлебцов. — Саратов: СГУ им. Н.Г.Чернышевского, 2009 — 35 с.

17 Бегунов И.Б. Получение наностержней серебра методом контролируемого роста на ядрах кристаллизации / И.Б. Бегунов, М.Ю. Королева, Е.В. Юртов // Успехи в химии и хим. технологии. — 2014. — Т. 28, № 6. — С. 37–39.

18 Васильева С.Ю. Сорбционное концентрирование пирена наночастицами серебра и его люминесцентное определение в водных растворах / С.Ю. Васильева, А.Ю. Оленин, Г.И. Романовская, Ю.А. Крутяков, В.И. Погонин, А.С. Коротков и др. // Журн. аналит. хим. — 2009. — Т. 64, № 12. — С. 1244–1250.

19 Jiang M. CTAB micelles assisted rGO–AgNP hybrids for SERS detection of polycyclic aromatic hydrocarbons / M. Jiang, Zh. Qian, X. Zhou, X. Xin, J. Wu, Ch. Chen et al. // Phys. Chem. Chem. Phys. — 2015. — Vol. 17. — P. 21158–21163.

20 Gao Y. CTAB-triggered Ag aggregates for reproducible SERS analysis of urinary polycyclic aromatic hydrocarbon metabolites / Y. Gao, L. Li, X. Zhang, X. Wang, W. Ji, J. Zhao et al. // Chem. Commun. — 2019. — Vol. 55. –P. 2146–2149.

21 Evanoff D.D. Jr. Synthesis and optical properties of silver nanoparticles and arrays / D.D. Jr. Evanoff, G. Chumanov // Chem. Phys. Chem. — 2005. — Vol. 6, № 7. — P. 1221–1231.

Р.Х. Джанабекова, М.С. Ким, Н.Х. Ибраев

Коллоидты күміс төсеніштерінде полициклді хош иісті көмірсутектерді беті-күшейтілген комбинациондық шашырау әдісімен анықтау

Мақалада цетилтриметиламмоний бромидімен (ЦТАБ) тұрақтандырылған, коллоидтық күміспен қапталған төсеніштер бетінде полициклді хош иісті көмірсутектерді (ПХК) беті-күшейтілген комбинациондық шашырау (SERS) әдісімен анықтау мүмкіндігі туралы айтылған. Цетилтриметиламмоний бромиді металл нанобөлшектерін тұрақтандырушысы ғана емес, сонымен қатар плазмондық күміс нанобөлшектердің күшейтілген электромагниттік өрісінің жанында ПХК гидрофобты молекулаларының шоғырлануына ықпал ететін модификациялаушы зат рөлін атқаратындығы көрсетілген. Модель аналиттері ретінде антрацен мен пирен қолданылған. Дайындалған SERS-белсенді қабыршақтарының сезімталдығын анықтау үшін талданатын заттардың концентрациясы $2\cdot10^{-4}$–10^{-6} моль/л диапазонындағы спирттік ерітінділері қолданылған. Алынған қабыршақтарда антрацен мен пирен ерітінділердің сигнал алған ең төменгі концентрациясы сәйкесінше $2{,}5\cdot10^{-6}$ М және $5\cdot10^{-5}$ М құрайды. Бұл нәтижелер қабыршақтардың пиренмен салыстырғанда антраценге сезімтал екенін көрсетеді. Сонымен қатар, жұмыста әртүрлі ПХК молекулаларын құрамдас бөліктерді алдын-ала бөлмей, күрделі қоспада өзіне тән шыңдарға сәйкес анықтауға болатындығы көрсетілген.

Кілт сөздер: беті-күшейтілген комбинациондық шашырау, полициклді хош иісті көмірсутектер, антрацен, пирен, күміс нанобөлшектері, цетилтриметиламмоний бромиді, SERS сенсоры, плазмондық нанобөлшектер.

Р.Х. Джанабекова, М.С. Ким, Н.Х. Ибраев

Определение полициклических ароматических углеводородов методом поверхностно-усиленного комбинационного рассеяния на подложках коллоидного серебра

В статье сообщается о возможности определения полициклических ароматических углеводородов (ПАУ) методом поверхностно-усиленного комбинационного рассеяния (SERS) на подложках, покрытых коллоидным серебром, стабилизированным цетилтриметиламмония бромидом (ЦТАБ). Показано, что цетилтриметиламмония бромид выполняет роль не только стабилизатора наночастиц металла, но и роль модифицирующего агента, способствующего концентрации гидрофобных молекул ПАУ вблизи усиленного электромагнитного поля плазмонных наночастиц серебра. В качестве модельных аналитов были использованы антрацен и пирен. Для определения чувствительности приготовленного SERS-активного покрытия использованы спиртовые растворы анализируемых веществ с концентрациями в диапазоне $2 \cdot 10^{-4}$–10^{-6} моль/л. Наименьшие концентрации растворов, для которых на полученных подложках обнаруживаются антрацен и пирен, составляют $2{,}5 \cdot 10^{-6}$ М и $5 \cdot 10^{-5}$ М соответственно. Эти результаты указывают на то, что подложки более чувствительны к антрацену, чем к пирену. В работе также показано, что различные молекулы ПАУ могут быть обнаружены по характерным пикам в сложной смеси без предварительного разделения компонентов.

Ключевые слова: поверхностно-усиленное комбинационное рассеяние, полициклические ароматические углеводороды, антрацен, пирен, наночастицы серебра, цетилтриметиламмония бромид, SERS сенсор, плазмонные частицы.

References

1 Drugov, Yu.S. (2000). *Ekolohicheskaia analiticheskaia khimiia [Ecological analytical chemistry]*. Moscow: Moskva [in Russian].

2 Drugov, Yu.S., Belikov, A.V., Diakova, G.A., & Tulchinskii, V.M. (1984). *Metody analiza zahriaznenii vozdukha [Air pollution analysis methods]*. Moscow: Khimiia [in Russian].

3 Plaza-Bolanos, P., Frenich, A.G., & Vidal, J.L.M. (2010). Polycyclic aromatic hydrocarbons in food and beverages. Analytical methods and trends. *J. Chromatogr. A, 1217,* 6303–6326.

4 Moret, S., & Conte, L.S. (2000). Polycyclic aromatic hydrocarbons in edible fats and oils: occurrence and analytical methods. *J. Chromatogr. A., 882,* 245–253.

5 Moskovits, M. (1985). Surface-enhanced spectroscopy. *Rev. Mod. Phys., 57,* 783–826.

6 Etchegoin, L. R. (2008). *Principles of Surface-Enhanced Raman Spectroscopy and Related Plasmonic Effects.* Amsterdam: Elsevier Science.

7 Chang, R., & Furtak, T. (Eds.). (1984). *Hihantskoe kombinatzionnoe rasseianie [Surface Enhanced Raman Scattering]*. Moscow: Mir [in Russian].

8 Etchegoin, P.G., & Le Ru, E.C. (2008). A perspective on single molecule SERS: current status and future challenges. *Phys. Chem. Chem. Phys., 10,* 6079–6089.

9 Shliuker, S.M. (Eds.). (2017). *Poverkhnostno-usilennaia ramanovskaia spektroskopiia (SERS): analiticheskie, biofizicheckie i biomeditsinskie prilozheniia [Surface-enhanced Raman spectroscopy (SERS): analysis, biophysical and biomedical applications]*. Moscow: Technosphera [in Russian].

10 Gu, X,. Tian, Sh., Zhou, Q., Adkins, J., Gu, Zh., & Li, X., et al. (2013). SERS detection of polycyclic aromatic hydrocarbons on a bowl-shaped silver cavity substrate. *RSC Adv., 3,* 25989–25996.

11 Jones, C.L., Bantz, K.C., & Haynes, C.L. (2009). Partition layer-modified substrates for reversible surface-enhanced Raman scattering detection of polycyclic aromatic hydrocarbons. *Anal. Bioanal. Chem., 394,* 303–311.

12 Guerrini, L., Garcia-Ramos, J.V., Domingo, C., & Sanchez-Cortes, S. (2006). Functionalization of Ag Nanoparticles with Dithiocarbamate Calix [4] arene As an Effective Supramolecular Host for the Surface-Enhanced Raman Scattering Detection of Polycyclic Aromatic Hydrocarbons. *Langmuir, 22,* 10924–10926.

13 Shi, X., Kwon, Y.-H., Ma, J., Zheng, R., Wang, C., & Kronfeldt, H.D. (2013). Trace analysis of polycyclic aromatic hydrocarbons using calixarene layered gold colloid film as substrates for surface-enhanced Raman scattering. *J. Raman Spectrosc., 44,* 41–46.

14 Xie, Y., Wang, X., Han, X., Xue, X., Ji, W., & Qi, Z., et al. (2010). Sensing of polycyclic aromatic hydrocarbons with cyclodextrin inclusion complexes on silver nanoparticles by surface-enhanced Raman scattering. *Analyst., 135,* 1389–1394.

15 Xie, Y., Wang, X., Han, X., Song, W., Ruan, W., & Liu, J., et al. (2011). Selective SERS detection of each polycyclic aromatic hydrocarbon (PAH) in a mixture of five kinds of PAHs. *J. Raman Spectrosc., 42,* 945–950.

16 Bogatyrev, V.A., Dymkan, L.A., & Khlebszov, N.G. (2009). *Metody sinteza nanochastits s plazmonnym rezonansom [Synthesis methods for plasmon resonance nanoparticles]*. Saratov: SGU [in Russian].

17 Begunov, I.B., Koroleva, M.Yu., & Yurtov, E.V. (2014). Polucheniie nanosterzhnei serebra metodom kontroliruiemoho rosta na yadrakh kristsllizatsii [Preparation of silver nanorods by controlled growth method on crystallization nuclei]. *Uspekhi khimii i khimicheskoi tekhnolohii, 28, 6,* 37–39 [in Russian].

18 Vasilyeva, S.Yu., Olenin, A.Yu., Romanovskaya, G.I., Krutyakov, Yu.A., Pogonin, V.I., & Korotkov, A.S., et al. (2009). Sorbtsionnoe kontzentrirovanie pirena i eho liuminestzentnoe opredelenie v vodnykh rastvorakh [Sorption concentration of pyrene by silver nanoparticles and its luminescent determination in aqueous solutions]. *Zhurnal analiticheskoi khimii, 64, 12,* 1244–1250 [in Russian].

19 Jiang, M., Qian, Zh., Zhou, X., Xin, X., Wu, J., & Chen, Ch., et al. (2015). CTAB micelles assisted rGO–AgNP hybrids for SERS detection of polycyclic aromatic hydrocarbons. *Phys. Chem. Chem. Phys., 17,* 21158–21163.

20 Gao, Y., Li, L., Zhang, X., Wang, X., Ji, W., & Zhao, J., et al. (2019). CTAB-triggered Ag aggregates for reproducible SERS analysis of urinary polycyclic aromatic hydrocarbon metabolites. *Chem. Commun., 55,* 2146–2149.

21 Evanoff, D.D. Jr., & Chumanov, G. (2005). Synthesis and optical properties of silver nanoparticles and arrays. *Chem. Phys. Chem., 7,* 1221–1231.

DOI 10.31489/2020Ph2/32-42

UDC 620.192:534 – 16:53.887.45

R.A. Laas[1], P.N. Khorsov[1], A.P. Surzhikov[1], A.A. Bespalko[1],
A.S. Gyngazov[2], D.Zh. Karabekova[3], A.K. Khassenov[3]

[1]National Research Tomsk Polytechnic University, Tomsk, Russia;
[2]Joint-stock company «Sibkabel», Tomsk, Russia;
[3]Ye.A. Buketov Karaganda State University, Kazakhstan
(E-mail: romanlaas@tpu.ru)

Two-Dimensional Ray Mathematical Model of Mechanoelectric Transformations Method for Location of Macrodefects Identification in Solid Dielectric Structures

Method of mechanoelectric transformations can be applied to determine both horizontal position and the depth of a defect in solid nonconductor samples. The method is based on phenomenon of electromagnetic emission in sources of mechanoelectric transformations, such as cracks, voids and impurities of sample structure. It has been shown that method can be used to evaluate integrated stress-strain state of solid dielectric materials. The method is also capable of finding defects is the sample volume, but the robust methodology has to be developed. To develop a methodology of the proper scanning process the experimental setup was created. This work represents ray model of this setup. The model allows us to research pulse characteristics of the response signal considering a variety of excitation signal parameters, defect locations and depths. The model includes dimensions of real sample. Pulse characteristics for response signals of single-period excitation waves with 100 kHz, 300 kHz, and 600 kHz frequencies were obtained. It is shown that increasing the frequency of excitation increases the accuracy of estimating the depth of macrodefects. Time-response characteristics of the signal are most informative.

Keywords: mechanoelectric transformations, acoustic control, nondestructive testing, mathematical model, solid dielectric structures, defectoscopy, response signal, excitation wave.

Introduction

Acoustic methods are widely used to search and control macrodefects in structures. Most of them are based on pulsed excitation of the test object by the acoustic wave and the following study of response characteristics associated with a macrodefect [1–5].

Numerous acoustic methods of searching defect coordinates have been developed [6–8].

The disadvantage of these methods is the requirement of reliable acoustic contact between the receiver and the object of control. The response signal may be distorted due to heterogeneity of the surface mechanical properties of the sample, which leads to instability in the transient characteristic of the contact.

However, there are methods, which do not require reliable surface contact, for example, the method of mechanoelectric transformations (MET). It is found that in solid dielectric under certain conditions like stress electromagnetic emission appears on the surfaces of cracks and defects [9]. Double electric layers at the interfaces of dissimilar materials are sources of MET, as well as natural piezoelectric inclusions (quartz sand in concrete, for example). The method of electromagnetic emission can be informative to determine stress-strain state of materials, but the method is considered passive. Further investigations have shown that it is possible to induce an electromagnetic response by acoustic excitation of the sample [10–13]. Studies indicate that the MET method is suitable for defectoscopy of solid dielectrics. First, there were investigations on registration of response signals for samples made of epoxy resin with addition of sand, which contained lots of quartz [14]. To determine whether results of studies are redundant, statistic methods were utilized, for instance, those based on Students t-distribution [15]. These methods utilize integrated response characteristics to evaluate bulk and surface defects [16]. The response signal received from the surface area above defect is distinguishable from those signals received from areas without defects since correlation drops dramatically in «defected» areas.

During ultrasonic testing, acoustic energy is being transferred to an electric signal in a localized acoustic transducer. Unlike that, transducers in MET method are located in the sample itself, so that the response signal is the superposition of signals from all the MET sources. As a result, a response signal is being received right after excitation and clearly carries no information about defects whatsoever. The excitation wave than reaches the defect and reflects back to the surface, creating the useful response signal that sums up with the parasitic one. Later on, the wave reflected from further boundaries if the sample also contributed to the integrated signal.

It is also possible to utilize the reverberation effect to enhance the MET method. The main advantage of reverberation is the repeated intersections of the excitation zones of inhomogeneities by acoustic waves, that is displayed in response parameters. The reverberation makes it possible to accumulate distortions of wavefronts [17, 18].

The aim of this work is to evaluate the most suitable parameters of excitation and response signals to localize the defect.

Methods and materials

A new method of nondestructive testing has been developed in Tomsk Polytechnic University — method of mechanoelectric transformations (MET). Acoustic impulse of a given form excites dielectric sample. The excitation wave interferes with MET sources, which partially transfer acoustic energy to weak electromagnetic field. The capacitance sensor located close to the surface then transforms electromagnetic signal to current, which is then registered. Sources of MET include double electric layers at the interfaces of dissimilar materials and natural piezoelectric inclusions (quartz sand in concrete, for example). The main advantage of MET method over other acoustic methods is that MET method does not require reliable surface contact. This method can require no physical contact with a sample at all if laser beam is used as an excitation source [19].

Studies indicate that the MET method is suitable for defectoscopy of solid dielectrics.

During ultrasonic testing, acoustic energy is being transferred to an electric signal in a localized acoustic transducer. Unlike that, transducers in MET method are located in the sample itself, so that the response signal is the superposition of signals from all the MET sources. As a result, a response signal is being received right after excitation and clearly carries no information about defects whatsoever. The excitation wave than reaches the defect and reflects back to the surface, creating the useful response signal that sums up with the parasitic one. Later on, the wave reflected from further boundaries if the sample also contributed to the integrated signal.

To describe received electric signal from sample with distant MET sources ray mathematical model was developed [20].

The full biasing current I over the segment of the detector is determined as following:

$$I = \frac{Q}{S_s} \cdot \int_{s_s} \int_{s_r} \left\{ \frac{dh}{dt} \cdot \left[\frac{1}{r^3} \cdot \left(\frac{3 \cdot H^2}{r^2} - 1 \right) \right] - \frac{dH}{dt} \cdot \left[\frac{3 \cdot h \cdot H}{r^5} \cdot \left(\frac{5 \cdot H^2}{r^2} - 3 \right) \right] \right\} \cdot ds_s \cdot ds_r$$

Q — is a bound charge of a single MET source; S_u — is a square of a MET source; *h)* — is a width of a source H — is a distance between MET source and the receiver.; *r(t)* — is the length of the radius vector between the element of MET source and the element or receiver surface, considering reflections from boundaries of the sample.; ds_r — elementary surface of the reciever; ds_s — the element of surface area of MET source. Time indexes for H, h and r are left out.

Derivatives with respect to h and H are obtained from the equation for longitudal deformation δl and its connection to mechanical normal stress σ in elastic area.

Since the mechanical stress is not uniform in space, when calculating the deformation between two points, it is necessary to summarize the instantaneous elementary deformations, within which the mechanical stress can be considered unchanged. When calculating the strain rate across the width of the probe, the instantaneous mechanical stress can be considered constant due to the small value of h and the expression for the vertical component of the derivative h with respect to time has the form:

$$\frac{dh}{dt} = k \cdot \sigma_0 \cdot \frac{\frac{dF}{dt}\left(\mathrm{t} - \frac{\left|\vec{r}\right|}{\nu}\right) \cdot \mathrm{r}_{hz} \cdot h}{E^2 \cdot \left|\vec{r_h}\right|}$$

where k — is the coefficient having a length dimension equal to the distance from the center of the spherical wave to the region of tension formation σ_0, which is equal, in a first approximation, to the ratio of the impact force to the contact area of the spherical surface of the excitation source with the sample; $\vec{r}$ — radius vector from the region of impact formation to a given point, taking into account reflections from the control object boundaries; $\left|\vec{r}_h\right|$ — the radius vector module from the point of impact to the given point of the MET source, r_{hz} — is the projection of the specified radius vector on the vertical axis; *F(t-r/v)* — equation of the excitation wave; ν — is the speed of sound in control object.

When calculating the expression for the vertical component of the derivative with respect to H, it is necessary to take into account the heterogeneity of the mechanical stress, therefore, it has the following form

$$\frac{dH}{dt} = \frac{k \cdot \sigma_0}{E} \cdot \int_0^H \frac{\frac{dF}{dt}(t - \frac{|\vec{r_z}|}{v}) \cdot r_{zz}}{|\vec{r_z}|^2} \cdot dz,$$

where r_{zz} — is the vertical component of $\vec{r}_z$, $|\vec{r}_z|$ — is the radius vector module from the point of impact to the point of the given line connecting the point on the MEP source with the point on the receiver plate. The vertical component of the induction vector is calculated along this line.

where is the vertical component, is the radius vector module from the point of impact to the point of the given line connecting the point on the MEP source with the point on the receiver plate. The vertical component of the induction vector is calculated along this line.

As can be seen from expression above for the bias current, the response signal consists of two components. One component is associated with a change in time of the width of the MET source, (component h); the other component — with a change in the distance between the surface elements of the MET source and the signal receiver (component H). From this expression it follows that each of these components can change its sign at certain angles between the vertical axis and the direction of the radius vector from the MET source to the receiver surface element. Therefore, the total response signal can be either a result of either arithmetic summation of the two components, or subtraction. Moreover, depending on the size and position of the surfaces of the MET source and the receiver, we can get a common signal as the sum of elementary responses, where not all components have the same sign.

In general, the described mathematical model shows that with a uniform distribution of the MET sources over the sample, those sources located near the signal receiver make the greatest contribution to the electrical response. Nevertheless, under certain conditions of the distribution of MET sources, the electrical response, which in this case can be called parasitic, begins to form almost without delay at the moment of excitation of the sample. After the acoustic wave reaches the surface of the defect, the response reflected from the microdefect of the wave begins to mix with the already existing response. Over time, acoustic waves reflected from the boundaries of the sample begin to influence the response.

To identify criteria of the defects, which can be found and assessed with MET method the experimental setup was created [21, 22]. Figure 1 shows the scheme of the setup.

A coordinatograph allows positioning the sending-receipt unit (SRU) above the specific place of the sample surface. The SRU consists of piezoelectric transducer and differential capacitive probe. The transducer emits a series of acoustic impulses. The shape and length of each impulse is determined by concerns of specific experiment and controlled via special software. The measurement input of the probe is located several millimeters above the surface of the sample. It receives electric component of electro-magnetic signal, which consists of both noise and informative signal. The generation and digitizing device (GDD) is based on multifunction Data acquisition device NI USB-6356. The output of GDD is connected to the high-voltage amplifier (HA) to amplify the signal before it comes to transducer. Multiple excitations are used to improve signal/noise ratio. Up to 256 measurements are summed up and averaged.

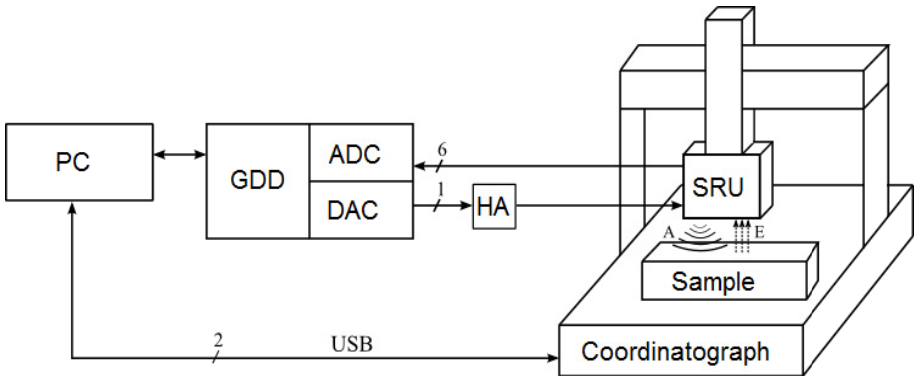

Figure 1. The experimental setup

The setup was used to find out what kind of defects can be found with MET method.

The sample is a 100 mm thick concrete block with holes. Three holes have a diameter of 25 mm and depths 40, 60 and 75 mm.

It turned out that parasitic response signals are significantly affecting the response signal as a whole, so that it is difficult to choose optimal criteria for defects, which could be localized my MET method. For the same reason it is impossible to estimate suitable parameters of excitation waves right away.

The aim of this work is to show in a two-dimensional mathematical model that takes into account the ability to set the dimensions of the surfaces of the acoustic excitation source, macrodefect and the electrical response receiver, as well as the coordinates of the macrodefect, which excitation and response parameters are most effective for determining the coordinates of macrodefects in solid dielectrics.

Let us consider the following system: the source of the signal, receiver and defect, all located on plain surface (Figure 2). Here *a* depicts the source; *b* is the receiver; *c* is the defect.

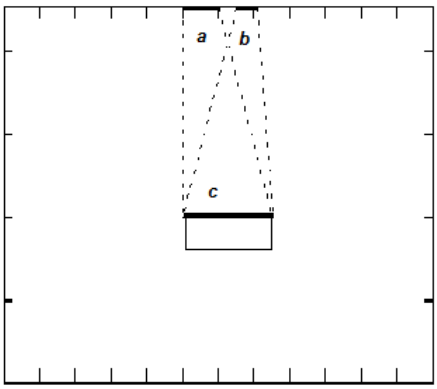

Figure 2. The scheme of experimental setup for studying electromagnetic responses when a sample is excited by an acoustic pulse of a given shape, where a is acoustic wave emitter; b is response signal receiver; c is the defect

Dashed lines portray rays which contribute to response signal formation. The model considers real dimensions of emitter, receiver, defects and their locations.

The length of emitter is 10 mm, receivers is 6 mm.

The source of the signal emits an acoustic excitation wave from each point of the surface of the emitter. The surface area is defined as a site with a linear size $\delta l = \delta t \cdot v$, where v is the speed of sound in a concrete sample (3200 m / s); δt is the digitization interval.

The rays fall on the surface of the defect and are emitted into the region of the sample located in the immediate vicinity of the surface of the receiver. In this area, the level of the electromagnetic signal due to mechanoelectric transformations is the greatest.

The program sums up all the elementary responses from each ray emitted by the surface of the defect, which, in turn, is a superposition of rays from each point of the source of the acoustic signal.

The distances that each beam travels between the surface of the source and the macrodefect, as well as the surface of the macrodefect and receiver, were calculated. The response signals from each ray falling into the same time were summed. Each elementary response signal was calculated based on the sphericity of the acoustic wave, i.e. acoustic attenuation was taken into account inversely with distance. The delay time of the arrival of the rays to the receiver was also calculated to form the integral time dependence of the response. The resulting dependence is the impulse characteristic of the response signal for a given configuration of the emitter — defect — receiver system.

The program also calculated the impulse response characteristics when the source — receiver system was shifted relative to the defect, which simulated the scanning system for the sample.

Impulse characteristics were calculated for three depths of macrodefects: 25 mm, 40 mm and 60 mm. In addition, the impulse response characteristics were calculated upon reflection of the excitation pulse from the bottom of the sample (100 mm).

Figure 3 shows the impulse response characteristics at a defect depth of (25, 40, 60) mm and with no defects respectively, under conditions when the sensor system is above the corresponding defect. The abscissa shows the relative distances that the acoustic rays travel.

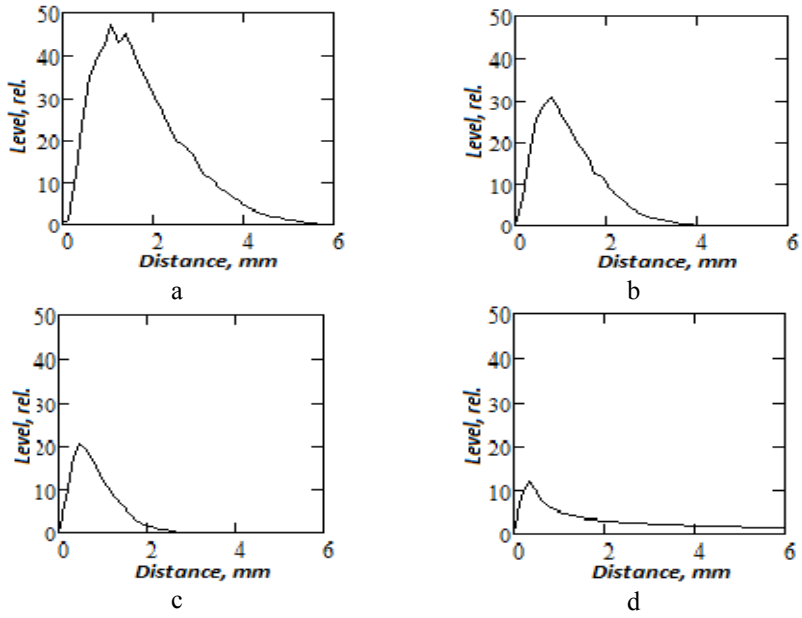

Figure 3. Impulse response characteristics at a defect depth when the sensor system is above the corresponding defect, a) 25 mm; b) 40 mm; c) 60 mm; d) without defect

As can be seen from the figures, for the given linear dimensions of the receiver, defect, and emitter, the range of distances that the rays of the acoustic excitation wave propagate at a defect depth of 25 mm is 6 mm, at a depth of 40 mm — 4 mm, and at a depth of 60 mm — 3 mm. When the excitation signal is reflected from the bottom of the sample, the interval of the impulse response is 18 mm. In this case, there is a strong surge of the signal at the beginning of the impulse response. Figure 4 shows the impulse response characteristics at a defect depth of (25, 40, and 60) mm and with no defects underneath, respectively, under conditions when the sensor system is 10 mm shifted relative to the defect.

When the SRU is shifted relative to the defect, the response signal decreases and the impulse response expands. The range of distances for depths 25, 40 and 60 mm is 12, 8, and 6 mm, respectively.

Figure 5 shows the calculations of the maximum levels of the impulse response as a function of the bias and bias offset relative to the defect.

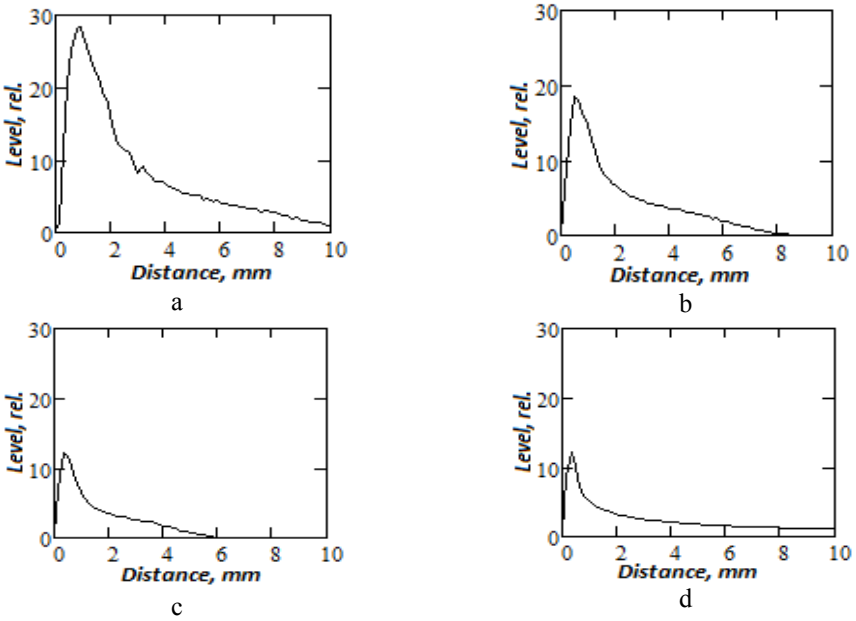

Figure 4. Impulse response characteristics when the sensor system is 10 mm shifted relative to the corresponding defects: a) 25 mm; b) 40 mm; c) 60 mm; d) without defect

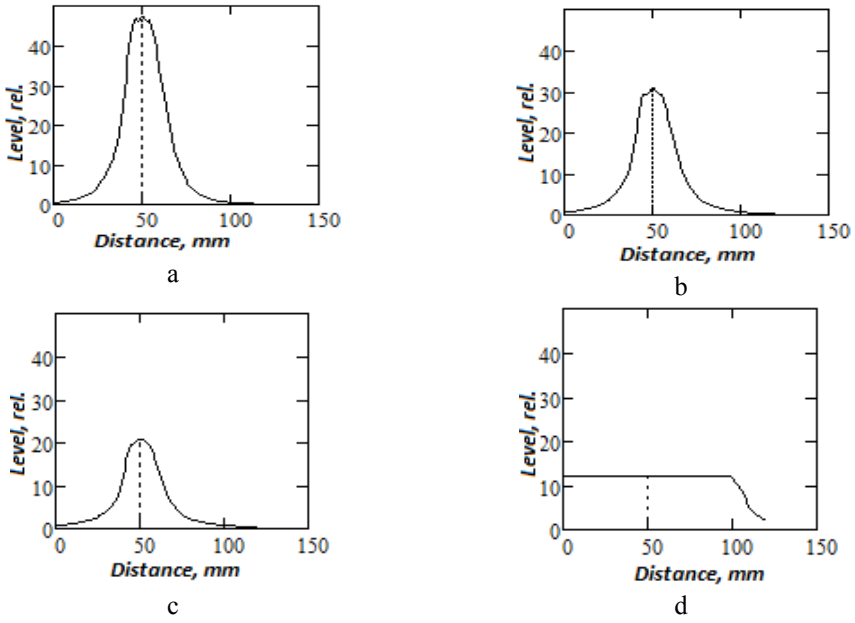

Figure 5. The maxima of the impulse response levels when the SRU is shifted relative to the corresponding defect depth: a) 25 mm; b) 40 mm; c) 60 mm; d) without defect

As can be seen from Figure 5a, the maximum response when the acoustic excitation wave is reflected from the bottom is in fact independent of the displacement of the emitter and receiver assembly with respect to the defect. The vertical dashed line corresponds to the position of the SRU over the defect.

Studying the impulse characteristics, it is possible to calculate the responses when a pulse of a given shape is applied to the sample.

A rectangular radio pulse *u(t)* was used as an excitation pulse in the model.

On the graphs of impulse responses along the ordinate axis, the intensities are plotted. Therefore, to obtain the response *res(t)* when an acoustic pulse of a given shape is exposed to a sample, it is necessary to perform the convolution operation of its time dependence with the corresponding impulse response

$$res(\mathrm{t}) = \sum_{\tau=0}^{t} imp(\tau) \cdot u(t-\tau)$$

where *imp (t)* is the impulse response; *u (t)* is the time dependence of the excitation pulse.

To solve the problem of determining the location of a macrodefect, as well as a possible assessment of its linear dimensions, we consider the responses at various frequencies and durations of the excitation pulse.

The presented responses are shown upon excitation of a sample with a rectangular radio pulse with a frequency of 100 kHz for a period of 1 period in Figure 6.

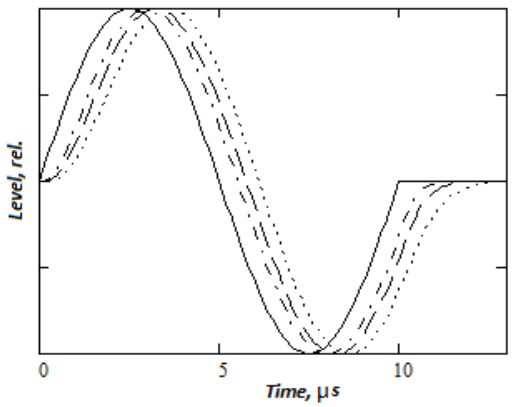

Figure 6: The responses when a sample was excited by a rectangular radio pulse with a frequency of 100 kHz for a period of 1 period in the zones of defects with a depth of 25 mm (dots), 40 mm (dashed line), 60 mm (dashed-dotted line) and the shape of the excitation pulse (solid line).

As follows from the figure, there is an increase in the duration of the response with a decrease in the depth of the defect. Figures 6 and 7 show that with increasing frequency, the degree of increase in duration increases.

As can be seen from all the figures, the waveforms of the responses are distorted to one degree or another with respect to the excitation pulse. It follows from a theory that the response duration is the sum of the duration of the initial pulse (in our case, the period of the corresponding frequency) and the duration of the characteristic with which the convolution is carried out. Therefore, the response duration is delayed with respect to the initial pulse [21–23].

The duration of the impulse response in the ray approximation of the propagation of an acoustic wave depends both on the depth of the defect, on the surface of which the excitation wave is reflected, and on its linear dimensions, as well as on the sum of the linear dimensions of the excitation source, receiver, and the gap between them.

Therefore, in general, the difference between the duration of the response and the duration of the excitation pulse is an indicator of the depth of the location of defects [24, 25].

The response signal is generated in a special way when the acoustic excitation wave is reflected from the bottom of the sample, which is due to the relatively large surface from which the acoustic excitation wave signal is reflected.

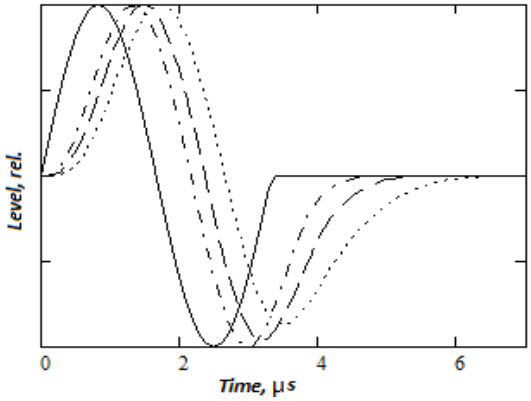

Figure 7. The responses when a sample was excited by a rectangular radio pulse with a frequency of 300 kHz for a period of 1 period in the zones of defects with a depth of 25 mm (dots), 40 mm (dashed line), 60 mm (dash-dotted line) and the shape of the excitation pulse (solid line)

Figure 7 and 8 show the given responses for frequencies of 300 kHz and 600 kHz.

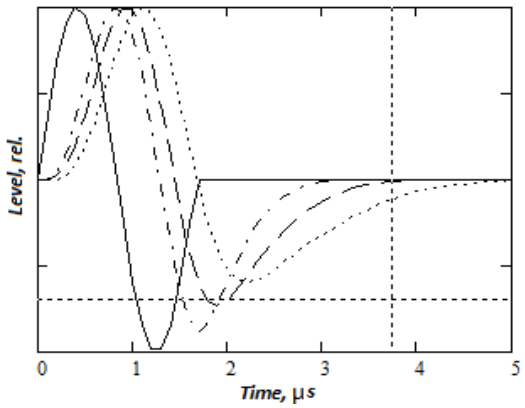

Figure 8. The responses given when a sample was excited by a rectangular radio pulse with a frequency of 600 kHz for a period of 1 period in the zones of defects with a depth of 25 mm (dots), 40 mm (dashed line), 60 mm (dashed-dotted line) and the shape of the excitation pulse (solid line)

Consider the response behavior in the spectral region. Figure 9 shows fragments of the amplitude-frequency characteristics (up to the first bend) of responses under the influence of a pulse with a frequency of 100 kHz for defect depths (25, 40, 60) mm, as well as the frequency response of the excitation pulse.

As can be seen from the Figure 9, at a frequency of 100 kHz, all frequency response lines almost merge. At the same time, it is seen that the response frequency response when reflected from the bottom of the sample has a feature that is probably due to the manifestation of interference due to the superposition of acoustic waves whose path lengths exceed the coherence interval.

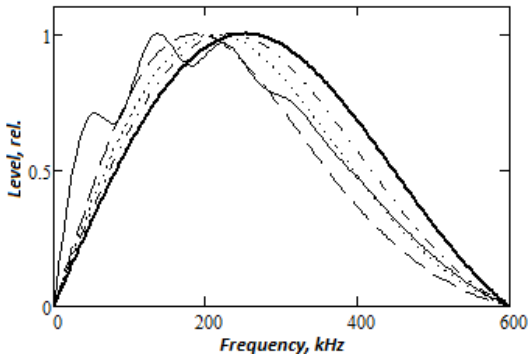

Figure 9. The amplitude-frequency characteristics of responses when reflected from defects at defect depths of 25 mm (dashed line), 40 mm (dots), 60 mm (dashed-dotted line), from the bottom of the sample (thin solid line) and the excitation pulse (thick solid line) at a frequency of 100 kHz

Figures 8 and 9 show the frequency response of the responses and the excitation pulse for the same depths for the frequencies 300 kHz and 600 kHz.

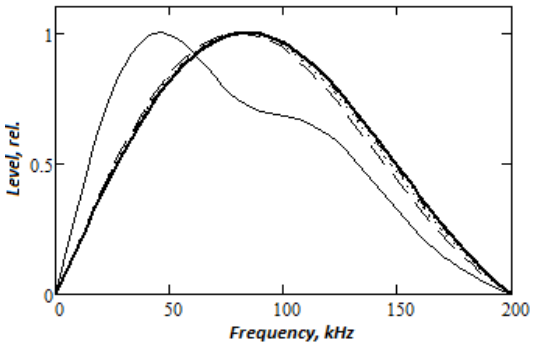

Figure 10. The amplitude-frequency characteristics of responses when reflected from defects at defect depths of 25 mm (dashed line), 40 mm (dots), 60 mm (dashed-dotted line), from the bottom of the sample (thin solid line) and the excitation pulse (bold solid line) at a frequency of 300 kHz

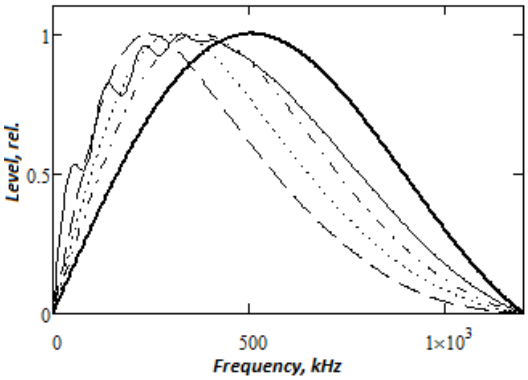

Figure 11. The amplitude-frequency characteristics of responses when reflected from defects at defect depths of 25 mm (dashed line), 40 mm (dots), 60 mm (dashed-dotted line), from the bottom of the sample (thin solid line) and the excitation pulse (thick solid line) at a frequency of 600 kHz

It follows from Figure 10 that, at a frequency of 300 kHz, the maxima of the frequency response of the responses relative to the frequency response of the initial excitation naturally shift to the low-frequency re-

gion with a decrease in the depth of the defect. The nature of the response from the bottom of the sample becomes more complex.

And finally, in figure 11, at a frequency of 600 kHz, the manifestation of the displacement of the maxima of the frequency response increases significantly.

Conclusion

Based on the analysis of responses calculated using the two-dimensional ray model, the following conclusions can be drawn:

– the steepness of the impulse response when scanning along a sample with a defect increases with decreasing depth of the defect;

– the difference between the response duration and the excitation pulse duration at a given excitation frequency is an indicator of the depth of the location of defects;

– the degree of expansion of the response increases with increasing frequency of pulsed excitation;

– increasing the frequency of excitation increases the accuracy of estimating the depth of microdefects.

The work has been done with the financial support of the Russian Science Foundation, project No. 19-19-00178 (TPU - 5.2053.RNF.2019).

References

1 Mozgovoi N.I. The implication of acoustic method to control composite metal components / N.I. Mozgovoi, Ya.G. Mozgovaya, E.A.Pashkova // Metals treatment: technology, equipment, instruments. — 2015. — 3. — P. 68–71.

2 Blackshire J.L., Sathish S. Near-field ultrasonic scattering from surface-breaking cracks / J.L. Blackshire, S. Sathish // Applied Physics Letters. — 2002. — 80(18). — P. 3422–3444.

3 Seher, M. Numerical and experimental study of crack depth measurement in concrete using diffuse ultrasound / M. Seher, C.-W. In, J.-Y. Kim, K.E. Kurtis, L.J. Jacobs // Journal of Nondestructive Evaluation. — 2013. — 32. — P. 81–92.

4 Chitnalah A. Pulse echo method for nonlinear ultrasound parameter measurement / A. Chitnalah, D. Kourtiche, H. Jakjoud, M. Nadi // Electronic Journal Technical Acoustics. — 2007. — 13. — P. 138–145.

5 Bostrom A. Ultrasonic probe modeling and nondestructive crack detection / A. Bostrom, H. Wirdelius // Electronic Journal Technical Acoustics. — 1995. — 97. — P. 2836–2848.

6 Carpinteri A. Reliable onset time determination and source location of acoustic emissions in concrete structures / A. Carpinteri, J. Xu, G. Lacidogna, A. Manuello // Cement and Concrete Composites. — 2012. — 34(4). — P. 529–537.

7 Philippids T. Strength degradation due to fatigue –induced matrix cracking in FRP composites: An acoustic emission predictive model / T. Philippids, T. Assimakopoulou // Composites Science and Technology. 2008. — 68. — P. 15–16.

8 Shah A.A. Non-destructive evaluation of concrete in damaged and undamaged states / A.A. Shah, Y. Ribakov // Material Design. — 2009. — 30. — P. 3504–3511.

9 Wollbrandt M. The generation of high energies of bodies under destruction / M. Wollbrandt, Yu. Chrustalyov, E. Linke // DAN SSSR. — 1975. — 225(2). — P. 342–344.

10 Fursa T. The effect of filler grain size on effectiveness of method of mechanoelectric transformations in concrete / T. Fursa, V. Gordeev // Letters to the Journal of technical physics. — 2000. — 26(3). — P. 30–34.

11 Koktavy P. Experimental study of electromagnetic emission signals generated by crack generation in composite materials / P. Koktavy // Measurement Science & Technology. — 2009. — 20(1).

12 Aydin, A., Prance, R.J. Prance, H., & Harland, C.J. (2009). Observation of pressure stimulated voltages in rocks using an electric potential sensor. Applied Physics Letters, 95, 12, 124102–3.

13 Fursa T.V. Electromagnetic diagnostics of composite materials / T.V. Fursa, A.P. Surzhikov, N.N. Khorsov // Proceedings of the 8th China-Russia Symposium on New Materials and Technologies. (pp. 138–140). China, Guang-Zhou, 2005.

14 Крамер Г. Математические методы статистики. — М.: Мир, 1975. — 648 с.

15 Fursa T. Development of mechanoelectric method of estimation of defects coordinates for concrete samples / T. Fursa, K. Osipov, D. Dann // Control, Diagnostics. — 2012. — 11. — P. 66–69.

16 Khorsov P. The Application of Reverberation in Method of Mechanoelectrical Transformations for Estimation of Stress-Strain State in Solid Dielectric Matter / P. Khorsov, R. Laas, A. Surzhikov // Materials Science Forum 2019. — 970. — P. 47–54.

17 Van Damme B. Defect localization using the nonlinear impact modulation technique / B. Van Damme, K. Van Den Abeele // Emerging Technologies in Non Destructive Testing. — 2011. — 5. — 301–305.

18 Хорсов Н.Н. Математическая модель регистрации отклика при акустоэлектрическом преобразовании в образце с включением в виде двойного электрического слоя при точечном ударном возбуждении / Н.Н. Хорсов // Изв. вузов. Физика. — 2007. — Т. 50, № 2. — С. 69–77.

19 Khaydarov B.K. Composite stratified-hardened containers for synthesis of diamond polycrystals of a type carbonado / B.K. Khaydarov, V.P. Makarov, K. Khaydarov // Bulletin of the University of Karaganda-Physics. 2018. —4(92). — P. 101–106.

20 Demirli R. Ultrasonic flaw detection and imaging through reverberant layers via subspace analysis and projection / R. Demirli, M.G. Amin, X. Shen, Y.D. Zhang // Advances in Acoustics and Vibration. — 2012. — 957379. DOI:10.1155/2012/957379

21 Garnier V. Acoustic techniques for concrete evaluation: improvements, comparisons and consistency / V. Garnier, B. Piwakowski, O. Abraham, G. Villain, C. Payan, J.F. Chaix // Construction Building Materials. — 2013. — 43. — P. 598–614.

22 Surzhikov A. A thermoanalysis of phase transformations and linear shrinkage kinetics of ceramics made from ultrafine plasmochemical ZrO_2(Y)-Al_2O_3 powders / A. Surzhikov, T. Frangulyan, S. Ghyngazov // Journal of Thermal Analysis and Calorimetry. — 2014. — 115, 2. — P. 1439–1445.

23 Copuroglu, E., & Mehmetoglu, T. (2019). Analytical evaluation of the Uehling potential using binomial expansion theorems /Copuroglu, E., & Mehmetoglu, T.// Bulletin of the University of Karaganda-Physics, 3(95), 17–21.

24 Surzhikov A.P. Physics of magnetic phenomena: Investigation of electroconductivity of lithium pentaferrite / A.P. Surzhikov, T.S. Frangulyan, S.A. Ghyngazov, E.N. Lisenko, O.V. Galtseva // Russian Physics Journal. — 2006. — 49, 5. — P. 506–510. DOI**:** 10.1007/s11182–006–0133–6

Р.А. Лаас, П.Н. Хорсов, А.П. Суржиков, А.А. Беспалько,
А.С. Гынгазов, Д.Ж. Карабекова, А.К. Хасенов

Қатты диэлектриктерде макроақаулардың орнын табуға арналған механоэлектрлік түрлендіргіштер әдісінің екі өлшемді сәулелік математикалық моделі

Қатты өткізбейтін үлгілердің көлденең күйін де, ақаудың тереңдігін де анықтау үшін механоэлектрлік қайта құру әдісін қолдануға болады. Бұл механоэлектрлік қайта құрылу көздеріндегі электромагниттік сәулелену құбылысына негізделген, мысалы, жарық құрылымдары, қуыстар және сынама құрылымының қоспалары. Көрсетілген әдісті қатты диэлектрлік материалдардың интеграцияланған кернеулі күйін бағалауда қолдануға болады. Сондай-ақ, әдіс үлгі көлеміндегі ақауларды анықтауға қабілетті, бірақ оның сенімді әдістемесін құру қажет. Сканерлеу процесін дұрыс жүргізу әдістемесін жасау үшін эксперименттік қондырғы құрастырылған. Жұмыста осы қондырғының сәулелік моделі ұсынылған. Модель қоздыру сигналының әртүрлі параметрлерін, ақаулардың орналасуы мен тереңдігін ескере отырып, жауап сигналының импульстік сипаттамаларын зерттеуге мүмкіндік береді. Модель нақты үлгінің өлшемдерін қамтиды. 100 кГц, 300 және 600 кГц жиіліктері бар бір кезеңді қозу толқындарының жауап сигналдары үшін импульстік сипаттамалар алынған. Қозу жиілігін арттыру арқылы макроақаулардың тереңдігін бағалау дәлдігін жоғарылатуға болатыны көрсетілген. Сигналдың уақыттық сипаттамалары ең ақпаратты болып табылады.

Кілт сөздер: механоэлектрлік түрлену, акустикалық бақылау, бұзбай бақылау, сәулелік-математикалық модель, қатты диэлектрлік құрылымдар, дефектоскопия, жауап сигналы, қозу толқыны.

Р.А. Лаас, П.Н. Хорсов, А.П. Суржиков, А.А. Беспалько,
А.С. Гынгазов, Д.Ж. Карабекова, А.К. Хасенов

Двумерная лучевая математическая модель метода механоэлектрических преобразований для поиска местоположения макродефектов в твердых диэлектриках

Метод механоэлектрических преобразований может быть применен для определения как горизонтального положения, так и глубины дефекта в твердых непроводящих образцах. Он основан на явлении электромагнитного излучения в источниках механоэлектрических преобразований, таких как трещины, пустоты и примеси структуры образца. Показано, что указанный метод может быть использован для оценки интегрального напряженно-деформированного состояния твердых диэлектрических материалов. Кроме того, способен обнаруживать дефекты в объеме образца, однако необходимо разработать надежную методологию. Для разработки методологии правильного процесса сканирования была создана экспериментальная установка. Эта работа представляет лучевую модель этой установки. Модель позволяет исследовать импульсные характеристики ответного сигнала с учетом различных параметров сигнала возбуждения, местоположения дефектов и глубины. Включает в себя размеры реального образца. Получены импульсные характеристики для ответных сигналов одноперiодических волн возбуждения с частотами 100, 300 и 600 кГц. Показано, что увеличение частоты возбуждения повышает точность оценки глубины макродефектов. Временные характеристики сигнала являются наиболее информативными.

Ключевые слова: механоэлектрические преобразования, акустический контроль, неразрушающий контроль, лучевая математическая модель, дефектоскопия, возбуждающий сигнал, сигнал отклика, твердые диэлектрические структуры.

References

1 Mozgovoi, N.I., Mozgovaya, Ya.G., & Pashkova, E.A. (2015). The implication of acoustic method to control composite metal components. *Metals treatment: technology, equipment, instruments, 3,* 68–71.

2 Blackshire, J.L., & Sathish, S. (2002). Near-field ultrasonic scattering from surface-breaking cracks. *Applied Physics Letters, 80(18)*, 3422–3444.

3 Seher, M., In, C.-W., Kim, J.-Y., Kurtis, K.E., & Jacobs, L.J. (2013). Numerical and experimental study of crack depth measurement in concrete using diffuse ultrasound. *Journal of Nondestructive Evaluation, 32*, 81–92.

4 Chitnalah, A., Kourtiche, D., Jakjoud, H., & Nadi, M. (2007). Pulse echo method for nonlinear ultrasound parameter measurement. *Electronic Journal Technical Acoustics, 13*, 138–145.

5 Bostrom, A., & Wirdelius, H. (1995). Ultrasonic probe modeling and nondestructive crack detection. *Electronic Journal Technical Acoustics. 97,* 2836–2848.

6 Carpinteri, A., Xu, J., Lacidogna, G., & Manuello, A. (2012), Reliable onset time determination and source location of acoustic emissions in concrete structures*. Cement and Concrete Composites, 34(4),* 529–537.

7 Philippids, T., & Assimakopoulou, T. (2008). Strength degradation due to fatigue –induced matrix cracking in FRP composites: An acoustic emission predictive model. *Composites Science and Technology, 68,* 15–16.

8 Shah, A.A., & Ribakov, Y. (2009). Non-destructive evaluation of concrete in damaged and undamaged states. *Material Design, 30,* 3504–3511.

9 Wollbrandt, M., Chrustalyov, Yu., & Linke, E. (1975). The generation of high energies of bodies under destruction. *DAN SSSR, 225(2),* 342–344.

10 Fursa, T., & Gordeev, V. (2000). The effect of filler grain size on effectiveness of method of mechanoelectric transformations in concrete*. Letters to the Journal of technical physics, 26(3),* 30–34.

11 Koktavy, P. (2009). Experimental study of electromagnetic emission signals generated by crack generation in composite materials. *Measurement Science & Technology 20(1)*.

12 Aydin, A., Prance, R.J. Prance, H., & Harland, C.J. (2009). Observation of pressure stimulated voltages in rocks using an electric potential sensor. *Applied Physics Letters, 95, 12,* 124102–3.

13 Fursa, T.V., Surzhikov, A.P., & Khorsov, N.N. (2005). Electromagnetic diagnostics of composite materials. Proceedings *of the 8th China-Russia Symposium on New Materials and Technologies.* (pp. 138–140). China, Guang-Zhou.

14 Kramer, G. (1975). *Matematicheskie metody statistiki [Methods of mathematical Statistics]*. Moscow: Mir [in Russian].

15 Fursa, T., Osipov, K., Dann, D. (2012). Development of mechanoelectric method of estimation of defects coordinates for concrete samples, *Control, Diagnostics, 11,* 66–69.

16 Khorsov, P., Laas, R., & Surzhikov A. (2019). The Application of Reverberation in Method of Mechanoelectrical Transformations for Estimation of Stress-Strain State in Solid Dielectric Matter, *Materials Science Forum 970,* 47–54.

17 Van Damme B., & Van Den Abeele, K. (2011.) Defect localization using the nonlinear impact modulation technique, *Emerging Technologies in Non Destructive Testing, 5,* 301–305.

18 Khorsov, N.N. (2007). Matematicheskaia model rehistratsii otklika pri akustoelektricheskom preobrazovanii v obraztse s vkliucheniem v vide dvoinoho elektricheskoho sloia pri tochechnom udarnom vozbuzhdenii [Mathematical model of response registration in acoustoelectric transformation in a sample with inclusion in the form of a double electric layer under point shock excitation]. *Izvestiia vuzov. Fizika — University news. Physics, Vol. 50, 2,* 69–77 [in Russian].

19 Khaydarov, B. K., Makarov, V. P., & Khaydarov, K. (2018). Composite stratified-hardened containers for synthesis of diamond polycrystals of a type carbonado, *Bulletin of the University of Karaganda-Physics, 4(92),* 101–106.

20 Demirli, R., Amin, M.G., Shen, X., & Zhang Y.D. (2012). Ultrasonic flaw detection and imaging through reverberant layers via subspace analysis and projection. *Advances in Acoustics and Vibration, 957379.* doi:10.1155/2012/957379

21 Garnier, V., Piwakowski, B., Abraham, O., Villain, G., Payan, C. & Chaix, J.F. (2013). Acoustic techniques for concrete evaluation: improvements, comparisons and consistency. *Construction Building Materials, 43,)* 598–614.

22 Surzhikov, A., Frangulyan, T., Ghyngazov, S. (2014). A thermoanalysis of phase transformations and linear shrinkage kinetics of ceramics made from ultrafine plasmochemical $ZrO_2(Y)$-Al_2O_3 powders. J*ournal of Thermal Analysis and Calorimetry*, 115, 2, 1439–1445.

23 Copuroglu, E., & Mehmetoglu, T. (2019). Analytical evaluation of the Uehling potential using binomial expansion theorems. *Bulletin of the University of Karaganda-Physics, 3(95),* 17–21.

24 Surzhikov, A.P., Frangulyan, T.S., Ghyngazov, S.A., Lisenko, E.N., Galtseva, O.V. (2006). Physics of magnetic phenomena: Investigation of electroconductivity of lithium pentaferrite. *Russian Physics Journal,* 49, 5, 506–510. doi**:** 10.1007/s11182–006–0133–6

DOI 10.31489/2020Ph2/43-49

UDC 546.:654+33+732+742+562+549.748+621.315.592

Sh.B. Kassenova[1], Zh.I. Sagintayeva[1], B.K. Kassenov[1],
E.E. Kuanyshbekov[1], Zh.S. Bekturganov[2], A.K. Zeinidenov[2]

[1]*Abishev Chemical-Metallurgical Institute, Karaganda, Kazakhstan;*
[2]*Ye.A. Buketov Karaganda State University, Kazakhstan*
(E-mail: kasenov1946@mail.ru)

Electrophysical characteristics of nanodimensional cobalte-cuprate-manganite $LaNa_2CoCuMnO_6$ and nickelite-cuprate-manganite $LaNa_2NiCuMnO_6$

The temperature dependences of the electric capacity, dielectric constant and electrical resistance of cobalte-cuprate-manganite of lanthanum and sodium of $LaNa_2CoCuMnO_6$ and nickelite-cuprate-manganite of lanthanum and sodium of $LaNa_2NiCuMnO_6$ were investigated on the LCR-800 serial device (manufactured by Taiwan) at the operating frequencies of 1 kHz, 5 kHz, and 10 kHz in interval of 293–483 K through 10 K continuously in dry air. It was determined that $LaNa_2CoCuMnO_6$ in interval of 293–483 K shows the semiconductor conductivity. A band gap (Δ E) is 0.54eV. The compound has the high values of the dielectric constant, which are equal $2.17\cdot10^6$ (1 kHz), $2.31\cdot10^5$ (5 kHz), $8.22\cdot10^4$ (10 kHz) at 293 K and $8.49\cdot10^8$ (5 kHz), $7.87\cdot10^7$ (10 kHz) at 483 K. $LaNa_2NiCuMnO_6$ in interval of 293–483 K demonstrates the semiconductor conductivity (Δ E = 0.48 eV), at 433–443 K — the metallic conductivity and at 453–483 K — the semiconductor conductivity (Δ E = 2.33 eV).The values of the dielectric constant are $4.97\cdot10^3$ (1 kHz), $9.2\cdot10^2$ (5 kHz), $5.1\cdot10^1$ (10 kHz) at 293 K and $1.02\cdot10^6$ (1 kHz), $1.98\cdot10^5$ (5 kHz) and $9.76\cdot10^4$ (10 kHz) at 483 K. The compounds can be classified as the narrow-band gap semiconductors and they are of interest for the semiconductor and microcapacitor technologies.

Keywords: electrophysics, cobalte, nickelite, cuprate, manganite, lanthanum, sodium, dielectric constant, electrical resistance.

Introduction

The compounds, based on the manganites, nickelites, cuprates and cobaltites of the rare-earth elements doped with oxides of the alkali and alkaline earth metals, have the unique physicochemical properties such as semiconductor, superconductive, ferroelectric, para-, ferro-, antiferromagnetic and other properties [1–4].

It should be pointed that the compounds based on lanthanum and strontium nickelates have the high values of the dielectric constant [5]. The Chemical-Metallurgical Institute performs the systematic and targeted studies on the synthesis and investigation of the physicochemical characteristics of manganites, ferrites, chromites, cuprates, cobaltites, nickelites of the rare earths doped with oxides of the alkali and alkaline earth metals with the valuable properties [6–10].

The purpose of this paper is to investigate the electrophysical properties of nanodimensional cobalte-cuprate-manganite of lanthanum and sodium of $LaNa_2CoCuMnO_6$ and nickelite-cuprate-manganite of lanthanum and sodium of $LaNa_2NiCuMnO_6$. The mentioned compounds synthesized with the ceramic technology in the interval of 800–1200 °C by the interaction of stoichiometric amounts of La_2O_3, CoO, NiO, CuO, Mn_2O_3 and Na_2CO_3. By milling of polycrystalline samples on Retsch MM301 vibration mill (Germany) were obtained their nanodimensional (nanocluster) particles, which sizes were defined on the atomic-force microscope JSPM-5400 Scanning Probe Microscope «JEOL» (Japan). It was found that both compounds are crystallized in a isometric system in the structure with the following parameters of grid: $LaNa_2CoCuMnO_6$ a=14.43±0.02Å; V^o=3005.5±0.06 Å^3; Z=4; $V^o_{elec.cell}$ =751.38±0.02 Å^3; $\rho_{roent.}$=3.86; $\rho_{pick.}$==3.72±0.01 g/cm^3, $LaNa_2NiCuMnO_6$ — a=14.19±0.02 Å, V^o=2859.42±0.06 Å^3, Z=4, $V^o_{elec.cell}$ =714.86±0.01 Å^3, $\rho_{roent.}$=3.38; ρ_{pick}=3.29±0.02 g/cm^3 [11–13].

Results and discussion

The measurements of the electrophysical properties were carried out according to the procedures [14, 15].

The investigation of the electrical characteristics (dielectric constant and electrical resistance) was made with the measuring of the electric capacity of the samples on the LCR-800 (Taiwan) serial device at the operating frequency of 1 kHz, 5 kHz and 10 kHz continuously in dry air in a thermostatic mode with holding time at each fixed temperature.

Some plane-parallel samples were preliminarily made as disks with 10 mm diameter and 5–6 mm thickness with a binder additive (~1.5 %). The pressing was carried out under a pressure of 20 kg/cm^2. The received disks were fired in a silit furnace at 200 °C for 6 h. Then they were thoroughly double-sided grinding.

The dielectric constant was determined from the electric capacity of a sample at the known values of thickness and a surface area of electrodes. The Sawyer-Tower circuit was used to receive correlations between the electric induction D and electric field E. The visual observation of D (hysteresis loop of E) was made on the C1–83 oscilloscope with potential divider consisting of resistance of 6 mOhm and 700 kOhm and a reference capacitor of 0.15 μF. The frequency of generator is 300 Hz.

The samples were placed in the furnace in all temperature studies. Temperature was measured with a chromel-alumel thermocouple connected to B2–34 voltmeter (± 0.1 mV). The rate-of-change of temperature is ~5 K/min. A value of the dielectric constant at each temperature was defined from formula:

Then they were thoroughly double-sided grinding.

$$\varepsilon = \frac{C}{C_0}, \tag{1}$$

where $C_0 = \frac{\varepsilon_0 \cdot S}{d}$ — a capacity of capacitor without a test substance (aerial).

The band gap (ΔE) of the test substance was calculated under formula:

$$\Delta E = \frac{2kT_1T_2}{0.43(T_2 - T_1)} \lg \frac{R_1}{R_2}, \tag{2}$$

where k — Boltzmann constant equal to 8.6173303·10–^{5} eV·K^{-1}, R_1 — resistance at T_1, R_2 — resistance at T_2.

The dielectric constant of a standard substance — barium titanate ($BaTiO_3$) was measured at frequencies of 1 kHz, 5 kHz, and 10 kHz to confirm the received data. Values defined in an experiment of the dielectric constant at 293 K at frequencies of 1 kHz and 5 kHz are satisfactory with its recommended value of 1400 ± 250 [16–18]. In addition, the observed changes in the electrical conductivity of $BaTiO_3$ at 383 K in all frequencies (1 kHz, 5 kHz, and 10 kHz) are consistent with its transition from the perovskite cubic phase *Pm3m* to the tetragonal (polar) ferroelectric phase with space group *P4mm* [16–18].

It should be pointed that despite the lower values of the dielectric constant of $BaTiO_3$ in frequency of 10 kHz and at T equal to 293 K, 303 K, 313 K, all ε values of $BaTiO_3$ in all three frequencies (1 kHz, 5 kHz and 10 kHz) at 313–483 K have approximately the same values up to 2150 which testifies that a change in frequency does not particularly influence on the temperature dependence of the dielectric constant of $BaTiO_3$ at 313–483 K.

Figure 1 and table 1 below demonstrate the results of the electrophysical characteristics of the studied compounds.

Table 1

Dependence of electrical resistance (R) and dielectric constant (ε) on temperature of $LaNa_2CoCuMnO_6$ and $LaNa_2NiCuMnO_6$at various frequencies

T, K	ε	lgε	lg R	ε	lgε	lg R
1	2	3	4	5	6	7
$LaNa_2CoCuMnO_6$				$LaNa_2NiCuMnO_6$		
Measurement frequency 1 kHz						
293	2171210	6,34	4,28	4971	3,70	5,72
303	1803567	6,24	4,23	5883	3,77	5,67
313	1404926	6,15	4,12	7746	3,89	5,57
323	1576730	6,20	3,96	11857	4,07	5,43
333	2049087	6,31	3,82	17811	4,25	5,29
343	2677028	6,43	3,70	27406	4,44	5,14
353	3203737	6,51	3,62	39710	4,60	5,00
363	4104119	6,61	3,54	54742	4,74	4,87
373	5784119	6,76	3,46	71452	4,85	4,77
383	8776221	6,94	3,38	97729	4,99	4,64

1	2	3	4	5	6	7
393	13976221	7,15	3,28	131335	5,12	4,52
403	26967304	7,43	3,13	165215	5,22	4,43
413	60578344	7,78	3,01	229605	5,36	4,30
423	242335457	8,38	2,86	339679	5,53	4,16
433	404076433	8,61	2,77	377230	5,58	4,16
443	604526539	8,78	2,67	343902	5,54	4,28
453	742734607	8,87	2,59	435548	5,64	4,23
463	849248408<	8,93<	2,51	608350	5,78	4,12
473	849248408<	8,93<	2,41	762270	5,88	4,04
483	849248408<	8,93<	2,35	1016889	6,01	3,93
Measurement frequency5 kHz						
293	230921	5,36	4,26	920	2,96	5,49
303	210887	5,32	4,20	1079	3,03	5,45
313	217248	5,34	4,08	1419	3,15	5,37
323	311142	5,49	3,92	2207	3,34	5,25
333	446505	5,65	3,77	3253	3,51	5,14
343	601911	5,78	3,65	5072	3,71	5,01
353	693461	5,84	3,57	7616	3,88	4,88
363	850701	5,93	3,49	10984	4,04	4,76
373	1139363	6,06	3,41	14833	4,17	4,66
383	1613673	6,21	3,34	20838	4,32	4,54
393	2401699	6,38	3,25	28602	4,46	4,42
403	4458684	6,65	3,11	36620	4,56	4,33
413	9542251	6,98	2,99	51147	4,71	4,21
423	34073036	7,53	2,85	75204	4,88	4,07
433	55324841	7,74	2,76	79651	4,90	4,09
443	82969851	7,92	2,66	69204	4,84	4,22
453	103753716	8,02	2,58	85219	4,93	4,16
463	123745223	8,09	2,51	118284	5,07	4,07
473	158989384	8,20	2,40	148467	5,17	3,99
483	180696391	8,26	2,34	198510	5,30	3,88
Measurement frequency10 kHz						
293	82189	4,92	4,24	51	1,71	5,34
303	80797	4,91	4,17	593	2,77	5,31
313	97036	4,99	4,04	763	2,88	5,24
323	150225	5,18	3,87	1147	3,06	5,14
333	223618	5,35	3,74	1649	3,22	5,03
343	301792	5,48	3,63	2498	3,40	4,92
353	347406	5,54	3,55	3736	3,57	4,80
363	424773	5,63	3,47	5361	3,73	4,70
373	561792	5,75	3,39	7312	3,86	4,60
383	777214	5,89	3,32	10376	4,02	4,49
393	1128577	6,05	3,23	14534	4,16	4,37
403	2073461	6,32	3,09	18904	4,28	4,28
413	4425478	6,65	2,98	26702	4,43	4,16
423	14367728	7,16	2,84	39228	4,59	4,03
433	22727813	7,36	2,75	39566	4,60	4,07
443	34175796	7,53	2,65	33516	4,53	4,19
453	43345223	7,64	2,57	40940	4,61	4,14
463	52411040	7,72	2,50	57187	4,76	4,04
473	68501911	7,84	2,40	72250	4,86	3,96
483	78744798	7,90	2,34	97570	4,99	3,85

The results of this investigation given in the table 1 and figure 1 show that $LaNa_2CoCuMnO_6$ has the semiconductor conductivity in the temperature interval at 293–483 K and measurement frequencies of 1, 5, and 10 kHz, the band gap is 0.54 eV and it can be fitted to the narrow-band gap semiconductors.

This compound has the high values of the dielectric constant. Thus, $LaNa_2CoCuMnO_6$ at 293 K has the following values of the dielectric capacity (ε): $2.17 \cdot 10^6$ (1 kHz), $2.31 \cdot 10^5$ (5 kHz), $8.22 \cdot 10^4$ (10 kHz) and at 483 K — < $8.49 \cdot 10^8$ (1 kHz), $1.81 \cdot 10^8$ (5 kHz) and $7.87 \cdot 10^7$ (10 kHz).

$LaNa_2NiCuMnO_6$ in interval of 293–483 K demonstrates the semiconductor conductivity, at 433–443 K — the metallic conductivity and at 453–483 K — the semiconductor conductivity. The band gap at 293–433 K is 0.48 eV, and at 443–483 K — 2.33 eV, and this compound can be fitted to narrow-band gap semiconductors.

$LaNa_2NiCuMnO_6$ at 293 K has the following values of the dielectric capacity — $4.97 \cdot 10^3$ (1 kHz), $9.2 \cdot 10^2$ (5 kHz), $5.1 \cdot 10$ (10 kHz) and at 483 K — $1.02 \cdot 10^6$ (1 kHz), $1.98 \cdot 10^5$ (5 kHz) and $9.76 \cdot 10^4$ (10 kHz).

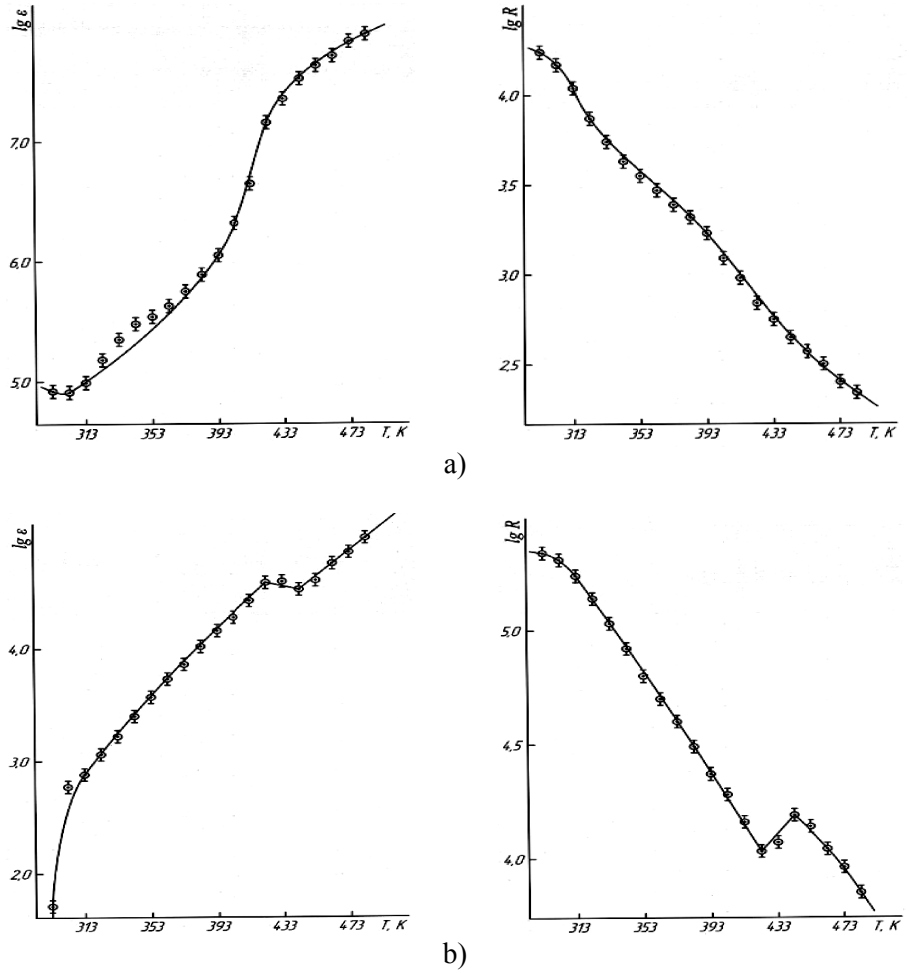

Figure 1. Dependence of dielectric constant (ε) and electrical resistance (R) of $LaNa_2CoCuMnO_6$ (a) and $LaNa_2NiCuMnO_6$ (b) on temperature at measurement frequency of 10 kHz

Conclusion

The temperature dependences of the dielectric constant and electrical resistance of the new nanodimensional $LaNa_2CoCuMnO_6$ and $LaNa_2NiCuMnO_6$ were first investigated in the interval of 293–483 K. It was found that $LaNa_2CoCuMnO_6$ is of interest for the semiconductor and microcapacitor technologies, having the high values of the dielectric constant at all measured frequencies of 1, 5, and 10 kHz.

$LaNa_2NiCuMnO_6$ compound is of interest for the semiconductor technology. Both compounds belong to narrow-band gap semiconductors.

Acknowledgments

The work was performed within the Contract No. 65 dated 23.02.2018 signed between Committee of science of the Ministry of Education and Science of the Republic of Kazakhstan and Abishev Chemical-Metallurgical Institute, the Grant Code of Individual Registration Number: AP05131317; AP05131333).

References

1 Третьяков Ю.Д. Новые поколения неорганических функциональных материалов / Ю.Д. Третьяков, О.А. Брылёв // Журн. Рос. хим. общ-ва им. Д.И. Менделеева. — 2000. — Т. 44, № 4. — С. 10–16.

2 Третьяков Ю.Д. Химические принципы получения металлооксидных сверхпроводников / Ю.Д. Третьяков, Е.А. Гудилин // Успехи химии. — 2000. — Т. 69, № 1. — С. 3–40.

3 Sukanti Behera. Synthesis, structure and thermoelectric properties of $La_{1-x}Na_xCoO_3$ perovskite oxides / Sukanti Behera, Vinayak. B. Kamble, Satish Vittac, Arun M. Umarji, C. Shivakumara // Bulletin of Materials Science. — 2017. — Vol. 40. — Iss. 7. — P. 1291–1299.

4 Sadykov V. $La_{0.8}Sr_{0.2}Ni_{0.4}Fe_{0.6}O_3$–$Ce_{0.8}Gd_{0.2}O_{2-\delta}$ Nanocomposite as Mixed Ionic–Electronic Conducting Material for SOFC Cathode and Oxygen Permeable Membranes: Synthesis and Properties / V. Sadykov, T. Kharlamova, A. Smirnova // Composite Interfaces. — 2009. — Vol. 16. — P. 407–431.

5 Ерин Ю. Найдено вещество с гигантским значением диэлектрической проницаемости [Электронный ресурс] / Ю. Ерин // Химия и химики. — 2009. — № 1. — Режим доступа: http://chemistry-chemists.com/N1_2009/16–22.pdf

6 Касенов Б.К. Двойные и тройные манганиты, ферриты и хромиты щелочных, щелочноземельных и редкоземельных металлов / Б.К. Касенов, Ш.Б. Касенова, Ж.И. Сагинтаева, Б.Т. Ермагамбет, Н.С. Бектурганов, И.М. Оскембеков. — М.: Науч. мир, 2017. — 416 с.

7 Касенова Ш.Б. Теплоемкость и термодинамические функции наноструктурированных частиц купрато-манганитов $LaM_2^{II}CuMnO_6$ (M^{II} – Mg, Ca) в интервале 298,15–673 К / Ш.Б. Касенова, Б.К. Касенов, Ж.И. Сагинтаева, К.Т. Ермаганбетов, Е.Е. Куанышбеков, А.А. Сейсенова, Д.И. Смагулова // ЖФХ. — 2014. — Т. 88, № 5. — С. 836–840.

8 Касенов Б.К. Теплоемость и термодинамические функции манганитов $NdM^{II}_2CoMnO_6$ (M^{II} – Mg, Ca, Sr, Ba) в интервале 298,15–673 К / Б.К. Касенов, Ш.Б. Касенова, Ж.И. Сагинтаева, М.О. Туртубаева, Ш.К. Амерханова, Р.Н. Николов // ТВТ. — 2016. — Т. 54, № 4. — С. 540–544.

9 Касенов Б.К. Теплоемкость и термодинамические функции новых наноразмерных ферро-хромо-манганитов $LaM^{II}_{0,5}FeCrMnO_{6,5}$ (M^{II} – Mg, Ca, Sr, Ba) / Б.К. Касенов, Ш.Б. Касенова, Ж.И. Сагинтаева, М.О. Туртубаева, К.С. Какенов, Г.А. Есенбаева // ЖФХ. — 2017. — Т. 91, № 3. — С. 410–416.

10 Касенова Ш.Б. Калориметрическое исследование теплоемкости никелито-манганитов LaM_2NiMnO_5 (M — Li, Na, K) в интервале температур 298,15–673 К / Ш.Б. Касенова, Ж.И. Сагинтаева, Б.К. Касенов, М.О. Туртубаева, К.Т. Рустембеков, И. Стоев // ТВТ. — 2017. − Т. 55, № 3. — С. 480–483.

11 Kasenova Sh.B. New nano-sized (nanocluster) cobalt-cuprate-manganites of lanthane and metals and alkaline metals and their X-ray diffraction study / Sh.B. Kasenova, B.K. Kasenov, Zh.I. Sagintaeva, M.O. Turtubaeva, E.E. Kuanyshbekov // News of the Academy of sciences of the Republic of Kazakhstan. Series chemistry and technology. — 2018. — No. 3. — P. 39–43.

12 Sagintaeva Zh.I. Synthesis and X-ray of new nanosized (nanocluster) nickelite-cuprate-manganites of lanthanum and alkaline metals / Zh.I. Sagintaeva, B.K. Kasenov, Sh.B. Kasenova, M.O. Turtubaeva, E.E. Kuanyshbekov // News of the Academy of sciences of the Republic of Kazakhstan. Series chemistry and technology. — 2018. — No. 3. — P. 44–48.

13 Касенов Б.К. Новые замещенные поликристаллические и наноразмерные манганиты / Б.К. Касенов, Ш.Б. Касенова, Ж.И. Сагинтаева, Б.Т. Ермагамбет, Е.Е. Куанышбеков, М.О. Туртубаева, А.Ж. Бектурганова. — Караганда: Экожан, 2019. — 108 с.

14 Окадзаки К. Технология керамических диэлектриков / К. Окадзаки. — М.: Энергия, 1976. — 256 с.

15 Жумадилов Е.К. Исследование электрофизических свойств хромита $GdSrCr_2O_{5,5}$ / Е.К. Жумадилов, С.Ж. Давренбеков, Е.С. Мустафин, Б.К. Касенов, С.Т. Едильбаева // Вестн. НАН РК. — 2004. — № 5. — С. 114–118.

16 Фесенко Е.Г. Семейство перовскита и сегнетоэлектричество / Е.Г. Фесенко. — М.: Атомиздат, 1972. — 248 с.

17 Веневцев Ю.Н. Сегнето- и антисегнетоэлектрики семейства титаната бария / Ю.Н. Веневцев, Е.Д. Политова, С.А. Иванов. — М.: Химия, 1985. — 256 с.

18 Лайнс М. Сегнетоэлектрики и родственные им материалы / М. Лайнс, А. Гласс. — М.: Мир, 1981. — 736 с.

Ш.Б. Қасенова, Ж.И. Сағынтаева, Б.Қ. Қасенов,
Е.Е. Қуанышбеков, Ж.С. Бектұрғанов, А.К. Зейниденов

Наноөлшемді $LaNa_2CoCuMnO_6$кобальт-купрат-манганитімен $LaNa_2NiCuMnO_6$ никелит-купрат-манганитінің электрофизикалық сипаттамалары

10 К арқылы 293–483 интервалында 1 кГц, 5 кГц және 10 кГц жиілікте жұмыс істейтін LCR-800 (Тайвань өндірісінің) сериялы қондырғысында $LaNa_2CoCuMnO_6$лантан мен натрий кобальт-купрат-

манганиті және $LaNa_2NiCuMnO_6$лантан мен натрий никелит-купрат-манганитінің электрсыйымдылықтары, диэлектрлік өтімділіктері, электрқарсылықтарының температураға тәуелділіктері үздіксіз құрғақ ауада зерттелген. $LaNa_2CoCuMnO_6$қосылысының 293–483 К аралықта жартылай өткізгіштік қасиет танытуы анықталды. Тыйым салу аймақ ені (Δ Е) 0.54 эВ тең. Қосылыс 293 К $2{,}17\cdot10^6$ (1 кГц), $2{,}31\cdot10^5$ (5 кГц), $8{,}22\cdot10^4$ (10 кГц) және 483 К-де $8{,}49\cdot10^8$ (5 кГц), $7{,}87\cdot10^7$ (10 кГц) тең болатын диэлектрлік өтімділіктің алып мәніне ие. $LaNa_2NiCuMnO_6$ қосылысы 293–483 К аралықта (Δ Е = 0.48 эВ) жартылайөткізгіштік, 433–443 К-де — металдық және 453–483 К-де — (Δ Е = 2,33 эВ) қайта жартылайөткізгіштік қасиетке ие. Диэлектрлік өтімділік мәндері 293 К-де $4{,}97\cdot10^3$ (1 кГц), $9{,}2\cdot10^2$ (5 кГц), $5{,}1\cdot10^1$ (10 кГц) және 483 К-де $1{,}02\cdot10^6$ (1 кГц), $1{,}98\cdot10^5$ (5 кГц) және $9{,}76\cdot10^4$ (10 кГц) тең. Қосылыстарды жіңішке аймақты (қуыс аймақты) жартылайөткізгіштерге жатқызуға болады және олар жартылайөткізгіштер мен микроконденсаторлар технологиясы үшін қызығушылық тудырады.

Кілт сөздер: электрофизика, кобальт, никелит, купрат, манганит, лантан, натрий, диэлектрлік өтімділік, электрқарсылық.

Ш.Б. Касенова, Ж.И. Сагинтаева, Б.К. Касенов,
Е.Е. Куанышбеков, Ж.С. Бектурганов, А.К. Зейниденов

Электрофизические характеристики наноразмерных кобальто-купрато-манганита $LaNa_2CoCuMnO_6$ и никелито-купрато-манганита $LaNa_2NiCuMnO_6$

На серийном приборе LCR–800 (производство Тайвань) при рабочих частотах 1, 5 и 10 кГц в интервале 293–483 К через 10 К непрерывно в сухом воздухе исследованы температурные зависимости электроемкости, диэлектрической проницаемости, электросопротивления кобальто-купрато-манганита лантана и натрия $LaNa_2CoCuMnO_6$ и никелито-купрато-манганита лантана и натрия $LaNa_2NiCuMnO_6$. Установлено, что $LaNa_2CoCuMnO_6$ в интервале 293–483 К проявляет полупроводниковый характер проводимости. Ширина запрещенной зоны (Δ Е) равна 0,54 эВ. Соединение обладает гигантскими значениями диэлектрической проницаемости, которые равны при 293 К $2{,}17\cdot10^6$ (1 кГц); $2{,}31\cdot10^5$ (5 кГц); $8{,}22\cdot10^4$ (10 кГц) и при 483 К $8{,}49\cdot10^8$ (5 кГц); $7{,}87\cdot10^7$ (10 кГц). $LaNa_2NiCuMnO_6$ в интервале 293–483 К также проявляет полупроводниковую (Δ Е = 0.48 эВ), при 433–443 К — металлическую и при 453–483 К — опять полупроводниковую проводимость (Δ Е = 2,33 эВ). Значения диэлектрической проницаемости равны при 293 К $4{,}97\cdot10^3$ (1 кГц); $9{,}2\cdot10^2$ (5 кГц); $5{,}1\cdot10^1$ (10 кГц) и при 483 К $1{,}02\cdot10^6$ (1 кГц); $1{,}98\cdot10^5$ (5 кГц) и $9{,}76\cdot10^4$ (10 кГц). Соединения можно отнести к узкозондовым полупроводникам, которые представляют интерес для полупроводниковой и микроконденсаторной технологии.

Ключевые слова: электрофизика, кобальт, никелит, купрат, манганит, лантан, натрий, диэлектрическая проницаемость, электросопротивление.

References

1 Tretyakov, Yu.D., & Brylyov, O.A. (2000). Novye pokoleniia neorhanicheskikh funktsionalnykh materialov [New generations of inorganic functional materials]. *Zhurnal Rossiiskoho himicheskoho obshchestva imeni D.I. Mendeleeva — Journal of the Russian Chemical Society named after D.I. Mendeleev, Vol. 44, 4,* 10–16 [in Russian].

2 Tretyakov, Yu.D., & Gudilin, E.A. (2000). Khimicheskie printsipy polucheniia metallooksidnykh sverkhprovodnikov [Chemical principles of the receiving of metal-oxide superconductors]. *Uspekhi khimii — Russian Chemical Reviews, Vol. 69, 1,* 3–40 [in Russian].

3 Behera, S., Kamble, V.B., Vittac, S., Umarji, A.M., & Shivakumara, C. (2017). Synthesis, structure and thermoelectric properties of $La_{1-x}Na_xCoO_3$ perovskite oxides. *Bulletin of Materials Science, Vol. 40,* Issue 7, 1291–1299. DOI: 10.1007/s12034–017–1498–6.

4 Sadykov, V., Kharlamova, T., & Smirnova, A. (2009). $La_{0.8}Sr_{0.2}Ni_{0.4}Fe_{0.6}O_3$–$Ce_{0.8}Gd_{0.2}O_{2-\delta}$ Nanocomposite as Mixed Ionic–Electronic Conducting Material for SOFC Cathode and Oxygen Permeable Membranes: Synthesis and Properties. *Composite Interfaces, Vol. 16,* 407–431. DOI: 10.1163/156855409x450855.

5 Erin, Yu. (2009). Naideno veshchestvo s hihantskim znacheniem dielektricheskoi pronitsaemosti [Substance with high value of dielectric capacitivity was found]. *Khimiia i khimiki — Chemistry and Chemists, 1.* Retrieved from http://chemistry-chemists.com/N1_2009/16–22.pdf [in Russian].

6 Kasenov, B.K., Kasenova, Sh.B., Sagintaeva, Zh.I., Ermagambet, B.T., Bekturganov, N.S., & Oskembekov, I.M. (2017). *Dvoinye i troinye manhanity, ferrity i khromity shchelochnykh, shchelochnozemelnykh i redkozemelnykh metallov* [*Double and triple manganites, ferrites and chromites of alkali, alkaline earth and rare earth metals*]. Moscow: Nauchnyi mir [in Russian].

7 Kasenova, Sh.B., Kasenov, B.K., Sagintaeva, Zh.I., Ermaganbetov, K.T., Kuanyshbekov, E.E., Sejsenova, A.A., & Smagulova, D.I. (2014). Teploemkost i termodinamicheskie funktsii nanostrukturirovannykh chastic kuprato-manhanitov

$LaM_2^{II}CuMnO_6$ (M^{II} – Mg, Ca) v intervale 298,15–673 K [Heat capacity and thermodynamic functions of $LaM_2^{II}CuMnO_6$ (M^{II} – Mg, Ca) nanostructured cuprate-manganite particles in the range of 298.15–673 K]. *Zhurnal fizicheskoi khimii — Russian Journal of Physical Chemistry, Vol. 88, 5,* 836–840. DOI: 10.7868/s0044453714050112 [in Russian].

8 Kasenov, B.K., Kasenova, Sh.B., Sagintaeva, Zh.I., Turtubaeva, M.O., Amerhanova, Sh.K., & Nikolov, R.N. (2016). Teploemkost i termodinamicheskie funktsii manhanitov $NdM^{II}_2CoMnO_6$ (M^{II} – Mg, Ca, Sr, Ba) v intervale 298,15–673 K [Heat capacity and thermodynamic functions of manganites $NdM^{II}_2CoMnO_6$ (M^{II} – Mg, Ca, Sr, Ba) in the range of 298.15–673 K]. *Teplofizika vysokikh temperatur — High Temperature, Vol. 54, 4,* 540–544. DOI: 10.7868/s0040364416040104 [in Russian].

9 Kasenov, B.K., Kasenova, Sh.B., Sagintaeva, Zh.I., Turtubaeva, M.O., Kakenov, K.S., & Esenbaeva, G.A. (2017). Teploemkost i termodinamicheskie funktsii novykh nanorazmernykh ferro-hromo-manhanitov $LaM^{II}_{0,5}FeCrMnO_{6,5}$ (M^{II} – Mg, Ca, Sr, Ba) [Heat capacity and thermodynamic functions of new nanoscale ferro-chromo-manganites $LaM^{II}_{0,5}FeCrMnO_{6,5}$ (M^{II} – Mg, Ca, Sr, Ba)]. *Zhurnal fizicheskoi khimii — Russian Journal of Physical Chemistry, Vol. 91, 3,* 410–416. DOI: 10.7868/s0044453717030116 [in Russian].

10 Kasenova, Sh.B., Sagintaeva, Zh.I., Kasenov, B.K., Turtubaeva, M.O., Rustembekov, K.T., & Stoev, I. (2017). Kalorimetricheskoe issledovanie teploemkosti nikelito-manhanitov LaM_2NiMnO_5 (M – Li, Na, K) v intervale temperatur 298, 15–673 K [Calorimetric study of the heat capacity of LaM_2NiMnO_5 (M – Li, Na, K) nickelite-manganites in the temperature range 298.15–673 K]. *Teplofizika vysokikh temperatur — High Temperature, Vol. 55, 3,* 480–483. DOI: 10.7868/s0040364417030024 [in Russian].

11 Kasenova, Sh.B., Kasenov, B.K., Sagintaeva, Zh.I., Turtubaeva, M.O., & Kuanyshbekov, E.E. (2018). New nano-sized (nanocluster) cobalt-cuprate-manganites of lanthane and metals and alkaline metals and their X-ray diffraction study. *News of the Academy of sciences of the Republic of Kazakhstan. Series chemistry and technology, 3,* 39–43.

12 Sagintaeva, Zh.I., Kasenov, B.K., Kasenova, Sh.B., Turtubaeva, M.O., & Kuanyshbekov, E.E. (2018). Synthesis and X-ray of new nanosized (nanocluster) nickelite-cuprate-manganites of lanthanum and alkaline metals. *News of the Academy of sciences of the Republic of Kazakhstan. Series chemistry and technology, 3,* 44–48.

13 Kasenov, B.K., Kasenova, Sh.B., Sagintaeva, Zh.I., Ermagambet, B.T., Kuanyshbekov, E.E., Turtubaeva, M.O., & Bekturganova, A.Zh. (2019). *Novye zameshchennye polikristallicheskie i nanorazmernye manhanity* [*New substituted polycrystalline and nanosized manganites*]. Karaganda: Ekozhan [in Russian].

14 Okadzaki, K. (1976). *Tekhnolohiia keramicheskikh dielektrikov [Technology of ceramic dielectrics]*. Moscow: Enerhiia [in Russian].

15 Zhumadilov, E.K., Davrenbekov, S.Zh., Mustafin, E.S., Kasenov, B.K., & Edilbaeva, S.T. (2004). Issledovanie elektrofizicheskikh svoistv khromita $GdSrCr_2O_{5,5}$ [Investigation of electrophysical properties of chromite of $GdSrCr_2O_{5,5}$]. *Vestnik Natsionalnoi akademii nauk Respubliki Kazakhstan — Bulletin of the National Academy of Sciences of the Republic of Kazakhstan, 5,* 114–118 [in Russian].

16 Fesenko, E.G. (1972). *Semeistvo perovskita i sehnetoelektrichestvo* [*Perovskite family and ferroelectricity*]. Moscow: Atomizdat [in Russian].

17 Venevtsev, Yu.N., Politova, E.D., & Ivanov, S.A. (1985). *Sehneto- i antisehnetoelektriki semeistva titanata bariia* [*Ferroelectric and antiferroelectrics of barium titanate family*]. Moscow: Khimiia [in Russian].

18 Lines, M., & Glass, A. (1981). *Sehnetoelektriki i rodstvennye im materialy* [*Ferroelectrics and related materials*]. Moscow: Mir [in Russian].

DOI 10.31489/2020Ph2/50-59

UDC 629.3.017.5

A.A. Kashkanov[1], A.P. Rotshtein[2], V.Yu. Kucheruk[3], V.A. Kashkanov[3]

[1]Kharkiv National Automobile and Highway University, Ukraine;
[2]Jerusalem College of Technology, Machon Lev, Jerusalem, Israel
[3]Vinnytsia National Technical University, Ukraine
(E-mail: a.kashkanov@gmail.com)

Tyre-Road friction Coefficient: Estimation Adaptive System

This paper offers an upgraded method for estimating the magnitude of friction between tyres of a motor vehicle and a road surface while investigating road accidents. The above-mentioned method is based on the resultant data of tyre-and-road interworking field tests in case of emergency braking. Such estimation of the magnitude of friction is to be carried out with a focus on the factors affecting the friction processes in the tyre-and-road contact. The most important factors, which are included in the synthesized adaptive system used for friction coefficient estimation, have been defined based on the theoretical analysis of the data of deceleration and braking length of motor vehicles. The study of the existing expert methods used for estimating the level of tyre-and-road engagement and the effect of such level on the motional parameters of a motor vehicle has demonstrated the need for upgrading of the existing approaches. Unlike the existing practices, the friction coefficient estimation adaptive system offered by the authors hereof is a self-trainable system. Such system reduces any simulation uncertainty and the probability of occurrence of Type 1 and Type 2 errors. Such result is achieved owing to the fact that the system takes into account the upgraded design of the present-day brake systems and tyres, as well as the speed of motor vehicles and load of their wheels; the system is also efficient because it makes use of the up-to-date mathematical methods which are able to process raw (initial) data under conditions of stochastic and fuzzy uncertainty. The approach offered hereby has demonstrated its efficiency for motor vehicles belonging to categories M1 and N1 and has proven its potential applicability for other categories of motor vehicles.

Keywords: friction coefficient, tyre, road surface, deceleration process, estimation adaptive system, road accident investigation.

Introduction

Braking of motor vehicles (MVs), where the efficiency of braking depends on the tyre-to-surface frictional capacity, is the basic technique to prevent road accidents [1, 2]. The parameter used to assess the efficiency of tyre-and-road engagement is the value of the static friction coefficient (friction coefficient φ), while, when the wheels are being locked, such parameter is the value of the coefficient of sliding friction (frictional drag coefficient) which is usually lower than the friction coefficient. The non-dimensional value φ for ordinary tyres varies within the range of (0; 1] [3]. The near-zero values φ indicate a smooth slippery surface in the tyre-and-road contact, which is characterized by low values of frictional forces (longitudinal, latitudinal and sidewise friction). The higher the value φ, the higher frictional forces which are to be overpowered or transferred.

The tyre grip on the road is a result of complex processes running within the tyre-and-road contact area. It depends on a number of factors (Fig. 1), of which the most significant are the type and condition of the road surface; the tyre's design and condition, as well as the operating conditions [4, 5].

The resultant force applied by the tyre to the road is a vectorial sum of the latitudinal and longitudinal forces (Fig. 2). It increases in line with the increasing frictional capacity within the tyre-and-road contact area or in line with the increasing load on the wheel [3, 4].

The value of the coefficient of adhesion (the tyre-road friction coefficient) in the course of analyzing the road accident (RA) can be determined in one of the three ways [1, 2, 6]:

– basing on the data provided by the motor vehicle's steering, safety and comfort electronic systems;
– by the way of test and trial;
– using the experimentally determined reference data.

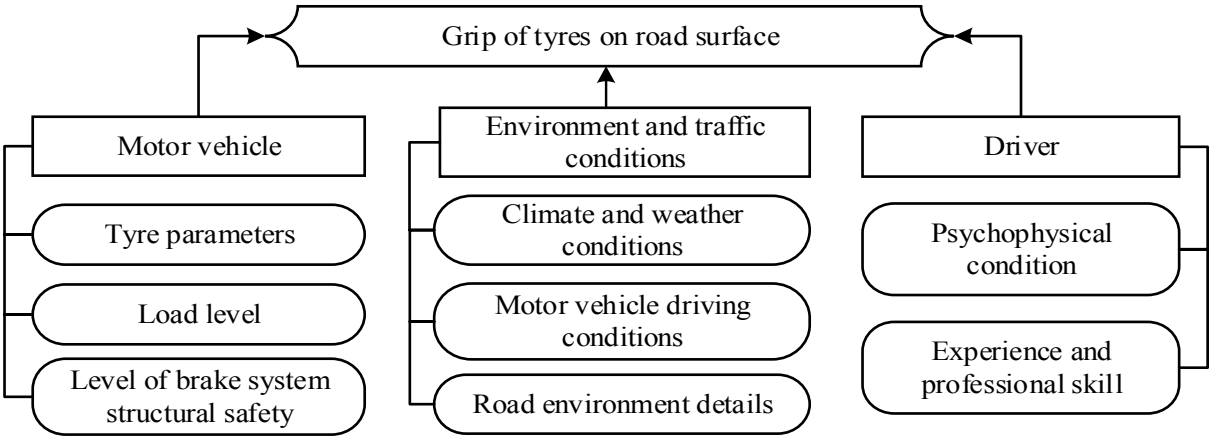

Figure 1. The factors affecting the potential tyre-to-surface grip capacity

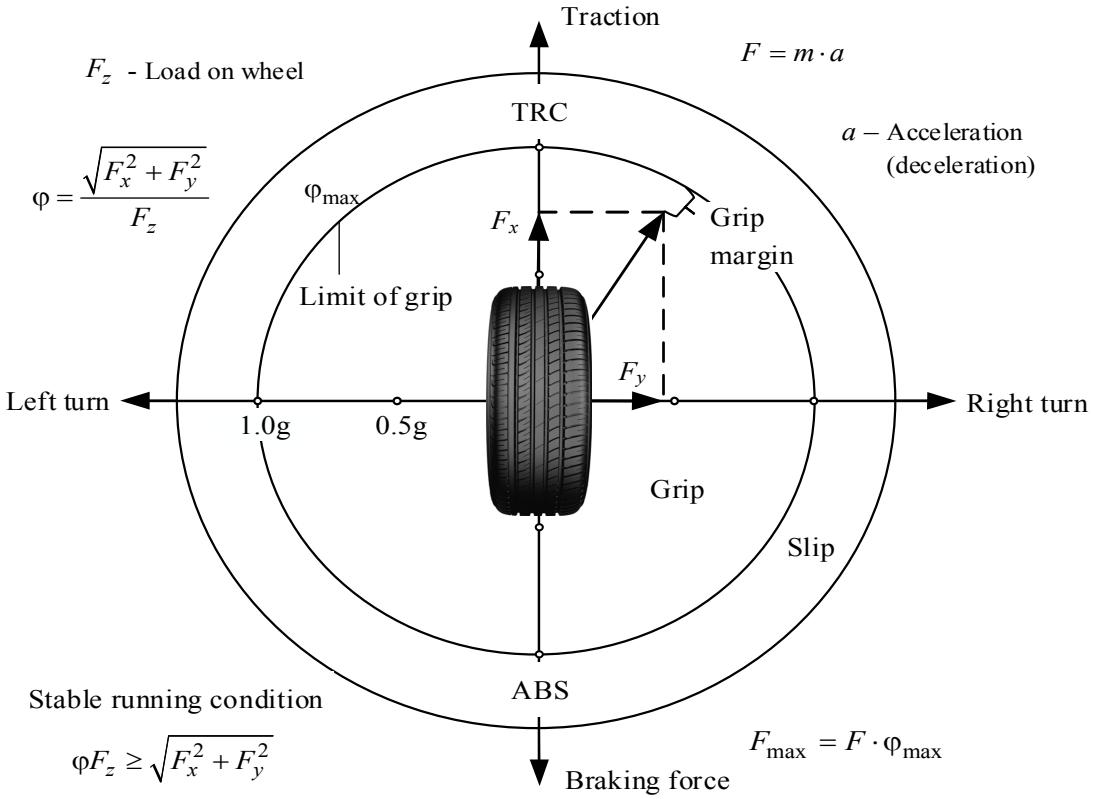

Figure 2. Forces applied on within tyre in Kamm Circle

The first method is rather new. Its wide application is, however, restricted because determining the traffic parameters on the basis of the data provided by the on-board electronic data recorders (EDR) is only possible where such systems are installed on board. The percentage of such motor vehicles in the global fleet of motor vehicles is rather low, yet tending to grow each year [7, 8].

The Best Practice Manual for Road Accident Reconstruction issued by the European Network of Forensic Science Institutes [2] recommends, while assessing the tyre-and-road engagement, to perform an investigative experiment under the on-scene or similar roads conditions. In doing so, experts experimentally determine the coefficient of adhesion (the tyre-road friction coefficient) or the braking length, or, else, the rate of deceleration, for such parameters identify the friction processes occurring in the tyre-and-road contact. However, application of such method is not always possible for a number of external reasons [1].

In case when such experiment cannot be conducted, the values of the coefficient of adhesion, the rate of deceleration or the braking length can be determined with the use of using the experimentally determined reference data [2] or assumed as standard values, as defined by the Traffic Rules and/or a regulatory document such as Council Directive 71/320/EEC. The braking efficiency parameters can also be determined by way of calculations using the formulas widely applicable in the expert practices [1, 9] and found out on the basis of the driver-vehicle-road-environment (DVRE) mathematical models.

In using the DVRE systemic mathematical models, the level of uncertainty of the rated parameters depends on the accuracy of the input parameters and on the assumed structure of the model which is just an approximation to the reality. While using the data provided by the EDRs, an uncertainty of the rated parameters can result from errors in the motor vehicle's running measurements and from an inaccurate result of the recorded data processing. The accuracy of experimental methods depends both on the test procedure, on the test equipment and on the quality of the measured data processing [10, 11].

This study is intended to upgrade the existing approaches to estimating the coefficient of adhesion and the braking efficiency parameters in the course of a road accident investigation while performing a technical examination of a motor vehicle under the conditions of stochastic and fuzzy uncertainty.

Identification Methods and Structure of Adhesion Coefficient Estimation System

The adaptive system for estimating the coefficient of adhesion has been developed on the basis of the method for identification of nonlinear objects by fuzzy knowledge bases [**Ошибка! Источник ссылки не найден.**] in Anfis Neuro-Fuzzy Inference System [13] included in the Fuzzy Logic Toolbox for Matlab computing environment [14]. The system was built up in a two-phase process, where the first phase focuses on the structural identification and the second one on the parametric identification.

During the structural identification phase, the structure of dependence of the tyre-road friction coefficient (coefficient of adhesion) on the impact factors (Fig. 3) was built on the basis of the if-then rule. The parametric identification was performed via selecting such parameters in the knowledge base which would have provided the maximum approximation between the simulation results and the experimental data.

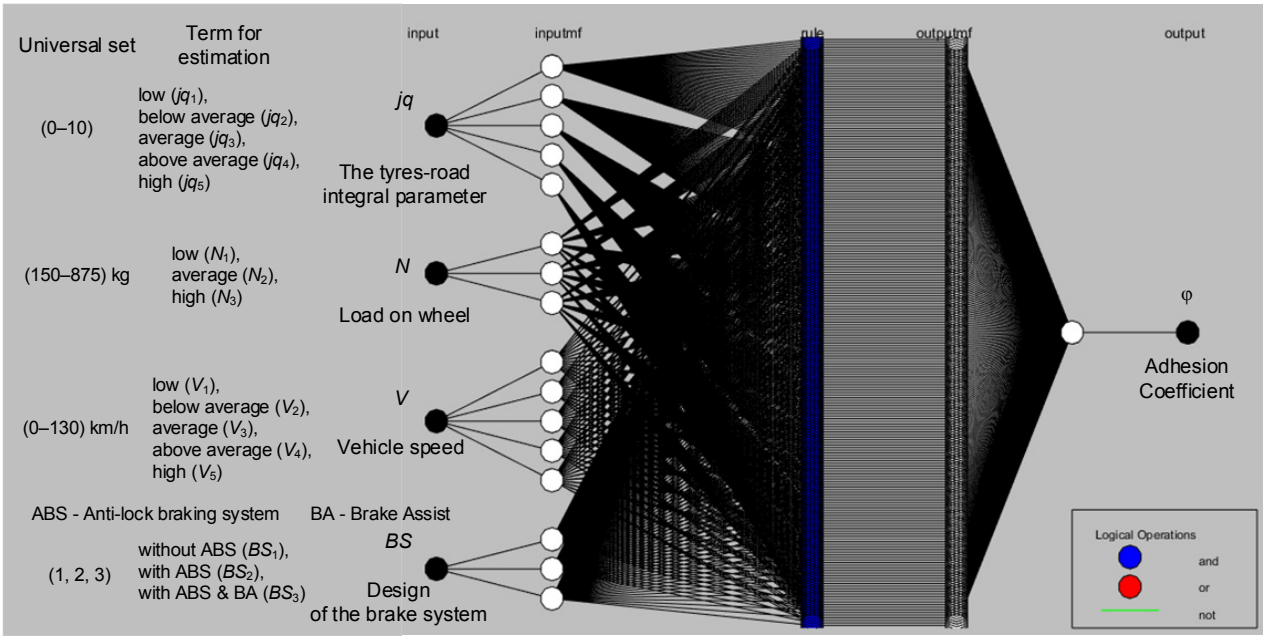

Figure 3. Structure of Tyre-Road Friction Coefficient Estimation System

As shown by Fig. 3, the neuro-fuzzy network of the system consists of five layers. Each node of the first layer is a term incorporating the Gaussian membership function [14]

$$\mu_j(x_i) = e^{-\frac{1}{2}\left(\frac{x_i - c_{ij}}{\sigma_{ij}}\right)^2}, \quad (1)$$

where $\mu_j(x_i)$ is a fuzzy set membership function a_{ij}; c_{ij} and σ_{ij} are a maximum coordinate and a concentration factor – the membership function parameters.

The quantity of the second-layer nodes is equal to the quantity of rules in Sugeno fuzzy knowledge base [13] (as is clear from Fig.3, for this case the number of the rules amounts to m = 5*3*5*3 = 225). Each second-layer node is associated with those first-layer nodes which make up antecedents of the respective rule. The node output is a degree of fulfillment of the rule τ_r, incorporated by the node which is equal to the product of the input signals.

All two hundred and twenty five nodes of the third layer determine the relative degree of fulfillment of the relevant fuzzy rule τ_r*

$$\tau_r^* = \tau_r / \sum_{j=\overline{1,m}} \tau_j. \quad (2)$$

The fourth-layer nodes specify the contribution of the fuzzy rules to the network output φ.

$$\varphi_r = \tau_r^* \cdot \left(b_{0,r} + b_{1,r} \cdot jq + b_{2,r} \cdot N + b_{3,r} \cdot V + b_{4,r} \cdot BS\right), \quad (3)$$

where $b_{q,r}$ – are the coefficients of the r-rule consequent function (r = 1, 2, …, 225; q = 0, 1, 2, 3, 4).

The single node of the fifth layer aggregates the contributions of all rules

$$\varphi = \varphi_1 + \ldots + \varphi_j + \ldots + \varphi_m. \quad (4)$$

All factors which affect the tyre-road friction coefficient (the coefficient of adhesion) (Fig. 3) are considered as linguistic variables which are assigned to the respective universal sets and are estimated via the fuzzy terms. The list of the most significant factors has been established by reviewing the data furnished by the Bosch experts [3, 15] and based on our own theoretical findings [10, 16, 17].

The recommendations for estimating the tyres-road integral parameter *jq* are given in Table 1 below.

The rules for the if-then logical statement have been automatically formulated in Anfis neuro-fuzzy editor in the Matlab computing environment.

Experimental Research into Tyre-Road Engagement in Case of Emergency Braking and System Parametric Identification

The potential engagement between the automobile's wheels and the road surface can be estimated based on the results of the experimental assessment of the rate of steady deceleration j in case of emergency braking. Basing on the given values j, a motor expert is able to estimate objectively the braking length of the motor vehicle and its speed at the start of braking. The acquired experimental data relating to the braking dynamics of Category M1 and N1 motor vehicles, which were published by the authors hereof in their paper [17], were used to ensure the process of parametric identification of the neuro-fuzzy system (Fig. 4).

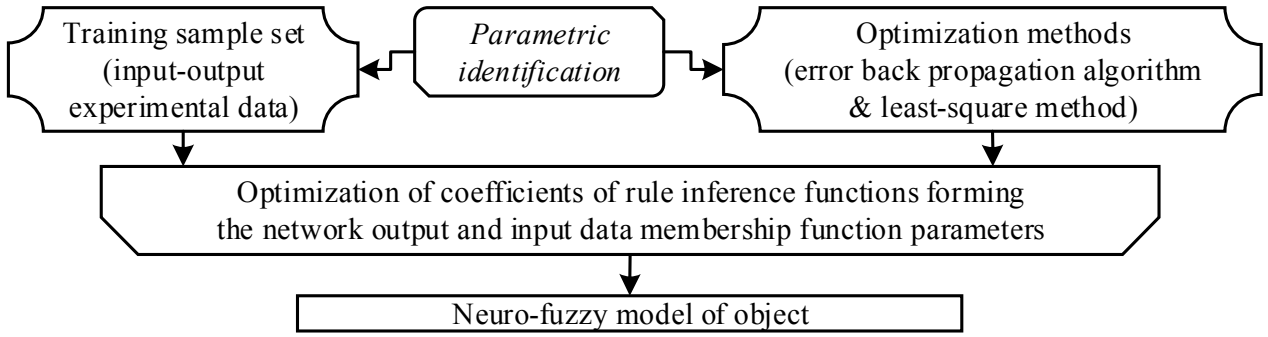

Figure 4. Schematic diagram of neuro-fuzzy system parametric identification

In order to create a training sample set and a test sample set for neuro-fuzzy system parametric identification, the authors hereof kept writing down the values of the factors influencing the tyre-road friction coefficient (the coefficient of adhesion) (see Fig. 3) and the tyre-road friction coefficient per se. As a result, the

authors have acquired an experimental database (5670 input-output data pairs), a fragment of which is shown in Table 2, below. The said database was then used to create a training sample set (3400 input-output data pairs) and a test sample set (2270 input-output data pairs).

Table 1

Recommended Values for Tyre-Road Integral Parameter *jq*

Type of Road Surface	Tyre Condition	Road Surface Condition		
		Dry	Wet & Clean	Wet & Dirty
Cement-concrete pavement	New*	7,85-8,34	6,38-6,87	3,92-4,41
	Worn-out**	8,83-10,0	4,91-5,40	1,96-2,45
Asphalt-concrete pavement with roughening treatment	New	7,85-8,34	5,89-6,38	4,41-5,40
	Worn-out	8,83-10,0	4,41-4,91	2,45-3,43
Hot asphalt-concrete pavement w/o roughening treatment	New	7,85-8,34	4,91-5,89	3,43-3,92
	Worn-out	8,83-10,0	3,92-4,41	2,43-2,94
Cold asphalt-concrete pavement	New	5,89-6,87	3,92-4,91	2,94-3,43
	Worn-out	7,36-8,34	2,45-3,43	1,96-2,94
Bitumen-coated crushed-stone and gravel pavement with roughening treatment	New	5,89-6,87	4,91-5,89	2,94-3,43
	Worn-out	7,36-8,34	3,43-4,41	1,96-2,94
Bitumen-coated crushed-stone and gravel pavement w/o roughening treatment	New	5,4-5,89	4,41-4,91	2,43-2,94
	Worn-out	6,38-7,36	2,45-3,43	1,96-2,45
Crushed-stone and gravel surface	New	5,89-6,87	5,40-5,89	2,43-2,94
	Worn-out	7,36-8,34	3,92-4,41	1,96-2,45
Surfaced earth road	New	4,41-4,91	2,45-3,92	1,96
	Worn-out	5,4-5,89	1,96-2,94	1,96
Loose snow	New	1,47-3,43		
	Worn-out	1,18-2,45		
Grader-rolled snow	New	2,35-2,75		
	Worn-out	1,67-2,06		
Rolled smooth snow w/o ice crust	New	2,16-2,45		
	Worn-out	1,47-1,77		
Rolled smooth snow with ice crust	New	1,18-1,47		
	Worn-out	1,18-1,47		
Rolled smooth snow with ice crust after sanding at the rate of 0.1 m^3 per 1000 m^2 of road	New	1,67-1,86		
	Worn-out	1,47-1,67		
Rolled smooth snow with ice crust after sanding at the rate of 0.4 m^3 per 1000 m^2 of road	New	2,45-3,73		
	Worn-out	1,96-2,94		
Icy road	New	0,88-1,47	0-0,78	
	Worn-out			

*New – up to 50% tyre tread wear,
**Worn-out – 50 to 100% tyre tread wear, yet not less than 1.6-mm tyre tread height

Table 2

Experimental Database (fragment)

jq	9,7	0,78	3,92	6,87	5,89	5,4	8,34	7,85	4,91	9	2,45	1,96
N	150	250	325	325	725	200	650	275	475	375	300	500
V	20	60	80	80	80	20	100	40	80	130	60	100
BS	1	3	2	2	1	1	3	1	3	3	3	2
φ	0,825	0,075	0,333	0,584	0,384	0,453	0,665	0,627	0,427	0,754	0,232	0,157

Fig. 5, below, demonstrates the training process of the adaptive neuro-fuzzy system used to identify the tyre-road friction coefficient (the coefficient of adhesion) on the basis of the input-output data in Matlab Anfis Editor with the use of the error back propagation algorithm combined with the least-square method.

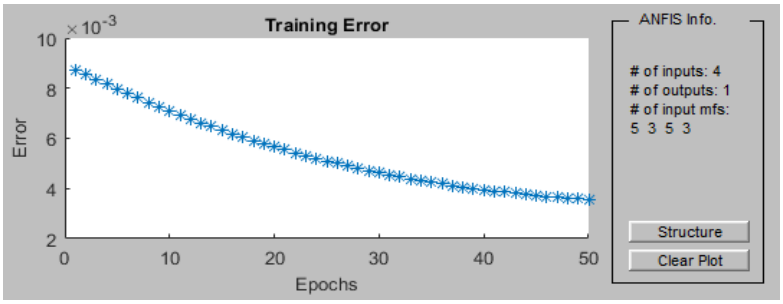

Figure 5. Adaptive neuro-fuzzy system training process

As is clear from Fig. 5, the training process was completed at Epoch 46, and since then the prediction error did not virtually change. The parameters of the membership functions for the input variables, upon completion of the training process, are given in Table 3, below.

Table 3

Parameters of Membership Functions for Factors Affecting the Coefficient of Adhesion

Factor	Universal set	Estimating terms	Post-training membership function parameters	
			Maximum coordinate c_{ij}	Concentration factor σ_{ij}
jq	(0–10)	*jq*1, *jq*2, *jq*3, *jq*4, *jq*5	0.0590850487694922 2.50888607968828 4.9965620984888 7.49073784735645 9.90873828689305	1.21303528289064 1.29362727632086 1.32563448443905 1.29871407906703 1.21900000000000
N	(150–875) kg	*N*1, *N*2, *N*3	150.000359668698 512.500041047082 874.999647086585	153.94025595164 153.940298272589 153.940274751047
V	(0–130) km/h	*V*1, *V*2, *V*3, *V*4, *V*5	0.0000334931228812 32.5000120855364 64.999862248206 97.4998567966736 130.000045723149	13.8014376704274 13.8015719754217 13.8014329230444 13.8016196963052 13.8013863343706
BS	(1,2,3)	*BS*1, *BS*2, *BS*3	0.999998025382338 1.99999606577894 2.99999810282448	0.424656245081971 0.424659477853096 0.424665371752738

The parameters of the membership functions (MF) for the output variable are given in Table 4, below.

Table 4

Specifications of Membership Functions for Coefficient of Adhesion (fragment)

MF Number	1	2	3	4	5	6	7	8	9	10	11	12	13	14
1	2	3	4	5	6	7	8	9	10	11	12	13	14	15
MF Parameter	-0.0255	-0.0218	-0.0496	-0.0092	-0.0276	0.0014	-0.0102	-0.0087	-0.0145	-0.0094	-0.0114	-0.0113	-0.0091	-0.0108
MF Number	15	16	17	18	19	20	21	22	23	24	25	26	27	28
MF Parameter	-0.0115	-0.0068	-0.0154	-0.0062	-0.0094	-0.0068	-0.0139	-0.0087	-0.0103	-0.0102	-0.0081	-0.0098	-0.0107	-0.0077
MF Number	29	30	31	32	33	34	35	36	37	38	39	40	41	…
MF Parameter	-0.0101	-0.0100	-0.0113	-0.0063	-0.0123	-0.0073	-0.0093	-0.0095	-0.0078	-0.0084	-0.0102	-0.0074	-0.0087	…
MF Number	46	47	48	49	50	51	52	53	54	55	56	57	58	59
MF Parameter	0.2205	0.2031	0.2812	0.2022	0.2251	0.2453	0.1950	0.2182	0.2424	0.1855	0.2194	0.2299	0.1755	0.2179
MF Number	60	61	62	63	64	65	66	67	68	69	70	71	72	…
MF Parameter	0.2183	0.1879	0.1931	0.2320	0.1808	0.1936	0.2253	0.1732	0.1953	0.2149	0.1643	0.1951	0.2043	…

1	2	3	4	5	6	7	8	9	10	11	12	13	14	15
MF Number	101	102	103	104	105	106	107	108	109	110	111	112	113	114
MF Parameter	0.4498	0.4709	0.3596	0.4469	0.4470	0.3880	0.3889	0.4816	0.3708	0.4004	0.4592	0.3551	0.3999	0.4406
MF Number	115	116	117	118	119	120	121	122	123	124	125	126	127	…
MF Parameter	0.3371	0.3997	0.4184	0.3220	0.3994	0.4000	0.3507	0.3535	0.4342	0.3247	0.3500	0.4026	0.3138	…
MF Number	217	218	219	220	221	222	223	224	225	Universal set (0 1]				
MF Parameter	0.6367	0.7167	0.7898	0.6047	0.7173	0.7512	0.5728	0.7114	0.7115	Type: constant				

A comparison of the prediction error in estimating the value of the tyre-road friction coefficient (the coefficient of adhesion) using various methods is given in Table 5, below.

Table 5

Prediction Error in Estimating the Value of Tyre-Road Friction Coefficient Using Various Methods

Parameter	Hybrid neuro-fuzzy model	Existing fuzzy model [16]	Linear model	Nonlinear model
RMSE	0.0035	0.0089	0.0291	0.0101
Mean relative error	1.79%	3.97%	15.35%	14.76%
Maximum relative error	3.09%	8.12%	62.03%	40.22%
Number of data pairs in training sample and test sample sets	5670	64	5670	5670

The nonlinear model for predicting the value of the tyre-road friction coefficient (see Table 5 above) reads as

$$\varphi = -0.0316 + 0.0823 \cdot jq + 0.00001 \cdot N + 0.0001 \cdot V + 0.0272 \cdot BS + 0.00001 \cdot jq^2 + \\ + 0.00001 \cdot N^2 - 0.00001 \cdot V^2 - 0.0041 \cdot BS^2 - 0.00001 \cdot jq \cdot N - 0.0001 \cdot jq \cdot V + \\ + 0.008 \cdot jq \cdot BS + 0.00001 \cdot N \cdot V - -0.00001 \cdot N \cdot BS - 0.0001 \cdot V \cdot BS. \quad (5)$$

The linear model for predicting the value of the tyre-road friction coefficient (see Table 5 above) reads as

$$\varphi = 0.0164 + 0.0789 \cdot jq - 0.0001 \cdot N - 0.0004 \cdot V + 0.0392 \cdot BS. \quad (6)$$

As is clear from Table 5, the offered adaptive neuro-fuzzy system for identification of the value of the tyre-road friction coefficient is the most accurate one (the mean prediction error being 1.79%, and the maximum error 3.09%), so it can be recommended for application in performing technical examination of amotor vehicle in the course of a road accident investigation.

The adaptive neuro-fuzzy system for identification of the value of the tyre-road friction coefficient, developed by the authors hereof, is a self-trainable system, provided the experimental database (see table 2 above) is being updated and replenished; it can demonstrate, as reference data, the unifactor and multifactor interrelations of the parameters under study. The quality of the interrelations of the parameters in question depends on the contents and scope of the experimental base.

Conclusions

1. The development of the on-board electronic steering, safety and comfort systems in motor vehicles, as well as innovations in the tyre production processes increase the tyre-and-road engagement capacity, thus entailing the need to upgrade the existing regulations and methods used for estimating the braking properties of motor vehicles.

2. Any expert findings, when used as evidence, are to be substantiated with true and veracious output data, as well as by the fitness and adequacy of the methods used to investigate the road accident in question. The widely-used methods which use the reference data to determine the rated parameters, can often only roughly estimate the range of probable values for the output variables, basing on the grounds of stochastic uncertainty, thus impairing the objectivity of the decision to be made in the course of investigation into the cause of a road accident.

3. The above-said approach allows dealing with the output data which can bear stochastic and/or fuzzy uncertainty. This decreases the range of probable estimates in the course of simulation and enhances the objectiveness of the decisions being made. Therefore, the offered adaptive neuro-fuzzy system for estimating the value of the tyre-road friction coefficient can be recommended as an alternative solution to the existing road accident investigation practices.

References

1 Struble D. Automotive accident reconstruction: practices and principles / D. Struble // Boca Raton: CRC Press. — 2013. — 498 p.

2 European Network of Forensic Science Institutes. Best Practice Manual for Road Accident Reconstruction, ENFSI, ENFSI-BPM-RAA-01. Version 01 – November 2015. [Electronic resource]. — Access mode: http://enfsi.eu/wp-content/uploads/2016/09/4._road_accident_reconstruction_0.pdf.

3 Reif K. Bosch Automotive Handbook. 9th Edition / K. Reif, K.H. Dietsche & others // Karlsruhe: Robert Bosch GmbH. — 2014. — 1544 p.

4 Pacejka Hans B. Tyre and vehicle dynamics / B. Pacejka Hans // 3rd Ed. Butterworth-Heinemann, Elsevier. — 2012. — 629 p.

5 A Policy on Geometric Design of Highways and Streets. — AASHTO Green Book. — 7th Ed. — 2018. — 1047 p.

6 Kanwar Bharat. Singh Estimation of tire-road friction coefficient and its application in chassis control systems / Kanwar Bharat Singh, Saied Taheri // Systems Science & Control Engineering. — 2015. — № 3 (1). — P. 39–61. DOI: 10.1080/21642583.2014.985804.

7 Marco P daSilva Analysis of Event Data Recorder Data for Vehicle Safety Improvement [Electronic resource]. — Access mode: http://www.nhtsa.gov/DOT/NHTSA/NRD/ Multimedia/PDFs/EDR/Research/811015.pdf.

8 Hynd D. Study on the benefits resulting from the installation of Event Data Recorders [Electronic resource] / D. Hynd, M. McCarthy. — Access mode: https://ec.europa.eu/transport/sites/transport/files/docs/study_edr_2014.pdf.

9 Туренко А.М. Автотехнічна експертиза. Дослідження обставин ДТП: підручник для вищих навчальних закладів / А.М. Туренко, В.І. Клименко, О.В. Сараев, С.В. Данець // Харків: ХНАХУ, 2013. — 320 с.

10 Кашканов А.А. Невизначеність вихідних даних та її вплив на результати дослідження параметрів руху учасників ДТП / А.А. Кашканов // Вісник машинобудування та транспорту. — № 2(8). — 2018. — С. 35–44.

11 Wach W. Uncertainty of calculation results in vehicle collision analysis / W. Wach, J. Unarski // Forensic Science International. — 2007. — Vol. 167(2). — P. 181–188. DOI: 10.1016/j.forsciint.2006.06.061.

12 Rotshtein A. Fuzzy Evidence in Identification, Forecasting and Diagnosis / A. Rotshtein, H. Rakytyanska // Berlin: Springer, 2012. — 313 p. DOI: https://doi.org/10.1007/978–3-642–25786–5.

13 Jang J.-S.R. ANFIS: Adaptive-Network-based Fuzzy Inference Systems / J.-S.R. Jang // IEEE Transactions on Systems, Man, and Cybernetics. — 1993. — Vol. 23. — № 3. — P. 665–685.

14 Штовба С.Д. Проектирование нечетких систем средствами MATLAB / С.Д. Штовба. — М.: Горячая линия-Телеком, 2007. — 288 с.

15 Bosch analysis: driver assistance systems continue their strong advance [Electronic resource]. — Access mode: https://www.bosch-presse.de/pressportal/de/en/bosch-analysis-driver-assistance-systems-continue-their-strong-advance-148032.html

16 Кашканов В. А. Інтелектуальна технологія ідентифікації коефіцієнта зчеплення при автотехнічній експертизі ДТП : монографія / В.А. Кашканов, В.М. Ребедайло, А.А. Кашканов, В.П. Кужель. — Вінниця: ВНТУ, 2011. — 128 с.

17 Kashkanov A.A. Inertial evaluation of the tyre-road interaction during emergency braking / A.A. Kashkanov, V.M. Diorditsa, V. Yu. Kucheruk, D. Zh. Karabekova, A.K. Khassenov, A.M. Sharzadin // Bulletin of the University of Karaganda-Physics. — 2019. — № 2(94). — P. 82–91. DOI: 10.31489/2019Ph2/82–91.

А.А. Кашканов, А.П. Ротштейн, В.Ю. Кучерук, В.А. Кашканов

Автомобиль шиналарының жолға ілінісу коэффициенті: бағалаудың бейімделген жүйесі

Жол-көлік оқиғаларын тергеу кезінде көлік құралдары шиналарының жолға ілінісу коэффициентін бағалаудың жетілдірілген әдістемесі ұсынылған. Базалық негізгі әдіс шұғыл тежеу кезінде автомобиль шиналарының жолмен өзара әрекеттесуін эксперименттік зерттеу нәтижелері болып табылады. Ілінісу коэффициентін бағалау шинаның жолмен байланысындағы үйкеліс процестеріне елеулі әсер ететін параметрлер бойынша жүргізілген. Ілінісу коэффициентін бағалаудың синтезделген бейімделу жүйесіне енгізілген ең салмақты параметрлер көлік құралдарының баяулауы мен тежегіш жолының көрсеткіштерін теориялық талдау негізінде анықталды. Автомобиль шиналарының жолмен өзара іс-қимыл сапасын және оның көлік құралдарының қозғалыс параметрлеріне әсерін бағалаудың қолда бар сараптамалық әдістерін зерттеу қолданыстағы тәсілдерді жетілдіру қажеттігін көрсеткен. Ілінісу коэффициентін бағалаудың әзірленген адаптивті жүйесі, қолданыстағылардан айырмашылығы, өзін-өзі оқытуға қабілетті. Ол модельдеудің белгісіздігін азайтуға және бірінші және екінші түрдегі қателердің пайда болу ықтималдығын қысқартуға мүмкіндік береді. Мұндай нәтижеге тежегіш жүйелері мен автомобиль шиналары конструкциясының дамуын, көлік құралдарының қозғалыс жылдамдығын және олардың дөңгелектерінің жүктелуін, стохастикалық және анық белгісіздік жағдайында бастапқы деректерді өңдеуге қабілетті қазіргі заманғы математикалық әдістерді қолдану есебінен қол жеткізілген. Ұсынылған тәсіл М1, N1 санаттағы автомобильдер үшін өзінің тиімділігін көрсеткен және көлік құралдарының басқа санаттары үшін одан әрі зерттеулер жүргізу келешегін растаған.

Кілт сөздер: ілінісу коэффициенті, автомобиль шинасы, жол жабыны, тежеу процесі, бағалаудың бейімделген жүйесі, жол-көлік оқиғаларының сараптамасы.

А.А. Кашканов, А.П. Ротштейн, В.Ю. Кучерук, В.А. Кашканов

Коэффициент сцепления автомобильных шин с дорогой: адаптивная система оценки

Предложена усовершенствованная методика оценки коэффициента сцепления шин транспортных средств с дорогой при расследовании дорожно-транспортных происшествий. Базовой основой методики являются результаты обработки экспериментальных исследований взаимодействия автомобильных шин с дорогой при экстренном торможении. Оценка коэффициента сцепления производится по параметрам, которые существенно влияют на процессы трения в контакте шины с дорогой. Наиболее весомые параметры, включенные в синтезированную адаптивную систему оценки коэффициента сцепления, были выявлены на основе теоретического анализа показателей замедления и тормозного пути транспортных средств. Исследование существующих экспертных методов оценки качества взаимодействия автомобильных шин с дорогой и его влияние на параметры движения транспортных средств показали необходимость усовершенствования существующих подходов. Разработанная адаптивная система оценки коэффициента сцепления, в отличие от существующих, способна к самообучению. Она позволяет уменьшить неопределенность моделирования и сократить вероятность появления ошибок первого и второго рода. Такой результат достигается благодаря учету развития конструкции тормозных систем и автомобильных шин, скорости движения транспортных средств и загруженности их колес, применения современных математических методов, способных обрабатывать исходные данные в условиях наличия стохастической и нечеткой неопределенности. Предложенный подход показал свою эффективность для автомобилей категорий M1, N1 и подтвердил перспективу проведения дальнейших исследований для других категорий транспортных средств.

Ключевые слова: коэффициент сцепления, автомобильная шина, дорожное покрытие, процесс торможения, адаптивная система оценки, экспертиза дорожно-транспортных происшествий.

References

1 Struble, D. (2013). *Automotive accident reconstruction: practices and principles.* Boca Raton: CRC Press.

2 European Network of Forensic Science Institutes (2019). Best Practice Manual for Road Accident Reconstruction, ENFSI, ENFSI-BPM-RAA-01. Version 01 – November 2015. *enfsi.eu.* Retrieved from http://enfsi.eu/wp-content/uploads/2016/09/4._road_accident_reconstruction_0.pdf.

3 Reif, K., & Dietsche K.-H. et al. (2014). *Bosch Automotive Handbook.* (9th Ed.). Karlsruhe: Robert Bosch GmbH.

4 Pacejka Hans, B. (2012). *Tyre and vehicle dynamics.* (3rd Ed.). Butterworth-Heinemann, Elsevier.

5 A Policy on Geometric Design of Highways and Streets (2018). 7th Ed. AASHTO Green Book.1047.

6 Kanwar Bharat Singh & Saied Taheri (2015). Estimation of tire-road friction coefficient and its application in chassis control systems. Systems Science & Control Engineering, 3:1, 39–61. DOI: 10.1080/21642583.2014.985804.

7 Marco P daSilva (2008). Analysis of Event Data Recorder Data for Vehicle Safety Improvement. Retrieved from http://www.nhtsa.gov/DOT/NHTSA/NRD/Multimedia/PDFs/EDR/Research/811015.pdf.

8 Hynd, D., & McCarthy, M. (2014). Study on the benefits resulting from the installation of Event Data Recorders. Retrieved from https://ec.europa.eu/transport/sites/ transport/files/docs/study_edr_2014.pdf.

9 Turenko, A.M., Klymenko, V.I., Sarayev, O.V., & Danecz, S.V. (2013). Avtotexnichna eksperty`za. Doslidzhennya obstavy`n DTP: pidruchny`k dlya vy`shhy`x navchal`ny`x zakladiv [Autotechnical examination. Investigation of accident-related problems: textbook for higher education institutions]. Kharkiv: KhNAHU [in Ukrainian].

10 Kashkanov, A.A. (2018). Nevyznachenist vykhidnykh danykh ta yii vplyv na rezultaty doslidzhennia parametriv rukhu uchasnykiv DTP [The uncertainty of the original data and its impact on the results of the study parameters of the movement of participants in an accident], Journal of Mechanical Engineering and Transport. Vinnytsia National Technical University, 2(8), 35–44, [in Ukrainian].

11 Wach W., & Unarski J. (2007). Uncertainty of calculation results in vehicle collision analysis. Forensic Science International 167(2), 181–188. DOI: 10.1016/j.forsciint.2006.06.061.

12 Rotshtein A. and H. Rakytyanska. (2012). Fuzzy Evidence in Identification, Forecasting and Diagnosis. Berlin: Springer, 313. DOI: https://doi.org/10.1007/978–3-642–25786–5.

13 Jang, J. -S. R. (1993). ANFIS: Adaptive-Network-based Fuzzy Inference Systems, IEEE Transactions on Systems, Man, and Cybernetics, 23, 3, 665–685.

14 Shtovba, S.D. (2007). *Proektirovanie nechetkikh sistem sredstvami MATLAB [Design of fuzzy systems using MATLAB]*. Moscow: Horiachaia liniia-Telekom [in Russian].

15 Bosch analysis: driver assistance systems continue their strong advance. (2020). *bosch-presse.de.* Retrieved from https://www.bosch-presse.de/pressportal/de/en/bosch-analysis-driver-assistance-systems-continue-their-strong-advance-148032.html

16 Kashkanov, V.A., Rebedailo, V.M., Kashkanov, A.A., & Kuzhel, V.P. (2011). *Intelektualna tekhnolohiia identifikatsii koeffitsiienta zcheplennia pry avtotekhnichnii ekspertyzi DTP [Intelligent technology for identification the adhesion factor at examination traffic accident]*. Vinnytsia: VNTU [in Ukrainian].

17 Kashkanov, A.A., Diorditsa, V.M., Kucheruk, V.Yu., Karabekova, D.Zh., Khassenov, A.K., & Sharzadin, A.M. (2019). Inertial evaluation of the tyre-road interaction during emergency braking. *Bulletin of the University of Karaganda-Physics, 2(94),* 82–91. DOI: 10.31489/2019Ph2/82–91.

DOI 10.31489/2020Ph2/60-67

UDC 681.518.5

Valerii F. Hraniak[1], Vasyl V. Kukharchuk[1], Volodymyr Y. Kucheruk[1],
Samoil Sh. Katsyv[1], D.Zh. Karabekova[2], A.K. Khassenov[2]

[1]*Vinnitsa national technical university, Ukraine*
[2]*Ye.A. Buketov Karaganda State University, Kazakhstan*
(E-mail: titanxp2000@ukr.net)

Mathematical model of capacitance micromechanical accelerometer in static and dynamic operating modes

Monitoring and early diagnosis systems, on which the protection function of both hydroturbines and auxiliary power equipment rely, are becoming increasingly relevant. One of the most promising methods of technical control and diagnostics of hydo units is the analysis of their vibro-acoustic characteristics. But a significant technical problem that arises in the construction of such systems is the limited use of known sensors of vibration velocity and vibration displacement due to the fact that the rotary speed of hydro units is usually below the lower limit of operation of sensors of this type. One of the promising ways to solve this problem is using capacitive micromechanical accelerometers. However, the existing mathematical models describing this type of accelerometers have low accuracy, which limits their practical using. The mathematical models of the capacitive micromechanical accelerometer for static and dynamic modes of operation are developed in this article. It was established that this accelerometer has a constant sensitivity, therefore its static characteristic is linear. It is shown that in the dynamic mode of operation of a capacitive micromechanical accelerometer has a dynamic error component, the cause of which is its own displacement of the moving part of the sensor, which is due to the inertial properties of the moving part and elastic properties of stretch marks. The mathematical dependence of the absolute dynamic error of the capacitive micromechanical accelerometer is obtained, the removal of which from the measurement results will improve the accuracy of the specified primary measuring transducer.

Keywords: capacitive micromechanical accelerometer, mathematical model, dynamic mode of operation, static mode of operation, dynamic error.

Introduction

As of today, a strong tendency has developed to construct systems for technical inspection and diagnostics of electric power machines based on analysis of their vibroacoustic characteristics. This is due to both a high informational content of this parameter and with the opportunity to measure the said parameter directly in electric machine's operational mode without the need to intervene into its design [1, 2]. However, a significant technical problem that arises during construction of systems for inspection and diagnostics of low-speed electric machines (including hydropower units of HPPs and PSPPs) lies in a considerable limitation on the use of known sensors of vibration velocity and vibration displacement due to the fact that rotary revolution speed in such machines is normally lower than the lower boundary of operation for sensors of this type [3]. One of the approaches to solution of this problems lies in the use of accelerometerers. That said, when analyzing technical characteristics of known vibration accelerometers [4], one of the most promising ones to be used in systems for technical inspection and diagnostics of low-speed electric machines is a capacitance micromechanical accelerometer. This can be explained by its low inertial mass (of some 0.1 mcg), high overload capability (of some 10,000 g without sensor's breakdown) and a wide frequency range of operation (from static acceleration to single units of kilohertz). However, it follows from analytical review of accompanying engineering documentation and scientific-and-technical literature [4, 5] that existing mathematical models describing this variety of accelerometers are quite approximate. So, development of mathematical model of this primary measuring transformer is a relevant research-and-application task of considerable practical significance.

Setting the task

The sensing element of micromechanical capacitance accelerometer is conventionally presented as a structural diagram shown in fig. 1. It represents a differential condenser-type structure with an air dielectric. Condenser's electrodes are cut from a flat piece of polysilicon some 2 mcm thick. This condenser's stationary electrodes are represented by simple cantilever bars situated at the height of some 1.3 mcm from crystal's

surface in the air on polysilicon anchor columns welded to the crystal at the molecular level. The sensor's design comprises more than 50 such sensing elements (elementary cells). Acceleration sensor's inertial mass during the sensor's accelerated movement becomes displaced in relation to the crystal's other part. Its finger-like protrusions form condenser's movable electrode. Both sides of this structure rest against anchor columns. Stretches that hold the inertial mass play the role of a mechanical spring of constant elasticity that restricts mass motion and ensures its return to the initial position. Displacement of movable part in relation to the stationary one causes change in capacity of each elementary cell of capacitance micromechanical accelerometer, which corresponds to the primary measuring transformation of «acceleration into capacity» type [6].

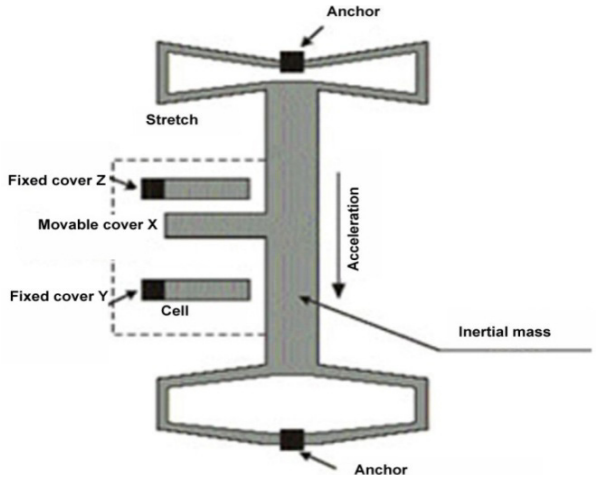

Figure 1. Structural diagram of capacitance micromechanical accelerometer's sensing element

The next measuring transformation being implemented during acceleration measurement using capacitance micromechanical accelerometer is transformation of «capacity into voltage» type, which in sensors of ADXLxxx series by Analog Devices is implemented by devices located immediately in the sensor's housing, in their essence being its component part [7, 8].

The aim of the work is to obtain a high-precision mathematical model that would describe the relationship between the input and output signals of the accelerometer in static and dynamic modes. The need for such the model is due to the using of the measuring transducer, as part of the technical diagnostic system of ow-speed electric machines (hydro units), in real time of their operation. Therefore, let us describe the highlighted measuring transformations in mathematical terms.

Analysis of approaches to problem solution

Under acceleration, inertia force may be determined based on Newton's second law as follows [9]:

$$F_{ei} = m_e \cdot a, \tag{1}$$

where m_e — the mass of the elementary cell's movable part; a — the acceleration of the elementary cell's movable part

Inertia force is counterbalanced by the spring's counter force

$$F_{np} = k \cdot X, \tag{2}$$

where X — mass displacement in relation to the equilibrium position; k — elasticity coefficient of elementary cell's stretches.

Having equated the inertia force and spring's counter force that is present in static mode of operation (measurement of uniform acceleration), we will obtain

$$a = \frac{k}{m_e} X = S_e \cdot X, \tag{3}$$

where S_e — sensitivity of capacitance micromechanical accelerometer's elementary cell

It follows from (3) that sensitivity of capacitance micromechanical accelerometer's elementary cell is a constant parameter, the value of which depends on sensor's structural parameters (k and m_e).

Since displacement of inertial mass takes place in the plane of polysilicon film, the sensor's sensitivity axis also lies in this plane and, correspondingly, it is parallel to the plane of printed board, on which the sensing element is situated.

At rest (constant-speed movement), all «fingers» of movable electrode, thanks to stretch's action, are located at the same distance from the stationary electrode's couple of «fingers». At any acceleration, movable electrodes approach to one of assemblies of stationary electrodes and move away from others. As a result, relative displacement becomes nonuniform, and capacity between movable electrode and each of movable electrodes changes in proportion to vibration acceleration. Id est:

$$\Delta C_e = \alpha \cdot X, \tag{4}$$

where ΔC_e — the change of capacity of the sensor's elementary cell.

Since capacitance micromechanical sensor contains n elementary cells being identical by their structure, located in the same plane, with their capacities connected between each other in parallel, we can write as follows:

$$\varepsilon = a_1 = a_2 = \ldots = a_n, \tag{5}$$

where ε — the acceleration measured by the sensor (input physical value).

$$\Delta C = \sum_{i=1}^{n} \Delta C_{ei}, \tag{6}$$

where ΔC — the change in capacity of capacitance micromechanical accelerometer.

$$m = \sum_{i=1}^{n} m_{ei}, \tag{7}$$

where m — the mass of the movable part of capacitance micromechanical accelerometer.

Such being the case, having assumed the averaged value of elasticity coefficient of stretches of its elementary cells as the elasticity coefficient of stretches of capacitance micromechanical accelerometer, we will obtain:

$$\varepsilon = \frac{k}{m} X. \tag{9}$$

Considering that, according to stated technical characteristics of sensors of ADXLxxx series by Analog Devices, technical characteristics of which we will use from now on, the time constant of measuring transformers of «capacity into voltage» type is considerably less than the time constant of inertial mass, and the change in value of output voltage of the sensor (after transformers of «capacity into voltage») is proportionate to the change in capacity of sensing element [7, 8], we will obtain:

$$U = \beta \cdot \Delta C = \beta \cdot \gamma \cdot X = \frac{\beta \cdot \gamma \cdot m}{k} \varepsilon, \tag{10}$$

where β — proportionality coefficient of capacity transformation into increase of the sensor's output voltage; γ — proportionality coefficient of transformation of the sensor's movable part displacement in relation to stationary one into capacity increase.

Such being the case, the sensor's sensitivity may be determined as follows:

$$S = \frac{dU}{d\varepsilon} = \frac{\beta \cdot \gamma \cdot m}{k}. \tag{11}$$

The sensor's static characteristics for sensitivity of 0.1 V·sq. s/m, which is typical for sensors of ADXL320 series by Analog Devices [7] is shown in fig. 2

Expression (10) is the mathematical model of capacitance micromechanical accelerometer in the static mode of operation. However, since static mode of operation is rather an exclusive than a standard mode in the systems for technical inspection and diagnostics of low-speed electric machines and this sensor was designed to work in slightly other measuring systems, for which only the normalization of the dynamic component of the error was sufficient, in order to solve the task set one should obtain the mathematical model that would take into account dynamic specificities of operation of accelerometers of this type.

As has been noted above, the change in capacity of capacitance micromechanical accelerometer is linearly connected with displacement of the sensor's movable part. Since the sensor's movable part is cushioned on stretches, in case of its destabilization own damped oscillations will arise, overlaying the forced displacement of equilibrium point. Id est:

$$X(t) = X_в(t) + X_{пр}(t), \tag{12}$$

where $X(t)$ — the dependency of general displacement of the sensor's movable part in relation to the stationary one; $X_{пр}(t)$ — the forced component of general displacement of the sensor's movable part, which is determined by external influence (sensor's acceleration); $X_в(t)$ — own displacement of the sensor's movable part in relation to the stationary one determined by own inertial movement.

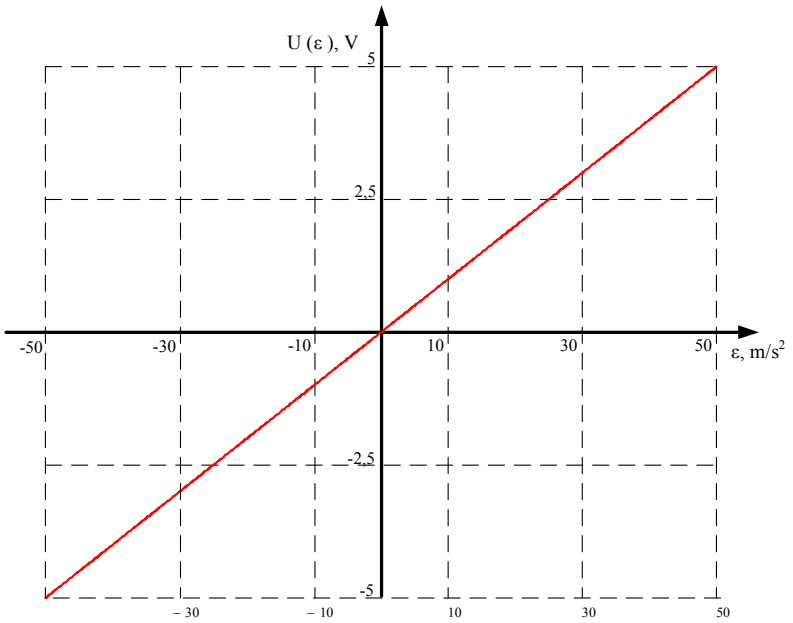

Figure 2. Static characteristics of capacitance micromechanical accelerometer ADXL320

Since forced component of the general displacement of the sensor's movable part is exclusively determined by external influence, then in the absence (compensatedness) of gravitation component's projection onto the measuring axis, which brings an additive error component into an output signal of capacitance micromechanical sensor [10], this may be determined as:

$$X_{пр}(t) = \frac{m}{k}\varepsilon(t). \tag{13}$$

In its turn, own component of displacement of the sensor's movable part is determined by presence of «elastic pendulum» mechanical system. So, under the action of constant i-agitation this may be described by expression [11]:

$$\frac{d^2X_{вi}(t)}{dt^2} + \frac{P}{m}\frac{dX_{вi}(t)}{dt} + \frac{k}{m}\cdot X_{вi}(t) = 0, \tag{14}$$

where P — the coefficient of resistance to displacement of the movable part; $X_{вi}(t)$ — displacement of the sensor's movable part in relation to equilibrium position from i-agitation.

Then general displacement of the sensor's movable part in relation to the stationary one under the action of constant i-agitation will be described by the following nonuniform differential of second order:

$$\frac{d^2X_i(t)}{dt^2} + \frac{P}{m}\frac{dX_i(t)}{dt} + \frac{k}{m}\cdot X_i(t) + \frac{m}{k}\varepsilon_i = 0. \tag{15}$$

Since in real-world sensor the inertial resistance coefficient is fairly minor, while stretches have quite a high stiffness [8], the following inequation will be implemented:

$$\left(\frac{P}{m}\right)^2 - \frac{4k}{m} < 0, \tag{16}$$

and solution of (15) in relation to $X_i(t)$ will look as follows:

$$X_{вi}(t) = e^{-\xi\omega_0 t}(A_i\cos(\omega_0 t) + B_i\sin(\omega_0 t)) + X_{пр}, \tag{17}$$

where A_i *and* B_i — the integration constant determined by initial conditions; $X_{пр}$ — the coordinate of equilibrium position under resultant of system of forces; ω_0 — the cyclic frequency of own oscillations of the sensor's movable part; ξ — the coefficient of proportionality between cyclic frequency of own oscillations and coefficient of their damping. That said:

$$\omega_0 = \sqrt{\frac{k}{m}}, \tag{18}$$

and,

$$\xi = \frac{P}{2\sqrt{k \cdot m}}, \tag{19}$$

Then own general displacement of the sensor's movable part, based on its temporal implementation may approximately be found out as follows:

$$X(t) = \sum_{i=1}^{n} X(t - i \cdot T_\partial), \tag{20}$$

where T_∂ — the system's discretization interval.

Expression (20) enables us to evaluate the experimental value of instantaneous displacement of the sensor's movable part, with application of its interpretations for theoretical analysis of metrological characteristics of capacitance micromechanical sensor being quite complicated. Hence, to solve this problem it is advisable to use the transient characteristics of own displacement of the sensor's movable part in relation to the stationary one *h(t)* depending on the sensor's acceleration, which may quite easily be calculated based on its passport data. Such being the case, general displacement of the movable part may be determined as follows:

$$X(t) = \varepsilon(0) \cdot h(t) + \int_0^t \frac{d\varepsilon(t)}{dt} h(t - \tau) d\tau. \tag{21}$$

We will obtain a typical transient characteristics of capacitance micromechanical accelerometer for sensor ADXL320 by Analog Devices. It follows from the analysis of its passport data that a typical throughput capacity of such an accelerometer type does not exceed 2.5 kHz [7]. Hence, the period of mechanical transient process, with regard to the sampling theorem, may be determined as follows:

$$t_{nn} = \frac{1}{2 f_{\max}} = \frac{1}{2 \cdot 2500} = 0,0002 \ (c), \tag{22}$$

where f_{max} — the sensor's throughput capacity.

Considering that actual duration of mechanical transient process is linked to its time constant with the following relationship:

$$\tau = \frac{1}{5} t_{nn} = \frac{1}{\xi \omega_0} = 40 \ (мкс), \tag{23}$$

we will obtain the value of the real part of characteristic equation root that describes the mechanical transient process of the accelerometer's movable part:

$$\xi \omega_0 = \frac{10^5}{4} = 25000 \ \ (c^{-1}). \tag{24}$$

By substituting (18) and (19) into (24), and having performed some mathematical transformations, we will obtain:

$$\frac{P}{2m} = 25000 \ (c^{-1}). \tag{25}$$

Considering that the mass of the movable part of capacitance micromechanical accelerometer is somewhat 1.3 mcg [6, 12], the coefficient of resistance to the movable part's displacement will have the value of somewhat $65 \cdot 10^{-3}$ kg/s. That said, while the elasticity coefficient of elementary cell's stretches has the value of some 1,300 N/m [12], then

$$\omega_0 = \sqrt{\frac{1,3 \cdot 10^3}{1,3 \cdot 10^{-6}}} \approx 31,6 \cdot 10^2 \ (рад / с). \tag{26}$$

In order to calculate (17), let us assume independent initial conditions and forced components that correspond to the input signal that varies according to the Heaviside function. Id est, the sensor's movement starts at zero speed and zero time moment with the acceleration of 1 m/sq. s, has the direction contrary to positive displacement of the sensor's movable part and continues up to final completion of mechanical tran-

sient process (has an indefinite duration) without changing the direction of movement. Such being the case, the exciting force to be applied to the sensor's movable part may be determined according to (1):

$$F_{зр} = m \cdot a = 1{,}3 \cdot 10^{-6} \cdot 1 = 1{,}3 \cdot 10^{-6}\ (H). \tag{27}$$

That said, the new equilibrium position of the movable part may be calculated as follows:

$$X_{пр} = \frac{F_{зр}}{k} = \frac{1{,}3 \cdot 10^{-6}}{1{,}3 \cdot 10^{3}} \approx 1\ (нм). \tag{28}$$

Since initial zero conditions are linked to the sensor's previous mode of operation (its zero displacement and speed), then, according to the conditions set forth above, we have:

$$\begin{cases} X_{ві}(0) = 0, \\ v_{ві}(0) = 0. \end{cases} \tag{29}$$

Such being the case, the speed of the sensor's movable part will be described using the following expression:

$$v_{ві}(t) = \frac{dX_{ві}(t)}{dt} = \omega_0 e^{-\xi\omega_0 t}(B_i \cos(\omega_0 t) + A_i \sin(\omega_0 t)) - \xi\omega_0 e^{-\xi\omega_0 t}(A_i \cos(\omega_0 t) + B_i \sin(\omega_0 t)) \tag{30}$$

Having solved the system that includes (17) and (30) taking into account the initial conditions (29), in relation to integration constants for time moment t=0, we will obtain:

$$\begin{cases} A \approx -10^{-9}, \\ B \approx -7{,}91 \cdot 10^{-10}. \end{cases} \tag{31}$$

Having substituted the value of forced component of the sensor's movable part displacement (28) and integration constants (31 into (17), we will obtain the transient characteristics of capacitance micromechanical sensor ADXL320. Graphic interpretation of this dynamic metrological characteristic is shown in fig. 3.

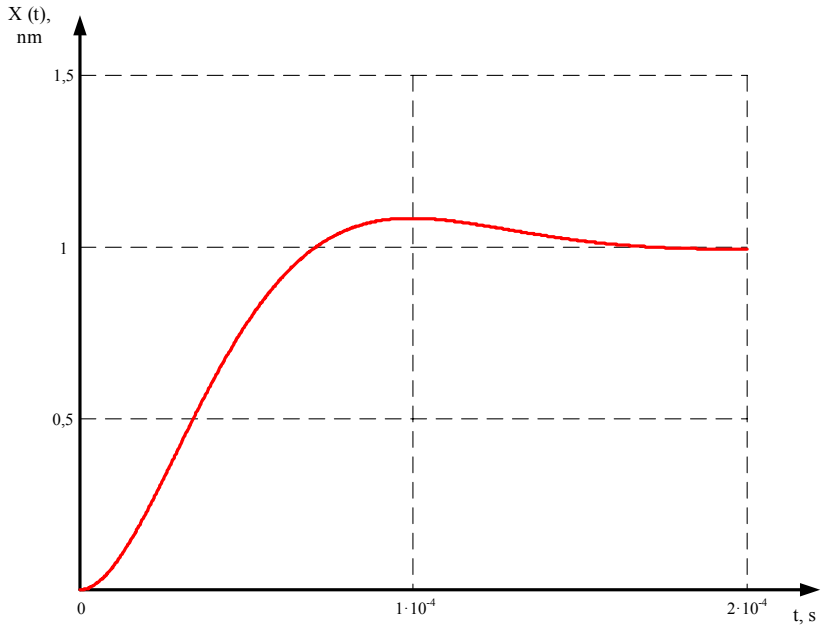

Figure 3. Transient characteristic of capacitance micromechanical accelerometer ADXL320

Taking into account (10), we will obtain the voltage variation function at the sensor's output:

$$U(t) = \beta \cdot \gamma \cdot X(t). \tag{32}$$

Or having substituted into (32) dependency (9), which is normally used when establishing the equation of transformation of capacitance micromechanical accelerometer:

$$U(t) = \frac{\beta \cdot \gamma \cdot m}{k}\left(\varepsilon(t) + \Delta_д(t)\right) = \frac{\beta \cdot \gamma \cdot m}{k}\varepsilon(t) + \frac{\beta \cdot \gamma \cdot m}{k}\Delta_д(t), \tag{33}$$

where $\varepsilon(t)$ — the acceleration value being measured; $\Delta_д(t)$ — the dynamic error that arises as a result of own displacement of the sensor's movable part in relation to the stationary one, conditioned by its inertia.

Expression (21) with due regard to (9) for a random temporal variation of measuring acceleration may be written as follows:

$$U(t) = \frac{\beta \cdot \gamma \cdot m}{k}\left(\varepsilon(0) \cdot h(t) + \int_0^t \frac{d\varepsilon(t)}{dt} h(t-\tau) d\tau \right). \tag{34}$$

In its nature, dependency (34) is the mathematical model of capacitance micromechanical accelerometer that describes the dynamic mode of its operation.

Having regard to (33) and (34), we will obtain the expression to evaluate the value of the absolute dynamic error of capacitance micromechanical accelerometer:

$$\Delta_\partial = \frac{\frac{\beta \cdot \gamma \cdot m}{k}\left(\varepsilon(0) \cdot h(t) + \int_0^t \frac{d\varepsilon(t)}{dt} h(t-\tau) d\tau \right) - \frac{\beta \cdot \gamma \cdot m}{k}\varepsilon(t)}{\frac{\beta \cdot \gamma \cdot m}{k}} = \tag{32}$$

$$= \varepsilon(0) \cdot h(t) + \int_0^t \frac{d\varepsilon(t)}{dt} h(t-\tau) d\tau - \varepsilon(t).$$

Conclusions

1. Obtained was the mathematical model of capacitance micromechanical accelerometer in the static mode of operation, which allows establishing the unambiguous connection between the value of acceleration of the sensor's housing and the value of its output voltage. It was established that this accelerometer has constant sensitivity, so its static characteristics is linear.

2. Obtained was the mathematical model of capacitance micromechanical accelerometer in the dynamic mode of operation, which allows establishing the unambiguous connection between the value of acceleration of the sensor's housing and the value of its output voltage. It was demonstrated that, in the dynamic mode of operation, this sensor is characterized by dynamic error conditioned by the movable part's inertial properties and elasticity of stretches.

3. Obtained was the mathematical dependency of the absolute dynamic error of capacitance micromechanical accelerometer, withdrawal of which from measurement results allows raising the precision of the said primary measuring transformer.

References

1 Levitsky, A.S. (2010). Improving efficiency of diagnostics of powerful hydro units due to the use of capacitive meters of mechanical defect parameters. *Hydropower of Ukraine, 4,* 10–13.

2 Hraniak, V.F., Kukharchuk, V.V., & Kucheruk, V.Y. et al. (2018). Using instantaneous cross-correlation coefficients of vibration signals for technical condition monitoring in rotating electric power machine. *Bulletin of the University of Karaganda-Physics, 1,* 72–80.

3 Hraniak, V.F., Kazyv, S.Sh., & Kukharchuk, V.V. (2017). Correlation approach to determination of weight coefficients of artificial neural network for vibro-diagnostics of hydro units. *Bulletin of Academy of Engineering of Ukraine, 4,* 100–105.

4 Frieden, J. (2015). *Modern sensors.* Moscow, Russia: Technosphere.

5 Aleshina, B.S., Veremeenko, K.K., & Chernomorsky, A.I. (2006). *Orientation and navigation of moving objects: modern information technology.* Moscow, Russia: PHYSMATLITIS.

6 Kukharchuk, V.V., Vedmitskyi, Y.G., Hraniak, V.F. (2019). *Measurement of rotational motion parameters of electromechanical energy converters in transient modes.* Vinnytsia, Ukraine: VNTU.

7 Analog Devices. Small and Thin ±5 *g* Accelerometer ADXL320. Datasheet, 16.

8 Sysoeva, S. (2006). Car accelerometers. Part 5. The prospective elemental base of surface silicon capacitive MEMS accelerometers, 4, 28–39.

9 Rao, S. S. (2007). *Vibration of continuous systems.* New York, USA: Jon Wiley & Sons.

10 Hraniak, V.F., Kukharchuk, V.V., & Bilichenko, V.V. et al. (2019). Correlation method for calculation of weight coefficients of artificial neural-like networking hydraulic units' diagnostic systems. *Proceeding of SPIE. Photonics Applications in Astronomy, Communications, Industry and High-Energy Physics Experiments,* 11176, 7.

11 Shcheglova, I.Y., & Boguslavsky, A.A. (2009). *Modeling of oscillatory processes (for example, physical problems).* Kolomna, Russia: Kolomna State Pedagogical Institute.

12 Kukharchuk, V.V., Kucheruk, V.Y., Volodarsky, E.T., & Grabko, V.V. (2013). *Fundamentals of metrology and electrical measurements.* Kherson, Ukraine: Old-plus.

В.Ф. Граняк, В.В. Кухарчук, В.Ю. Кучерук, С.Ш. Кацыв, Д.Ж. Карабекова, А.К. Хасенов

Статикалық және динамикалық жұмыс тәртіптеріндегі сыйымдылық микромеханикалық акселерометрдің математикалық моделі

Бақылау және ерте диагностикалау жүйесі үлкен өзектілікке ие болуда, оларға су турбинасы сияқты қосалқы күштік жабдықтарды қорғау функциясы жатады. Гидроагрегаттарды техникалық бақылау мен диагностикалаудың ең перспективалы әдістерінің бірі олардың діріл – акустикалық сипаттамаларын талдау болып табылады. Бірақ мұндай жүйелерді құру кезінде пайда болатын маңызды техникалық мәселе, гидроагрегаттардың роторлық айналу жиілігі әдетте осы типті сенсорлар жұмысының төменгі шегінен аз болғандықтан, діріл жылдамдығы мен дірілді ығыстырудың белгілі сенсорларын қолданудың шектеулілігі болып табылады. Бұл мәселені шешудің перспективалық жолдарының бірі сыйымдылық микромеханикалық акселерометрлерді пайдалану. Алайда, акселерометрлердің осы түрін сипаттайтын қазіргі математикалық модельдер олардың практикалық қолданылуын шектейтін дәлдігі де бар. Жұмыста статикалық және динамикалық жұмыс тәртіптеріне арналған сыйымдылық микромеханикалық акселерометрдің математикалық модельдері әзірленген. Бұл акселерометрдің тұрақты сезімталдығы бар екені анықталды, сондықтан оның статикалық сипаттамасы сызықтық болып табылады. Сыйымдылық микромеханикалық акселерометрдің динамикалық жұмыс режимінде динамикалық құраушы қателігі бар, оның пайда болу себебі датчиктің жылжымалы бөлігінің өздігінен тазартылуы, бұл жылжымалы бөліктің инерциялық қасиеттерімен және созылулардың серпінді қасиеттерімен байланысты. Сыйымдылық микромеханикалық акселерометрдің абсолюттік динамикалық қателігінің математикалық тәуелділігі алынды, оны өлшеу нәтижесінен алу көрсетілген бастапқы өлшеу түрлендіргішінің дәлдігін арттыруға мүмкіндік береді.

Кілт сөздер: сыйымдылық микромеханикалық акселерометр, математикалық модель, динамикалық жұмыс тәртібі, статикалық жұмыс тәртібі, динамикалық қателік.

В.Ф. Граняк, В.В. Кухарчук, В.Ю. Кучерук, С.Ш. Кацыв, Д.Ж. Карабекова, А.К. Хасенов

Математическая модель емкостного микромеханического акселерометра в статическом и динамическом режимах работы

Все большую актуальность приобретают системы контроля и раннего диагностирования, на которые полагается функция защиты как гидротурбин, так и вспомогательного силового оборудования. Одним из наиболее перспективных методов технического контроля и диагностики гидроагрегатов является анализ их вибро- и акустических характеристик. Но существенной технической проблемой, возникающей при построении таких систем, является ограниченность применения известных сенсоров виброскорости и вибросмещения, вследствие того, что роторная частота вращения гидроагрегатов обычно ниже нижнего предела работы сенсоров данного типа. Одним из перспективных путей решения этой проблемы является использование емкостных микромеханических акселерометров. Однако существующие математические модели, описывающие этот вид акселерометров, имеют низкую точность, что ограничивает их практическое использование. В работе разработаны математические модели емкостного микромеханического акселерометра для статического и динамического режимов работы. Установлено, что данный акселерометр имеет постоянную чувствительность, поэтому его статическая характеристика является линейной. Показано, что в динамическом режиме работы емкостной микромеханический акселерометр имеет динамическую составляющую погрешности, причиной возникновения которой является собственное перемещение подвижной части датчика, что обусловлено инерционными свойствами подвижной части и упругими свойствами растяжек. Получена математическая зависимость абсолютной динамической погрешности емкостного микромеханического акселерометра, изъятие которой из результатов измерения позволит повысить точность указанного первичного измерительного преобразователя.

Ключевые слова: емкостный микромеханический акселерометр, математическая модель, динамический режим работы, статический режим работы, динамическая погрешность.

DOI 10.31489/2020Ph2/68-74

UDC 621.791

B.K. Rakhadilov[1], Y.Y. Tabiyeva[*,1,2], G.K. Uazyrkhanova[2], L.G. Zhurerova[2], N.A. Popova[3]

[1]S. Amanzholov East-Kazakhstan State University, Ust-Kamenogorsk, Kazakhstan;
[2]D. Serikbayev East-Kazakhstan State Technical University, Ust-Kamenogorsk, Kazakhstan;
[3]Tomsk State Architecture and Building University, Tomsk, Russia
(E-mail: erkezhan.tabieva@mail.ru)

Effect of electrolyte-plasma surface hardening on structure wheel steel 2

This paper examines the influence of electrolyte-plasma surface hardening on the structure and microhardness of wheel steel mark 2. In the work electrolyte-plasma surface hardening was carried out in an electrolyte made from an aqueous solution 10 % carbamide $(NH_2)_2CO$ 20 % sodium carbonate Na_2CO_3. The processing time was 2 seconds, Tmax = 850–900 ºC; U= 320V; I=40A. According to the results of the scanning transmission electron microscopy, the electrolyte-plasma surface hardening caused a change in the morphological constituents of mark 2 steel. In the initial state, the matrix of steel is a α-phase, the morphological components of which are fragmented ferrite, unfragmented ferrite and pearlite. After electrolytic-plasma surface hardening, a batch, high-temperature plate and low-temperature plate martensit is formed on the surface of the sample. Investigations have been carried out on microhardness determination on cross-section of wheel steel samples after quenching in aqueous solution of electrolyte. It is found that after electrolytic-plasma surface hardening, the microhardening values of this hardened surface layer increased ~ 3 times compared to the steel matrix, and the thickness of the hardened layer is 1000–1500 microns.

Keywords: electrolytic-plasma surface hardening, wheel steel, transmission electron microscopy, fine structure, microhardness, morphology, martensite.

Introduction

It is known, that the development of new materials with hardened surface and layers in machinery and metallurgy can promote better performance characteristics of the structure, higher reliability as well as provide energy and resource saving [1–2]. The effective method of surface hardening of iron-carbon steels is the treatment of electrolytic plasma, when due to high-speed heating and cooling in the thermal influence zone, the structure changes as a result of phase transitions that provide the necessary operational characteristics of the working surface of the parts [3–4]. An important feature of plasma hardening is the possibility of its effective application for additional hardening of the surface of parts that have passed conventional volumetric thermal treatment.

The problem of service life and economical use of railway products is closely related to the strength and tribological properties of products made of wheel steels [5–6]. To improve the already existing properties of wheel steels, it is necessary to carefully and comprehensively analyze the influence of surface hardening on the steel structure, since it is by changing the structural components that it is possible to achieve the necessary mechanical characteristics of the working surfaces of the parts.

In view of this fact, given research is focused on studying phase composition, fine structure and mechanical properties of wheel steel 2 before electrolyte plasma surface hardening and after that one.

Material and methods of research

Wheel steel mark 2 applied in fabricating railway wheel-sets tires has been chosen as study object. According to GOST 398–96 the condition of heat treatment of mark 2 wheel steel in initial condition: In its initial state steel mark 2 represents material exposed to hardening from 890^0C for 2–2.5hours with cooling in warm water (30–60^0C) followed by tempering at 580^0C for 2.5–3 hours.

Some steel samples were cut out of the wheel tire as parallelepiped in size 15×15×10 mm^3. The sample was free from deformation and thermal effect under slow cutting speed and low load. According to GOST 398–96, chemical composition of steel (in %) is C-0.57–0.65; Mn-0.50–0.90; Si-0.22–0.45; V — not exceeded 0.10; S — not exceeded 0.030 and P- not exceeded 0.035 respectively.

Given experimental research was realized by joint efforts of specialists in National Research Laboratory for collective use, S. Amanzholov East Kazakhstan State University (EKSU), Center of Advanced Develop-

ment «VERITAS», D. Serikbayev East Kazakhstan State Technical University (EKSTU) and Research laboratories of Tomsk State University of Architecture and Building (RF).

The fine structure was studied qualitatively and quantitatively by transmission electron diffraction microscopy (TEM) technique on thin foils in EM-125 electron microscope at an accelerating voltage of 125 kV. Working magnification was equal to 25.000 times in the microscope column. The morphology of the surface structure was studied on the raster electron microscope JSM-6390LV, equipped with the energy-dispersive analysis prefix INCA Energy Penta FET X3. The microhardness of steel samples was measured in PMT-3M machine in accordance with GOST 9450–76, with loads on the indenter of 100g and holding time for 10 seconds.

Electrolyte-plasma surface hardening of the steel was carried out in the cathode mode in electrolyte-plasma treatment machine [7], scheme (fig.1a) and processing (fig.1b) shown in Figure 1.

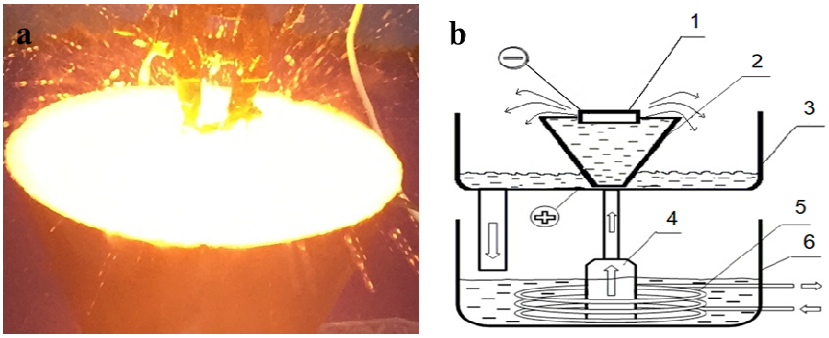

1– in-process part; 2 — conic stainless steel electrolytic cell;
3– bottom plate; 4–pump; 5– heat exchanger; 6– bath filled with electrolyte

Figure 1. Process of processing of an electrolyte plasma sample (a) and functional diagram (b) of the machine

High-current rectifier with output power of 360V/60A as DC was used as a power source. The samples were processed by rapid heating for 2 seconds followed by cooling in a flowing electrolyte. The process was realized under the following parameters: electrolyte composition (%, mass): 10 % urea $(NH_2)_2CO$ + 20 % sodium carbonate Na_2CO_3+70 % water, processing lasted for 2 seconds, T_{max} = 850–900 °C; U= 320V; I=40A.

Results and its discussion

The results of experimental studies on structural-phase state of steel mark 2 showed that in its initial state the steel matrix represents α-phase — solid solution of carbon and alloying elements in α-Fe with BCC matrix.

Lamellar pearlite and ferrite are morphological components of α- phase. Lamellar perlite, almost ideal, i.e. it is a conglomerate of alternating parallel plates ferrite and cementite [8]. Ferrite (α-phase) in the pearlit has a volumetric-centered cubic (BCC) crystal lattice.

Mutual parallelism of the lamellas [9] means that, firstly, different lamellas of the same phase within the colony have the same orientation and, secondly, mutual orientation of two phases (their orientation ratio) provides best coupling of two crystal lattices along the habit surface of the lamellas. It is established [10] that Bagaryatsky orientation relationship is observed between ferrite and cementite in nearly every pearlite colony, which is not related to the carbon content in the steel. It should be noted that steel alloying doesn't have an effect on crystallographic characteristics within the pearlite [10].

The volume ratio of lamellar pearlite is 35 % along the material (table 1).

It should be noted that the planning method was used to determine the volume fraction, which is reduced to the measurement of the total area of sections of this structural component on a certain area of the foil.

The conclusion of the working formula of this method is based on the principle of Cavalieri-Aker-Glagolev [11; 50]. It postulates the relationship between the Area (P_S) and Volume (P_V) shares:

$$P_V = P_S, \quad (1)$$

This is one of the fundamental relationships of stereology postulated by S.A. Saltykov [11; 51]. The working formula of the planning method has the following form:

$$P_S = \frac{S}{L^2} = \frac{V}{L^3} = P_V, \quad (2)$$

Where S and V are the area and volume occupied by the corresponding structural component in the sample element representing the L-rib cube.

Ferrite in the initial state of the mark 2 steel is present in the form of non-segmented and fragmented ferrites. The volume share of non-segmented ferrite is ~10 %. The volume of fragmented ferrite is 55 %. The surface hardening carried out resulted in the formation of packet-plate martensite. The volume share of pacts of martensite is 60 %, plate low-temperature martensite is 10 %, plate high-temperature martensite is 30 %.

It is also known that martensite transformation almost always does not take place completely [8–10]. This leads to the presence in the material of a certain amount of residual austenite (γ phase). The crystal lattices of residual austenite and the α-phase, regardless of the type and location of residual austenite, are always interconnected by the Kurdyumov — Sachs orientation relation [11; 67].

The volume fraction of residual austenite (γ-phase) in lath martensite is 6.5 %.

Studies have shown that in mark 2 steel after surface hardening inside all crystals of martensitis there are particles of cement. Crystalline grates of cement and α-phase are connected among themselves by the orientation ratio of Bagaryatskiy [11;20]. The volume fraction of cementite in lath martensite is 0.27 %, in low–temperature lamellar martensite is 0.95 % and in high-temperature lamellar martensite is 2 %. (table 1). The volume fraction of cement (δ_{FeC}) was calculated using the formula [12]:

$$\delta_{Fe_3C} = \frac{V_{Fe_3C}}{t \cdot r^2}, \quad (3)$$

Where V_{Fe_3C} — is the average volume of one particle of cement, t — is the thickness of the foil, r — is the average distance between particles.

Figure 2 shows an electron-microscopic image of the fine structure of mark 2 steel before and after electrolytic-plasma surface hardening. Mark 2 steel is ferrite-pearlite steel, as evidenced by the microscopic image of this steel in the delivery states (Fig.2a) where P–pearlite is marked in the image, FF — fragmented ferrite. The white arrow marks a chain of small fragments on the border of grains «pearlit — ferrite». In the microscopic image, after plasma surface hardening (Fig.2b), the structure of the wheel steel consists of packet-plate martensite. Figure 2b shows L–packet martensit, Figure 2c shows LL–lamellar low-temperature martensit, HL–lamellar high-temperature martensit. On the boundaries of martensitic crystals — interlayer of residual austenite (γ).

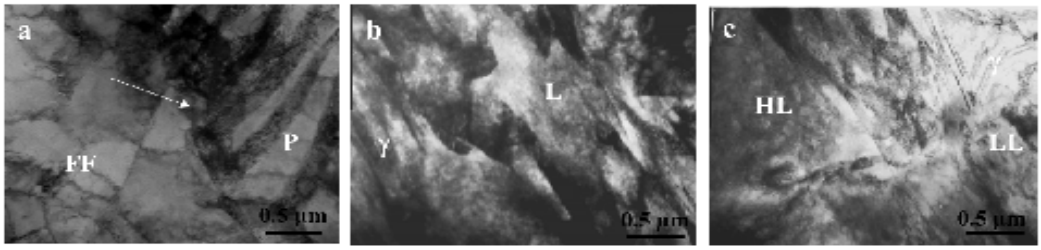

Figure 2. Electron microscopic image of fine structure of steel 2
before (a) and after (b, c) electrolyte-plasma surface hardening

Studies have shown that surface hardening of steel 2 subjected to electrolyte-plasma surface hardening in an electrolyte plasma, structural changes were detected.

Figure 3 (a-c) shows the microstructure of the steel cross section after treatment in an electrolyte containing an aqueous solution of 10 % carbamide $(NH_2)_2CO$ and 20 % sodium carbonate Na_2CO_3 with a treatment time of 2 seconds at a temperature of 860 °C.

As can be seen from Figure 3, the electrolyte-plasma surface hardening led to a change in the microstructure of the cross section, where the zoning of structures typical of electrolyte-plasma treatment is visible. The cross-sectional structure consists of 3 zones: 1 zone — a zone of surface hardening with a thickness of 1000–1500 μm, 2 zone — a zone of thermal influence, 3 zone — a matrix.

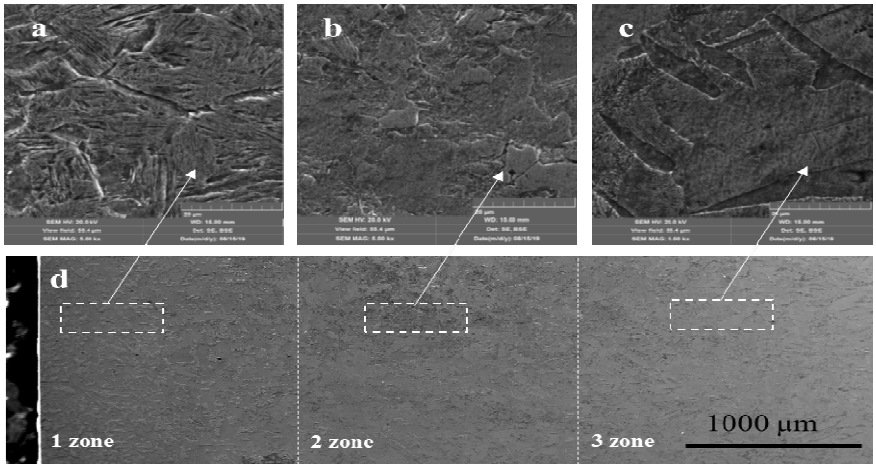

a) a hardened layer; b) a transition layer; c) non-hardened layer; d) general view

Figure 3. Pictures of the microstructure along the cross section of steel mark 2 after electrolyte-plasma surface hardening

Table 1

Phase composition of steel mark 2 before and after electrolyte-plasma surface hardening

Phase Composition Parameters	before EPSH			after EPSH					
		Ferrite		Martensite					
	Pearlite	Fragmented	Unfragmented	Lath	Lamellar low-temperature	Lamellar high-temperature	The proportion of γ-Fe in LM, %	Cementite in LM, %	$M_{23}C_6$ carbides in LM, %
Volume fraction (P_V), %	35	55	10	60	10	30	6,5	2	2.7
Totally in the material, %	100			100			7.2	0.86	0.8

*Note: Data were obtained according to the calculations by formulas [1–3] from electron microscopic images.

As is known, one of the most important properties of the surface layer, which significantly affects the strength characteristics, is microhardness, the value of which in the initial state (matrix) of steel mark 2 is ~ 140 HV. In this work, we studied the changes in the microhardness of a specimen of steel mark 2 over a cross section after electrolytic plasma surface hardening. According to the results obtained, the average microhardness in the surface hardening zone is ~ 420 HV, in the heat-affected zone it is ~ 260 HV and, accordingly, in the steel mark 2 matrix, the microhardness remains unchanged.

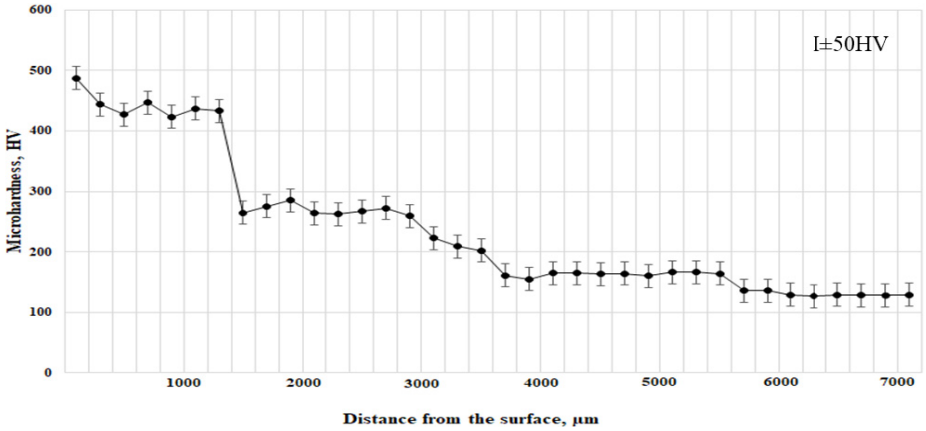

Figure 4. Distribution of microhardness over the cross section of steel mark 2 after electrolyte-plasma surface hardening

Conclusion

In conclusion, the analysis of study results of phase composition, fine structure and mechanical properties of wheel steel mark 2 before and after electrolyte-plasma surface hardening has shown:

– In its initial state, matrix of steel mark 2 represents 1) α-phase the volume ratio of unfragmented ferrite is ~10 % and 55 % of fragmented one respectively, 2) pearlite with a volume of ~ 35 %;

– It was revealed that the morphological components of the structure of steel mark 2 after EPSH at Tmax = 850–900 ºC and the exposure time of 2 s are: martensite in the form of packet martensite with a volume fraction of 60 %, lamellar low-temperature and lamellar high-temperature martensites with volume fractions of ~ 10 % and ~ 30 %, respectively;

– It was determined that electrolyte-plasma surface hardening leads to a change and hardening of the surface layer of mark 2 steel, the thickness of the hardened layer is ~ 1000–1500 μm, and the microhardness increases by ~ 3 times.

The work was supported as part of scientific-research grant of the Ministry of Education and science of the Republic of Kazakhstan (BR 05236748).

References

1 Tabieva, E. Influence of Electrolyte-Plasma Hardening Technological Parameters on the Structure and Properties of Banding Steel 2 / E.E. Tabieva., L.G. Zhurerova, D. Baizhan // Key Engineering Materials. — 2020. — Vol. 839. — P. 57–62.

2 Wang L. Microstructure features on rolling surfaces of railway rails subjected / L. Wang, A. Pyzalla, W. Stadlbauer // Journal of Materials and Engineering. — 2003. — A359. — P. 31–43.

3 Rakhadilov B.K. Electrolyte-plasma surface hardening of 65G and 20GL low-alloy steels / B.K. Rakhadilov, L.G. Zhurerova, A.V. Pavlov // Bulletin of the University of Karaganda-Physics. — 2016. — Vol. 4(84). — P. 8–13.

4 Rakhadilov B.K. Change in high-temperature wear resistance of high-speed steel by plasma nitriding / B.K. Rakhadilov, L.G. Zhurerova, M. Scheffler, A.K. Khassenov.// Bulletin of the University of Karaganda-Physics. — 2018. — Vol. 3(91). — P. 59–65.

5 Rakhadilov B.K. Plasma-electrolytic Nitriding of 0.3Cr-1Mn-1Si-Fe Construction Steel / B.K. Rakhadilov, E.E. Tabieva., L.G. Zhurerova // METAL 2019 — 28th International Conference on Metallurgy and Materials, Conference Proceedings. — 2019. — P. 1174–1179.

6 Wang M. Effects of high-temperature deformation and cooling process on the microstructure and mechanical properties of an ultrahigh-strength pearlite steel / M. Wang, F. Zhang, Z. Yang // Materials & Design. — 2017. — Vol. 114. — P. 102–110.

7 Skakov M.K. Installation of electrolytic-plasma processing / M.K. Skakov, B.K. Rahadilov, D.B. Zarva, A.V. Gulkin // Innovative patent for the invention of the Republic of Kazakhstan: IPC C255F 7/00 — № 29978 / Application. 03/02/2014; Publ. 15.06.2015, Bul. № 6.

8 Lobanov M.L. Investigation of Special Misorientations in Lath Martensite of Low Carbon Steel Using the Method of Orientation Microscopy / M.L. Lobanov, G.M. Rusakov, A.A. Redikul'tsev, S.V. Belikov, M.S. Karabanalov, E.R. Struina // The Physics of Metals and Metallography. — 2016. — Vol. 117. — P. 254–259.

9 Albou A. Nanoscale characterization of the evolution of the twin–matrix orientation in Fe–Mn–C twinning-induced plasticity steel by means of transmission electron microscopy orientation mapping / A. Albou, M. Galceran, K. Renard, S. Godet, P.J. Jacques // Scripta Materialia. — 2013. — Vol. 68. — P. 400–403.

10 Кащенко М.П. Связь различных габитусов с вариантами ориентационных соотношений при γ-α мартенситном превращении в динамической теории / М.П. Кащенко, К.Н. Джемилев, В.Г. Чащина // Фундаментальные проблемы современного материаловедения. — 2012. — № 1. — С. 50–56.

11 Гришунин В.А. Повышение усталостной долговечности рельсовой стали электронно-пучковой обработкой: дис. канд. техн. наук: 05.16.01 – «Металловедение и термическая обработка металлов и сплавов» / В.А. Гришунин. — Новокузнецк, 2014. — 181 с.

12 Курдюмов Г.В. Превращения в железе и сталях / Г.В. Курдюмов, Л.М. Утевский, Р.И. Энтин. — М.: Наука, 1977. — 232 с.

Б.К. Рахадилов, Е.Е. Табиева, Г.К. Уазырханова, Л.Г. Журерова, Н.А. Попова

Электролитті-плазмалық беттік шынықтырудың 2 маркалы дөңгелек болаттың құрылымына әсері

Мақала электролитті-плазмалық беттік шынықтырудың 2 маркалы дөңгелек болат үлгілерінің жұмыс бетінің құрылымы мен микроқаттылығына әсерін зерттеуге арналған. Жұмыс электролитті-плазмалық беттік шыңдау 10 % карбамид $(NH_2)_2CO$ + 20 % натрий карбонатының Na_2CO_3 сулы ерітіндісінен

жасалған электролитте жүзеге асырылған. Өңдеу уақыты 2 сек, T_{max} = 850–900 ºС; U= 320V; I=40A болды. Жарық беретін электрондық микроскопияның нәтижелеріне сәйкес электролитті-плазмалық беттік шыңдау 2 маркалы болаттың морфологиялық құраушыларының өзгеруіне алып келгенін көрсетеді. Бастапқы жағдайында болаттың морфологиялық құраушылары фрагменттелген феррит, фрагменттелмеген феррит және перлиттен құралып, ал матрица α-фазадан тұрады. Электролитті-плазмалық беттік шынықтырудан кейін үлгінің бетінде пакетті (рейкалы, тақтайша тәріздес), жоғары температуралы қатпарлы және төмен температуралы қатпарлы мартенсит түзіледі. Электролиттің сулы ерітіндісінде шынықтырылғаннан кейін дөңгелек болат үлгілерінің көлденең қимасы бойынша микроқаттылықты анықтауға зерттеулер жүргізілген. Электролитті-плазмалық беттік шынықтырудан кейін осы беттік қабаттың микроқаттылығының мәні болаттың матрицасымен салыстырғанда ~ 3 есе өскенін, ал шынықтырылған қабаттың қалыңдығы 1000–1500 мкм құрайтынын көрсеткен.

Кілт сөздер: электролитті-плазмалық беттік шынықтыру, дөңгелек болат, трансмиссиялық электрондық микроскопия, жұқа құрылым, микроқаттылық, морфология, мартенсит.

Б.К. Рахадилов, Е.Е. Табиева, Г.К. Уазырханова, Л.Г. Журерова, Н.А. Попова

Влияние электролитно-плазменной поверхностной закалки на структуру колесной стали марки 2

Статья посвящена исследованию влияния электролитно-плазменной поверхностной закалки на структуру и микротвердость рабочей поверхности образцов колесной стали марки 2. Электролитно-плазменную поверхностную закалку осуществляли в электролите из водного раствора 10-процентного карбамида $(NH_2)_2CO$ + 20-процентного карбоната натрия Na_2CO_3. Время обработки составляло 2 сек, T_{max} = 850–900 ºС; U= 320V; I=40A. Согласно результатам просвечивающей электронной микроскопии электролитно-плазменная поверхностная закалка привела к изменению морфологических составляющих стали марки 2. В исходном состоянии матрица стали представляет собой α-фазу, морфологическими составляющими которой являются фрагментированный феррит, нефрагментированный феррит и перлит. После электролитно-плазменной поверхностной закалки на поверхности образца формируется пакетный, высокотемпературный пластинчатый и низкотемпературный пластинчатый мартенсит. Проведены исследования на определение микротвердости по поперечному сечению образцов колесной стали после закалки в водном растворе электролита. Установлено, что после электролитно-плазменной поверхностной закалки значение микротвердости данного закаленного поверхностного слоя повысилось в ~ 3 раза по сравнению с матрицей стали, а толщина закаленного слоя составила 1000–1500 мкм.

Ключевые слова: электролитно-плазменная поверхностная закалка, колесная сталь, просвечивающая электронная микроскопия, тонкая структура, микротвердость, морфология, мартенсит.

References

1 Tabieva, E., Zhurerova, L., & Baizhan, D. (2020). Influence of Electrolyte-Plasma Hardening Technological Parameters on the Structure and Properties of Banding Steel 2. *Key Engineering Materials*, 839, 57–62.

2 Wang, L., Pyzalla, A., & Stadlbauer, W. (2003). Microstructure features on rolling surfaces of railway rails subjected. *Journal of Materials and Engineering*, A 359, 31–43.

3 Rakhadilov, B.K., Zhurerova, L.G., & Pavlov, A.V. (2016). Electrolyte-plasma surface hardening of 65G and 20GL low-alloy steels. *Bulletin of the University of Karaganda-Physics, 4,* 84, 8–13.

4 Rakhadilov, B.K., Zhurerova, L.G., Scheffler, M., & Khassenov, A.K. (2018). Change in high-temperature wear resistance of high-speed steel by plasma nitriding. *Bulletin of the University of Karaganda-Physics, 3,* 91, 59–65.

5 Rakhadilov, B.K., Tabieva, E., & Zhurerova, L. (2019). Plasma-electrolytic Nitriding of 0.3Cr-1Mn-1Si-Fe Construction Steel. *METAL 2019 — 28th International Conference on Metallurgy and Materials. Conference Proceedings,* 1174–1179.

6 Wang, M., Zhang, F., & Yang, Z. (2017). Effects of high-temperature deformation and cooling process on the microstructure and mechanical properties of an ultrahigh-strength pearlite steel. *Materials & Design, 114,* 102–110.

7 Skakov M.K., Rahadilov B.K., Zarva D.B., & Gulkin A.V. Installation of electrolytic-plasma processing. *Innovative patent for the invention of the Republic of Kazakhstan*: IPC C255F 7/00 — № 29978 / Application. 03/02/2014; Publ. 15.06.2015, Bul. № 6.

8 Lobanov, M.L., Rusakov, G.M., Redikul'tsev, A.A., Belikov, S.V., Karabanalov, M.S., & Struina, E.R. (2016). Investigation of Special Misorientations in Lath Martensite of Low Carbon Steel Using the Method of Orientation Microscopy. *The Physics of Metals and Metallography*, 117, 254–259.

9 Albou, A., Galceran, M., Renard, K., Godet S., & Jacques, P.J. (2013). Nanoscale characterization of the evolution of the twin–matrix orientation in Fe–Mn–C twinning-induced plasticity steel by means of transmission electron microscopy orientation mapping. *Scripta Materialia, Vol. 68,* 400–403.

10 Kashchenko, M.P., Dzhemilev, K.N., & Chashchina, V.G. (2012). Sviaz razlichnykh habitusov s variantami orientatsionnykh sootnoshenii pri γ-α-martensitnom prevrashchenii v dinamicheskoi teorii [The variety of different habitus with variants of orientation

relations at γ-α martensitic transformation in dynamic theory]. *Fundamental problems of modern materials science, 9,* 456 [in Russian].

11 Grishunin, V.A. (2014). Povyshenie ustalostnoi dolhovechnosti relsov stali elektronno-puchkovoi obrabotkoi [Increase of fatigue durability of rail steel by electron-beam processing]. *Candidate's thesis*. Novokuznetsk [in Russian].

12 Kurdyumov, G.V., Utevsky, L.M., & Entin, R.I. (1977). *Prevrashcheniia v zheleze i staliakh [Transformations in iron and steel]*. Moscow: Nauka [in Russian].

DOI 10.31489/2020Ph2/75-82

UDC 621.793

B.K. Rakhadilov[1], D.N. Kakimzhanov[2], N. Kantai[2], P. Kowalewski[3], R.S. Kozhanova[1]

[1]S. Amanzholov East Kazakhstan State University, Ust-Kamenogorsk, Kazakhstan;
[2]D. Serikbayev East Kazakhstan State Technical University, Ust-Kamenogorsk, Kazakhstan;
[3]Wroclaw University of Science and Technology, Wroclaw, Poland
(E-mail: rakhadilovb@mail.ru)

Research of annealing influence on the hardness of detonation coatings from zirconium dioxide

The article studied the effect of annealing on the structure and properties of zirconium dioxide coatings obtained by detonation spraying. Detonation spraying was realized on a computerized detonation spraying complex of the new generation CCDS2000. Thermal annealing of coated samples was performed at temperatures of 900 °C, 1000 °C, and 1100 °C. It was determined that the microhardness of zirconium dioxide coatings increases by 10–25 % depending on the annealing temperature after annealing. The results of nanoindentation showed that the nanohardness of the coatings after annealing at 1000 °C increases by 50 %. It was determined that after annealing at 1000 °C, the elastic modulus of the coatings increases, which indicates a decrease in plasticity and an increase in the strength of the coatings.. X-ray diffraction analysis showed that the phase composition of coatings before and after annealing consists of t-ZrO_2. After annealing occurs there is an increase in the degree of t-ZrO_2 tetragonality. Electron microscopic analysis showed that an increase in the number and size of micro-continuity in the form of thin layers after annealing. Determined that increase the hardness of zirconium dioxide after annealing at 900–1100 °C is associated with a higher degree of tetragonality t-ZrO_2 phase.

Keywords: zirconium dioxide, coating, detonation spraying, hardness, annealing, microstructure, phase, indentation.

Introduction

High-speed spraying methods can significantly expand the capabilities of traditional thermal spraying coatings used to protect parts from wear and corrosion [1–4]. Gas-thermal high-speed methods for producing coatings include methods of detonation [5], high velocity air-gas plasma (HVAGP) [6] and high velocity oil flame (HVOF) spraying [7]. Among them, the most promising is detonation spraying. Detonation spraying is one of the methods of thermal spraying of coatings, which is carried out using a special detonation gun filled with explosive gas mixture. A powdery spray material is used to form a coating. In the process of detonation, the particles of the powder are accelerated to high speeds (up to 1000 m/s), their melting and deposition on the sprayed surface [8].

The detonation method is promising for obtaining heat-resistant and heat-protective coatings on the blades of gas turbine engines due to the low porosity of the coatings and the saving of the chemical composition of the initial powder in the coatings, as well as the high adhesion strength of the coatings. Zirconium dioxide coatings are often used as upper thermal barrier layers of heat-protective coatings [9, 10]. There is very little work devoted to the study of zirconium dioxide obtained by detonation coatings. At the same time, detonation coatings allows one to obtain a set of properties necessary for heat-protective coatings: high adhesion of the coating, thickness up to 300 μm, significant porosity, as well as the ability to adjust the structure and properties of the coating by selecting processing parameters. Therefore, the study of structural transformations in detonation coatings of zirconium dioxide during heat treatments is of great interest. This work is devoted to studying the impact of thermal annealing on the structure and hardness of zirconium dioxide coatings.

Materials and methods of research

Detonation coatings were obtained on a computerized complex of new generation detonation spraying CCDS2000 (Computer Controlled Detonation Spraying), [11–14]. A general view and a schematic diagram of the detonation spraying process are presented in figure 1. The channel inside the gun barrel is filled with gases using a high-precision gas distribution system, which is controlled by a computer. The process begins with filling the channel with carrier gas. After that, a certain portion of the explosive mixture is supplied in

such a way that a layered gas medium is formed, consisting of an explosive charge and a carrier gas. Using a carrier gas stream, the powder is injected into the barrel (using a computer-controlled feeder) and forms a cloud. The substrate is placed at a certain distance from the exit from the trunk. After part of the powder is injected, the computer gives a signal to initiate detonation. This is realized using an electric spark. The duration of explosive combustion of a charge is about 1 ms. a detonation wave is formed in the explosive mixture, which in the carrier gas transforms into a shock wave. Detonation products (heated to 3500–4500 K) and carrier gas (heated by a shock wave to 1000–1500 k) move at a supersonic speed. The interaction time of gases with the sprayed particles is 2–5 ms. Particle velocities can reach 800 m s-1 [15–18].

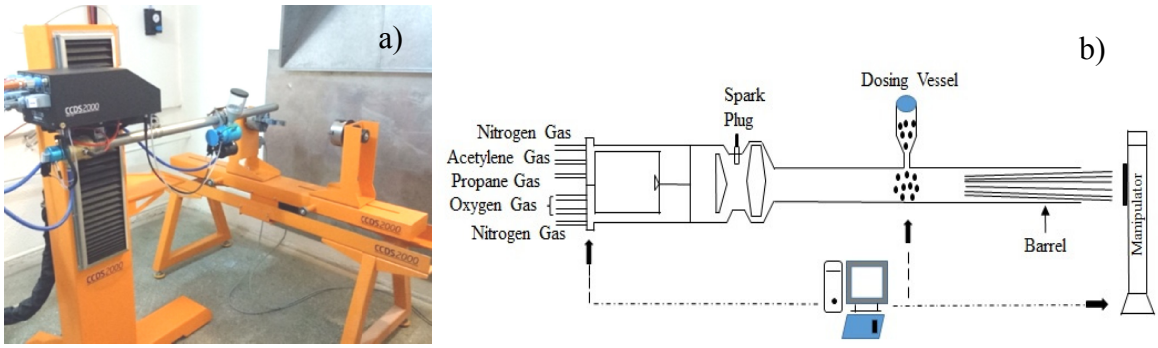

Figure 1. Computerized detonation complex CCDS200 (a) and its circuit diagram (b)

Sainless steel 12Cr18Ni10T was chosen as a substrate. The samples were sandblasted before coating. A powder of zirconium dioxide stabilized with yttrium oxide was used to obtain coatings. The particle size of the powder was up to 25–30 μm. Thermal annealing of the coated samples was carried out in a laboratory tube resistance furnace SUOL-0.4.4/12-M2-U4.2 in a vacuum of 10^{-2} Pa at temperatures of 900 °C, 1000 °C, and 1100 °C during 1 h. The temperature was measured and controlled by a VRT-2 precision thermoregulator using two thermocouples of the CCI 1378 type. The microstructure of the coatings was studied by metallographic analysis using a Neophot-21 microscope and scanning electron microscopy using JSM-6390LV and PhenomProX scanning electron microscopes. The microhardness of the samples was measured by the indentation method of a diamond indenter on a PMT-3 device in accordance with GOST 9450–76, at a load of 200 g and exposure under a load of 10 s. The phase composition of the samples was studied by X-ray diffraction analysis on an X'PertPro diffractometer using CuKα radiation. The measurement of hardness and elastic modulus was determined by the indentation method on a «NanoScan — 4D compact» nanohardness meter in accordance with GOST R 8.748–2011 and ISO 14577 indentation with a load of 0.1 N.

Research results and Discussion

The figure 2 presents the microstructure of the coatings before and after annealing. The thickness of the coatings was 360–370 μm. The coating has a porous structure. The average pore size is 5 μm.

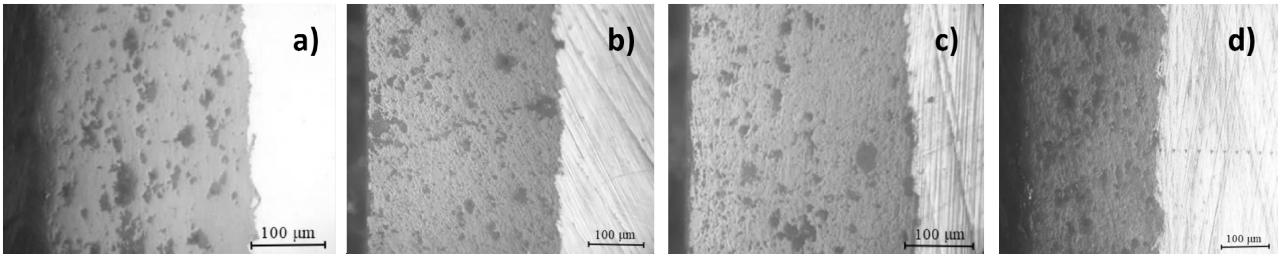

Figure 2. Microstructure of coatings from zirconium dioxide before (a) and after annealing at 900 °C (b), 1000 °C (c) and 1100 °C (d)

Figure 3 shows SEM-images of coatings and the results of X-ray microanalysis. The coating has a classic structure characteristic of gas thermal spraying methods. The coating is characterized by the presence of high density and uniformity as well as the presence of individual pores. Two groups of pores can be distinguished: rounded micro-discontinuities several micrometers in size and micro-discontinuities in the form of

thin interlayers, the size of which is several tens of micrometers in length and 0.3–1.0 μm in thickness. Thin layers are formed as a result of the spreading of molten particles of the sprayed metal over the surface. The results of X-ray microspectral analysis show that the formed coating is characterized by a more uniform distribution of all the chemical elements that make up the composition.

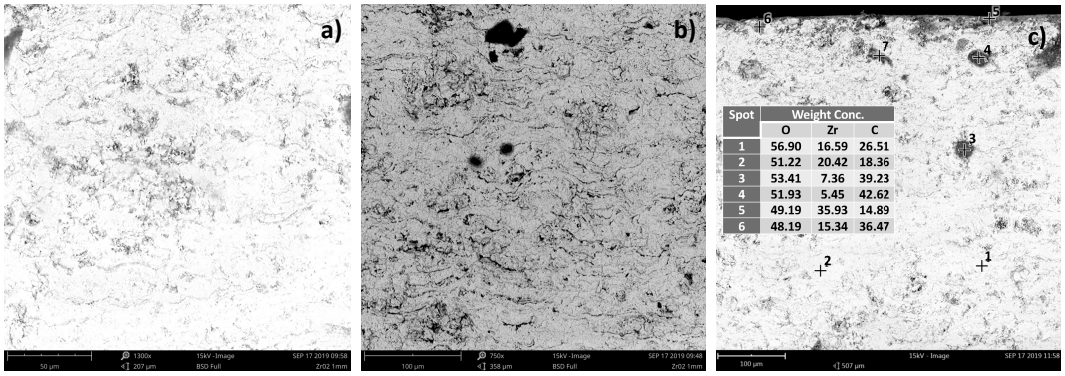

Figure 3. SEM-image of the surface (a), cross-section (b) of coatings
of zirconium dioxide and the results of micro X-ray spectral analysis (c)

Figure 4 shows the dependences of the microhardness variation along the depth of the experiment sample before and after annealing at different temperatures. The maximum increase in microhardness is observed in samples after annealing at 1000 °C. The maximum depth of the hardened layer for all coatings is 400 μm, i.e. corresponds to the thickness of the coating.

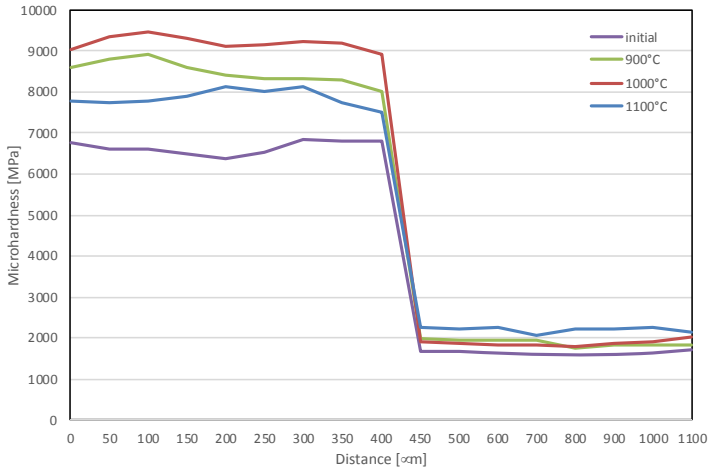

Figure 4. Microhardness of coatings from zirconium dioxide

The region of thermal influence and the diffusion zone are not observed according to metallographic analysis and microhardness. This is due to the fact that during detonation sputtering the substrate heats up to only 200–300 °C, that the surface of the substrate does not undergo structural and phase transformations, and also during annealing the diffusion processes do not occur between the zirconium dioxide coating and the iron-based substrate at the indicated temperatures.

We also studied the nanohardness of coatings by the nanoindentation method. Figure 5 presents the comparative nanoindentation curves for coatings before and after annealing. It is seen that the penetration depth of the nanoindenter into the coatings is 10 % less than the initial coating after annealing.

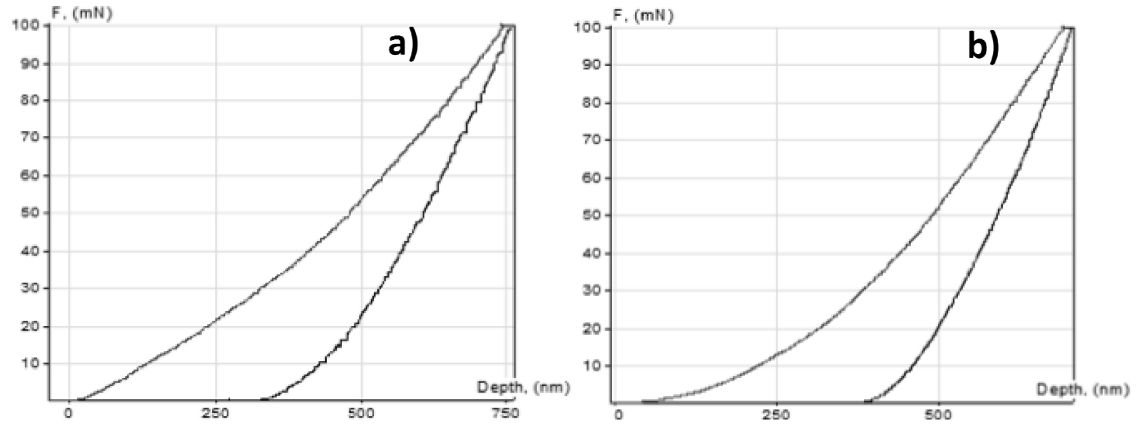

Figure 5. Nanoindentation curves of coatings from zirconium dioxide before (a) and after annealing under 900 °C (b)

The modules of elasticity and nanohardness of the coatings were determined on the results of nanoindentation (table 1). The results showed that the nanosolidity increases in comparison with the sample before and after annealing. In this case, the highest value of the nanohardness of 15.8 GPa is observed after annealing at 1000 °C. It can be seen that after annealing at 1000 °C, the elastic modulus of the coatings increases, which indicates a decrease in plasticity and an increase in the strength of the coatings.

Table 1

Results of nanoindentation

Coatings	Hanohardness, GPa	Young's modulus, GPa
ZrO_2 initial	9,9	176
ZrO_2 after annealing at 900°C	11,6	178
ZrO_2 after annealing at 1000°C	15,8	245
ZrO_2 after annealing at 1100°C	12,8	174

We can note a clear discrepancy (1.5 times) in the quantitative values of the results with good qualitative agreement by comparing the results of determining the hardness of the material at different loads on the indenter (microhardometry (figure 4) and nanosolidometry (table 1)). This can be explained by the fact that during nanocontact interaction, due to the small (tens of nanometers) dimensions of the indent, the degree of imperfection of the material under the indent is significantly reduced, which helps to bring the behavior of real material closer to ideal [19].

Figure 6 shows the diffraction patterns of the coatings before and after annealing. The results of x-ray structural analysis of coatings showed that the coating in the initial and after annealing consists of the t-ZrO_2 phase. The diffractogram of samples after annealing differs from the diffractogram before annealing in that instead of single lines (211) and (222), the t-ZrO_2 phase gives double lines. Also, after annealing the pairs of closely spaced each other lines (002) — (110) and (004) — (103), the t-ZrO_2 phases are moved wider apart. All this is related an increase in the tetragonality of the t-ZrO_2 phase. So as known [20] that the distance between paired lines depends on the c/a ratio. The larger it is, i.e., the greater the degree of tetragonality, the paired lines are further apart each other. In turn, the degree of tetragonality depends linearly on the oxygen content of zirconium dioxide. In our case, an increase in the degree of tetragonality after annealing due to an increase in the oxygen content is quite possible, since the annealing of the samples was carried out in a low vacuum.

Based on x-ray diffraction analysis, it can be claimed that the increase in the hardness of zirconium dioxide after annealing is associated with an increase in the tetrogonality of the t-ZrO_2 phase. Since the greater the degrees of tetragonality of the tetragonal phase, the higher the strength of the material [21].

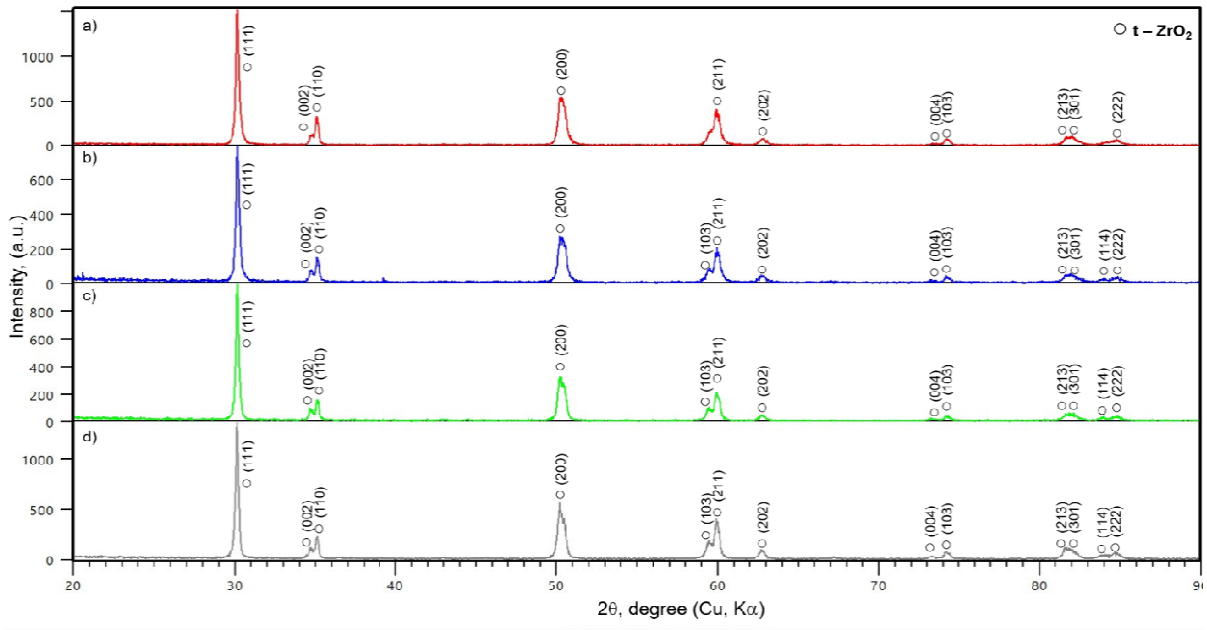

Figure 6. X-ray diffraction patterns of coatings from zirconium dioxide before (a) and after annealing at 900 °C (b), 1000 °C (c) and 1100 °C (d)

It can be seen on figure 7 that thermal extraction at 1000 °C based on structural influence is not provided. However, an increase in the number and size of micro continuities in the form of thin layers is observed. This helps to reduce internal stresses associated with operation. The formation of micro continuities in the form of thin interlayers is the reason for the strong discrepancy in the data on the microhardness and nanosolidness of the coating.

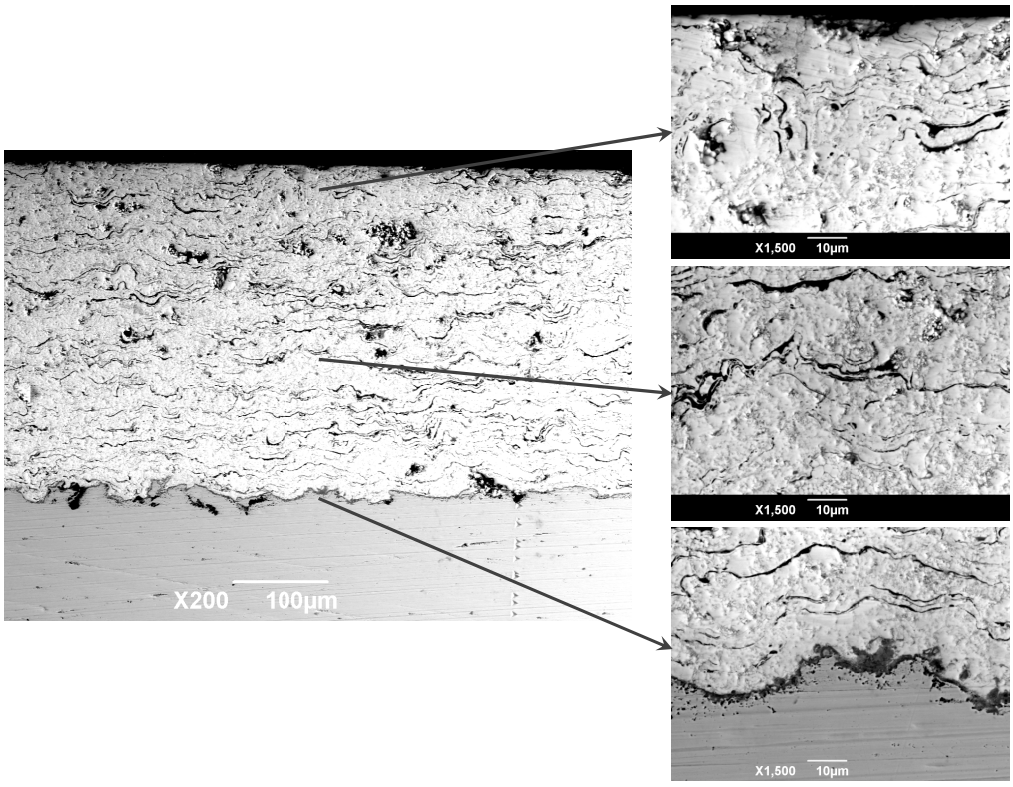

Figure 7. SEM-images of coatings from zirconium dioxide after annealing at 1000 °C

Conclusions

1. The coatings of zirconium dioxide with a thickness of 360–370 μm were obtained by the detonation method. It was determined that the coatings have pores and the average pore size is 5 μm by metallographic analysis method.

2. Electronic microscopic analysis showed that the resulting coatings are characterized by the presence of high density and uniformity, as well as the presence of individual pores. Two groups of pores have been identified: round micro-discontinuities several micrometers in size and micro-discontinuities in the form of thin interlayers, the size of which is several tens of micrometers in length and 0.3–1.0 μm in thickness. There is an increase in the number and size of micro-continuity in the form of thin layers after annealing.

3. X-ray diffraction analysis showed that the phase composition of coatings before and after annealing consists of t-ZrO_2. After annealing, there is an increase in the degree of t-ZrO_2 tetragonality.

4. It was determined that the microhardness of zirconium dioxide coatings increases by 10–25 % depending on the annealing temperature after annealing. The results of nanoindentation showed that the nanohardness of the coatings after annealing at 1000 °C increases on 50 % and reached to 15.8 GPa.

5. Determined that increase the hardness of zirconium dioxide after annealing at 900–1100 °C is associated with a higher degree of tetragonality t-ZrO_2 phase.

This research is funded by the Science Committee of the Ministry of Education and Science of the Republic of Kazakhstan (Grant No. BR05236748).

References

1 Sivkov A. High-speed thermal plasma deposition of copper coating on aluminum surface with strong substrate adhesion and low transient resistivity / A. Sivkov, Y. Shanenkova, A. Saigash, I. Shanenkova // Surface and Coatings Technology. — 2016. — Vol. 292. — P. 63–71.

2 Qun Wang Wear, erosion and corrosion resistance of HVOF-sprayed WC and Cr3C2 based coatings for electrolytic hard chrome replacement / Qun Wang, SisiLuo, Shaoyi Wang, Hui Wang, Chidambaram Seshadri Ramachandran // International Journal of Refractory Metals and Hard Materials. — 2019. — Vol. 81. — P. 242–252.

3 Yeskermessov D.K. Multi-component (Ti-Zr-Cr-Nb)N coatings': structure and properties / D.K. Yeskermessov, G.K. Uazyrkhanova, S.V. Plotnikov // Вестн. Караганд. ун-та. Сер. Физика. — 2017. — № 4 (88). — P. 8–17.

4 Jayaraj J. Corrosion behaviour of Ni−Zr−Ti−Si−Sn amorphous plasma spray coating [J] /D.J. Sordelet, D.H. Kim, Y.C. Kim, E. Fleury // Corrosion Science. — 2006. — Vol. 48. — P. 950−964.

5 Алонцева Д.Л. Модификация облучением структурно-фазового состояния и свойств порошковых покрытий, нанесенных плазменной струей на стальные подложки / Д.Л. Алонцева, Н.В. Прохоренкова // Вестн. Караганд. ун-та. Сер. Физика. — 2013. — № 3 (71). — С. 4–11.

6 Shaopeng Niu A comparative study of La0.6Sr0.4Co0.2Fe0.8O3− δ oxygen transport membranes deposited on porous metal supports prepared by supersonic air-gas plasma spraying (SAPS) and low pressure plasma spraying-physical vapor deposition (PS-PVD) /Shaopeng Niu, Kesong Zhou, Liping Xu, Changguang Deng, Min Liu, Jie Mao // Surface and Coatings Technology. — 2016. — Vol. 307. — Part A. — P. 963–970.

7 Student M.M. Structureand Wear Resistance of VC–FeCr and VC–FeCrCo Coatings Obtained by Supersonic Flame Spraying / M.M. Student, H.V. Pokhmurs'ka, Kh.R. Zadorozhna // Materials Science. — 2018. — Vol. 54. — P. 22–29.

8 Kadyrov E. Gas Dynamical Parameters of Detonation Powder Spraying / E. Kadyrov, V. Kadyrov // Therm. Spray Technol. — 1995. — 4(3). — P. 280–286.

9 Song X.M. Effect of melting state on the thermal shock resistance and thermal conductivity of APS ZrO2−7.5 wt.% Y2O3 coatings / X.M. Song, Z.W. Liu, T. Suhonen, T. Varis, L.P. Huang, X.B. Zheng, Y. Zeng // Surf. Coat. Tech. — 2015. — 270. — 132–138.

10 Fan Z.J. Influence of columnar grain microstructure on thermal shock resistance of laser re-melted ZrO2–7 wt.% Y2O3 coatings and their failure mechanism / Z.J. Fan, K.D. Wang, X. Dong, W.Q. Duan, X.S. Mei, W.J. Wang, J.L. Cui, J. Lv // Surf. Coat. Tech. — 2015. — 277. — P. 188–196.

11 Ulianitsky V.Y. Detonation spraying behavior of refractory metals: Case studies for Mo and Ta-based powders / V.Y. Ulianitsky, I.S. Batraev, A.A. Shtertser, D.V. Dudina, N.V. Bulina, I. Smurov, Detonation spraying behavior of refractory metals: Case studies for Mo and Ta-based powders // Advanced powder Technology. — 2018. — 29. — P. 1859–1864.

12 Mikhailov M.M. Thermo stabilizing BaTiO3 coatings synthesized by detonation spraying method / M.M. Mikhailov, V.Yu. Ul'yanitskii, V.A. Vlasov, A.N. Sokolovskiy, A.A. Lovitskii // Surface & Coatings Technology. — 2017. — 319. — P. 70–75.

13 Ulianitsky V.Y. The influence of the in situ for medandadded carbonon the formation of metastable Ni-based phases during detonation spraying / V.Y. Ulianitsky, D.V. Dudina, I.S. Batraev, D.K. Rybin, N.V. Bulina, A.V. Ukhina, B.B. Bokhonov // Materials Letters. — 2016. — 181. — P. 127–131.

14 Dudina D.V. Detonation spraying behavior of TiCx–Ti powders and the role of reactive processes in the coating formation / D.V. Dudina, G.A. Pribytkov, M.G. Krinitcyn, M.A. Korchagin, N.V. Bulina, B.B. Bokhonov, I.S. Batraev, D.K. Rybin, V.Y. Ulianitsky // Ceramics International. — 2016. — 42. — P. 690–696.

15 Rakhadilov B.K. Structure and properties of detonation coatings based on titanium carbosilicide / B.K. Rakhadilov, D.B. Buitkenov, B.T. Tuyakbaev, Zh.B. Sagdoldina, A.B. Kenesbekov // The 9th International Conference on Key Engineering Materials will be held in Oxford, United Kingdom. — 2019. — P. 301–306.

16 Ulianitsky V.Y. Computer-controlled detonation spraying: flexible control of the coating chemistry and microstructure / V.Y. Ulianitsky, D.V. Dudina, A. Shtertser, I. Smurov // Metals. — 2019. — Vol. 9, Iss. 12. — 1244.

17 Batraev I.S. Detonation spraying of copper: theoretical analysis and experimental studies / I.S. Batraev, V.Y. Ulianitsky, D.V. Dudina // Materials Today: Proceedings. — 2017. — 4. P. 11346–11350.

18 Buitkenov D. Influence of heat treatment on the phase composition and microhardness of coatings based on Ti3SiC2/TiC / D. Buitkenov, B. Rakhadilov, D. Erbolatuly, Zh. Sagdoldina // Key Engineering Materials. — 2019. — 839. — P. 137–143.

19 Nix W.D. Deformation at the nanometer and micrometer length scales: effects of strain gradients and dislocation starvation / W.D. Nix, J.R. Greer, G. Feug, E.T. Lilleoden // Thin Solid Films. — 2007. — Vol. 515. — P. 3152–3157.

20 Jia-Ping Zhang Rapid heat treatment to improve the thermal shock resistance of ZrO2 coating for SiC coated carbon/carbon composites / Jia-Ping Zhang, Qian-Gang Fu, Peng-Fei Zhang, Jun-Ling Qu, Rui-Mei Yuan, He-Jun Li // Surface & Coatings Technology. — 2016. — 285. — P. 24–30.

21 Акимов Г.Я. Влияние модификации тетрагональной фазы поверхностных слоев керамики на основе диоксида циркония на ее прочность / Г.Я. Акимов, В.М. Тимченко, Г.А. Маринин // Физика твердого тела. — 2005. — Т. 47. — Вып. 11. — С. 1978–1980.

Б.К. Рахадилов, Д.Н. Кәкімжанов, Н. Қантай, П. Ковалевский, Р.С. Қожанова

Цирконий диоксиді негізінде детонациялық жабындардың қаттылығына күйдірудің әсерін зерттеу

Мақалада детонациялық тозаңдату әдісімен алынған мырыш диоксиді негізінде жасалған жабындардың құрылымы мен қасиеттеріне күйдірудің әсері зерттелген. Детонациялық тозаңдандыру CCDS2000 жаңа буынды детонациялық тозаңдандыру компьютерленген кешенінде жүзеге асырылған. Қаптамасы бар үлгілерді термиялық күйдіру 900°С, 1000°С және 1100°С температураларында жүргізілген. Мырыш диоксидінен жасалған жабындардың микроқаттылығы күйдіргеннен кейін күйдіру температурасына байланысты 10–25 %-ға артатыны анықталды. Наноиндентірлеу нәтижелері, 1000°С кезінде күйдіруден кейінгі жабындардың наноқаттылығы 50 %-ға артатынын көрсеткен. 1000°С кезінде күйдіргеннен кейін жабындардың серпімділік модулі ұлғаяды, бұл жабындардың иілгіштігінің азаюы мен беріктігінің артуы анықталған. Мырыш диоксидінен күйдіруге дейінгі және одан кейінгі жабын жоғары тығыздықпен және біртектілігімен, кеуекті болуымен сипатталған. Рентгенқұрылымдық талдау нәтижелері, күйдіргенге дейін және одан кейін жабынның фазалық құрамы t-ZrO_2-ден тұратынын көрсеткен. Күйдіргеннен кейін тетрагональдік t-ZrO_2 деңгейінің өсуі байқалған. Электронды-микроскопиялық талдау нәтижелері күйдіргеннен кейін жұқа қабаттар түріндегі микроталшықтың мөлшері мен саны ұлғайғанын көрсетті. Мырыш диоксидінің 900–1100°С кезінде күйдіргеннен кейін қаттылығының жоғарылауы t-ZrO_2-фазасының тетрогональдік дәрежесінің жоғарылауымен байланысты екені анықталған.

Кілт сөздері: мырыш диоксиді, жабын, детонациялық тозаңдату, қаттылық, күйдіру, микроқұрылым, фаза, индентирлеу.

Б.К. Рахадилов, Д.Н. Какимжанов, Н. Кантай, П. Ковалевский, Р.С. Кожанова

Исследование влияния отжига на твердость детонационных покрытий из диоксида циркония

В статье изучено влияние отжига на структуру и свойства покрытий из диоксида циркония, полученных методом детонационного напыления. Детонационное напыление осуществляли на компьютеризированном комплексе детонационного напыления нового поколения CCDS 2000. Термический отжиг образцов с покрытием проводили при температурах 900, 1000 и 1100°С. Определено, что после отжига микротвердость покрытий из диоксида циркония увеличивается на 10–25 % в зависимости от температуры отжига. Результаты наноиндентирования показали, что нанотвердость покрытий после отжига при 1000°С повышается на 50 %. Определено, что после отжига при 1000°С модуль упругости покрытий увеличивается, что указывает на уменьшение пластичности и повышение прочности покрытий. Покрытие из диоксида циркония до и после отжига характеризуется наличием высокой плотности и однородности пор. Электронно-микроскопический анализ показал, что после отжига происходит увеличение количества и размеров микросплошности в виде тонких прослоек. Рентгеноструктурный анализ показал, что фазовый состав покрытий до и после отжига состоит из t-ZrO_2. После отжига наблюдается увеличение степени тетрагональности t-ZrO_2. Определено, что повышение

твердости диоксида циркония после отжига при 900–1100°С связано с увеличением степени тетрагональности t-ZrO_2-фазы.

Ключевые слова: диоксид циркония, покрытие, детонационное напыление, твердость, отжиг, микроструктура, фаза, индентирование.

References

1 Sivkov, A., Shanenkova, Y., Saigash, A., & Shanenkova, I. (2016). High-speed thermal plasma deposition of copper coating on aluminum surface with strong substrate adhesion and low transient resistivity. *Surface and Coatings Technology, 292,* 63–71

2 Qun Wang, Sisi Luo, Shaoyi Wang, & Hui Wang (2019). Chidambaram Seshadri Ramachandran Wear, erosion and corrosion resistance of HVOF-sprayed WC and Cr_3C_2 based coatings for electrolytic hard chrome replacement. *International Journal of Refractory Metals and Hard Materials, 81,* 242–252.

3 Yeskermessov, D.K., Uazyrkhanova, G.K., & Plotnikov, S.V. (2017). Multi-component (Ti-Zr-Cr-Nb)N coatings': structure and properties. *Bulletin of the University of Karaganda-Physics, 88,* 8–17.

4 Jayaraj, J, Sordelet, D.J, Kim, D.H, Kim, Y.C, & Fleury, E. (2006). Corrosion behaviour of Ni−Zr−Ti−Si−Sn amorphous plasma spray coating. *Corrosion Science, 48,* 950−964.

5 Alontseva, D.L., & Prokhorenkova, N.V. (2013). Modifikatsiia oblucheniem strukturno-fazovoho sostoianiia i svoistv poroshkovykh pokrytii, nanesennykh plazmennoi struei na stalnye podlozhki [Modification by irradiation of structural phase states and properties of powder coating deposited on a steel substrate by plasma jet]. *Vestnik Karahandinskoho universiteta. Seriia Fizika — Bulletin of the University of Karaganda. Physics series, 71,* 4–11 [in Russian].

6 Shaopeng Niu, Kesong Zhou, Liping Xu, Changguang Deng, Min Liu, & Jie Mao. (2016). A comparative study of La0.6Sr0.4Co0.2Fe0.8O3 − δ oxygen transport membranes deposited on porous metal supports prepared by supersonic air-gas plasma spraying (SAPS) and low pressure plasma spraying-physical vapor deposition (PS-PVD). *Surface and Coatings Technology, 307(A),* 963–970.

7 Student, M.M., Pokhmurs'ka, H.V., & Zadorozhna, Kh.R. (2018). Structure and Wear Resistance of VC–FeCr and VC–FeCrCo Coatings Obtained by Supersonic Flame Spraying. *Materials Science, 54,* 22–29.

8 Kadyrov, E., & Kadyrov, V. (1995). Gas Dynamical Parameters of Detonation Powder Spraying. *J. Therm. Spray Technol., 3,* 280–286.

9 Song, X.M., Liu Z.W., Suhonen, T., Varis, T., Huang, L.P., Zheng, X.B., & Zeng, Y. (2015). Effect of melting state on the thermal shock resistance and thermal conductivity of APS ZrO_2−7.5 wt.% Y_2O_3 coatings, *Surf. Coat. Tech., 270,* 132–138.

10 Fan, Z.J., Wang, K.D.,.Dong, X, Duan, W.Q., Mei, X.S., Wang, W.J., et al. (2015). Influence of columnar grain microstructure on thermal shock resistance of laser re-melted ZrO2–7 wt.% Y_2O_3 coatings and their failure mechanism. *Surf. Coat. Tech., 277,* 188–196.

11 Ulianitsky, V.Y., Batraev, I.S., Shtertser, A.A., Dudina, D.V., Bulina, N.V., & Smurov, I. (2018). Detonation spraying behaviour of refractory metals: Case studies for Moand Ta-based powders. *Advanced powder Technolog, 29,* 1859–1864.

12 Mikhailov, M.M., Ul'yanitskii, V.Yu., Vlasov, V.A., Sokolovskiy, A.N., & Lovitskii, A.A. (2017). Thermostabilizing BaTiO3 coatings synthesized by detonation spraying method. *Surface & Coatings Technology, 319,* 70–75.

13 Ulianitsky, V.Y., DudinaIgor, D.V., Batraev, S., Rybin, D.K., Bulina, N.V., Ukhina, A.V., & Bokhonov, B.B. (2016). The influence of the in-situ formed and added carbon on the formationof metastable Ni-based phases during detonation spraying. *Materials Letters, 181,* 127–131.

14 Dudina, D.V., Pribytkov, G.A., Krinitcyn, M.G., Korchagin, M.A., Bulina, N.V., Bokhonov, B.B., & Batraev, I.S., et.all. (2016). Detonation spraying behavior of TiCx–Ti powders and the role of reactiveprocesses in the coating formation. *Ceramics International, 42,* 690–696.

15 Rakhadilov, B.K., Buitkenov, D.B., Tuyakbaev, B.T., Sagdoldina, Zh.B., & Kenesbekov, A.B. (2019). Structure and properties of detonation coatings based on titanium carbosilicide. *The 9th International Conference on Key Engineering Materials will be held in Oxford, United Kingdom,* 301–306.

16 Ulianitsky, V.Y., Dudina, D.V., Shtertser, A., & Smurov, I. (2019). Computer-controlled detonation spraying: flexible control of the coating chemistry and microstructure. *Metals, 12,* 1244.

17 Batraev, I.S., Ulianitsky, V.Y., & Dudina, D.V. (2017). Detonation spraying of copper: theoretical analysis and experimental studies. *Materials Today: Proceedings, 4,* 11346–11350.

18 Buitkenov, D., Rakhadilov, B., Erbolatuly, D., & Sagdoldina, Zh. (2019). Influence of heat treatment on the phase composition and microhardness of coatings based on Ti_3SiC_2/TiC. *Key Engineering Materials, 839,* 137–143.

19 Nix, W.D., Greer, J.R., Feug, G., & Lilleoden, E.T. (2007) Deformation at the nanometer and micrometer length scales: effects of strain gradients and dislocation starvation. *Thin Solid Films, 515,* 3152–3157.

20 Jia-Ping Zhang, Qian-Gang Fu, Peng-Fei Zhang, Jun-Ling Qu, Rui-Mei Yuan, & He-Jun Li (2016). Rapid heat treatment to improve the thermal shock resistance of ZrO2 coating for SiC coated carbon/carbon composites. *Surface & Coatings Technology, 285,* 24–30.

21 Akimov, G.Ya., Timchenko, V.M. & Marinin, G.A. (2005). Vliianie modifikatsii tetrahonalnoi fazy poverhnostnykh sloev keramiki na osnove dioksida tsirkoniia na ee prochnost [Influence of modifications of the tetragonal phase of surface layers of ceramics based on zirconium dioxide on its strength]. *Fizika tverdoho tela — Solid state physics, Vol. 47, 11,* 1978–1980 [in Russian].

DOI 10.31489/2020Ph2/83-92

UDC 539.25

B.K. Rakhadilov[1], W.Wieleba[2], M.K. Kylyshkanov[1], A.B. Kenesbekov[1], M. Maulet[1]

[1]S. Amanzholov East Kazakhstan State University, Ust-Kamenogorsk, Kazakhstan;
[2]Wroclaw University of Science and Technology, Kazakhstan
(E-mail: rakhadilovb@mail.ru)

Structure and phase composition of high-speed steels

This work is devoted to the study of the structure and phase composition of high-speed steels R6M5, R9 and R18. High service properties of high-speed steel tools are achieved by heat treatment. Therefore, the sample blanks for the study were cut from cutting tools from R6M5, R9 and R18steels, which were subjected to the usual standard heat treatment for these steels. Installed that the structure of high-speed steels R6M5, R9 and R18 in the initial state, i.e. after standard heat treatment, consists of martensite and special carbides. The carbide particles are evenly distributed in the matrix and are close to the correct spherical shape. Thus in the structure of steels R6M5 and R9 are carbides of type M_6C, MC, and in the structure of steel R18 only carbides of the type M6C. EBSD analysis showed that M_6C carbides are most optimally combined with the Fe_3W_3C cubic phase, and the MS type carbide corresponds to the VC phase. Electron microscopic analysis showed that in addition to M_6C and MC carbides, high-speed steel contains small amounts of «cementite» type M_3C carbides.

Keywords: high-speed steel, structure, phase composition, carbide, heat treatment, cementite, martensite, tungsten.

Introduction

High cutting properties of high-speed steels are achieved by special alloying and complex heat treatment, providing a certain phase composition [1]. In addition, with cutting speed increases, the requirements for the heat resistance of steel increase [2]. The heat resistance of high-speed steels is due to alloying with their carbide-forming elements: tungsten, vanadium, molybdenum and chromium [3]. These elements, in certain temperature and time conditions, form in the steel particles of the carbide phase, which are the strengthening phase of the material [4,5]. A high heat resistance tool made of high-speed steels acquires after quenching and repeated tempering [6]. Tempering after quenching within the temperatures set for cutting tools leads to a decrease in the carbon content of martensite and the formation of ultramicroscopic carbides [7,8]. These carbides play an important role in the mechanical properties of steel, including in hardness, wear resistance, and heat resistance [9, 10]. Technological characteristics of high-speed steels are directly determined by the features of its microstructure. Therefore, research of the phase composition and fine structure of steel is a important objective. The main research methods previously used [11–13] were optical microscopy at small magnifications (up to 500 fold) and x-ray diffraction analysis. Quite often the main way to revelation and diagnostics the carbide phase was chemical dissolution and subsequent investigation of the sediment by x-ray diffraction analysis.

In this regard, the purpose of this work is to study and compare the structure and phase composition of high-speed steels R6M5, R9 and R18 using modern methods for studying the structure of metals and alloys.

Materials and methods of research

In accordance with the set tasks, tool high-speed steels R6M5, R9 and R18 were selected as the research material. The use of high-speed steels for cutting tools can increase the cutting speed several times, and the tool resistance-ten times [14]. The main distinguishing feature of high-speed steels is their high heat resistance or hardness (600–700^{o}C) in the presence of high hardness (63–70 HRC) and tool wear resistance. The unique properties of high-speed steels are achieved by special alloying and complex heat treatment, providing a certain phase composition [14]. Table 1 shows the chemical composition of high-speed steels R6M5, R9 and R18.

The choice of research materials is also justified by the fact that high-speed steels R6M5, R9, R18 are the most common in Metalworking, typical high-speed steels of moderate heat resistance [14].

Table 1

Chemical composition of high-speed steels R6M5, R9 and R18 (GOST 19265–73)

Steel grade	C	Mn	Si	Cr	W	V	Co	Mo	Ni	Cu	S	P
R9	0.85-0.95	before 0.50	before 0.50	3.80-4.40	8.50–9.50	2.30-2.70	before 0.50	before 1.00	before 0.40	-	before 0.03	before 0.03
R6M5	0.82-0.9	0,20-0.50	0,20-0.50	3.80-4.40	5.50-6.50	1.70–2.10	before 0.50	4.80–5.30	before 0.60	before 0.25	before 0.025	before 0.03
R18	0.73-0.83	0,20-0.50	0,20-0.50	3.80-4.40	17.00-18.50	1.00-1.40	before 0.50	before 1.00	before 0.60	before 0.25	before 0.03	before 0.03

High service properties of high-speed steel tools are achieved by heat treatment. Therefore, sample blanks with dimensions of 10x20x20 mm^3 for research were cut from cutting tools (disk cutter) made of R6M5, R9, and R18 steels subjected to the usual heat treatment for these steels [15] (Table 2).

Table 2

Modes of pre-heat treatment of high-speed steels

Steel grade	Types of heat treatment	
	Hardening	Tempering
R9	with 1240 °C in oil	560 °C (triple: the duration of each tempering is 1 h, cooling in the air)
R6M5	with 1230 °C in oil	560 °C (triple: the duration of each tempering is 1 h, cooling in the air)
R18	with 1270 °C in oil	560 °C (triple: the duration of each tempering is 1 h, cooling in the air)

Optical metallography was used to reveals the structure of the materials under study. An optical light microscope «ALTAMI-MET-1M» was used for metallographic analysis. For etching, a 4 % alcohol solution of nitric acid was used. X-ray diffraction studies samples of steel were performed using known methods of x-ray diffraction analysis using the D8 ADVANCE diffractometer. Diffractograms were taken using CuK_{α}-radiation (λ=2,2897 A˚) at a voltage of kV. Decrypting of diffractograms was carried out manually using standard techniques and the PDF-4 database, and the quantitative analysis was performed using the Powder Cell program. The morphology and elemental composition of the samples were studied a raster electron microscope JSM-6390LV. Studies of the phase composition of carbide phases and their sizes were performed EBSD analysis (diffraction analysis of backscattered electrons) on a system with electronic and focused ion beams Quanta 200 3D. Before the study, the samples were sanded and polished. For revealing the boundaries of the grains and particles of the carbide phases, chemical etching of the grinds in a 4 % alcohol solution of nitric acid was used (the etching time is 5–7 s). The structure and phase composition of R6M5 steel samples were investigated by the method transmission electron microscopy on thin foils with the help an EM-125 electron microscope at an accelerating voltage of 125 kV. Working magnification in the column of the microscope was chosen to be from 25000 to 50000 times To conduct research from the surface of the sample the sample was cut into plates (foil) with a thickness of 0.2–0.3 mm using electric spark cutting samples. The resulting foil was first thinned chemically in an electrolyte of 90 % hydrofluoric acid and 10 % perhydrol, and then electrolytically in a supersaturated solution of orthophosphoric acid with chromium anhydride at room temperature, an operating voltage of 20 V and a current density of 2–4 A/cm^2. The phase type was determined using images confirmed by microdiffraction patterns and dark-field images obtained in the reflexes of the corresponding phases.

Research results and Discussion

Figure 1 shows the microstructures of R6M5, R9 and R18 steels in their initial state, i.e. after standard heat treatment. The figure shows that the microstructures of R6M5, R9 and R18 steels are very similar to each other and consist of martensite tempering and special carbides (Figure 1).

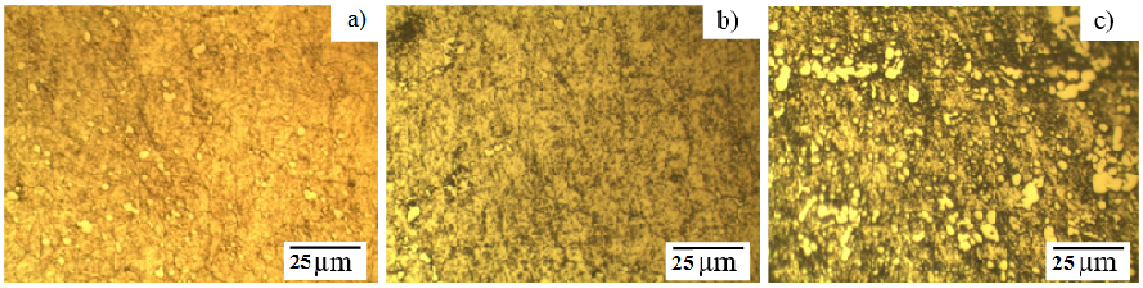

Figure 1. Microstructure of R6M5 (a), R9 (b) and R18 (c) steels

Figure 2 shows the SEM images of the surface of the steel R6M5, R9 and R18. The structure steel consists of martensite and carbides. The carbide particles are evenly distributed in the matrix and are close to the correct spherical shape. Two types of carbides are observed in the structure of high-speed steels R6M5 and R9: light and gray carbides (Figure 2 a, b, d). And only bright carbides are present in the structure of R18 steel (Figure 2c). Figure 2g shows the microstructure of R6M5 steel obtained using a semiconductor detector with backscattered electrons, giving surface pictures with chemical contrast with high spatial resolution. Grey carbides are clearly visible from this image. Thus, it can be established that after standard heat treatment, two types of carbides are present in the structure of R6M5 and R9 steels: very bright colors of carbides (bright carbides) are containing elements above the atomic number and gray carbides containing elements below the atomic number, and only bright carbides are present in the structure of R18 steel. The volume fraction of each fraction was evaluated. The sizes of carbide particles in the studied steels are also determined. The results of quantitative parameters of the steel structure are shown in Table 3.

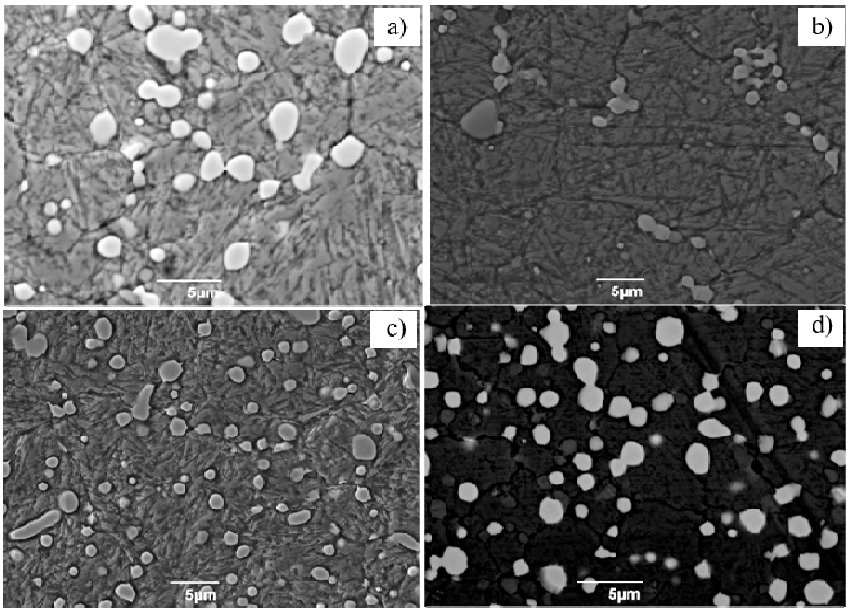

Figure 2. Microstructure of the surface of high-speed steels R6M5 (a, d), R9 (b), R18 (c)

Table 3

Quantitative parameters of structure of steel R6M5, R9 and R18

No	Sample	Carbides	Volume fraction	Average particle size
1	R6M5	bright carbides	10.4±0.6 %	2.1 µm
		dark carbides	2.3±0.4 %	0.8 µm
2	R9	bright carbides	3.1±0.6 %	1.6 µm
		dark carbides	1.7±0.4 %	1.8 µm
3	R18	bright carbides	13.4±0.6 %	1.9 µm

To identify the composition of carbides and their distribution, a map of the distribution of alloying elements in the steel structure was obtained. The General distribution of alloying elements in the structure of R6M5, R9, and R18 steels is shown in Figures 3, 4, and 5, respectively. The drawings show that the bright spherical carbides are enriched with tungsten and molybdenum, while the gray ones are enriched with vanadium. The obtained maps of the distribution of alloying elements confirmed that there present two types of carbides in the structure of R6M5 and R9 steels — bright and dark and only bright ones in the structure of R18 steel. The absence of gray carbides that are enriched with vanadium in the structure of R18 steel may be due to the fact that the content of vanadium in the composition of R18 steel is low compared to R6M5 and R9 steels. In addition, Figure 5 shows that the main mass of vanadium is located in bright carbides in the structure of R18 steel. It should be borne in mind that V, W, Mo, and Cr are carbide-forming elements. In other words, carbides of these metals have high binding energy and stability [15,16]. This is why most of the alloying elements are found in carbides, rather than in solid solution.

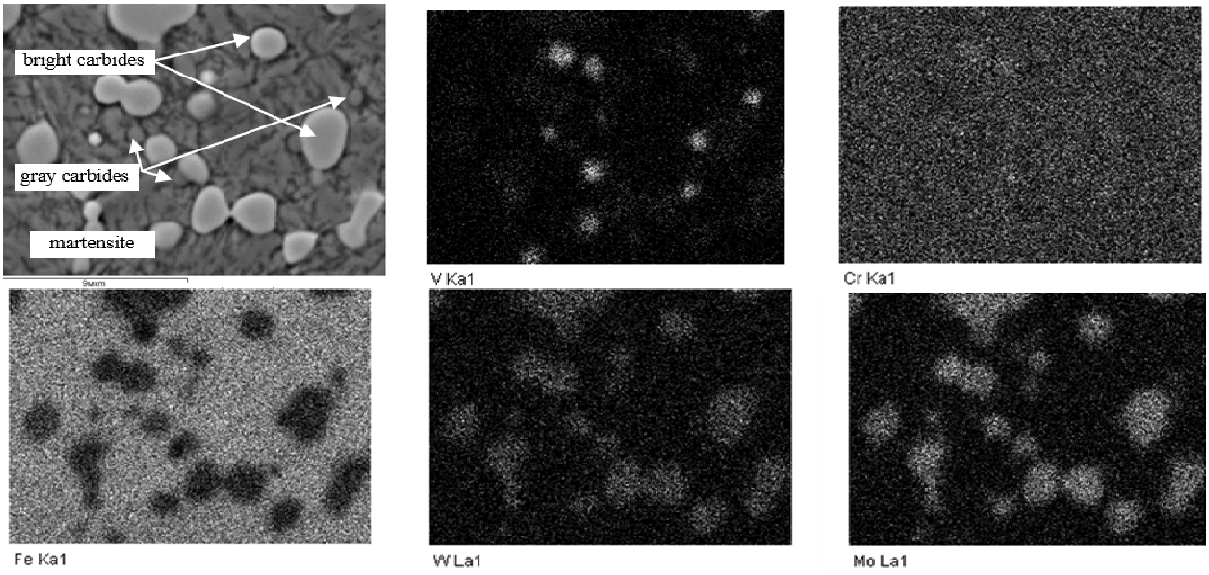

Figure 3. Surface microstructure and map distribution of R6M5 steel alloying elements

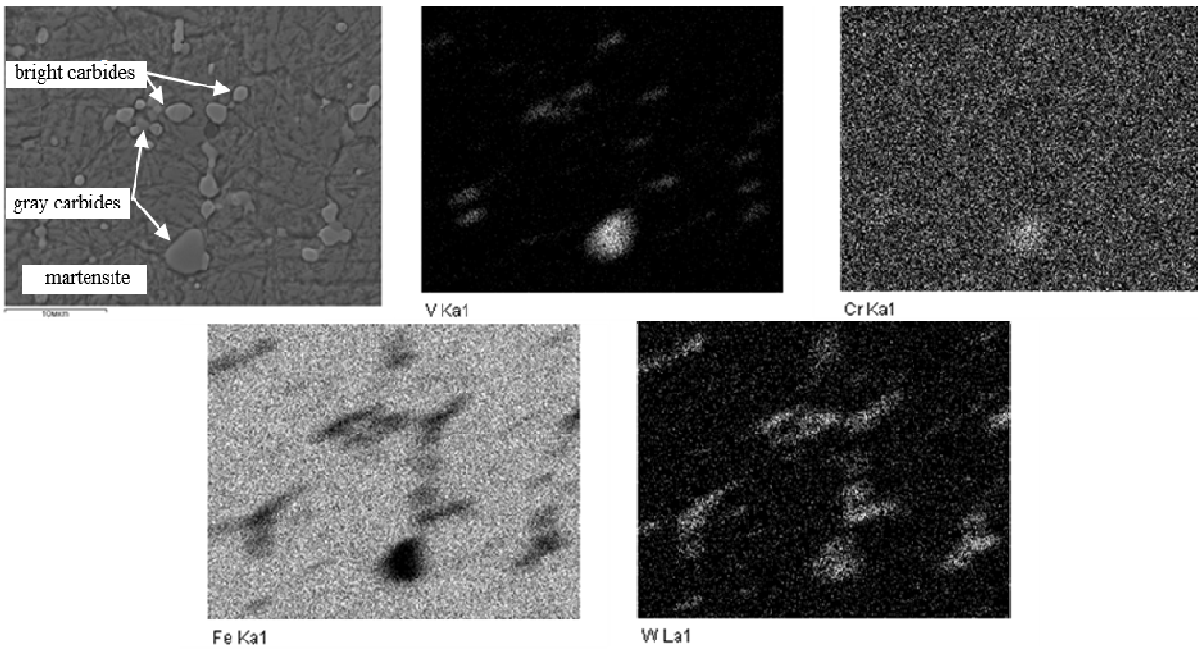

Figure 4. Surface microstructure and distribution map distribution of R9 steel alloying elements

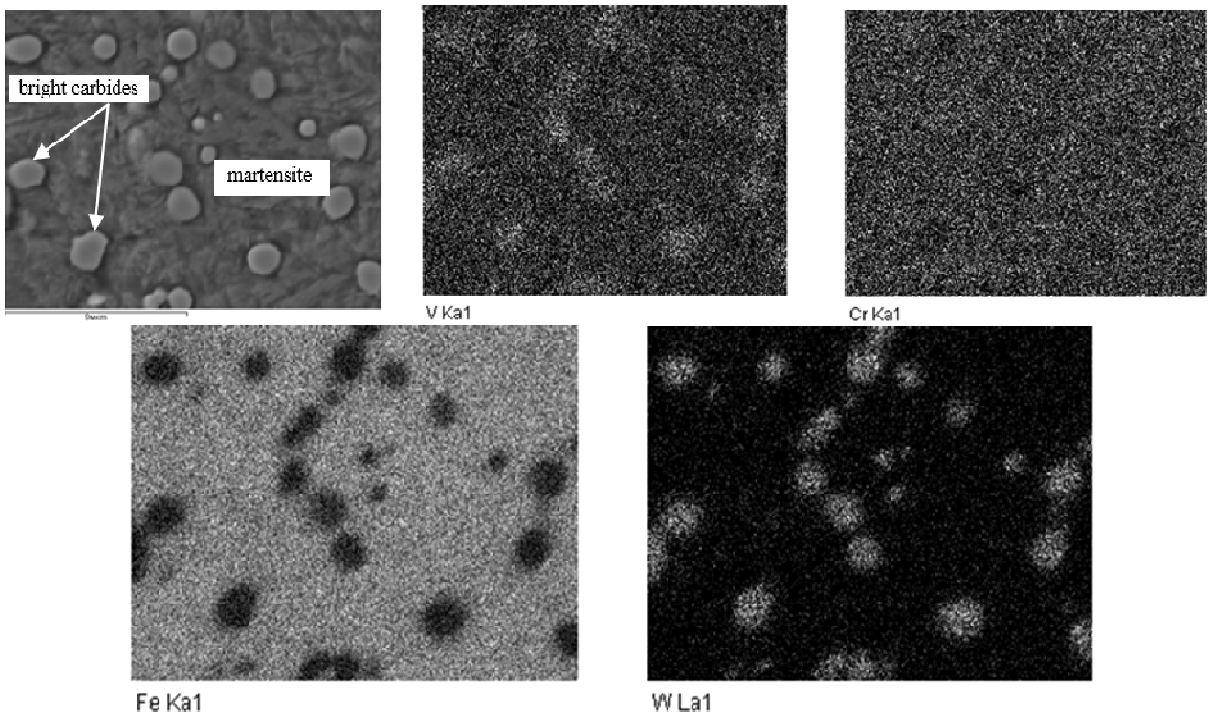

Figure 5. Surface microstructure and map distribution of R18 steel alloying elements

To determine the elemental composition of the particles of the released carbides and matrix (martensite), a microprobe analysis was performed (Figure 6). Table 4 shows the content of alloying elements in carbides and matrix for R6M5, R9 and R18 steels. Tungsten, molybdenum, vanadium, and chromium form special carbides in steel: M_6C based on tungsten and molybdenum, MC based on vanadium, and $M_{23}C_6$ based on chromium. The results of mapping and microprobe analysis show that M_6C and MC carbides are present in the structure of R6M5 steel after standard heat treatment, and $M_{23}C_6$ carbides are absent, which is in good agreement with the literature data [16–18]. However, in some papers [19,20], it is stated that after standard heat treatment, only M_6C-type carbide particles are present in the structure of R6M5 steel. Apparently, this is due to the small volume fraction of MC-type carbide particles and the similarity of these particles to the matrix, which does not allow them to be detected. In addition, the methods used in these studies have limitations when detecting carbide particles with a small concentration. Therefore, in this work, along with X-ray phase analysis, special methods of raster electron microscopy are used.

Table 4

Content of alloying elements in the structural constituent of high-speed steels

structural constituent	Content of elements, % (mass.)				
	V	Cr	Fe	Mo	W
R6M5					
Bright carbides	3.42	3.31	30.85	26.05	36.37
Dark carbides	26.47	4.45	30.82	16.62	21.64
Martensite	1.33	4.62	84.50	4.25	5.30
R9					
Bright carbides	3.15	3.52	28.83	3.1	61.4
Dark carbides	28.64	4.55	40.99	-	25.82
Martensite	3.11	4.95	80.78	-	11.16
R18					
Bright carbides	3.50	3.80	34.77	2.7	55.23
Martensite	1.07	4.64	84.39	-	9.90

The assumed configuration of M6C carbide is between the formulas $Fe_3(W, Mo)_3C$ — $Fe_3(W, Mo)_2C$ [21]. In other words, along with tungsten and molybdenum atoms, M6C carbide can located to 2/3 of the total number of metal atoms. Besides it, chromium and vanadium atoms can be dissolved, which replace iron atoms. Based on the results of the microprobe analysis, it can be assumed that the gray carbide particles are MC carbides based on vanadium.

Figure 6 shows diffractograms of R6M5, R9, and R18 steels. X-ray diffraction analysis showed that in the initial state, i.e., after heat treatment, the structure of R6M5 and R9 steels present the α-phase and M_6C, MC carbides, and only M_6C carbides in the structure of R18 steel. The results of X-ray diffraction analysis are shown in Table 5. Thus, X-ray diffraction analysis confirmed that the main carbides in the studied steel are M_6C and MC carbides. It was determined that M_6C type carbides that have a complex HCC crystal lattice and a spatial group Fd3m correspond to the composition of Fe_3W_3C, and MS type carbides that have a cubic crystal lattice and a spatial group Fm3m correspond to the composition of VC. It should be borne in mind that the M_6C type carbide can have the form of both Fe_3W_3C and Fe_3Mo_3C. As you know, one of the advantages of x-ray diffraction analysis (XRD) is that the peak position and lattice parameters can be determined fairly accurately. Nevertheless, in this case, when studying individual carbides, it is advisable to apply EBSD analysis. Therefore, to confirm the results of X-ray diffraction analysis was studied the crystal structure of M6C and MS carbides by EBSD analysis with help a reflected electron detector on a scanning microscope (system) with electronic and focused ion beams.

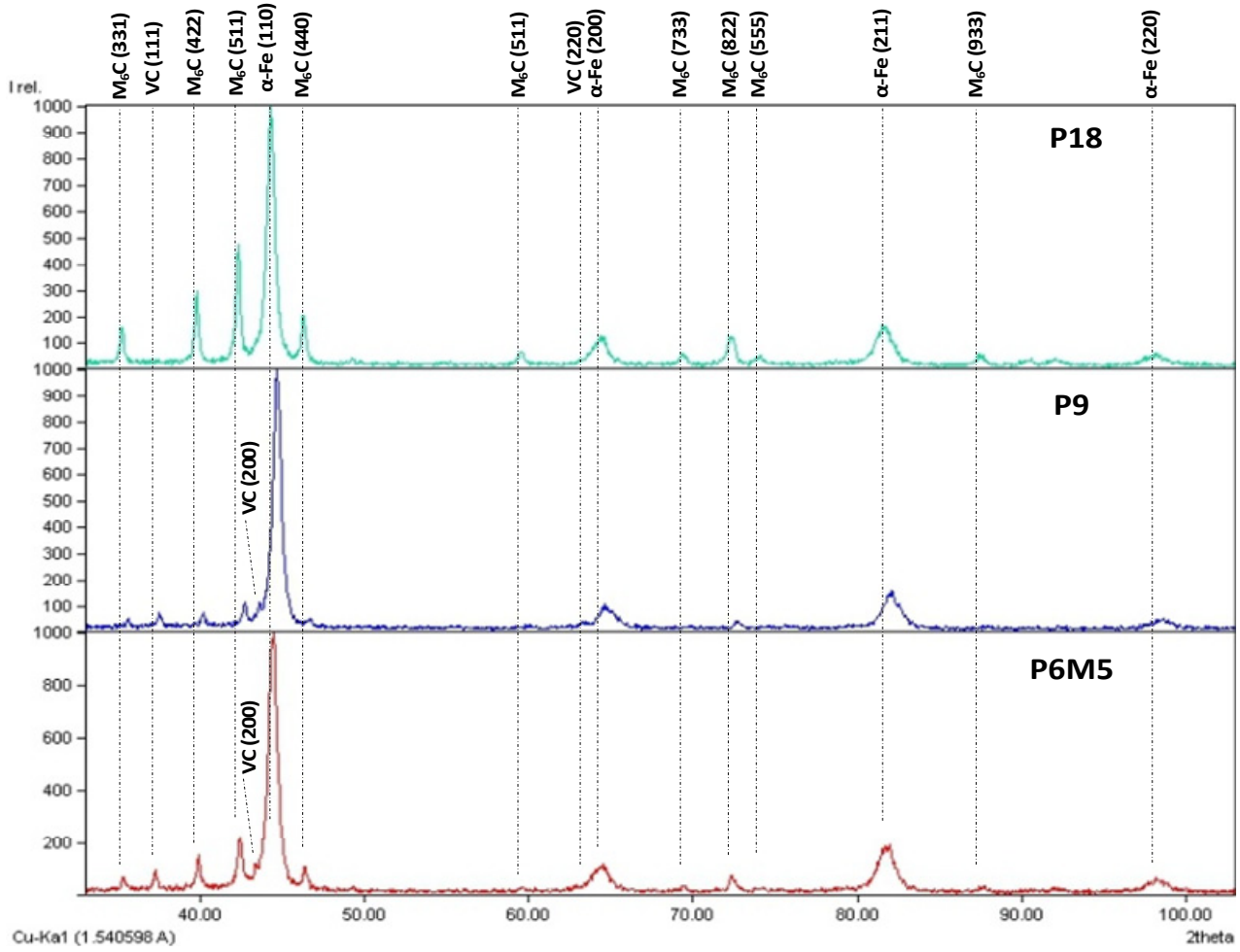

Figure 6. Diffractograms of high-speed steels in the initial state (after heat treatment)

Table 5

Results of x-ray diffraction analysis

Sample	The detected phase	Vol.frac.phases %	Lattice parameters, nm	The Sizes RCS, nm
R9, initial	α-Fe	81	0.28680	23.30 (all ref.)
	M_6C	11.8	1.10543	26.14 (100)
	MC	7.2	0.41566	25.01 (100)
R6M5, initial	α-Fe	75.2	0.28781	19.20 (all ref.)
	M_6C	13.7	1,10867	38.77 (all ref.)
	MC	11,1	0.41663	18.72 (100)
R18, initial	α-Fe	72.2	0.28720	50.36 (all ref.)
	M_6C	27.8	1.10429	39.43 (100)

Figure 7 shows the results of EBSD analysis of the R6M5 steel surface. EBSD analysis showed that tungsten-rich M_6C carbides are most optimally combined with the cubic phase of Fe_3W_3C, and MC-type carbides correspond to the VC phase. However, it is worth noting that in this case, Fe_3W_3C may also mean that other carbide-forming elements are present in the form of M_6C carbides.

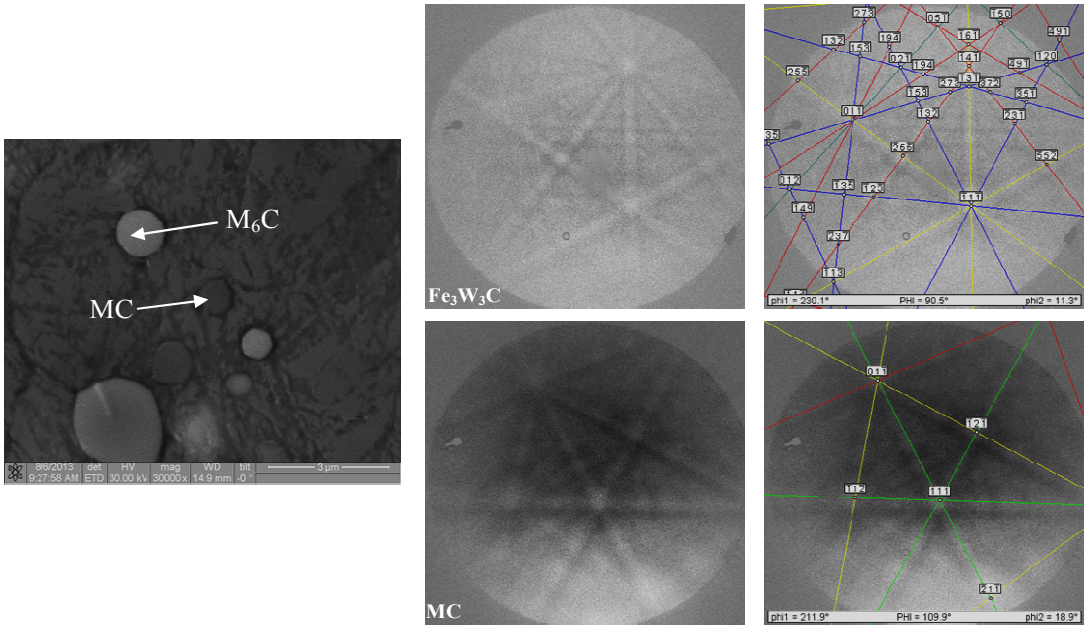

Figure 7. Results of EBSD analysis of R6M5 steel

Electron microscopic analysis showed that except in addition to M_6C and MC carbides, are present in steel in small amounts of carbides «cementite» type M_3C (Figure 8). Note the highest solubility in the cementite crystal lattice have that manganese and chromium atoms, slight solubility of the atoms of vanadium, molybdenum and tungsten. These particles are formed during quenching in the process of «self-leave» of steel due to the heat preserved in the material.

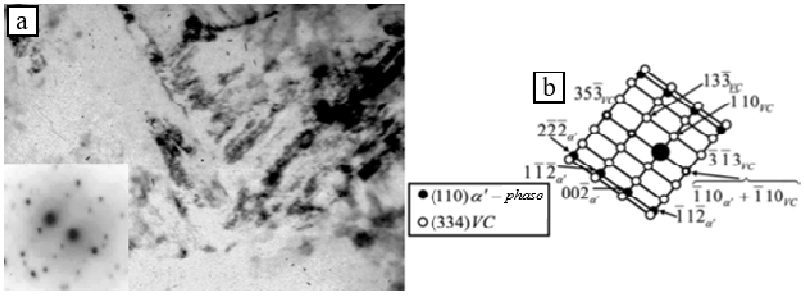

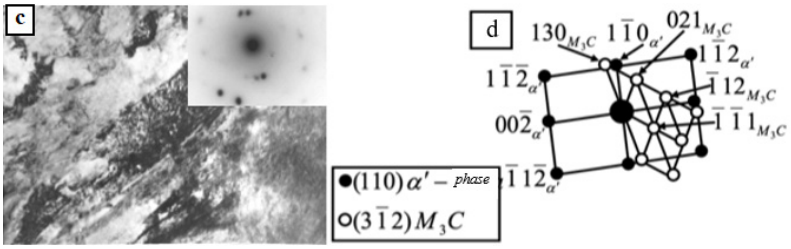

Figure 8. TEM image of P6M5 steel: a, c- brightfield image; b, d -induced microdiffraction pattern scheme

Thus, we characterized the structures and carbide phases of high-speed steels R6M5, R9 and R18 in the initial state, i.e. after standard heat treatment. The research of structural-phase states before a certain treatment is necessary in terms of revelation patterns of changes in the structure and its influence on properties. Since the physical and mechanical properties of high-speed steel in large measure by the structure and state of the carbide phases and their shape, size, and distribution in volume.

Conclusions

It was found that the structure of high-speed steels R6M5, R9 and R18 in the initial state, i.e. after standard heat treatment, consists of the α' — phase and special carbides. At that the structure of R6M5 and R9 steels contains M_6C and MC carbides, while in the structure of R18 steel contains only M_6C carbides type. Using method X-ray diffraction analysis and EBSD analysis, it was found that M_6C-type carbides which have a complex HCC crystal lattice and a spatial group Fd3m correspond to the composition of Fe_3W_3C, and MC-type carbides that have a cubic crystal lattice and a spatial group Fm3m correspond to the composition of VC.

This research is funded by the Science Committee of the Ministry of Education and Science of the Republic of Kazakhstan (Grant No. BR05236748).

References

1 Моисеев В.Ф. Инструментальные материалы / В.Ф. Моисеев, С.Н. Григорьев. — М.: МГТУ Станкин, 2005. — 248 с.

2 Firouzdor V. Effect of deep cryogenic treatment on wear resistance and tool life of M2 HSS drill / V. Firouzdor, E. Nejati, F. Khomamizadeh // Journal of Materials Processing Technology. — 2008. — Vol. 206(1–3). — P. 467–472.

3 Гученко С.А. Композиционные ионно-плазменные покрытия / С.А. Гученко, В.Ч. Лауринас, О.Н. Завацкая // Вестн. Караганд. ун-та. Сер. Физика. — 2014. — № 3(75). — С. 16–27.

4 Rahadilov B.K., Electrolyte-plasma surface hardening of 65G and 20GL low-alloy steels / B.K. Rakhadilov, L.G. Zhurerova, A.V. Pavlov, W. Wieleba // Bulletin of the University of Karaganda-Physics. — 2016. — Vol. 4(84). — P. 8–14.

5 Skakov M. Microstructure and tribological properties of electrolytic plasma nitrided high-speed steel / M. Skakov, B. Rakhadilov, M. Scheffler, E. Batyrbekov // Materials Testing. — 2015. — 57(4). — C. 360–364.

6 Chaus A.S. Structure and Properties of Cast Rapidly Cooled High-Speed Steel R6M5 / A.S. Chaus, F.I. Rudnitskii // Metal Science and Heat Treatment. — 2003. — Vol. 45. — P. 157–162.

7 Liu ZY. Microstructure evolution during sintering of injection molded M2 high speed steel / ZY. Liu, NH. Loh, KA. Khor, SB.Tor // Materials Science and Engineering A. — 2000. — Vol. 293(1–2). — P. 46–55.

8 Candane D. Effect of cryogenic treatment on microstructure and wear characteristics of AISI M35 HSS / D. Candane, N. Alagumurthi, K. Palaniradja // International Journal of Materials Science and Applications. — 2013. — Vol. 2(2). — P. 56–65.

9 Šolić S. Effect of deep cryogenic treatment on mechanical and tribological properties of PM S390 MC high-speed steel / S. Šolić, F. Cajner, V. Leskovšek // MP Materials Testing. — 2012. — Vol. 10. — P. 688–693.

10 Skakov M. Influence of electrolyte plasma treatment on structure, phase composition and microhardness of steel P6M5 / M. Skakov, B. Rakhadilov, M. Sheffler // Key Engineering Materials. — 2013. — Vol. 531–532. — P. 627–631.

11 Самсонов Г.В. Тугоплавкие соединения / Г.В. Самсонов, И.М. Винницкий. — М.: Металлургия, 1976. — 560 с.

12 Геллер Ю.А. Инструментальные стали / Ю.А. Геллер. — М.: Металлургия, 1983. — 527 с.

13 Bochnowskia W. Primary and secondary carbides in high-speed steels after conventional heat treatment and laser modification / W. Bochnowskia, H. Leitner, Ł. Majorc, R. Ebner, B. Major // Materials Chemistry and Physics. — 2003. — Vol. 81(2–3). — P. 503–506.

14 Гольдштейн М.И. Специальные стали / М.И. Гольдштейн, С.В. Грачев, Ю.Г. Векслер // Специальные стали. — М.: Металлургия, 1985. — 408 с.

15 Гуляев А.П. Теория быстрорежущей стали / А.П. Гуляев // МиТОМ. — 1998. — № 11. — С. 27–32.

16 Кремнев Л.С. Теория легирования и создание на ее основе теплостойких инструментальных сталей и сплавов оптимального состава / Л.С. Кремнев // Металловедение и термическая обработка металлов. — 2008. — № 11. — С. 18–28.

17 Skakov M. Specifics of microstructure and phase composition of high-speed steel R6M5 / M. Skakov, B. Rakhadilov, G. Karipbayeva // Applied Mechanics and Materials. — 2013. — Vol. 404. — P. 20–24.

18 Воробьева Г.А. Инструментальные материалы: инструментальные стали и сплавы / Г.А. Воробьева, Е.Е. Складнова. — Ч. 1. — СПб., 2003. — 100 с.

19 Guenzel R. Pulsed electron-beam treatment of high-speed steel current tools: struchire-phase transformation and wear resistance / R. Guenzel, W. Matz, Yu.F. Ivanov, V.P. Rothtein // 1st International Congress on Radiation Physics, high current electronics, and modification of materials. — Tomsk, Russia. — 2000. — Vol. 3. — P. 303–307.

20 Ivanov Yu. Pulsed electron beams melting of high-speed steel: structural phase transformations and wear resistance / Yu. Ivanov, W. Matz, V. Rotshtein, R. Gunzel, N. Shevchenko // Surface and Coatings Technology. — 2002. — No. 150. — P. 188–198.

21 Гольдшмидт Х.Дж. Сплавы внедрения / Х.Дж. Гольдшмидт. — М.: Мир, 1971. — 424 с.

Б.К. Рахадилов, В. Виелеба, М.К. Кылышканов, А.Б. Кенесбеков, М. Маулет

Жылдамкесетін болаттардың құрылымы мен фазалық құрамы

Мақала Р6М5, Р9 және Р18 жылдамкесетін болаттардың құрылымы мен фазалық құрамын зерттеуге арналған. Жылдамкескіш болаттан жасалған құралдың жоғары қызметтік қасиеттеріне термиялық өңдеу арқылы қол жеткізіледі. Сондықтан зерттеуге арналған үлгі дайындамалары Р6М5, Р9 және Р18 болаттарынан жасалған кескіш құралдардан, осы болаттар үшін стандартты термоөңдеуге ұшыраған. Бастапқы күйіндегі Р6М5, Р9 және Р18 жылдамкесетін болаттардың құрылымы, яғни стандартты термоөңдеуден кейін мартенсит пен арнайы карбидтерден тұрады. Карбидтердің бөлшектері матрицада біркелкі бөлінген және дұрыс сфералық формаға жақын. Бұл ретте Р6М5 және Р9 болаттарының құрылымында M_6C, МС типті карбидтер, ал Р18 болатының құрылымында тек M_6C типті карбидтер бар. КШЭД (EBSD)-талдау M_6C карбидтері Fe_3W_3C кубтық фазасымен ең оңтайлы үйлесетінін көрсеткен, ал МС типті карбид VC фазасына сәйкес келеді. Электрондық-микроскопиялық талдау тез кесілетін болаттағы M_6C және МС карбидтерінен басқа M_3C «цементитті» типті карбидтердің аз мөлшерде бар екені анықталған.

Кілт сөздер: жылдамкесетін болат, құрылым, фазалық құрам, карбид, термиялық өңдеу, цементит, мартенсит, вольфрам.

Б.К. Рахадилов, В. Виелеба, М.К. Кылышканов, А.Б. Кенесбеков, М. Маулет

Структура и фазовый состав быстрорежущих сталей

Статья посвящена исследованию структуры и фазового состава быстрорежущих сталей Р6М5, Р9 и Р18. Высокие служебные свойства инструмента из быстрорежущей стали достигаются термической обработкой. Поэтому заготовки образцов для исследования вырезали из режущих инструментов из сталей Р6М5, Р9 и Р18, подвергнутых обычной для этих сталей стандартной термообработке. Установлено, что структура быстрорежущих сталей Р6М5, Р9 и Р18 в исходном состоянии, т.е. после стандартной термообработки, состоит из мартенсита и специальных карбидов. Частицы карбидов равномерно распределены в матрице и близки к правильной сферической форме. При этом в структуре сталей Р6М5 и Р9 присутствуют карбиды типа M_6C, МС, а в структуре стали Р18 — только карбиды типа M_6C. ДОРЭ (EBSD)-анализ показал, что карбиды M_6C наиболее оптимально сочетаются с кубической фазой Fe_3W_3C, а карбидам типа МС соответствует фаза VC. Электронно-микроскопический анализ показал, что, кроме карбидов M_6C и МС, в быстрорежущей стали присутствуют в небольших количествах карбиды «цементитного» типа M_3C.

Ключевые слова: быстрорежущая сталь, структура, фазовый состав, карбид, термическая обработка, цементит, мартенсит, вольфрам.

References

1 Moiseev, V.F., & Grigorev, C.N. (2005). *Instrumentalnye materialy [Tool materials]*. (2d ed.). Moscow: MHTU Stankin [in Russian].

2 Firouzdor, V., Nejati, E., & Khomamizadeh, F. (2008). Effect of deep cryogenic treatment on wear resistance and tool life of M2 HSS drill. *Journal of Materials Processing Technology, 206(1–3),* 467–472.

3 Guchenko, S.A., Laurinas, V.Ch., & Zavatskaya, O.N. (2014). Kompozitsionnye ionno-plazmennye pokrytiia [Composite ion-plasma coatings]. *Vestnik Karahandinskoho universiteta. Seriia Fizika — Bulletin of the University of Karaganda. Physics series, 3(75),* 16–27 [in Russian].

4 Rahadilov, B.K., Zhurerova, L.G., Pavlov, A.V., & Wieleba, W. (2016). Electrolyte-plasma surface hardening of 65G and 20GL low-alloy steels. *Bulletin of the University of Karaganda-Physics, 4(84),* 8–14.

5 Skakov, M., Rakhadilov, B., Scheffler, M., & Batyrbekov, E. (2015). Microstructure and tribological properties of electrolytic plasma nitrided high-speed steel. *Materials Testing, 57(4),* 360–364.

6 Chaus, A.S., & Rudnitskii F.I. (2003). Structure and Properties of Cast Rapidly Cooled High-Speed Steel R6M5. *Metal Science and Heat Treatment, 45,* 157–162.

7 Liu, Z.Y., Loh, N.H., Khor, K.A., & Tor S.B. (2000). Microstructure evolution during sintering of injection molded M2 high speed steel. *Materials Science and Engineering A, 293,* 46–55.

8 Candane1, D., Alagumurthi, N., & Palaniradja K. (2013). Effect of cryogenic treatment on microstructure and wear characteristics of AISI M35 HSS. *International Journal of Materials Science and Applications, 2(2),* 56–65.

9 Šolić, S., Cajner, F., Leskovšek, V. (2012). Effect of deep cryogenic treatment on mechanical and tribological properties of PM S390 MC high-speed steel. *MP Materials Testing, 10,* 688–693.

10 Skakov, M., Rakhadilov, B., & Sheffler, M., (2013). Influence of electrolyte plasma treatment on structure, phase composition and microhardness of steel P6M5. *Key Engineering Materials, 531–532,* 627–631.

11 Samsonov, G.V., & Vinnitskii, I.M. (1976). *Tuhoplavkie soedineniia [Refractory compounds]*. Moscow: Metallurhiia [in Russian].

12 Geller, Yu.A. (1983). *Instrumentalnye stali [Tool steels]*. Moscow: Metallurhiia [in Russian].

13 Bochnowskiac, W., Leitnerb, H., Majorcd, Ł., Ebnerb, R., & Major, B. (2003). Primary and secondary carbides in high-speed steels after conventional heat treatment and laser modification. *Materials Chemistry and Physics, 81(2–3),* 503–506.

14 Goldishtein, M.I., Grachev, S.V. & Veksler, Yu.G. (1985). *Spetsialnye stali [Special steels]*. Moscow: Metallurhia [in Russian].

15 Guliaev, A.P. (1998). Teoria bystrorezhushei stali [Theory of high speed steel]. *MiTOM, 11,* 27–32 [in Russian].

16 Kremnev, L.S. (2008). Teoria lehirovaniia i sozdanie na ee osnove teplostoikikh instrumentalnykh stalei i splavov optimalnoho sostava [The alloying theory And the creation on its basis of heat-resistant tool steels and alloys of optimal composition]. *Metallovedenie i termicheskaia obrabotka metallov, 11,* 18–28 [in Russian].

17 Skakov, M., Rakhadilov, B., & Karipbayeva, G. (2013). Specifics of microstructure and phase composition of high-speed steel R6M5. *Applied Mechanics and Materials, 404,* 20–24.

18 Vorobeva, G.A., & Skladnova, E.E. (2003). *Instrumentalnye materialy: instrumentalnye stali i splavy [Tool Materials: Tool Steels & Alloys]*. Saint Petersburg [in Russian].

19 Guenzel, R., Matz, W., Ivanov, Yu.F., & Rothtein V.P. (2000). Pulsed electron-beam treatment of high-speed steel current tools: struchire-phase transformation and wear resistance. *1st International Congress on Radiation Physics, high current electronics, and modification of materials, 3,* 303–307. Tomsk, Russia.

20 Ivanov, Yu., Matz, W., Rotshtein, V., Gunzel, R., & Shevchenko N. (2002). Pulsed electron beams melting of high-speed steel: structural phase transformations and wear resistance. *Surface and Coatings Technology, 150,* 188–198.

21 Goldshmidt, H.Dzh. (1971). *Splavy vnedreniia [Introduction alloys]*. Moscow: Mir [in Russian].

DOI 10.31489/2020Ph2/93-100

UDC 62–531.7

A. Nizhegorodov[1], A. Gavrilin[2], B. Moyzes[2], K. Kuvshinov[2]

[1]Irkutsk National Research Technical University, Russia;
2National Research Tomsk Polytechnic University, Tomsk, Russia
(E-mail: nastromo_irkutsk@mail.ru)

The development of baking technology for bulk materials based on the use of alternative electric furnace

The article based on the experimental data and it describes the development of a rational design of an oscillatory system for controlled vibrational feeding of bulk materials during their heat treatment in furnaces with a vibratory base plate, which, together with the moving trolley on elastic connections, is the basis to transfer bulk material in the thermal field of an electric heating system with set processing time. To create non-symmetric oscillations and to obtain unidirectional material motion at the horizontal furnace position, the conical springs are used. They should provide a gently inclined resonant peak, which can significantly reduce the sensitivity of the oscillating system to fluctuations of the natural frequency and excitation frequency, stiffness, friction and other factors under high temperatures and instability of the electrical network. However, the total elastic characteristic of the oscillatory system which is obtained as a result of the experiments consists of conical and cylindrical springs and shows a weakly expressed nonlinearity. Therefore, to achieve a transport effect it will require the installation of the entire furnace unit at an angle to the horizon. According to the available experimental data, a linear model of the oscillatory system was utilized.

*Keywords***:** an electric furnace for bulk materials burning, vibrating base plate, oscillating system, nonlinear elastic characteristic, amplitude-frequency characteristic, sensitivity of the oscillating system to external factors.

Introduction

Vermiculite and materials based on it are widely used, so its processing technology is given wide attention [1–4].

The concept of electric furnaces with a vibrating base plate [5–10] appeared as an alternative to modular-trigger furnaces for puffing-up vermiculite concentrates [11]. In a number of works, for example, in [12] there are studies of the heat transfer processes of radiant energy to the processed bulk medium and other energy aspects. These studies showed that the energy efficiency of new furnaces is much greater than the modular-trigger electrical units: the energy density of vermiculite baking has decreased from 170...175 to 75...82 mJ/m^3. Besides the heating system, which transfers heat of radiant energy to the treated medium, the new furnace contains an oscillating system — the oscillating system is a vibrating base plate, which is designed to control the time of transportation of bulk materials in the hot compartment of baking furnace due to the vibration transport effect.

The purpose of the research is to create a rational design of an oscillatory system and to work out the modes of vibro-displacement of bulk materials as well as figure out the required time for their heat treatment on the base of experiments with a vibrating base plate of a prototype of an electric furnace of a new design.

Experimental

The research was carried out on a full-scale physical model (single-phase prototype) (Figure 1).

For a better understanding the design of a furnace with a vibrating base plate shown in Fig. 2 let us consider its construction diagram. Dosing chamber for bulk material 2 is fixed on the frame 1. From the dosing chamber the bulk material is transferred through the tray 3 to the base plate surface 4, which thermally insulated underneath by heat-resistant felt 5.

Figure 1. Furnace prototype with a vibrating base plate: 1 is the drum doser; 2 is the doser drive; 3 is the trigger tray; 4 is the thermal lid; 5 is the heating system; 6 is the frame

There are fasteners 7 on the thermal lid 6 to hold the heating elements 8 which located above the base plate with a gap providing free movement of the bulk medium along its surface. The base plate is fixed on the moving trolley 9 equipped with bearings 10 which are mounted in the guides. The track is spring-loaded on the left by cylindrical springs 11, on the right — by conical springs 12.

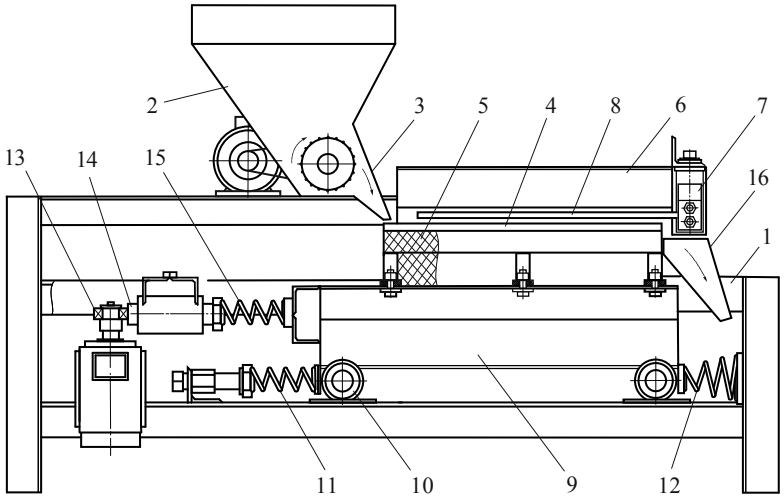

Figure 2. Constructive diagram of furnace prototype (shown in the horizontal position): 1 is the frame; 2 is the dosing chamber for bulk material; 3 is the tray; 4 is the base plate surface; 5 is the heat-resistant felt; 6 is the thermal lid; 7 is the fastener; 8 is the heating element; 9 is the moving trolley; 10 is the bearing; 11 is the cylindrical spring; 12 is the conical spring

The drive engine is equipped with the eccentric bearing fit 13, and therefore impacts on the plunger 14 by its shaft and through the spring 15 excites the vibrations of the moving trolley 9 with the base plate 4, due to which a vibrating-transport effect arises and the heat-treated material is poured through the tray 16.

From the point of view of the total springs elasticity, the oscillatory system is not symmetrical.

The conical springs 12 (Figure 2) were used with the purpose to obtain a nonlinear static characteristic of the oscillatory system and mounted on the side which the bulk material should move [13–17]. In addition, in a non-symmetrical system, the resonance peak on the amplitude-frequency characteristic (AFC) slightly declines to the left, which makes it possible to reduce the sensitivity of the oscillating system to frequency fluctuations, rigidity, friction, etc. in high-temperature conditions and non-stability of the electric network.

Another factor that determines the process of vibrational transportation of bulk product is the dynamic surface tilt which in this case is provided by the tilt of the furnace frame [17–20].

Results and Discussion

Figure 3 shows a diagram of the oscillating system, which contains four cylindrical springs of stiffness c_1, one coil spring of stiffness c_2 and four conical springs with variable stiffness c_k.

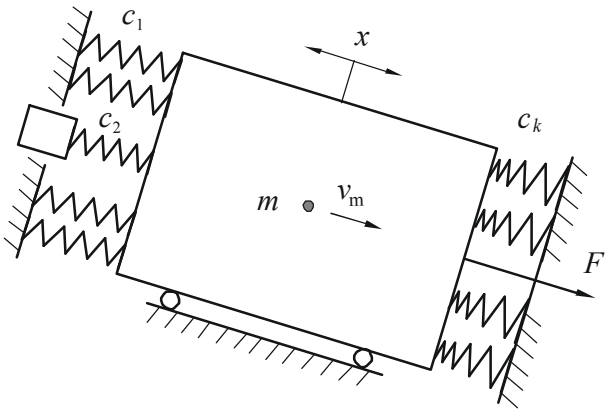

Figure 3. The diagram of oscillatory system

To evaluate the degree of nonlinearity of the oscillatory system as a whole (moving trolley 9, Figure 2), the following experiment was carried out. Using the lever tensioner and a dynamometer F2–13780, the track shifted toward the slope (Figure 3).

The ratio of the lever arms (meter) was:

– in the first case — 1.825/0.18=10.14;

– at the opposite movement — 1.665/0.305=5.46;

so in the first case the dynamometer was multiplied by 10.14, in the second — by 5.46.

The results of measurements are given in Table 1.

Table 1

The results of static loading system

Shift toward the slope		Shift away from the slope	
Compressive force F, [N]	Moving x, [10^{-3} m]	Compressive force F, [N]	Moving x, [10^{-3} m]
0	0	0	0
507.3	2.0	211.1	0.5
1054.7	4.0	481.2	2.0
1521.4	6.0	7785.6	3.1
2028.4	7.9	982.0	4.1
2535.9	9.4	–	–

In Figure 4, the experimental points are plotted according to the data of Table 1. The thicker graph reflects the degree of nonlinearity of the oscillatory system, the thin one — linear interpretation of the static elastic characteristic [21–23].

It is obvious that the oscillatory system is characterized by a very weak nonlinearity: firstly because of influence of the cylindrical springs with constant rigidity; secondly, the displacement x must be too large, to effect the variable rigidity of the conical springs. Therefore, we can consider the total rigidity of the system as a linear interpretation of the elastic characteristic (Figure 4), especially taking into account the result

which were obtained during the dynamic tests — the amplitude of the oscillations in the resonance does not exceed 10 mm.

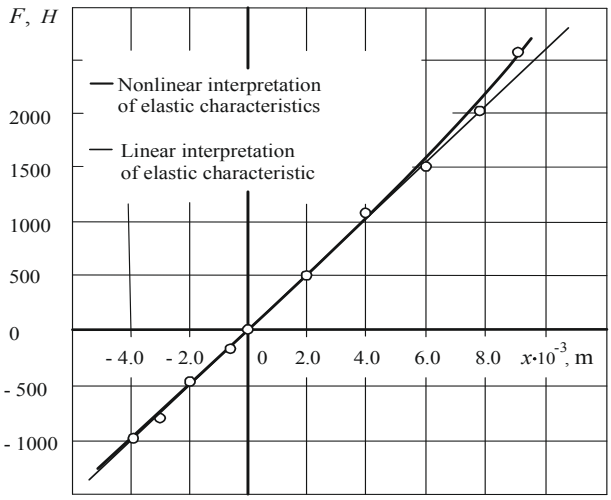

Figure 4. Static chart of the oscillating system

Table 2 shows the results of one of the conical springs loading.

Table 2

Conical spring

Compressive force F, [N]	Absolute deformation x, [10–^{3} m]
0	0
41.69	1.45
137.34	4.75
196.2	6.35
290.38	9.05
340.4	9.85
393.38	11.95
427.70	13.45
691.79	17.55
767.14	19.55

Using the data of Table 2, let us determine the average rigidity value c_k (N/m):

$$c_k = \frac{1}{9}\left(\frac{F_1}{x_1}+\frac{F_2}{x_2}+\frac{F_3}{x_3}+\frac{F_4}{x_4}+\frac{F_5}{x_5}+\frac{F_6}{x_6}+\frac{F_7}{x_7}+\frac{F_8}{x_8}+\frac{F_9}{x_9}\right)=\frac{1}{9}\left(\frac{41.69}{0.00145}+\frac{137.34}{0.00475}+\right.$$

$$\left.+\frac{196.2}{0.00635}+\frac{290.38}{0.00905}+\frac{340.4}{0.00985}+\frac{393.38}{0.01195}+\frac{427.7}{0.01345}+\frac{681.79}{0.01755}+\frac{767.14}{0.01955}\right)=32944,$$

where F_i — the compression force of the spring (H), x_i — its corresponding absolute deformation (m).

Similarly, we determine the rigidity of springs c_1 and c_2 (tabular data are not given):

$$c_1 = \frac{1}{9}\left(\frac{F_1}{x_1}+\frac{F_2}{x_2}+\frac{F_3}{x_3}+\frac{F_4}{x_4}+\frac{F_5}{x_5}+\frac{F_6}{x_6}+\frac{F_7}{x_7}+\frac{F_8}{x_8}+\frac{F_9}{x_9}\right)=$$

$$=\frac{1}{9}\left(\frac{30.41}{0.0015}+\frac{41.69}{0.0034}+\frac{61.31}{0.0046}+\frac{91.23}{0.006}+\frac{100,55}{0.0074}+\frac{136.85}{0.0093}+\frac{147.15}{0.01}+\frac{192.3}{0.0116}+\frac{195.7}{0.0134}\right)=15030;$$

$$c_2 = \frac{1}{9}\left(\frac{F_1}{x_1}+\frac{F_2}{x_2}+\frac{F_3}{x_3}+\frac{F_4}{x_4}+\frac{F_5}{x_5}+\frac{F_6}{x_6}+\frac{F_7}{x_7}+\frac{F_8}{x_8}+\frac{F_9}{x_9}\right)=$$

$$=\frac{1}{9}\left(\frac{52.97}{0.002}+\frac{136.95}{0.0031}+\frac{195.8}{0.0042}+\frac{216.8}{0.0059}+\frac{290,38}{0.0066}+\frac{340.9}{0.0081}+\frac{392.6}{0.0097}+\frac{399.76}{0.0104}+\frac{441.94}{0.0111}\right)=39876.$$

In accordance with the diagram of oscillatory system (Fig. 3), its total rigidity will be equal (N/m):

$$c=4c_k+4c_1+c_2=4\cdot 32944+4\cdot 15030+39846=231742.$$

To calculate the natural frequency of the moving trolley with the base plate, it was weighed on an electronic scale PP 1001 V0 / 3A0R with an upper measurement limit of 150 kgf. As a result, the total mass (m) was equal — 76.4 kg.

For a given set of springs, the natural frequency of the oscillating system was equal, rad/s:

$$\omega_0 = \sqrt{\frac{c}{m}} = 55.1,$$

which corresponds to 8.77 Hz.

Conclusion

In addition to the electric heating system, which is used to create powerful temperature radiation and to transfer it to the processed bulk medium, a prototype of an electric furnace of a new design was added to the operation. The new furnace also contains an oscillating system in the form of a spring-loaded base plate designed to control the heat treatment process time of the material in the furnace due to the generated vibrating transport effect. The vibratory base plate on the moving trolley is a simple vibrating dispenser that provides the flow and time-controlled movement of bulk materials in the thermal field of the furnace.

We conducted the experiments where the total elastic characteristics of a set of conical and cylindrical springs were aimed to be worked out. The experiments proved that the oscillatory system exhibit a weak nonlinearity, which does not allow transporting bulk material at the horizontal position of the plate. And this requires the installation of a vibration base plate with a slope toward the material being moved in order to achieve a stationary transport process of the bulk material. Therefore, for further research, a linear model of the oscillating system was used for the process of working out the special parameters such as an analytical dependence for calculating the natural frequency of a spring-loaded base plate and the range of resonant oscillations. The parameters were worked out.

However, studies have not yet been completed, since the linear system has some drawbacks related to its high sensitivity to possible fluctuations of the natural frequency and excitation frequency, fluctuations of spring stiffness and friction forces and other factors in high temperature conditions and instability of the electrical network.

Acknowledgement

This work was carried out with financial support of the Program of Increasing the International Competitiveness of the Tomsk State University for 2013–2020.

References

1 Kogal J.E. Industrial minerals & rocks: commodities, markets and uses / J.E. Kogal, N.C. Trivedi, J.M. Barker, T.S. Krukowski. — Littleton: Society for Mining, Metallurgy, and Exploration Inc., 2009. — 1565 p.

2 Fuks L. Vermiculite as a potential component of the engineered barriers in low- and medium-level radioactive waste repositories / L. Fuks, I. Herdzik-Koniecko // Applied Clay Science. — 2018. — Vol. 161. — P. 139–150.

3 Rashad A.M. Vermiculite as a construction material: A short guide for Civil Engineer / A.M. Rashad // Construction and Building Materials. — 2016. — Vol. 125. — P. 53–62.

4 Hombostel C. Construction Materials: Types, Uses, and Applications / C. Hombostel. — New York: John Wiley & Sons, Inc., 1991. — 878 p.

5 Nizhegorodov A.I. Energy efficient electric furnace with moving hearth platform for firing vermiculite / A.I. Nizhegorodov // Refractories and Industrial Ceramics. — 2017. — Vol. 58. — № 1. — P. 29–34, doi 10.1007/s11148–017–0049–4

6 Shyamal S. Real-time energy management for electric arc furnace operation / S. Shyamal, C.L.E. Swartz // J. of Process Control. — 2019. — Vol. 74. — P. 50–62.

7 Contreras-Serna J. Study of heat transfer in a tubular-panel cooling system in the wall of an electric arc furnace / J. Contreras-Serna, C.I. Rivera-Solorio, M.A. Herrera-García // Applied Thermal Engineering. — 2019. — Vol. 148. — P. 43–56.

8 Bryanskikh T.V. Energy efficiency of electric furnaces with movable floor in firing of vermiculite concentrates of different size groups / T.V. Bryanskikh, D.V. Kokourov // Refractories and Industrial Ceramics. — 2017. — Vol. 58. — P. 368–373, doi:10.1007/s11148–017–0113–0.

9 Sutcun M. Influence of expanded vermiculite on physical properties and thermal conductivity of clay bricks / M. Sutcun // Ceramics International. — 2015. — Vol. 41. — P. 2819–2827.

10 Kariya J. Development of thermal storage material using vermiculite and calcium hydroxide / J. Ryu, Y. Kato // Applied Thermal Engineering. — 2016. Vol. 94. — P. 186–192.

11 Nizhegorodov A.I. Theory and practical use of modular-pouring electric furnaces for firing vermiculite / A.I. Nizhegorodov // Refractories and Industrial Ceramics. — 2105. — Vol. 56. — № 4. — P. 361–365, DOI 10.1007/s11148–015–9848–7

12 Nizhegorodov A.I. Testing a new alternative electric furnace for vermiculite concentrates heat treatment / A.I. Nizhegorodov, T.B. Bryanskikh, A.N. Gavrilin, B.B. Moyzes, G.V. Vavilova, A.V. Gradoboev, J. Tlusty, V. Tuzikova // Bulletin of the Tomsk Polytechnic University, Geo Assets Engineering. — 2018. — Vol. 329. — № 4. — P. 142–153.

13 Блехман И.И. Вибрация в технике: справоч.: [В 6 т.]. — Т. 2. Колебания нелинейных механических систем / И.И. Блехман; под ред. И.И. Блехмана. — М.: Машиностроение, 1979. — 351 с.

14 Weaver W.Jr. Vibration Problems In Engineering / W.Jr. Weaver, S.P. Timoshenko, D.H. Young. — New York: Wiley-Interscience, 1990. — 624 p.

15 Soleimanimehr H. The analysis of the Timoshenko transverse vibrations of workpiece in the ultrasonic vibration-assisted turning process and investigation of the machining error caused by this vibration / H. Soleimanimehr, M.J. Nategh, A.F. Najafabadi, A. Zarnan // Precision Engineering. 2018. — Vol. 54. — P. 99–106.

16 Paczkowski T. The Effect of Multidirectional Vibration On Electrochemical Machining / T. Paczkowski, A. Troszyński // Procedia Manufacturing. — 2018. — Vol. 22. — P. 41–48.

17 Бауман В.А. Вибрационные машины и процессы в строительстве / В.А. Бауман, И.И. Быховский. — М.: Высш. шк., 1977. — 255 с.

18 Wang Zh. Existence of periodic solutions for a class of damped vibration problems / Zh. Wang, J. Zhang // Comptes Rendus Mathematique. — 2018. — Vol. 356. — № 6. — P. 597–612.

19 Lin R.M. Development of a theoretical framework for vibration analysis of the class of problems described by fractional derivatives / R.M. Lin, T.Y. Ng // Mech. Syst. Signal Process. — 2019. — Vol. 116. — P. 78–96.

20 Fetyan Kh. Effect of motor vibration problem on the power quality of water pumping stations / Kh. Fetyan, D. El. Gazzar // Water Science. — 2014. — Vol. 28. — № 1. — P. 31–41.

21 Plotnikova I.V. Mathematic modeling of the method of measurement relative dielectric permeability / I.V. Plotnikova, N.V. Chicherina, A.B. Stepanov // IOP Conf. Series: Materials Science and Engineering. — 2018. — Vol. 363. — № 1 — 012006, doi: 10.1088/1757–899X/363/1/012006

22 Plotnikova I.V. Analysis of quality of welded joints of iron-concrete products / I.V. Plotnikova, L.A. Redko, N.V. Chicherina, O. Tchaikovskaya, J. Bastida // Materials Science Forum. — 2019. — Vol. 942. — P. 121–130, doi: 10.4028/www.scientific.net/MSF.942.121.

23 Goldshtein A.E. Detection of Insulation Defects in Automated In-Process Testing of Electric Wire during its Extrusion / A.E. Goldshtein, G.V. Vavilova, A. Rumkin, O. Starý // Modern Problems in Materials Processing, Manufacturing, Testing and Quality Assurance. — 2019. — Vol. 942 — P. 141–150, DOI: 10.4028/www.scientific.net/MSF.942.141.

А. Нижегородов, А. Гаврилин, Б. Мойзес, К. Кувшинов

Баламалы электрпешті пайдалану негізінде сусымалы материалдарды күйдіру технологиясын әзірлеу

Мақалада эксперименталды мәліметтер негізінде дірілді тірек плитасы бар пештерде оларды термоөңдеу кезінде сусымалы материалдарға реттейтін дірілді беру үшін тербелмелі жүйенің ұтымды құрылымын әзірлеу сипатталған, ол серпімді байланыстардағы жылжымалы арбамен бірге сусымалы материалдарды берілген өңдеу уақытымен электр қыздыру жүйесінің жылу өрісінде тасымалдау үшін негіз болып табылады. Симметриялы емес тербелістерді жасау және пештің көлденең жағдайында материалдың бір бағыттағы қозғалысын алу үшін конустық серіппелер қолданылған. Олар резонанстық шыңның қиғаштауын қамтамасыз етуі тиіс, бұл тербеліс жүйесінің жоғары температура мен электр желісінің тұрақсыздығы кезінде өз жиілігінің тербелісіне және қозу жиілігіне, қаттылыққа, үйкеліске және басқа да факторларға сезімталдығын айтарлықтай төмендетуге мүмкіндік береді. Алайда, эксперименттер нәтижесінде алынған тербеліс жүйесінің жалпы серпімді сипаттамасы конустық және цилиндрлік серіппелерден тұрады және әлсіз көрінбейтін сызықтықты көрсетеді. Сондықтан көліктік әсерге жету үшін горизонтқа бұрышпен барлық пеш агрегатын орнату қажет. Тәжірибелік деректер бойынша тербеліс жүйесінің сызықтық моделі қолданылған.

Кілт сөздер: сусымалы материалдарды күйдіруге арналған электр пеші, дірілді тірек плитасы, тербелмелі жүйе, сызықсыз-серпімді сипаттама, амплитудалық-жиілік сипаттамасы, тербелмелі жүйенің сыртқы факторларға сезімталдығы.

А. Нижегородов, А. Гаврилин, Б. Мойзес, К. Кувшинов

Разработка технологии обжига сыпучих материалов на основе использования альтернативной электропечи

В статье на основе экспериментальных данных описана разработка рациональной конструкции колебательной системы для регулируемой вибрационной подачи сыпучих материалов при их термообработке в печах с вибрационной опорной плитой, которая вместе с подвижной тележкой на упругих связях является основой для переноса сыпучих материалов в тепловом поле электронагревательной системы с заданным временем обработки. Для создания несимметричных колебаний и получения однонаправленного движения материала в горизонтальном положении печи используются конические пружины. Они должны обеспечивать пологий наклон резонансного пика, что позволяет значительно снизить чувствительность колебательной системы к колебаниям собственной частоты и частоты возбуждения, жесткости, трению и другим факторам при высоких температурах и нестабильности электрической сети. Однако общая упругая характеристика колебательной системы, полученная в результате экспериментов, состоит из конических и цилиндрических пружин и демонстрирует слабо выраженную нелинейность. Поэтому для достижения транспортного эффекта потребуется установка всего печного агрегата под углом к горизонту. По имеющимся экспериментальным данным, была использована линейная модель колебательной системы.

Ключевые слова: электрическая печь для обжига сыпучих материалов, вибрирующая опорная плита, колебательная система, нелинейно-упругая характеристика, амплитудно-частотная характеристика, чувствительность колебательной системы к внешним факторам.

References

1 Kogal, J.E., Trivedi, N.C., Barker, J.M., & Krukowski, T.S. (2009). Industrial minerals & rocks: commodities, markets and uses. *Society for Mining, Metallurgy, and Exploration, Inc., Littleton.*

2 Fuks, L., & Herdzik-Koniecko, I. (2018). Vermiculite as a potential component of the engineered barriers in low- and medium-level radioactive waste repositories. *Applied Clay Science*, *161*, 139–150.

3 Rashad, A.M. (2016). Vermiculite as a construction material: A short guide for Civil Engineer, *Construction and Building Materials, 125*, 53–62.

4 Hombostel, C. (1991). *Construction Materials: Types, Uses, and Applications.* John Wiley & Sons, Inc., New York.

5 Nizhegorodov, A.I. (2017). Energy efficient electric furnace with moving hearth platform for firing vermiculite. *Refractories and Industrial Ceramics, 58 (1)*, 29–34, doi: 10.1007/s11148–017–0049–4.

6 Shyamal S., & Swartz C.L.E. (2019). Real-time energy management for electric arc furnace operation. *J. of Process Control, 74*, 50–62.

7 Contreras-Serna, J., Rivera-Solorio, C.I., & Herrera-García, M.A. (2019). Study of heat transfer in a tubular-panel cooling system in the wall of an electric arc furnace. *Applied Thermal Engineering, 148*, 43–56.

8 Bryanskikh T.V., & Kokourov D.V. (2017). Energy efficiency of electric furnaces with movable floor in firing of vermiculite concentrates of different size groups. *Refractories and Industrial Ceramics, 58*, 368–373, doi:10.1007/s11148–017–0113–0.

9 Sutcun, M. (2015). Influence of expanded vermiculite on physical properties and thermal conductivity of clay bricks, *Ceramics International, 41*, 2819–2827.

10 Kariya, J., Ryu, J., & Kato, Y. (2016). Development of thermal storage material using vermiculite and calcium hydroxide. *Applied Thermal Engineering, 94*, 186–192.

11 Nizhegorodov, A.I. (2015). Theory and practical use of modular-pouring electric furnaces for firing vermiculite. *Refractories and Industrial Ceramics, 56 (4),* 361–365, doi: 10.1007/s11148–015–9848–7.

12 Nizhegorodov, A.I., Bryanskikh, T.B., Gavrilin, A.N., Moyzes, B.B., Vavilova, G.V., Gradoboev, A.V., Tlusty, J., & Tuzikova, V. (2018). Testing a new alternative electric furnace for vermiculite concentrates heat treatment. *Bulletin of the Tomsk Polytechnic University, Geo Assets Engineering, 329 (4)*, 142–153.

13 Blekhman, I.I. (1979). *Vibratsiia v tekhnike: spravochnik. Kolebaniia nelineinykh mekhanicheskikh sistem [Vibrations in engineering: reference book. Oscillations of nonlinear mechanical systems]. (Vol. 1-6; Vol. 2).* Moscow: Mashinostroenie [in Russian].

14 Weaver, W.Jr., Timoshenko, S.P., & Young, D.H. (1990). *Vibration Problems In Engineering*. Wiley-Interscience, New York.

15 Soleimanimehr, H., Nategh, M. J., Najafabadi, A.F., & Zarnan, A. (2018). The analysis of the Timoshenko transverse vibrations of workpiece in the ultrasonic vibration-assisted turning process and investigation of the machining error caused by this vibration, *Precision Engineering, 54*, 99–106.

16 Paczkowski, T., & Troszyński, A. (2018). The Effect of Multidirectional Vibration On Electrochemical Machining. *Procedia Manufacturing, 22*, 41–48

17 Bauman, V.A., & Bykhovskij, I.I. (1977). *Vibratsionnye mashiny i protsessy v stroitelstve [Vibration machines and processes in construction]*. Moscow: Vysshaia shkola [in Russian].

18 Wang, Zh., & Zhang, J. (2018). Existence of periodic solutions for a class of damped vibration problems. *Comptes Rendus Mathematique, 356 (6)*, 597–612.

19 Lin, R.M., & Ng, T.Y. (2019). Development of a theoretical framework for vibration analysis of the class of problems described by fractional derivatives. *Mech. Syst. Signal Process, 116*, 78–96.

20 Fetyan, Kh., & Gazzar, D. El. (2014). Effect of motor vibration problem on the power quality of water pumping stations, *Water Science, 28 (1)*, 31–41.

21 Plotnikova, I.V., Chicherina, N.V., & Stepanov, A.B. (2018). Mathematic modeling of the method of measurement relative dielectric permeability. *IOP Conf. Series: Materials Science and Engineering, 363 (1)*, 012006. doi: 10.1088/1757–899X/363/1/012006

22 Plotnikova, I.V., Redko, L.A., Chicherina, N.V., Tchaikovskaya, O., & Bastida, J. (2019). Analysis of quality of welded joints of iron-concrete products. *Materials Science Forum, 942*, 121–130. doi: 10.4028/www.scientific.net/MSF.942.121.

23 Goldshtein, A.E., Vavilova, G.V., Rumkin, A., & Starý, O. (2019). Detection of Insulation Defects in Automated In-Process Testing of Electric Wire during its Extrusion. *Modern Problems in Materials Processing, Manufacturing, Testing and Quality Assurance, 942*, 141–150. doi: 10.4028/www.scientific.net/MSF.942.141.

DOI 10.31489/2020Ph2/101-107

UDC 539.3

B. Kenzhegulov[1], Jaroslav Kultan[2], D.B. Alibiyev[3], A.Sh. Kazhikenova[3]

[1]Kh. Dosmukhamedov Atyrau State University, Atyrau, Kazakhstan;
[2]Ekonomicka univerzita v Bratislave Slovenska republika, Slovensko;
[3]Ye.A. Buketov Karaganda State University, Kazakhstan;
(E-mail: aigul-kazhikenova@mail.ru)

Numerical modeling of thermomechanical processes in heat-resistant alloys

This article presents a numerical simulation of thermomechanical processes in heat-resistant alloys. The authors develop the law of temperature distribution along the length of the physical body, which is considered as a rod of alloy EI-617. The authors also investigated the dependence of the magnitude of the elongation of the rod from a given temperature. To do this, the rod is conditionally divided into several elements, and then the study is carried out in one area. To determine the temperature dependence, the temperature distribution field is approximated by a full polynomial of the second degree, and approximation spline functions are introduced. Using a temperature gradient for one element, the functional expression characterizing the total thermal energy is written, first for the *(n-1)* element, then for the last *n*-th element. The total thermal energy is expressed by the formula $J = \sum_{i=1}^{n} J_i$. By minimizing the total thermal energy, we obtain a system of algebraic equations for determining the nodal values of temperatures. Applying the obtained values, the elongation of the element due to thermal expansion is calculated. The relationship between the temperature *T*, elongation Δl_T , «tensile» force R , and «tensile stress» σ. is shown in the work. It is shown that with increasing temperature, the above values proportionally increase.

Keywords: thermal expansion, modulus of elasticity, rod, elongation, thermal stress state, sampling.

Introduction

Intensive development of modern technological processes in the field of metal science creates favorable conditions for the production of more advanced heat-resistant alloys with high resistance to plastic deformation and destruction under the influence of high temperatures.

This article presents the experimental temperature dependences of the coefficient of thermal expansion and the elastic modulus of the alloy EI-617, which are determined experimentally. Taking into account the experimental dependence of the modulus of elasticity and the coefficient of thermal expansion of the alloy material on temperature, the problem of determining the field of temperature distribution, elongation, and thermal stress state of a rod of limited length made of EI-617 alloy is considered.

The coefficient of thermal expansion $\alpha\left(\frac{1}{^\circ C}\right)$ of this alloy is strictly dependent on temperature. In [1, 2] values are given at various temperatures. Studying experimental materials received the corresponding functional dependence

1) for $20^\circ C \le T \le 100^\circ C$, $\alpha = 0{,}0225 \cdot 10^{-6} \times T + 9{,}65 \cdot 10^{-6}\left(\frac{1}{^\circ C}\right)$

2) for $100^\circ C \le T \le 200^\circ C$, $\alpha = 0{,}013 \cdot 10^{-6} \times T + 10{,}6 \cdot 10^{-6}\left(\frac{1}{^\circ C}\right)$

3) for $200^\circ C \le T \le 300^\circ C$, $\alpha = 0{,}015 \cdot 10^{-6} \times T + 10{,}2 \cdot 10^{-6}\left(\frac{1}{^\circ C}\right)$

4) for $300^\circ C \le T \le 400^\circ C$, $\alpha = 0{,}023 \cdot 10^{-6} \times T + 7{,}8 \cdot 10^{-6}\left(\frac{1}{^\circ C}\right)$

5) for $400^\circ C \le T \le 500^\circ C$, $\alpha = 0{,}013 \cdot 10^{-6} \times T + 11{,}6 \cdot 10^{-6}\left(\frac{1}{^\circ C}\right)$

6) for $500^{\circ}C \le T \le 600^{\circ}C$, $\alpha = 0{,}02 \cdot 10^{-6} \times T + 8{,}3 \cdot 10^{-6}\left(\frac{1}{^{\circ}C}\right)$

7) for $600^{\circ}C \le T \le 700^{\circ}C$, $\alpha = 0{,}017 \cdot 10^{-6} \times T + 10{,}1 \cdot 10^{-6}\left(\frac{1}{^{\circ}C}\right)$

8) for $700^{\circ}C \le T \le 800^{\circ}C$, $\alpha = 0{,}012 \cdot 10^{-6} \times T + 13{,}6 \cdot 10^{-6}\left(\frac{1}{^{\circ}C}\right)$

Experimental

Let's consider a horizontal cylinder-shaped body (hereinafter referred to as the rod) of limited length and made of heat-resistant alloy EI-617.

The thermal conductivity of the rod material is denoted by $K_{xx}\left(\frac{W}{mc \cdot ^{\circ} C}\right)$. The coefficient of thermal expansion of the rod material is denoted by $\alpha = \alpha(T(x))\left(\frac{1}{^{\circ}C}\right)$. The length of the rod is denoted by $L(cm)$, and the cross-sectional area is denoted by $F(cm^2)$. We consider the left end of the body (rod) under consideration to be rigidly pinched, and the free end to the right. An axial tensile force $P(kG)$ is applied at the free end. We will direct the axis Ox from left to right. It coincides with the axis of the rod. Throughout the length of the rod, the area of the lateral surface, as well as through the cross-sectional area of the right end of the rod, is exchanged with the environment. In this case, the heat transfer coefficient is $h\left(\frac{W}{mc \cdot ^{\circ} C}\right)$, and the ambient temperature is $T_{at}\left(^{\circ}C\right)$. At the left pinched end of the rod, a constant temperature $T(x=0) = T_1$ is set [3,4]. The calculation scheme of the problem under consideration is given in Figure 1.

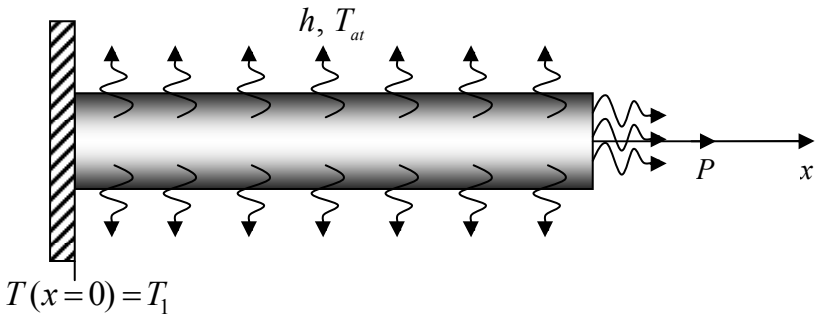

Figure 1. The calculation scheme of the problem.

The purpose of this article is to determine the law of the temperature distribution along the length of the rod under study, as well as the dependence of the rod elongation on the value of the given temperature $T(x=0) = T_1$. Here it is necessary to take into account the experimental dependence of the coefficient of thermal expansion of the material of the rod on temperature. To do this, we first discretize the test rod into n-elements of the same length $l = \frac{L}{n}(cm)$. For example, consider one discrete element. Within each local element, the temperature distribution field is approximated by a second-order full polynomial, i.e.

$$T(x) = ax^2 + bx + c\ ,\ 0 \le x \le l,\ a,\ b,\ c — const. \tag{1}$$

If within one local element accept that

$$T_i = T(x=0);\ \ T_j = T\left(x = \frac{l}{2}\right);\ \ T_k = T(x=l) \tag{2}$$

then within this element we can rewrite (1) in the following form

$$T(x)=\varphi_i(x)\cdot T_i+\varphi_j(x)\cdot T_j+\varphi_k(x)\cdot T_k,\ 0\le x\le l, \tag{3}$$

where $\varphi_i(x)$, $\varphi_j(x)$ and $\varphi_k(x)$ are approximate spline functions which are called form functions for a quadratic discrete element with three nodes. They have the following form:

$$\varphi_i(x)=\frac{l^2-3lx+2x^2}{l^2};\ \varphi_j(x)=\frac{4lx-4x^2}{l^2};\ \varphi_k(x)=\frac{2x^2-lx}{l^2};\ 0\le x\le l \tag{4}$$

Within one element, the temperature gradient is determined as follows:

$$\frac{\partial T}{\partial x}=\frac{\partial\varphi_i(x)}{\partial x}T_i+\frac{\partial\varphi_j(x)}{\partial x}T_j+\frac{\partial\varphi_k(x)}{\partial x}T_k,\ 0\le x\le l \tag{5}$$

For (n-1) elements we can write an expression of the functional that characterizes its total thermal energy:

$$J_i=\int_{V_i}\frac{K_{xx}}{2}\left(\frac{\partial T}{\partial x}\right)^2dV+\int_{S_{lSi}}\frac{h}{2}(T-T_{ar})^2dS \tag{6}$$

where $i=1\div(n-1)$; V_i is the volume of the i-th discrete element; S_{lSi} is the area of the lateral surface of the i-th element.

Now we can write an expression of a similar functional for the last n-th discrete element:

$$J_n=\int_{Vn}\frac{K_{xx}}{2}\left(\frac{\partial T}{\partial x}\right)^2dV+\int_{S_{lSi}}\frac{h}{2}(T-T_{at})^2dS+\int_{S_{x=L}}\frac{h}{2}(T-T_{at})^2dS \tag{7}$$

where $S(x=L)$ is the cross-sectional area of the right end of the investigated body through which heat exchange also takes place with the environment. Then for the investigated body as a whole, the expression of the functional that characterizes its total thermal energy has the following form:

$$J=\sum_{i=1}^{n}J_i \tag{8}$$

Now, minimizing J by the nodal temperature values, we obtain a resolving system of linear algebraic equations:

$$\frac{\partial J}{\partial T_i}=0,\ i=2\div(2n+1) \tag{9}$$

Here i changes from 2, because it is considered that $T_1=T(x=0)$ is given.

Results and Discussion

Using the Gauss method, solving system (9) determines the nodal temperature values. According to them, for each local discrete element, the following integral is calculated, the essence of which is the extension of the element due to thermal expansion:

$$\Delta l_i=\int_0^l\left[\varphi_i(x)\cdot\alpha_i+\varphi_j(x)\cdot\alpha_j+\varphi_k(x)\cdot\alpha_k\right]\left[\varphi_i(x)\cdot T_i+\varphi_j(x)\cdot T_j+\varphi_k(x)\cdot T_k\right]dx\ \ 0\le x\le l \tag{10}$$

Then the total elongation of the test body is determined by the following formula:

$$\Delta l=\sum_{i=1}^{n}\Delta l_i \tag{11}$$

It should be noted that for different values of the given temperature $T_1=T(x=0)$, the corresponding value of Δl is obtained.

For the purposes of a numerical study of dependencies of $\Delta l=\Delta l(T(x=0)=T_1)$, we take the following for initial data:

$$K_{xx}=72W/\left(cm\cdot{}^\circ C\right);\ h=10W/\left(cm^2\cdot{}^\circ C\right);\ T_{at}=40C;\ T(x=0)=T_1=(100\div800)^\circ C;$$

$$L=30cm;\ n=300;\ l=\frac{L}{n}=0{,}1cm;\ r=1cm;\ F=\pi r^2=\pi;\ P=2\pi r=2\pi.$$

The corresponding field of temperature distribution along the length of the rod with such initial data is shown in Figure 2.

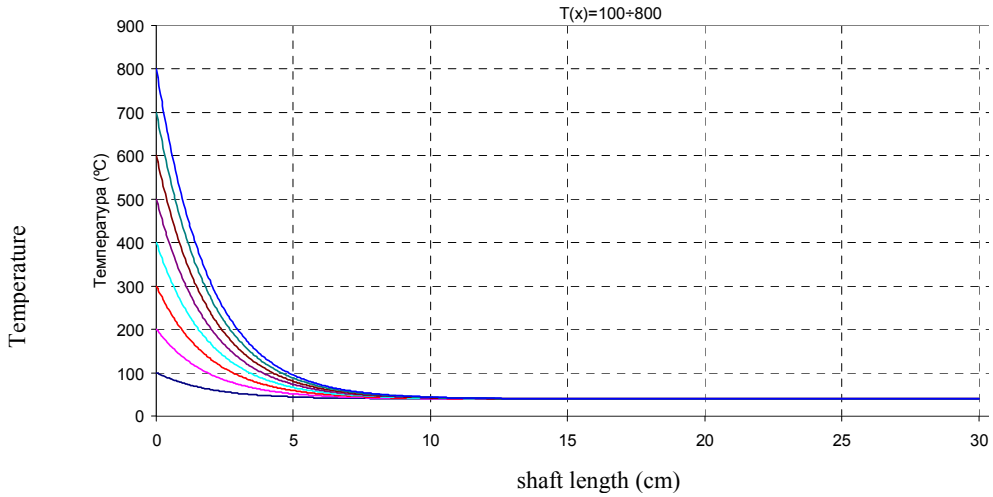

Figure 2. Dependence of $T=T(x)$ on T_1

Table 1

Dependence between T_1 and $\Delta l_T, R, \sigma$

№	$T_1(^\circ C)$	$\Delta l_T(cm)$	Equivalent «tensile» force $R(kG)$ at which such an elongation would result	Equivalent «tensile stress» $\sigma(kG/cm^2)$	$\overline{\Delta l_T}(cm)$ at $\alpha = const = 10{,}1\cdot 10^{-6}(1/^\circ C)$	Elongation in%	$k=\frac{\Delta l_T}{\overline{\Delta l_T}}$ (times)
1	100	0,014	2930,66	933,33	0,0133	0,047	1,052
2	200	0,0165	3454	1100	0,0152	0,055	1,085
3	300	0,0193	4040,1	1286,66	0,0171	0,064	1,129
4	400	0,02247	4703,72	1498	0,0190	0,075	1,183
5	500	0,0259	5432,2	1730	0,0209	0,086	1,239
6	600	0,0297	6217,2	1980	0,0228	0,1	1,303
7	700	0,03388	7092,2	2258,66	0,0247	0,113	1,372
8	800	0,038	7954,66	2533,33	0,0267	0,127	1,423

Figure 2 shows the temperature distribution field along the length of the rod at different values of T_1, and Table 1 shows the values of Δl_T at different values of T_1, i.e. dependence between T_1 and $\Delta l_T, R, \sigma$. Figure 2 shows that the temperature distribution field along the length of the rod will be a smooth curve. A graphic relationship between the values of the temperature source (T_1) and the corresponding elongation (Δl_T) of the rod from thermal expansion is shown in Figure 3.

When $T_1 = 100(^\circ C)$, starting with $x = 15{,}5(cm)$, i.e. at the site $15{,}5 \le x \le 30(cm)$ there is a constant temperature, the value of which is equal to $\approx 40(^\circ C)$. In this case, due to thermal expansion, the body (rod) is extended by $\Delta l_T = 0{,}014(cm)$. For comparison, it can be noted that this extension is equivalent to the extension of the rod, if it is stretched by force R=2930,66(kG). Naturally, on the basis of Hooke's law in this case a tensile stress of magnitude $\sigma = 933{,}33(kG/cm^2)$ would arise in the cross section of the rod.

When $T_1 = 200(^\circ C)$, i.e. with an increase in the set temperature by a factor of two, a $40(^\circ C)$ temperature field is observed in the area $19{,}2 \le x \le 30(cm)$. In this case, the elongation of the body (rod) is $\Delta l_T = 0{,}0165(cm)$ and will be 17.657 % greater than in the case $T_1 = 100(^\circ C)$. This magnitude of elongation

is equivalent to elongation of the rod under tensile load R=3454(kG). In this case, tensile stress would be $\sigma = 1100(kG/cm^2)$.

When $T_1 = 300(^\circ C)$, i.e. when to increase the value of the point temperature by three times the value $\Delta l_T = 0{,}0193(cm)$, which exceeds by 37.857 % than in the case $T_1 = 100(^\circ C)$. It should also be noted that in this case, at the site $21{,}1 \le x \le 30(cm)$ of the body (rod), a constant temperature is observed close to the ambient temperature of the body (rod). In this case, the value Δl_T is equivalent to stretching the considered rod with force R=4040,1(kG). In this case, the tensile stress arising in the cross sections would be $\sigma = 1286{,}66(kG/cm^2)$. It should be noted that for ordinary steels this voltage already exceeds the proportional limit.

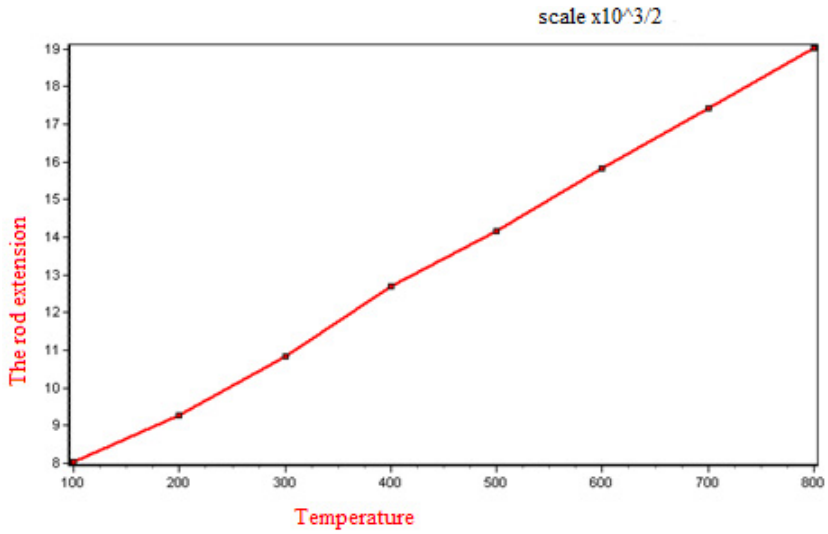

Figure 3 — Graphic relationship between T_1 and Δl_T

When $T_1 = 400(^\circ C)$, i.e. Now increasing the value T_1 four times, we have that $\Delta l_T = 0{,}02247(cm)$. This is equivalent to the elongation of the rod when it is stretched by a force whose magnitude is R=4703,72(kG). In this case, a tensile stress of magnitude $\sigma = 1498(kG/cm^2)$ would arise in the cross sections of the rod. Naturally for ordinary steels, this stress is considered destructive.

When $T_1 = 500(^\circ C)$, value $\Delta l_T = 0{,}02595(cm)$. This is 85 % more than the same value Δl_T at $T_1 = 100(^\circ C)$. It should be noted here that in order to obtain an elongation of the rod in size $\Delta l_T = 0{,}02595(cm)$ when it is stretched, it would be necessary to stretch with force R=5432,2(kG). At the same time, tensile stress $\sigma = 1730(kG/cm^2)$ would appear in the cross sections of the rod, which is large for ordinary steel structures.

With $T_1 = 600(^\circ C)$, the value $\Delta l_T = 0{,}0297(cm)$ and it will be 112.14 % more than Δl_T at $T_1 = 100(^\circ C)$. Equivalent tensile force would be equal to R=6217,2(kG) and the corresponding tensile stress would be equal to $\sigma = 1980(kG/cm^2)$. Comparing the results obtained, it is interesting to note that when the temperature value T_1 increases from $T_1 = 100(^\circ C)$ to $T_1 = 600(^\circ C)$, the values of $\Delta l_T, R, \sigma$ increase equally by 112.14 %.

References

1 Ноздрев В.Ф. Курс термодинамики / В.Ф. Ноздрев. — М.: Просвещение, 1967. — 248 с.
2 Сегерлинд Л. Применение метода конечных элементов / Л. Сегерлинд. — М.: Мир, 1979. — 392 с.

3 Kenzhegulov B. Numerical solution of problem of thermo elasticity with provision for dependencies between the factor of heat expansion and temperature / B. Kenzhegulov // International journal of scientific articles. Science and technology — 2009. — 5. — P. 3–7.

4 Kenzhegulov B. Numeral modeling of heat mechanical condition of core of limited lengths made of heat resistant alloy ANV -300 at presence of heat exchange, partial heat insulation, local temperature and axial spraining power / B. Kenzhegulov // International journal of scientific articles. Science and technology — 2009. — 5. — P. 8–14.

Б. Кенжегулов, Я. Култан, Д.Б. Алибиев, А.Ш. Кажикенова

Қызуға төзімді құйманың жылумеханикалық процестерін сандық модельдеу

Мақалада қызуға төзімді құйманың жылумеханикалық процестерін сандық модельдеу келтірілген. ЭИ-617 құймасынан жасалған сырықты негізге ала отырып, авторлар физикалық дененің ұзына бойы жылу таралу заңдылығы қарастырылған. Берілген жылуға сырықтың ұзару шамасының тәуелділігі зерттелген. Бұл үшін сырық шартты түрде бірнеше элементтерге бөлінеді, соның бір бөлігіне зерттеу жүргізілген. Жылу таралу өрісінің жылуға тәуелділігін анықтау үшін екінші ретті толық полиноммен аппроксимация жасаймыз және аппроксимациялық сплайн функция енгіземіз. Алдымен (n-1) элемент, сосын соңғы n элемент үшін толық жылу энергиясын өрнектейтін, жылу градиентінің көмегімен бір элемент үшін функционал өрнегі жазылады. Толық жылу энергиясы $J=\sum_{i=1}^{n} J_i$ формуласымен өрнектеледі. Толық жылу энергиясын минимизациялау арқылы түйінді нүктедегі жылудың мәнін анықтау үшін алгебралық теңдеулер жүйесін аламыз. Алынған мәндер арқылы, жылу ұлғаюдың есебінен элементтің ұзаруы есептеледі. Жұмыста T жылу, Δl_T ұзару, R(кГ) «созылу» күші, σ «созылу» кернеуінің өзара тәуелділігі келтірілген. Жылудың өсу есебінен аталған шамалардың пропорционалды өсетіндігі көрсетілген.

Кілт сөздер: жылудан ұлғаю, серпімділік модулі, сырық, сырықтың ұзаруы, жылукернеулік күйі, дискреттеу.

Б. Кенжегулов, Я. Култан, Д.Б. Алибиев, А.Ш. Кажикенова

Численное моделирование термомеханических процессов в жаропрочных сплавах

В статье приведено численное моделирование термических процессов в жаропрочных сплавах. Авторами разработан закон распределения температуры по длине физического тела, в качестве которого рассматривают стержень из сплава ЭИ-617. Кроме того, исследована зависимость величины удлинения стержня от заданной температуры. Для этого стержень условно поделен на несколько элементов, а затем исследование проводится на одном участке. Для определения температурной зависимости поле распределения температур аппроксимируется полным полиномом второй степени, а также вводятся аппроксимационные сплайн-функции. С помощью градиента температуры для одного элемента записывается выражение функционала, характеризующее полную тепловую энергию, сначала для (n-1)-го элемента, затем для последнего n-го элемента. Полная тепловая энергия выражена формулой $J=\sum_{i=1}^{n} J_i$.

Минимизируя полную тепловую энергию, получаем систему алгебраических уравнений для определения узловых значений температур. Применяя полученные значения, вычисляется удлинение элемента за счет теплового расширения. В работе приведена зависимость между температурой T, удлинением Δl_T, «растягивающей» силой R(кГ) и «растягивающим напряжением» σ. Показано, что с повышением температуры пропорционально увеличиваются и названные величины.

Ключевые слова: тепловое расширение, модуль упругости, стержень, удлинение, термонапряженное состояние, дискретизация.

References

1 Nozdrev, V.F. (1967). *Kurs termodinamiki [The course of thermodynamics]*. Moscow: Prosveshchenie [in Russian].

2 Segerlind, L. (1979). *Primenenie metoda konechnykh elementov [Applied Finite Element Analysis]*. Moscow: Mir [in Russian].

3 Kenzhegulov, B. (2009). Numerical solution of problem of thermo elasticity with provision for dependencies between the factor of heat expansion and temperature. *International journal of scientific articles. Science and technology, 5*, 3–7.

4 Kenzhegulov, B. (2009). Numeral modeling of heat mechanical condition of core of limited lengths made of heat resistant alloy ANV -300 at presence of heat exchange, partial heat insulation, local temperature and axial spraining power. *International journal of scientific articles. Science and technology, 5, 8–14*.

АСПАПТАР МЕН ЭКСПЕРИМЕНТ ТЕХНИКАСЫ
ПРИБОРЫ И МЕТОДЫ ЭКСПЕРИМЕНТА
INSTRUMENTS AND EXPERIMENTAL TECHNIQUES

DOI 10.31489/2020Ph2/108-118

UDC: 620.1.08 + 66–914.5

M.E. Guselnikov[1], Yu.V. Anishchenko[1], A.S. Gyngazov[2], A.K. Aimukhanov[3]

[1]Tomsk Polytechnic University,, Russia;
[2]Joint-stock company «Sibkabel», Tomsk, Russia;
[3]Ye.A. Buketov Karaganda State University, Kazakhstan
(E-mail: ajv@ tpu.ru)

Gas mixture composition control in fine organic synthesis

Fine organic synthesis includes a large number of stages. All its stages require determining the small quantities of impurities for initial and intermediate synthesis products. Fine organic synthesis is a complex process requiring automation. To automate the synthesis products' control device it is necessary to use the modern physico-chemical methods, which perform continuous measurements with high speed. This paper describes the hardware implementation of a device, based on infrared absorption analysis method. The absorption methods of substance composition analysis are based on the absorption of sounding radiation by the analysed component. The strength of the probing radiation passing through the mixture changes slightly at the small concentrations of the analysed component. Therefore, there is a problem of measuring small changes of a large signal. The absorption method of substance composition analysis can be used for analysis the composition of mixtures of gaseous organic substances. It enables to scan the optical frequency of the probe radiation by changing the angle of the interference filter. The proposed equipment allows determining the concentration of substances by overlapping their absorption spectra of infrared radiation.

Keywords: organic synthesis, analyzed gas, analysis of gas mixtures composition, infrared radiation (IR), spectrum of IR absorption coefficient, solid-state narrow-band interference optical filter, pyroelectric radiation receiver.

Introduction

Organic synthesis is a process of producing more complex organic substances from less complex organic or inorganic substances. People use the organic synthesis products extensively. Such products include: clothing, shoes, machine parts, toys, medicines, paints, dishes, etc.

There is basic and fine organic synthesis. Fine organic synthesis is the result of small-tonnage production of complex organic substances. Fine organic synthesis is based on a wide variety of chemical reactions, which are carried out by sophisticated equipment. Intermediate and by-products are formed at each stage of production. To improve the quality of complex production it is necessary to use the automatic control systems for production processes [1, 2].

Intermediate products of fine organic synthesis require fast and accurate control of their composition. These products may be solid, liquid or gaseous. The methods of analysis of solid and liquid composition enable the sampling of analyzed substance. These methods are well-studied and varied [3]. The methods of fast continuous analysis of gas mixtures composition are less diverse; therefore this work is devoted to their improvement.

Samples and Research Method

There are a lot of methods conducting the analysis of gas mixtures composition. Most of them have a high sensitivity to the non-measured components of the analyzed mixture, that is, they have a low selectivity of the measurement results. These methods include acoustic, ionization, diffusion, electrochemical methods as well as methods based on the thermal or ionization effects of the chemical reaction and changing the thermal conductivity of the analyzed mixture. These methods are effective in analyzing the mixture composition for more than two gases.

Fine organic synthesis often requires determining the composition of gas mixture, containing a large number of components. To solve this problem such methods as chromatography, mass spectroscopy and optical ones are used.

Chromatographic method of analysis of gas mixtures composition is based on separation the analyzed mixture's components due to effect of sorption. The separation of the gas mixture sample into components is carried out periodically in the chromatographic column. The disadvantages of this method include a low speed (it does not exceed two minutes), the necessity to use a carrier gas cylinder and to select a sorbent for each type of analyzed component.

Mass spectroscopy is based on separation of charged particles (usually ions) with different specific charges by magnetic field. This method uses pre-ionization of analyzed gas mixture. Complex, large and expensive equipment, including a vacuum pump must be used to apply this method.

Optical methods are based on the different abilities of the mixture components to interact with electromagnetic radiation of ultraviolet, visible and infrared (IR) wavelengths. Most gases do not interact with the visible wavelength range. Ultraviolet radiation mainly interacts with the atoms of gas molecules and it is used to determine the atomic composition of the analyzed mixture. To determine the molecular composition of gas mixtures, the most informative and universal methods are based on the interaction of the mixture components with infrared radiation.

There are several methods, which use the interaction of infrared radiation with gas molecules. They include the following:

1. Refractometric method based on the measurement of the refractive index of radiation. The measurement results of this method are characterized by low selectivity.
2. Methods based on laser scattering. They are mainly used for remote monitoring of atmospheric composition.
3. Methods based on the measurement of optical density, which are called absorption methods.

Each gas has its individual graph (spectrum) of IR absorption coefficient dependence from wavelength [4]. Therefore, absorption methods enable to determine selectively the quantity of components in the gas mixture. In the authors' view, absorption methods based on the measurement of IR absorption by a controlled component are quite universal and suitable for automation of thin organic synthesis.

The IR absorption method uses the characteristics of IR absorption spectra for different gases. The concentration of the controlled component of gas mixture is determined by the level of emission reduction that has passed through the analyzed mixture. Transmission the radiation with thickness l and frequency v by gas mixture is complied with the law of Buger-Lambert:

$$T_{\Gamma}(v) = \frac{I(v)}{I_0(v)} = \exp[-K(v)l] \tag{1}$$

$I_0(v)$ — the intensity of radiation before it passes the layer of the analyzed mixture; $I(v)$ — the intensity of radiation after it passes the layer of the analyzed mixture; $K(v)$ — gas mixture absorption coefficient for radiation with frequency v.

If the analyzed gas mixture contains L components, then according to Bayer's law, the absorption coefficient is described as:

$$K(v) = \sum_{j=1}^{L} C_j K_j(v) \tag{2}$$

$K_j(\nu)$ — radiation absorption coefficient for j component of the gas mixture; C_j — the concentration of the j component of the gas mixture.

The expressions (1) and (2) allow calculating the concentration of the j components, if the following conditions are met:

1. The selected probe radiation frequency (v_j) provides the ratio:

$$\max_{1\le i\le L, i\ne j} K_j \Big/ K_i$$

Ideally, this condition means that only one j component of gas mixture absorbs the radiation at a frequency v_j.

2. The radiation absorption coefficient by the j component of gas mixture $K_j(v_j)$ at the frequency v_j is known.

3. The frequency v_j of radiation transmission by analyzed gas mixture is measured.

To measure the radiation transmission T_Γ (v_j) by the gas mixture it is necessary to use the source of the probe radiation, the cuvette of the analyzed gas mixture's sample and the radiation receiver. The required frequency v_j of the probe radiation can be provided by the source of radiation with required frequency; by the radiation receiver, which is sensitive to radiation of a certain wavelength; by an additional spectral element, which enable to isolate the radiation of the required frequency.

The functions of infrared radiation transmission T_Γ (v_j) can be described as a set of radiation absorption lines. The radiation absorption line for j gas with the center at the frequency v_j is characterized by the intensity of the absorption line S_{ji} of the j gas at the spectral interval i, the width δ_{ji} under normal conditions, the distance d_{ji} to the next line. The spectrum of radiation absorption by gas in the IR area of the spectrum consists of a set of closely located absorption lines. This set of lines is called a radiation absorption band.

The functions of radiation transmission by gases can be calculated by using the radiation absorption of specific frequency of each line of the spectrum. It is also possible to calculate the absorption function using the formulas of spectra models, or find it experimentally. The method of spectrum models is the most versatile; it has acceptable complexity of gas concentrations' calculations. This method includes the modeling of gas spectra with a set of absorption lines, suggesting a certain law of their location, intensity and width.

If the intensity of the absorption lines are described by exponential statistical law of distribution, and the distance between the lines and their width are described by uniform law of distribution, the IR absorption function for the mixture of L gases is calculated by the expression [5]:

$$T_{\Gamma_i} = \exp \frac{-l\sum_{j=1}^{L} S_{ji}P_j \Big/ d_{ji}}{\sqrt{1 + l\sum_{j=1}^{L}\left(S_{ji}P_j \Big/ d_{ji}\right) \Big/ \pi\sum_{j=1}^{L}\sum_{k=1}^{L}\left(\delta_{ji}P_k\sigma_{jki} \Big/ d_{ji}\right)}} \qquad (3)$$

P_j — the concentration of the j gas in partial pressure units; σ_{jki} — the relative effectiveness of the optical collisions of j and k gas molecules; it characterizes the broadening of the absorption lines.

The expression (3) shows that the parameters of the absorption lines of infrared radiation depend on the composition of the gas mixture. In addition, the center of the absorption line v_j, its intensity S_{ji}, and width δ_{ji} depend on the temperature and pressure of the gas mixture. In measurements, if the frequency range is much more than the distance between the lines, the parameters of the radiation absorption band are more stable [5]. The allocation of such a frequency range can be provided by solid-state narrow-band interference optical filters [6].

It is difficult to calculate the concentrations P_j by using a well-known values of $T_{\Gamma i}$ in expression (3), because there is no effective mathematical methods enable to solve such systems of nonlinear equations and the obtained results may vary. Therefore, this expression must be simplified.

The research [5] shows that if the thickness of analyzed gas mixture is decreased and the components concentration P_j is small, the dependence of the absorption function on the components concentration can be described by linear absorption law:

$$T_{\Gamma_i} = 1 - l\sum_{j=1}^{L}\left(S_{ji}P_j \Big/ d_{ji}\right) \qquad (4)$$

The functional diagram of the simplest device for measuring the concentration P_j of analyzed gas mixture is given in Fig. 1.

Figure 1. The functional diagram of the simplest device for measuring the gas concentration

In this illustration, the blocks have the following functions:
1 — broadband infrared source;
2 — solid-state narrow-band interference optical filter;
3 — cuvette with analyzed gas mixture;
4 — IR-to-electrical converter;
5 — electronic circuit for signal processing and displaying measurement results

The simplest scheme has a number of significant disadvantages. Firstly, non-measured gases in the analyzed mixture influence the component's concentration measurement only if they do not absorb IR radiation in the transparency range of the narrow-band interference optical filter. However, this condition is not always possible. Secondly, minimum concentration P_j of the analyzed component forms the maximum output voltage of the IR emitter to the electrical signal. For linear law of radiation absorption, described by expression (4), this means the necessity to measure small changes of a high signal.

If the source of broadband infrared radiation is made as a spiral, which is placed in the focus of parabolic mirror, then the thermal balance equation of the scheme (Fig. 1) for the emitter's spiral is:

$$q_{el} = q'_{tc} + q_{tc} + q_{con} + q_{rad} \quad (5)$$

q_{el} — the energy, supplied to radiation source; q_{rad} — the energy, which creates infrared radiation; q_{tc} — the energy, which heats the device body by thermal conductivity in air; q'_{tc} — thermal conductivity through the current-carrying contacts; q_{con} — convective heat exchange.

The analysis of expression (5) shows that the power of probe radiation depends on the details of the scheme (Fig. 1) significantly.

The ambient temperature increase, the power of IR radiation also increases. The step value is approximately (0.3 — 0.4) * 10–^{3} watt*Kelvin^{-1}; it is 31 % in the range from -20 ˚C to +30 ˚C. The degree of deviation from linear dependence is up to 4.6 %. For these measurement errors, the linear absorption law described by expression (4) cannot be applied. The measurement of small concentrations of analyzed components is not achievable.

To reduce the dependence of the infrared radiation power on the ambient temperature by the minimum threshold of the determined concentration, the scheme (Fig. 1) is complemented by additional (reference) channel. This reference channel contains a cuvette. It is filled with a reference gas mixture, which includes the identical analyzed gas mixture, but without analyzed component. The analytical signal is the difference in the IR flow that passed through the main and additional cuvettes. These cuvettes are filled with analyzed and reference gas mixtures. To calculate the difference of IR flows, it is necessary to put them one after another to the converter of IR signal to electrical signal. The order of IR flow is provided by a mechanical modulator.

A typical scheme of gas mixture component concentration measurement with a mechanical modulator of probe radiation, main and additional reference measuring channels is shown on Fig. 2.

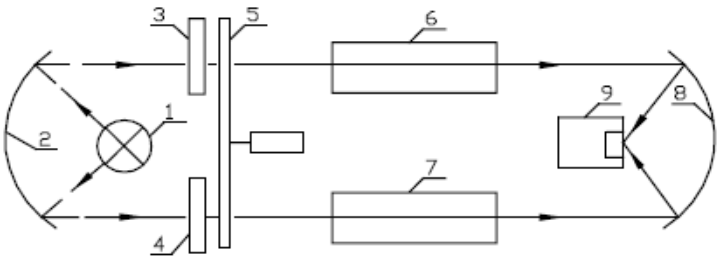

(1 — source of radiation; 2 — parabolic radiation flow detector; 3 and 4 — solid-state narrow-band interference optical filters; 5 — mechanical modulator; 6 — working cuvette; 7 — reference cuvette; 8 — focusing system; 9 — converter of IR signal into electrical signal).

Figure 2. Differential symmetric scheme of the device, which implements the absorption spectral method for measuring the gases concentration

In this scheme, the pyroelectric radiation receiver is used as converter of IR signal into electrical signal [7]. This type of converter, for example, the IRA-E410S1, is characterized by high sensitivity and a wide (from 2 to 20 microns) wavelength range of perceived IR radiation. The receiver only responds to changes in IR radiation, therefore it is necessary to use the probe radiation modulator. The electrical signal from the receiver output is AC signal. This allows applying the simultaneous detection for signal processing to further reduce measurement errors.

The scheme presented in Fig. 2 has a number of disadvantages. Firstly, the additional reference channel complicates the scheme of the measurement. Each additional element has changing over time parameters and is the source of additional error of measurement results. Secondly, the additional reference cuvette *7* cannot be completely identical to the working cuvette *6* in parameters and external effects. The reference cuvette *7* must be well sealed while the analyzed gas mixture is passed through the working cuvette. Therefore, it is difficult to achieve the same temperature of these elements of the measurement device. In addition, the walls and windows of working cuvette are more vulnerable to contamination. All these processes create a difference in IR flows on the outputs of cuvettes *6* and *7* when they do not have a measured component of the analyzed mixture. As a result, the minimum detected concentration of the analyzed gas is increased. Thirdly, the use of a mechanical modulator causes a number of specific interference. For example, interference caused by the mechanical luff of the modulator parts.

Results and Discussion

This article proposes a measuring scheme without above-mentioned disadvantages. The main idea of the scheme includes the modulation the optical frequency of probe IR. To implement the absorption spectral method for gas concentration measurement, the solid-state narrowband interference optical filters are used. Such filters determine the required spectral interval of the probe radiation. The solid state narrowband interference optical filters are designed as a set of transparent films, which are placed at a transparent for IR radiation substrate. These films alternate large and small values of refractive parameters [8]. The optical frequency of the emitted radiation depends on the thickness of films placed at the substrate. When the radiation decrease's angle on the filter is changed, its spectral characteristics (the dependence of the transmission T on the wavelength λ) also are changed. This dependence is shown on Fig. 3 [8].

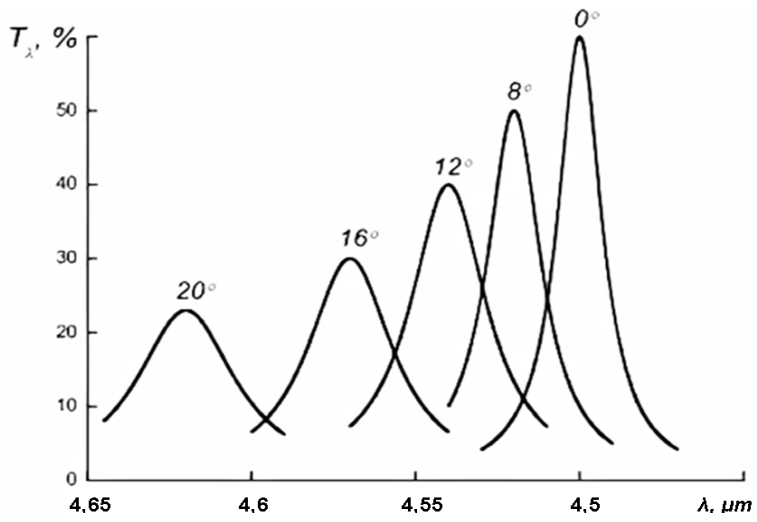

Figure 3. The dependence of the filter's spectral light transmission on the radiation decrease's angle

The work of the scheme will be discussed by measuring the carbon monoxide concentration in gas mixture. This gas is widely used in organic synthesis.

It is proposed to form a beam of parallel rays of a wide-range IR. This beam of rays is passed through a narrow-band interference optical filter at an angle that changes according to the sinusoidal law. For example, using a filter similar to shown on Fig.3 and changing the angle from 0 to 16˚, the IR wavelength, which corresponds to the maximum filter transmission, will vary from 4.5 to 4.67 μm.

Fig. 4 shows the dependence of radiation absorption by carbon monoxide on the IR wavelength. The figure presents that the IR of 4.5 μm is weakly absorbed by carbon monoxide. The maximum of IR absorption corresponds to a wavelength of 4.67 μm.

It is proposed to pass IR flow, modulated by filter on optical frequency, through the analyzed gas mixture. The intensity of the passed radiation through the gas mixture is monitored by the IR receiver. If carbon monoxide is not present in the analyzed gas mixture, there should be no output signal of the receiver. The appearance of carbon monoxide in the analyzed gas mixture causes output signal of the receiver. The amplitude of this signal is proportional to low concentrations of carbon monoxide.

The Fig. 5 presents the implementation scheme of the absorption method of gas mixture component's concentration measurement by modulating the optical frequency of IR.

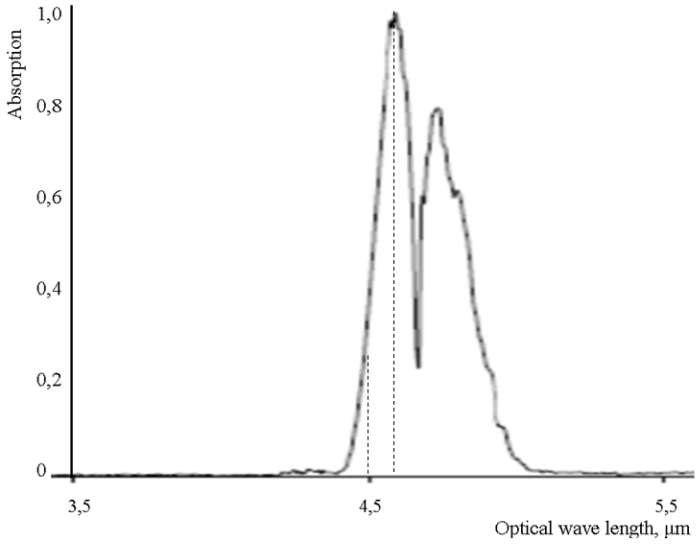

Figure 4. The dependence of radiation absorption by carbon monoxide on the frequency of infrared radiation

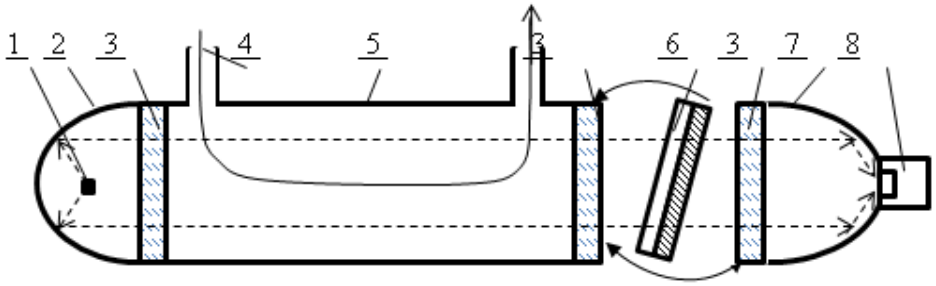

Figure 5. Implementation scheme of the absorption method of gas mixture component's concentration measurement by modulating the optical frequency of IR

The scheme contains the following elements: a broadband IR source (1), made as a spiral placed in the focus of a parabolic mirror (2); windows made of fluorite CaF_2, which is transparent for IR material (3); cuvette (5) with analyzed gas mixture (4); solid-state narrow-band interference optical filter (6) with periodically changing installation angle; parabolic mirror (7), focusing radiation on the radiation receiver (8).

The used in this scheme pyroelectric radiation receiver IRA-E410S1 [7] is sensitive only to the signal, which is variable in time. The examination of this receiver shows that it has the highest sensitivity if the IR flow is changed in time with a frequency of about 7 Hz. Therefore, the mechanical drive for changing the angle of interference optical filter installation operates at a frequency of 7 Hz.

A study of scheme (Fig. 5) showed that if there is no carbon monoxide in the analyzed mixture (4), there is an output signal of the receiver (8). This can be explained by the fact that when the radiation decrease's angle to the narrow-band interference optical filter is deviated from 90°, the frequency of passed infrared radiation is decreased, the coefficient of light transmission of the filter is decreased and the width of the spectral range of the passed radiation is increased. Therefore, the changing the angle of the filter may

cause increase as well as decrease the intensity of radiation passed through the IR filter. Modulation radiation appears. This phenomenon reduces the effectiveness of proposed method significantly.

To reduce the dependence of the intensity of the radiation passing through the IR filter on the installation angle of this filter, a compensating device is proposed [8–10]. It is a disk connected to the IR filter at an angle φ. This angle is equal to the maximum angle of the IR filter installation and can vary from -φ to +φ periodically. The disk of compensating device contains a hole; its diameter is equal to the beam diameter of the infrared radiation filter. A scheme of connection the compensating device and the IR filter is presented at Figure 6. The IR filter (1) is placed in the mandrel (2), which makes rotational — oscillating movements at an angle of φ. The IR filter is attached by a nut (3). This nut is fitted with a compensating device (4). It is adjusted by rotating in relation to the IR filter. The adjusted compensation device is attached by a nut (5). Testing the scheme presented at figure 5, it was possible to reduce the modulation radiation by 16.5 times.

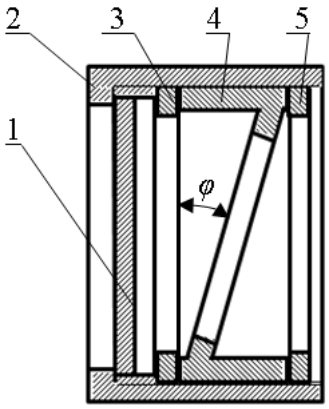

Figure 6. Connection the compensating device and the IR filter

Further analysis the influence of ambient temperature's change on output signal of the receiver (8) has revealed the effect of mirror reflection by the reverse side of the IR filter from the surface of the parabolic mirror on the surface of the receiver. To reduce this effect, the receiver window is replaced by a band interference filter that passes the radiation from 4.3 to 5.4 μm. These changes are presented in Fig. 7.

The final implementation scheme of the absorption method for gas concentration measurement in gas mixture by modulating the optical frequency of IR is shown in Fig. 7.

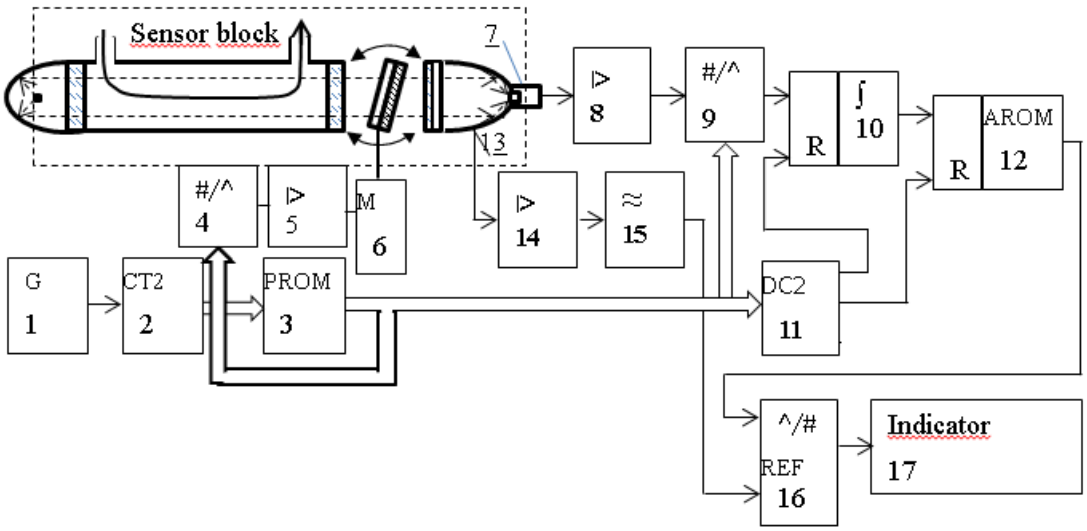

Figure 7. Functional implementation scheme of the absorption method for gas concentration measurement in gas mixture by modulating the optical frequency of IR

The proposed scheme has several blocks. The generator (1) generates pulses that are delivered to a binary counter (2). The binary code from the counter goes to the address inputs of the programmable read-only memory device (3). This device contains the sinusoidal function codes. These codes are converted to ana-

logue signal by a digital analogue converter (4), amplified by the amplifier (5) and change the installation angle of the interference IR filter according to the sinusoidal law by electromechanical drive (6).

The variable component of the analyzed gas mixture passed through the radiation is perceived by the receiver (7). The output signal from the receiver is amplified by the amplifier (8). Then to determine the amplitude of the variable signal accurately, synchronous detection operation is performed. The signal is multiplied by a sinusoidal function using a multiplying digital-to-analogue converter (9). The output signal of the converter is integrated by the integrated amplifier circuit (10) for 8 periods and is stored by the sample and storage device of the analogue signal (12). The decipher (11) carries out the synchronization of the reset commands of the integrated amplifier and the signal memory. The output analogue signal of the sampling and storage device (12) is proportional to the measured concentration of carbon oxide [11–13].

The constant component of the radiation, passed through the analyzed gas mixture, is perceived by the receiver (13). The compensated thermal elements TK-1 × 1.5 made on antimony-bismuth junctures are used as a receiver. The output signal of the receiver (13) is amplified by the amplifier (14) and goes to the low-pass filter (15).

To reduce the influence of cuvette window contamination and radiation intensity I_0 before passing through the gas mixture on the measurement results it is necessary to apply a signal division operation from the sample and storage device output (12) to the low pass filter output (15) [14–16]. The division operation is performed by analogue-digital converter (16). The results are displayed digitally by an indicator (17).

The dependence of the output signal U on time t at low concentrations C of the measured gas is described by the expression:

$$U(t) = K_R I T_{OS} \left[k\tau_m(\varphi(t))\delta_{0.5}(\varphi(t)) - C\int_0^\infty lK(\gamma)\tau_F(\varphi(t))d\gamma \right] = K_R I T_{OS}\left[A(t) - CB(t)\right] \quad (6)$$

K_R — IR conversion coefficient of receiver; I_0 — radiation intensity before passing through gas mixture; T_{OS} — radiation transmission function by optical system; k — coefficient of signal's variable component attenuation by compensation device (Figure 6); τ_m, φ, $\delta_{0.5}$ — maximum transmission, angle of installation and half width of IR filter; $K(\gamma)$ — the spectral characteristic of analyzed gas; $\tau_F(\gamma)$ — the spectral characteristic of the IR filter; γ — the optical frequency [17].

The test results of the scheme, implementing the absorption method of carbon monoxide concentration measurement in the air by modulating the optical frequency of IR radiation, are presented in Table 1.

Table 1

Test results of proposed method

Concentration of carbon oxide, ppm		Error $\Delta = 100(C_{CH} - C_A) / C_{CH}$, %
Absorption method, C_A	Chemical method, C_{CH}	
1 8 7	1 9 8	5 . 5
9 4	1 0 2	7 . 8
4 5	5 6	1 9 . 6
1 2	2 3	4 7 . 8

The table 1 shows that obtained results revealed satisfactory precision of measurement method.

Conclusion

The obtained results showed that the proposed equipment of implementation the absorption method for gas concentration measurement in gas mixture by modulating the optical frequency of IR reveals satisfactory precision with recognized chemical measuring methods. At the same time, the proposed equipment provides faster measurement time, which does not exceed one second. Therefore, the proposed equipment for gas components control is recommended to use in thin organic synthesis.

Acknowledgments

The research is carried out at Tomsk Polytechnic University within the framework of Tomsk Polytechnic University Competitiveness Enhancement Program.

References

1 Чупахин О.Н. Актуальные проблемы органического синтеза и анализа / отв. ред. акад. РАН О.Н. Чупахин, к.х.н. А.М. Дёмин // Екатеринбург: УрО РАН; Изд-во «АМБ», 2012. — 238 с.

2 Ogunnaike B., Ray W.H. Process Dynamics, Modeling and Control / B. Ogunnaike, W.H. Ray. — New York, Oxford: Oxford University Press, 1994. — 1260 p.

3 Jaimez J. Application of the assay of aflatoxins by liquid chromatography with fluorescence detection in food analysis / J. Jaimez, C.A. Fente, B.I. Vazquez, C.M. Franco, A. Cepeda, G. Mahuzier, P. Prognon // The Journal of Chromatography, B. — 2000. — Vol. 882. — P. 1–10.

4 Rothman L.S. The HITRAN 2012 molecular spectroscopic database / L.S. Rothman, I.E. Gordon, Y. Babikov, A. Barbe, D. Chris Benner, P.F. Bernath, M. Birk, L. Bizzocchi , V. Boudon, L.R. Brown, A. Campargue, K. Chance, E.A. Cohen, L.H. Coudert, V.M. Devi, B.J. Drouin, A. Fayt, J.M. Flaud, R.R. Gamache, J.J. Harrison, J.M. Hartmann, C. Hill, J.T. Hodges, D. Jacquemart, A. Jolly, J. Lamouroux, R.J. Le Roy, G. Li, D.A. Long, O.M. Lyulin, C.J. Mackie, S.T. Massie, S. Mikhailenko, H.S.P. Müller, O.V. Naumenko, A.V. Nikitin, J. Orpha, V. Perevalov, A. Perrin, E.R. Polovtseva, C. Richard, M.A.H. Smith, E. Starikova, K. Sung, S. Tashkun, J. Tennyson, G.C. Toon, V.G. Tyuterev, G. Wagner // The Journal of Quantitative Spectroscopy and Radiative Transfer. — 2013. — Vol. 130. — P. 4–50.

5 Бреслер П.И. Закономерности поглощения инфракрасной радиации в тонких слоях некоторых газов / П.И. Бреслер // Оптика и спектроскопия. — 1959. — № 7(5). — С. 608–620.

6 Macleod Angus H. Thin Film / H. Macleod Angus // Optical Filters (Series: Series in Optics and Optoelectronics), CRC Press Taylor & Francis Group. — 2010. — 808 p.

7 Каталог Murata [Электронный ресурс]. — Режим доступа: http:// www.murata.com (дата обращения 1.11.2019).

8 Ершов А.В. Многослойные оптические покрытия. Проектирование, материалы, особенности технологии получения методом электроннолучевого испарения: учеб.-метод. материал по программе повышения квалификации «Новые материалы электроники и оптоэлектроники для информационно-телекомуникационных систем» / А.В. Ершов, А.И. Машин // Нижний Новгород, 2006. — 99 с.

9 Патент Оптический газоанализатор. RU 2002 122 567. Заявка: 2002122567/28, 2002.08.20. Заявители: Открытое акционерное общество «Томский научно-исследовательский институт нефти и газа Восточной нефтяной компании». Авторы: А.А. Каверин, М.Э. Гусельников. — 2004. — 20 марта.

10 Luchnikov P.A. Deformable Polymer Dielectric Films in Phase Light Modulators / P.A. Luchnikov, V.V. Vetrova, N.P. Zubkov, O.A. Surzhikova, N.I. Chernova // IOP Conf. Ser.: Mater. Sci. Eng. — 2017. — 189 p. DOI: 10.1088/1757–899X/189/1/012027.

11 Luchnikov P.A. Defect formation in fluoropolymer films at their condensation from a gas phase / P.A. Luchnikov // IOP Conf. Ser.: Mater. Sci. Eng. — 2018. — 289. DOI: 10.1088/1757–899X/289/1/012037.

12 Antropov A.P. Composite material for optical oxygen sensor / A.P. Antropov, A.V. Ragutkin, P.V. Melnikov, P.A. Luchnikov, N.K. Zaitsev // IOP Conf. Ser.: Mater. Sci. Eng. — 2018. — 289 p.. doi: 10.1088/1757–899X/289/1/012031

13 Surzhikov, A. A thermoanalysis of phase transformations and linear shrinkage kinetics of ceramics made from ultrafine plasmochemical $ZrO_2(Y)$-Al_2O_3 powders / A. Surzhikov , T. Frangulyan, S. Ghyngazov // Journal of Thermal Analysis and Calorimetry. — 2014. — Vol. 115(2). — P. 1439–1445. DOI: 10.1007/s10973–013–3455-y

14 Toleuov G. Experimental study of free turbulent jet / G. Toleuov, M.S. Isataev, Zh.K. Seidulla, A. Dosanova, Zh. Tolen // Bulletin of the University of Karaganda-Physics. — 2019. — Vol. 1(93) — P. 79–86. DOI: 10.31489/2019Ph1/44–49

15 Ivchenko V.A. Development of Amorphized States in Subsurface Metal Regions under Radiation Exposure / V.A. Ivchenko // Technical Physics Letters. — 2013. — Vol. 39(4). — P. 357–359.

16 Barquist C.S. Low temperature transport measurementson atomically smooth metallic and oxygen deficient strontium titanate / C.S. Barquist, I.H. Kwak, J. Bauer, T. Edmonds, A. Biswas, Y. Lee // Journal of Physics: Conference Series. — 2014. — Vol. 568. — P. 1–5.

17 Analytical evaluation of the Uehling potential using binomial expansion theorems / E. Copuroglu, T. Mehmetoglu // Bulletin of the University of Karaganda-Physics. — 2019. — Vol. 3(95). — P. 17–21. DOI: 10.31489/2019Ph3/17–21.

М.Е. Гусельников, Ю.В. Анищенко, А.С. Гынгазов, А.К. Аймуханов

Жұқа органикалық синтезде газтәрізді компоненттердің құрамын бақылау

Жұқа органикалық синтез көптеген кезеңдерді қамтиды. Ол әр кезеңде бастапқы және аралық синтез өнімдерінің қоспаларының аз мөлшерін анықтауды талап етеді. Жұқа органикалық синтез — бұл автоматтандыруды қажет ететін күрделі процесс. Синтез өнімдерінің құрамын бақылау құрылғыларын автоматтандыру жоғары жылдамдықпен үздіксіз өлшеуді жүргізуге мүмкіндік беретін заманауи физика-химиялық әдістерді қолдануды қажет етеді. Газтәрізді органикалық заттардың күрделі қоспаларының құрамын инфрақызыл сіңіруді талдау әдісін қолданатын техникалық жабдықты аппараттық түрде енгізу ұсынылған. Заттардың құрамын талдауға арналған сіңіру әдістері зерттелетін компонент бойынша зонд сәулесінің сіңуіне негізделген. Зерттелетін қоспа арқылы берілетін зонд сәулесінің қуаты, зерттелетін компоненттің төмен концентрациясында аз мөлшерде өзгереді. Сондықтан үлкен сигналдағы кішкентай өзгерістерді өлшеу кезінде мәселе туындайды. Адсорбциялық талдау әдістерін құрамында органикалық заттары бар газ қоспаларының құрамын талдау үшін қолдануға болады. Әдістің ерекшелігі — зонд сәулесінің оптикалық жиілігін интерференциялық фильтрдің бұрышын өзгерту арқылы сканерлеу. Ұсынылған жабдық сізге

инфрақызыл сәулеленудің жұтылу спектрлерін қабаттастыру арқылы заттардың концентрациясын анықтауға мүмкіндік береді.

Кілт сөздер: органикалық синтез, талданған үлгі, газ қоспаларының құрамын талдау, инфрақызыл сәуле, инфрақызыл сәулеленудің жұтылу коэффициентінің спектрі, қатты денелі тар диапазондағы кедергі оптикалық сүзгі, пироэлектрлік сәулелену детекторы.

М.Э. Гусельников, Ю.В. Анищенко, А.С. Гынгазов, А.К. Аймуханов

Контроль состава газообразных компонентов при тонком органическом синтезе

Тонкий органический синтез содержит большое число стадий. Он требует на каждой стадии определения содержания малых количеств примесей исходных и промежуточных продуктов синтеза. Тонкий органический синтез является сложным технологическим процессом, требующим автоматизации. Автоматизация устройств контроля состава продуктов синтеза реализуется путем применения современных физико-химических методов, позволяющих проводить непрерывные измерения с высоким быстродействием. Авторами предложено аппаратурное распределение технических средств, реализующих метод инфракрасного абсорбционного анализа состава сложных смесей газообразных органических веществ. Абсорбционные методы анализа состава веществ основаны на поглощении зондирующего излучения анализируемым компонентом. Мощность зондирующего излучения, прошедшего через анализируемую смесь, при малых концентрациях анализируемого компонента изменяется на незначительную величину. Поэтому возникает задача измерения малых изменений большого сигнала. Адсорбционные методы анализа могут использоваться для анализа состава газовых смесей, содержащих органические вещества. Особенностью метода является сканирование оптической частоты зондирующего излучения путем изменения угла установки интерференционного фильтра. Предложенная аппаратура позволяет определять концентрации веществ при перекрывании их спектров поглощения инфракрасного излучения.

Ключевые слова: органический синтез, анализируемая проба, анализ состава газовых смесей, инфракрасное излучение, спектр коэффициента поглощения ИК излучения, твердотельный узкополосный интерференционный оптический фильтр, пироэлектрический приемник излучения.

References

1 Chupakhin, O.N., & Dyomin, A.M. (2012). *Aktualnye problemy orhanicheskoho sinteza i analiza [Current problems of organic synthesis and analysis]*. Ekaterinburg: URO RAS; Izdatelstvo «AMB» [in Russian].

2 Ogunnaike, B., & Ray, W.H. (1994). P*rocess Dynamics, Modeling and Control.* New York, Oxford: Oxford University Press.

3 Jaimez, J., Fente, C.A., Vazquez, B.I., Franco, C.M., Cepeda, A., Mahuzier, G., & Prognon P. (2000). Application of the assay of aflatoxins by liquid chromatography with fluorescence detection in food analysis. *The Journal of Chromatography,* B, 882, 1–10.

4 Rothman, L.S, Gordon, I.E., Babikov, Y., Barbe, A., Chris Benner, D., Bernath, P.F., Birk, M., Bizzocchi, L., Boudon, V., Brown, L.R., Campargue, A., Chance, K., Cohen, E.A., Coudert, L.H., Devi, V.M., Drouin, B.J., Fayt, A., Flaud, J.M., Gamache, R.R., Harrison J.J., Hartmann J. -M., Hill C., Hodges J.T., Jacquemart D., Jolly A., Lamouroux J., Le Roy, R.J., Li, G., Long, D.A, Lyulin, O.M., Mackie, C.J., Massie, S.T., Mikhailenko, S., Müller, H.S.P., Naumenko, O.V., Nikitin, A.V., Orpha, J., Perevalov, V., Perrin, A., Polovtseva, E.R., Richard, C., Smith, M.A.H., Starikova, E., Sung, K., Tashkun, S., Tennyson, J., Toon, G.C., Tyuterev, V.G., & Wagner G. (2013). The HITRAN 2012 molecular spectroscopic database. *The Journal of Quantitative Spectroscopy and Radiative Transfer*, 130, 4–50.

5 Bresler, P.I. (1959). Zakonomernosti pohloshcheniia infrakrasnoi radiatsii v tonkikh sloiakh nekotorykh hazov [Patterns of IR absorption in thin layers of some gases]. *Optics and spectroscopy, 7, 5,* 608–620 [in Russian].

6 Macleod Angus, H. (2010). Thin Film. Optical Filters (Series: Series in Optics and Optoelectronics). *CRC Press Taylor & Francis Group*, 808.

7 *Murata.com.* Information on Retrieved from http://www.murata.com [in Russian].

8 Ershov, A.V., & Mashin, A.I. (2006). Mnohosloinye opticheskie pokrytiia. Proektirovanie, materialy, osobennosti tekhnolohii polucheniia metodom elektronnoluchevoho ispareniia [Multi-layer optical coatings. Design, materials, features of the obtaining technology by electron-beam evaporation]. *Educational and methodical material on the program of advanced training «New materials of electronics and optoelectronics for information and telecommunications systems».* Nizhni Novhorod [in Russian].

9 Kaverin, A., & Guselnikov, M.E. (2002). *Opticheskii hazoanalizator [Patent Optical gas analyzer]* [in Russian].

10 Luchnikov, P.A., Vetrova, V.V., Zubkov, N.P., Surzhikova, O.A., & Chernova N.I. (2017). Deformable Polymer Dielectric Films in Phase Light Modulators. *IOP Conf. Ser.: Mater. Sci. Eng.*,189, DOI: 10.1088/1757–899X/189/1/012027.

11 Luchnikov, P.A. (2018). Defect formation in fluoropolymer films at their condensation from a gas phase. *IOP Conf. Ser.: Mater. Sci. Eng*. 289, DOI: 10.1088/1757–899X/289/1/012037.

12 Antropov, A.P., Ragutkin, A.V., Melnikov, P.V., Luchnikov, P.A., & Zaitsev N.K. (2018). Composite material for optical oxygen sensor. *IOP Conf. Ser.: Mater. Sci. Eng*., 289, DOI: 10.1088/1757–899X/289/1/012031

13 Surzhikov, A., Frangulyan, T., & Ghyngazov S. (2014). A thermoanalysis of phase transformations and linear shrinkage kinetics of ceramics made from ultrafine plasmochemical ZrO_2(Y)-Al_2O_3 powders. J*ournal of Thermal Analysis and Calorimetry*, 115(2), 1439–1445, DOI: 10.1007/s10973–013–3455-y

14 Toleuov, G., Isataev, M.S., Seidulla, Zh.K., Dosanova, A., & Tolen Zh. (2019). Experimental study of free turbulent jet. *Bulletin of the University of Karaganda-Physics, 1(93),* 79–86, DOI: 10.31489/2019Ph1/79–86

15 Ivchenko, V.A. (2013). Development of Amorphized States in Subsurface Metal Regions under Radiation Exposure. *Technical Physics Letters, 39(4),* 357–359.

16 Barquist, C.S., Kwak, I.H., Bauer, J., Edmonds, T., Biswas, A., & Lee, Y. (2014). Low temperature transport measurementson atomically smooth metallic and oxygen deficient strontium titanate. *Journal of Physics: Conference Series,* 568, 1–5, DOI: 10.1088/1742–6596/568/5/052004

17 Copuroglu, E., & Mehmetoglu, T. (2019). Analytical evaluation of the Uehling potential using binomial expansion theorems. *Bulletin of the University of Karaganda-Physics, 3(95),* 17–21, DOI: 10.31489/2019Ph3/17–21.

DOI 10.31489/2020Ph2/119-126

UDC 621.867.42

V. Hud[1], I. Hevko[1], O. Lyashuk[1], O. Hevko[1], M. Sokol[2], I. Shust[1]

[1]*Ternopil Ivan Puluj National Technical University, Ukraine;*
[2]*I.Ya. Gorbachevskyy Ternopil National Medical University, Ukraine*
(E-mail: vic_g@ukr.net)

Research of resonance vibrations of the system «Telescopic screw — bulk medium» caused by torsional vibrations

The article outlines the relevance of using the principle of telescopy in the process of creation screw conveyors, which nowadays are folded to obtain significant lengths, which makes their designs expensive and structurally unreasonably complicated. It has been shown an experimental equipment, which provides measurement results of the research process in a wide range with high accuracy in an automated control mode with the necessary data capture. Based on the constructed mathematical model, the dependences of the angular perturbation velocity on the physicomechanical and geometric parameters of the «telescopic screw — bulk medium» system have been obtained. Because of analytical relations describing the laws of variation of characteristic parameters for its oscillation resonance case have been received. It has been proved that for resonant oscillations, when there are significant angular velocities of rotation, the natural frequency of the bending oscillations is smaller and at the same time the amplitude of the transition through the resonance is smaller. The results of the amplitude of the transverse oscillations of the system for different values of the angular velocity of rotation in time during the transition through the internal resonance, which largely depends on the physicomechanical and geometric characteristics of the motion of the medium, have been presented.

Keywords: conveyors, mechanical systems, transporting-separating system, dynamic modeling, amplitude, resonance, telescopic screw, bulk medium, angular velocity of rotation, torsional vibrations.

Introduction

Screw conveyors are widely used in various sectors of the economy as independent mechanisms, and as part of various mechanical systems. They are often used as elements of agricultural machinery when harvesting for transshipment of various cargoes in the field. Screw conveyors as part of universal units for loading seeders, hoppers, reloaders and combine harvesters are usually complex and involve decomposition-folding using hydraulic or pneumatic equipment, which makes their designs too complicated and expensive.

Mainly for transportation of such cargoes rigid auger conveyors installed at different angles to the horizon are used, as well as flexible screw conveyors, the determination of the parameters and modes of which are described in the works [1–4].

In article [5–9] dependence in time of the amplitude and frequency of nonlinear vibrations of the feeder horizontal working body at its various geometric dimensions, the angular velocity of the working body rotation, the grain mixture mass per unit length, and the speed of its transportation

The works of [10–15] provide research findings on flow patterns of bulk materials depending on constructional and kinematic characteristics of screw operating tools, bunker type and solid particles, as well as frictional forces. Findings of mentioned researches shows on improved characteristics of screw conveyors during transportation of bulk materials.

Despite the large number of scientific works devoted to the development and study of the peculiarities of the work of screw conveyors, there is a wide range of unexplored issues related to their structural and functional characteristics. Therefore, telescopic screw conveyors have been developed to improve the structures and provide the necessary trajectory of material loading with screw conveyors. These telescopic screw conveyors will improve productivity on tracks with variable length and direction of overload, as well as performing related technological operations with transported raw materials [16]. According to the experimental and separate theoretical studies of the dynamics of the working bodies of screw conveyors [17–18], the movement of the manufacturing medium along the previous one affects the quantitative, and in some cases, the qualitative characteristics of their oscillations. However, due to the large angular rotational speeds of the screw in telescopic screw conveyors, asymmetry of the telescopic screw and external perturbations often cause oscillations in significant dynamic loads on the screw, especially in resonant cases. The study of dy-

namic loads arising in the auger of the telescopic conveyor will allow you to find the optimal mode of operation. These modes minimize dynamic loads and increase the service life of these conveyors.

Material and method

In order to study the characteristics of telescopic screw conveyors and based on our patent search and analysis of scientific literature, we synthesized telescopic screw conveyors [19–21] based on which a stand was designed and manufactured to study the transportation of bulk cargo (Fig. 1) [22]. To perform a research the following actions has been done in such order: load the hopper 14 with loose material, which from it enters the casing 3 on the auger 2, by which it is transported to the casing 6 to the auger 5, and then the bulk material through the discharge pipe 9 falls into the measuring vessel. The rotary movement of the auger 2 obtains through the belt drive 16 from the electrodrive 15, which is controlled from the PC 18 with the fixation of all the necessary data in a tabular or graphical form according to the developed methodology of experimental research. From the auger 2 rotary motion is transferred to the auger 5 due to the friction that occurs between the walls of the augers, which allows to carry out the process of overloading the bulk material. In this case, the performance of the telescopic screw conveyor at different casing fill rates and screw speeds is determined in a semi-automatic mode. The power characteristics can be determined by smooth and sudden start-up, reversal and simulation of various loads in an automated mode using a frequency converter and a personal computer.

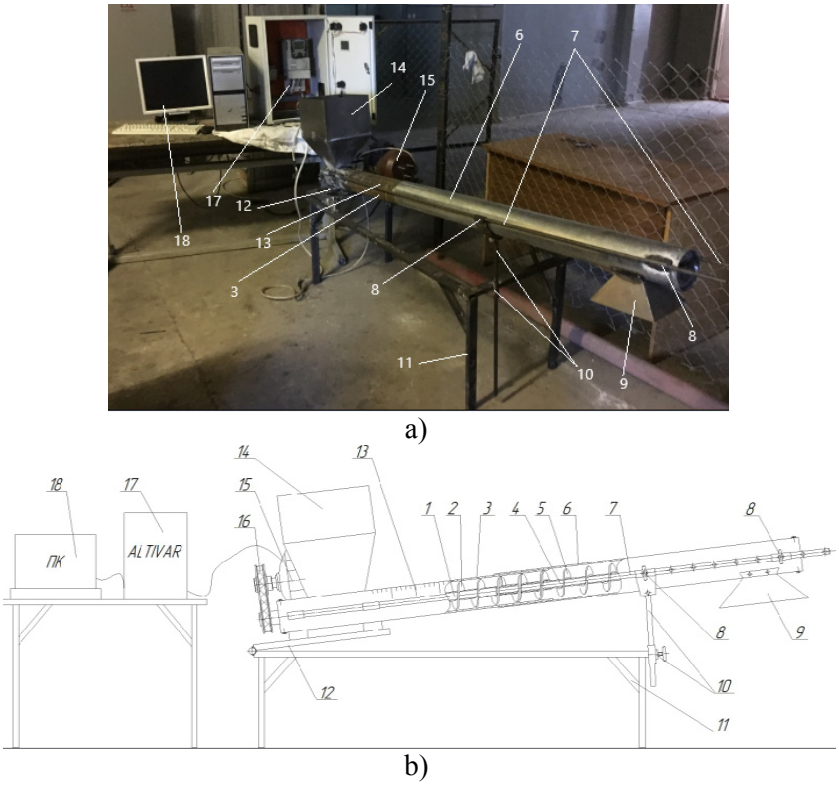

Figure 1. Stand for the study of the characteristics of telescopic screw conveyors: a) General view; b) design diagram; 1) fixed axial section of the screw; 2) auger fixed in the axial direction of the screw section; 3) the axially fixed part of the casing; 4) axially movable screw section; 5) auger movable in the axial direction of the screw section; 6) axially movable part of the casing; 7) guides; 8) fixation of guides; 9) unloading pipe; 10) support for adjusting the feed height of the material; 11) frame; 12) movable table; 13) scale of overlap of augers; 14) a hopper; 15) electric drive of the conveyor; 16) belt transfer; 17) drive frequency converter; 18) personal computer

Exploring the characteristics of telescopic screw conveyors established [19], the resonant vibrations of the system «Telescopic screw is a bulk medium» due to torsional vibrations. The most interesting and at the same time least studied case of complex vibrations in the screw of the telescopic conveyor is the case of internal resonance. Despite the limited amplitude of torsional vibrations in cases where the natural bending and indicated frequencies are close or connected by a rational ratio, the dynamic process of the «telescopic screw is a bulk medium» system is characterized by an increase in the amplitude of bend-

ing vibrations. To study them, first of all, we consider the terms of the dependences, taking into account the torsional vibrations of the telescopic screw.

These expressions are the following:

$$2(\rho_1+\rho_2)\frac{\partial\vartheta(z,t)}{\partial t}\frac{\partial w}{\partial t}+2(\rho_1+\rho_2)I\frac{\partial\vartheta(z,t)}{\partial t}\frac{\partial^3 w}{\partial t\partial x^2}+2(\rho_1+\rho_2)\Omega\frac{\partial\vartheta(z,t)}{\partial t}u+(\rho_1+\rho_2)\frac{\partial^2\vartheta(z,t)}{\partial t^2}w \quad (1)$$

Or

$$-2(\rho_1+\rho_2)\frac{\partial\vartheta(z,t)}{\partial t}\frac{\partial u}{\partial t}-2(\rho_1+\rho_2)I\frac{\partial\vartheta(z,t)}{\partial t}\frac{\partial^3 u}{\partial t\partial x^2}-2(\rho_1+\rho_2)\Omega\frac{\partial\vartheta(z,t)}{\partial t}w(\rho_1+\rho_2)\frac{\partial^2\vartheta(z,t)}{\partial t^2}u \quad (2)$$

Taking into account the law of rotational oscillations of a telescopic screw in the form

$$\vartheta(x,t)=h\sin\frac{k\pi}{l(\tau)}z\cos\vartheta,\ \vartheta=(\Theta t+\vartheta_0), \quad (3)$$

where a — is their amplitude, $\Theta=\frac{k\pi}{l(\tau)}\sqrt{\frac{GJ_0}{I_0}}$ — frequency, ϑ_0 - initial phase, I_0 the running moment of inertia relative to the neutral axis of the elastic body together with the medium, J_0 - is its equatorial moment of inertia, G — is the shear modulus.

Then the expressions of the right-hand side of the differential relations that take them into account are transformed to the form:

$$2a_s h\sin\frac{k\pi}{l}z\sin\frac{s\pi}{l}z\left\{\left(1-I\left(\frac{s\pi}{l}\right)^2+\frac{\Theta_k}{\omega_s}\right)\sin\psi_s\sin(\Theta_k t+\vartheta_0)-\frac{\Theta_k}{\omega_s}\cos\psi_s\cos(\Theta_k t+\vartheta_0)\right\}. \quad (4)$$

Let us consider them in more detail for the case where the forms of transverse and torsional oscillations are close in frequency i.e. $\omega_s=\Theta_k$. In that case, the additives of the right side of the general relations

$$\begin{aligned}\frac{\partial u(t,z)}{\partial t}&=-a\omega(\sin(\kappa z+\omega t+\phi)+\sin(\kappa z-\omega t-\phi),\\ \frac{\partial w(t,z)}{\partial t}&=a\omega(\cos(\kappa z+\omega t+\phi)-\cos(\kappa z-\omega t-\phi)).\end{aligned} \quad (5)$$

The effect on the dynamics of the system of torsional oscillations and the motion determines at of the medium expressions $\cos^2\psi_s$ and $\sin^2\psi_s$ replace accordingly for $\frac{1}{2}(1+\cos 2\psi_s)$ and $\frac{1}{2}(1-\cos 2\psi_s)$, system of differential equations

$$\begin{aligned}\frac{da}{dt}&=-\frac{1}{2\pi\omega l(\rho_1+\rho_2)}\int_0^l\int_0^{2\pi}\tilde f(a,z,\psi,\gamma,\vartheta)(\cos(\kappa z+\psi)-\cos(\kappa z-\psi))d\psi dz,\\ \frac{d\theta}{dt}&=\omega+\frac{1}{2a\pi\omega l(\rho_1+\rho_2)}\int_0^l\int_0^{2\pi}\tilde f(a,z,\psi,\gamma,\vartheta)(\sin(\kappa z+\psi)+\sin(\kappa z-\psi))d\psi dz,.\end{aligned} \quad (6)$$

After averaging over the linear variable and the external perturbation phase, it transforms to the form:

$$\frac{da}{dt}=-\frac{\varepsilon}{4\pi\omega_i l}\int_0^l\int_0^{2\pi}\tilde f(a,z,\psi_S,\gamma)(\cos(\kappa z+\phi+\gamma)-\cos(\kappa z-\phi+\gamma))d\gamma d\vartheta dz+$$

$$+2a_S\omega_S\Theta_k h\delta_k^S\left\{\left(1-I\left(\frac{s\pi}{l}\right)^2+\frac{\Theta_k}{\omega_S}\right)\sin 2(\omega t_S+\bar\gamma)\sin(\Theta_k t+\vartheta_0)-\frac{\Theta_k}{\omega_S}(1+\cos 2(\omega t_S+\varphi)\cos(\Theta_k t+\vartheta_0))\right\},$$

$$\frac{d\psi_S}{dt}=\omega_S+\frac{\varepsilon}{4a\pi\omega_S l}\int_0^{2\pi}\int_0^l\int_0^{2\pi}\tilde f(a,z,\psi_S,\gamma)(\sin(\kappa z+\phi+\gamma)+\sin(\kappa z-\phi+\gamma))d\gamma d\vartheta dz- \quad (7)$$

$$-a_s\omega_s\Theta_k h\delta_k^s\left\{\left(1-I\left(\frac{s\pi}{l}\right)^2+\frac{\Theta_k}{\omega_s}\right)\cos 2(\omega t_s+\overline{\gamma})\sin\left(\Theta_k t+\vartheta_0\right)-\frac{\Theta_k}{2\omega_s}\sin 2(\omega t_s+\overline{\gamma})\cos\left(\Theta_k t+\vartheta_0\right)\right\}$$

where $\delta_s^k=\frac{1}{l}\int_0^l\sin\frac{k\pi}{l}z\sin^2\kappa_s z dz$.

Relations (1) show that, if the condition is fulfilled $2\omega_s\approx\omega_{\vartheta k}$, there will be resonant transverse oscillations in the system, which are caused by torsional oscillations. To describe them, in the same way as for resonant oscillations at the frequency of external periodic perturbation, entering in equation (1) the phase difference $\phi_2=2\psi_s-\vartheta_k$ $(\phi_2+\vartheta_k=2\psi_s)$, we get:

$$\frac{da}{dt}=\frac{-\overline{\varepsilon}}{4\omega_s\pi l}\int_0^l\int_0^{2\pi}\tilde{f}(b_1,z,\psi_s,\gamma)\sin\kappa_s z\cos\psi_s dz d\gamma+ab_s\omega_s\omega_{\vartheta k}\delta_s^k\left(1-I\kappa_s^2+\frac{\Omega}{\omega_1}-\omega_{\vartheta 1}\right)\tilde{n}os\phi_2, \qquad (8)$$

$$\frac{d\phi_2}{dt}=2\omega_s-\omega_{\vartheta\pi}+\frac{-\overline{\varepsilon}}{4\omega_s b_s\pi l}\int_0^l\int_0^{2\pi}\tilde{f}(b_1,z,\psi_s,\gamma)\sin\kappa_s z\sin\psi_s dz d\gamma+a\omega_s\omega_{\vartheta k}\delta_1^k\left(1-I\kappa_1^2+\frac{\Omega}{\omega_1}-\omega_{\vartheta k}\right)\sin\phi_2$$

If the function $f_1\left(u,w,\frac{\partial u}{\partial t},...,\frac{\partial^3 w}{\partial z^3},\gamma\right)$ takes into account only the forces of resistance and external periodic perturbation, that is, expressed by the ratio

$$\begin{gathered}-\frac{da}{dt}\omega(\sin(\kappa z+\omega t+\varphi)+\sin(\kappa z-\omega t-\varphi))+a\omega\frac{d\varphi}{dt}(\cos(\kappa z+\omega t+\varphi)-\\-\cos(\kappa z-\omega t-\varphi))=\varepsilon\widetilde{f}(a,x,\psi,\vartheta),\\-a\frac{d\varphi}{dt}(\sin(\kappa z+\omega t+\varphi)+\sin(\kappa z-\omega t-\varphi))+\frac{da}{dt}(\cos(\kappa z+\omega t+\varphi)-\cos(\kappa z-\omega t-\varphi))=0,\\\frac{da}{dt}\omega(\cos(\kappa z+\omega t+\varphi)-\cos(\kappa z-\omega t-\varphi))-a\omega\frac{d\varphi}{dt}(\sin(\kappa z+\omega t+\varphi)+\\+\sin(\kappa z-\omega t-\phi))=\varepsilon\tilde{g}(a,z,\psi,\gamma,\vartheta),\end{gathered} \qquad (9)$$

where $\varepsilon\tilde{f}(a,x,\psi,\gamma,\vartheta),\varepsilon\tilde{g}(a,z,\psi,\gamma,\vartheta)$

Then the correspond to the values respectively of the function

$$f_1\left(u,w,\frac{\partial u}{\partial t},...,\frac{\partial^3 w}{\partial z^3},\gamma\right)+2(\rho_1+\rho_2)\frac{\partial\vartheta(z,t)}{\partial t}\frac{\partial w}{\partial t}+2(\rho_1+\rho_2)I\frac{\partial\vartheta(z,t)}{\partial t}\frac{\partial^3 w}{\partial t\partial x^2}+2(\rho_1+\rho_2)\Omega\frac{\partial\vartheta(z,t)}{\partial t}u+(\rho_1+\rho_2)\frac{\partial^2\vartheta(z,t)}{\partial t^2}w,$$

$$f_2\left(u,w,\frac{\partial u}{\partial t},...,\frac{\partial^3 w}{\partial z^3},\gamma\right)-2(\rho_1+\rho_2)\frac{\partial\vartheta(z,t)}{\partial t}\frac{\partial u}{\partial t}-2(\rho_1+\rho_2)I\frac{\partial\vartheta(z,t)}{\partial t}\frac{\partial^3 u}{\partial t\partial x^2}-2(\rho_1+\rho_2)\Omega\frac{\partial\vartheta(z,t)}{\partial t}w(\rho_1+\rho_2)\frac{\partial^2\vartheta(z,t)}{\partial t^2}u.$$

Then the transverse resonance oscillations caused by the torsional oscillations in the case are described by differential equations:

$$\begin{gathered}\frac{da}{dt}=\frac{k_1(\omega)^{s-1}}{(\rho_1+\rho_2)\pi}a^s+\frac{4}{3}ab_1\omega_{\vartheta 1}\left(1-I\kappa_1^2+\frac{\Omega}{\omega_1}-\frac{\omega_{\vartheta 1}}{\omega_1}\right)cos\phi_2,\\\frac{d\phi_2}{dt}=2\omega_1-\omega_{\vartheta 1}-\frac{\overline{k}_1 EI}{(\rho_1+\rho_2)}a^2-(\frac{\pi}{l})^2\frac{\rho_2}{8\omega(\rho_1+\rho_2)}V^2+\frac{4}{3}a\omega_{\vartheta 1}\left(1-I\kappa_1^2+\frac{\Omega}{\omega_1}-\frac{\omega_{\vartheta 1}}{\omega_1}\right)\sin\phi_2\end{gathered} \qquad (10)$$

In Figure 2 presents for different values of the angular velocity of rotation the change in the amplitude time of the transverse oscillations of the system during the transition of the internal resonance.

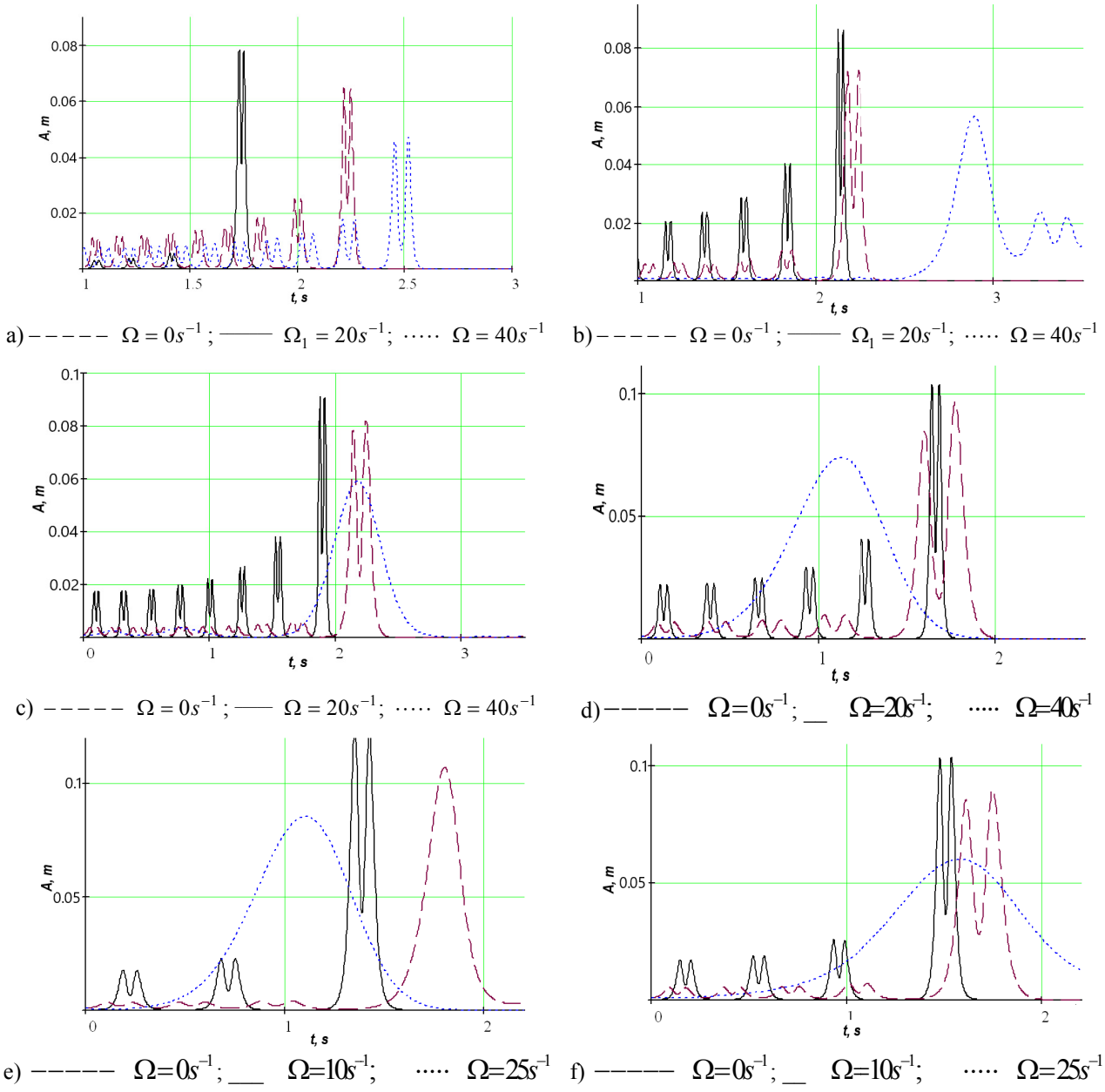

Figure 2. Changing the amplitude of the bending vibrations of the screw during the transition through internal resonance at $\rho_1 = 10$ kg/m; $I = 6 \cdot 10^{-6}$ kg/m^2; $E = 2{,}06 \cdot 10^{11}$ H/ m^2; $V = 10$ m/s: a) $\rho_2 = 0$ kg/m; $l = 6$ m; b) $\rho_2 = 10$ kg/m; $l = 6$ m; c) $\rho_2 = 20$ kg/m; $l = 6$ m; d) $\rho_2 = 30$ kg/m; $l = 6$ m; e) $\rho_2 = 30$ kg/m; $l = 8$ m; f) $\rho_2 = 15$ kg/m; $l = 8$ m

Discussion

The results show that both external and internal resonance can be avoided by changing the angular velocity of the auger, and as for the process of transition through the internal resonance, then:

– for higher angular velocities of rotation, the natural frequency of bending oscillations is smaller and simultaneously the amplitude of the transition is smaller;

– for larger values of the relative amount of motion of the medium, the amplitude of the transition through the internal resonance takes on a larger value.

Conclusions

Theoretical calculations of the resonance phenomenon have shown that external periodic forces or torsional vibrations of the telescopic screw itself have caused them. Differential equations of transverse oscillations of a rotating elastic body have been deduced under the motion condition of a continuous stream

of homogeneous medium on it with a constant relative linear velocity $V = 10$ m/s. Based on the constructed mathematical model, dependences have been obtained to determine the change in the amplitude of the transverse oscillations of the system during the transition of the internal resonance for different values of the angular velocity of rotation, depending on the physical-mechanical and geometric parameters of the system «telescopic screw-grain mixture» and the angular velocity of the screw rotary organ. It is established that for larger values of angular velocity of rotation of the working body the resonant frequency value is smaller (at $L = 6$ m = 20–40 s^{-1}). For working bodies of greater length, the amplitude of the transition through the resonance is greater (from 10–25 s^{-1} at $L = 8$ m) and increases from 0.0393 to 0.1023 m. However, it has established that the external and internal resonances of the system «telescopic screw — loose medium» can be avoided by changing the angular velocity of the working screw.

References

1 Hevko R.B. Determination of interaction parameters and grain material flow motion on screw conveyor elastic section surface / S.Z. Zalutskyi, Y.B. Hladyo, I.G. Tkachenko, O.L. Lyashuk, O.M. Pavlova, B.V. Pohrishchuk, O.M. Trokhaniak, N.V. Dobizha // INMATEH — Agricultural Engineering. — 2019. — 57 (1). — P. 123–134.

2 Haydl H.M. Design aspects of large-diameter tubular conveyor galleries / H.M. Haydl // Proceedings of the institution of civil engineers. Part 1 — Design and construction. — 1986. — 80. — P. 633–639.

3 Owen Philip J. Screw conveyor performance: comparison of discrete element modelling with laboratory experiments / Philip J. Owen, Paul W. Cleary // Progress in computational fluid dynamics. — 2010. — 10 (5–6). — P. 327–333.

4 Roberts Alan W. Bulk Solids. Optimizing Screw Conveyors / Alan W. Roberts // Chemical engineering. — 2015. — 122(2). — P. 62–67.

5 Lyashuk O.L. Mathematical model of bending vibrations of a horizontal feeder-mixer along the flow of grain mixture / O.L. Lyashuk, M.B. Sokil, V.M. Klendiy, O.P. Skyba, L.M. Slobodian // INMATEH — Agricultural Engineering. — 2018. — 55(2). — P. 33–42.

6 Lutsiv I.V. Investigation of dynamical impact loads in screw conveyer drives with safety clutches/ I.V. Lutsiv, I.B. Hevko, O.L. Lyashuk, T.S. Dubynyak // INMATEH — Agricultural Engineering. — 2017. — 51(1). — P. 69–77.

7 Hevko R.B. Development of a pneumatic screw conveyor design and substantiation of its parameters / R.B. Hevko, O.M. Strishenets, O.L. Lyashuk, I.G. Tkachenko, O.M. Klendii, V.O. Dzyura // INMATEH: Agricultural engineering. — 2018. — 54(1). — P. 153–160.

8 Hevko I. Resonant oscillation of vertical working part of conveyer-loader / I. Hevko , O. Lyashuk, M. Sokil, L. Slobodian, V. Hud, Yu. Vovk // Bulletin of the Karaganda University. Series PHYSICS. — 2019. — 2(94). — P. 73–81.

9 Hevko I.B. Investigation of the stability of the torsorial vibrations of a screw conveyer under the influence of pulse forces / I.B. Hevko, A.Ye. Dyachun, V.Z. Hud, L.R. Rohatynska, V.M. Klendiy // INMATEH — Agricultural Engineering. Polytechnic University of Bucharest. — 2015. — Vol. 45, № 1. — P. 77–86.

10 Fernandez J.W. Effect of screw design on hopper draw dawn by a horizontal screw feeder / J.W. Fernandez, P.W. Cleary, W. McBride // Seventh International Conference on CFD in the Minerals and Process Industries CSIRO: Melbourne: Australia 9–11 December: 1–6. — 2011.

11 Roberts Alan W. The influence of granular vortex motion on the volumetric performance of enclosed screw conveyors / Alan W. Roberts // Power technology. — 1999. — 104(1). — P. 56–67.

12 Sun X.X. Design method of a vertical screw conveyor based on Taylor-Couette-Poiseuille stable helical vortex / X.X. Sun, W.J. Meng, Y. Yuan // Advances in mechanical engineering. — 2017. — 9(7).

13 Schlesinger D. Screw conveyor calculation based on actual material properties / D. Schlesinger, A. Papkov // Powder Handling and Processing. — 1997. — 9(4).

14 Zareiforoush H. Effect of crop-screw parameters on rough rice grain damage in handling with a horizontal screw conveyor / H. Zareiforoush, M.H. Komarizadeh, M.R. Alizadeh // Journal of Food, Agriculture and Environment. — 2010. — 8(3–4). — P. 494–499.

15 Owen P.J. Prediction of screw conveyor performance using the Discrete Element Method (DEM) / P.J. Owen, P.W. Cleary // Powder Technology. — 2009. — 193(3). — P. 274–288.

16 Рогатинский Р.М. Научно-прикладные основы создания винтовых транспортно-технологических механизмов: моногр. / Р.М. Рогатинский, И.Б. Гевко, А.Е. Дячун. — Тернополь: ФОП «Паляница», 2014. — 280 с.

17 O. Lyashuk. Longitudinal-angular oscillation of wheeled vehicles with non-linear power characteristics of absorber system / O. Lyashuk, T. Pyndus, O. Marunych, M. Sokil // Вестн. Тернопол. нац. техн. ун-та. — 2016. — № 2 (83). — P. 82–89.

18 Сокол Б.И. Вынужденные колебания гибких трубчатых тел, вдоль которых движется сплошной поток среды / Б.И. Сокол, М.Б. Сокол // Вестн. Нац. ун-та «Львовская политехника» // Динамика, прочность и проектирование машин и приладив. — 2017. — № 866. — С. 60–65.

19 Рогатинский Р.М. Перспективные винтовые конвейеры: конструкции, расчет, исследования: моногр. / Р.М. Рогатинский, И.Б. Гевко, А.Л. Ляшук, В.З. Гудь, А.Е. Дячун, А.Л. Мельничук, Л.М. Слободян. — Тернополь: ФОП «Паляница», 2019. — 212 с.

20 Hevko B. Dynamics of auger working body of a multifunctional conveyor / B. Hevko, O. Lyashuk, M. Sokil, O. Skyba, O. Marunych, D. Shmatko // Bulletin of the Karaganda University. Series Mathematics. — 2018. — 1(89). — P. 105–113.

21 Lyashuk, O. Torsional oscillations of an auger multifunctional conveyor's screw working body with consideration of the dynamics of a processed medium continuous flow / O. Lyashuk, M. Sokil, Y. Vovk, A. Gupka, O. Marunych // Ukrainian Food Journal. — 2018. — 7(3). — P. 499–510.

22 Патент № 129581. Украина, МПК (2006.01) B65G 33/00, (2006.01) B65G 15/26, E02F 9/00, B65G 33/00. Телескопический винтовой конвейер / Гевко И.Б., Гудь В.З., Шуст И.М. заявители и патентообладатели. — № u201802391; Заявл. 12.03.2018. Опубл. 12.11.2018. — Бюл. № 21.

В. Гудь, И. Гевко, О. Ляшук, О. Гевко, М. Сокол, И. Шуст

Айналмалы тербелістермен негізделген «телескопиялық бұрама-сусымалы орта» жүйесінің резонанстық тербелістерін зерттеу

Мақалада бұрандалы тасымалдағыштарды жасау кезінде телескопия қағидатын пайдаланудың өзектілігі негізделген, олар бүгінде айтарлықтай ұзындығын алу үшін күрделі орындалады, бұл олардың конструкцияларын қымбат және құрылымдық тұрғыдан күрделі етеді. Деректерді қажетті тіркеумен басқарудың автоматтандырылған режимінде жоғары дәлдікпен кең ауқымда технологиялық процесті зерттеу нәтижелерін өлшеуді қамтамасыз ететін эксперименттік жабдық келтірілген. Құрылған математикалық модельдің негізінде «телескопиялық винт-сусымалы орта» жүйесінің физика механикалық және геометриялық параметрлерінен ауытқу бұрыштық жылдамдығының тәуелділігі алынды. Оның негізінде резонанстық жағдай үшін оның тербелістерінің анықтайтын параметрлерінің өзгеру заңдарын сипаттайтын аналитикалық қатынастар алынған. Резонанстық тербелістер кезінде, айналудың едәуір бұрыштық жылдамдығы болған кезде, иілгіш тербелістердің меншікті жиілігі аз және бір мезгілде резонанс арқылы өту амплитудасы аз екені анықталған. Ішкі резонанс арқылы өту кезінде уақыт бойынша айналудың бұрыштық жылдамдығының әртүрлі мәндері үшін жүйенің көлденең тербелісінің амплитудасының нәтижелері берілген, ол едәуір дәрежеде орта қозғалысының физика-механикалық және геометриялық сипаттамаларына байланысты.

Кілт сөздер: конвейерлер, механикалық жүйелер, көлік-бөлу жүйесі, динамикалық модельдеу, амплитудалар, резонанс, телескопиялық бұранда, сусымалы орта, бұрыштық айналу жылдамдығы, айналмалы тербелістер.

В. Гудь, И. Гевко, О. Ляшук, О. Гевко, М. Сокол, И. Шуст

Исследование резонансных колебаний системы «телескопический винт — сыпучая среда», обусловленных крутильными колебаниями

В статье обоснована актуальность использования принципа телескопии при создании винтовых транспортеров, которые сегодня для получения значительной длины выполняются сложенными, что делает их конструкции дорогими и конструктивно неоправданно сложными. Приведено экспериментальное оборудование, которое обеспечивает измерение результатов исследования технологического процесса в широком диапазоне с высокой точностью в автоматизированном режиме управления с необходимой фиксацией данных. На основе построенной математической модели получены зависимости угловой скорости возмущения от физико-механических и геометрических параметров системы «телескопический винт — сыпучая среда». На ее базе получены аналитические соотношения, описывающие законы изменения определяющих параметров его колебаний для резонансного случая. Установлено, что при резонансных колебаниях, когда есть значительные угловые скорости вращения, собственная частота изгибных колебаний и одновременно амплитуда перехода через резонанс меньше. Представлены результаты амплитуды поперечных колебаний системы для различных значений угловой скорости вращения во времени при переходе через внутренний резонанс, который в значительной степени зависит от физико-механических и геометрических характеристик движения среды.

Ключевые слова: конвейеры, механические системы, транспортно-разделительная система, динамическое моделирование, амплитуда, резонанс, телескопический винт, сыпучая среда, угловая скорость вращения, крутильные колебания.

References

1 Hevko, R.B., Zalutskyi, S.Z., Hladyo, Y.B., Tkachenko, I.G., Lyashuk, O.L., Pavlova, O.M., Pohrishchuk, B.V., Trokhaniak, O.M. & Dobizha, N.V. (2019). Determination of interaction parameters and grain material flow motion on screw conveyor elastic section surface. *INMATEH — Agricultural Engineering, 57 (1),* 123–134.

2 Haydl, H.M. (1986). Design aspects of large-diameter tubular conveyor galleries. *Proceedings of the institution of civil engineers. Part 1 — Design and construction, 80,* 633–639.

3 Owen Philip, J., Cleary Paul, W. (2010). Screw conveyor performance: comparison of discrete element modelling with laboratory experiments. *Progress in computational fluid dynamics*, *10 (5–6),* 327–333.

4 Roberts Alan, W., Bulk Solids (2015). Optimizing Screw Conveyors. *Chemical engineering*, *122(2),* 62–67.

5 Lyashuk, O.L., Sokil M.B., Klendiy V.M., Skyba O.P. & Slobodian L.M. (2018). Mathematical model of bending vibrations of a horizontal feeder-mixer along the flow of grain mixture. *INMATEH — Agricultural Engineering, 55(2),* 33–42.

6 Lutsiv, I.V, Hevko, I.B., Lyashuk, O.L. & Dubynyak, T.S. (2017). Investigation of dynamical impact loads in screw conveyer drives with safety clutches. *INMATEH — Agricultural Engineering*, *51(1),* 69–77.

7 Hevko, R.B., Strishenets, O.M., Lyashuk, O.L., Tkachenko, I.G., Klendii, O.M. & Dzyura, V.O. (2018). Development of a pneumatic screw conveyor design and substantiation of its parameters. *INMATEH — Agricultural engineering*, *54(1),* 153–160.

8 Hevko, I., Lyashuk, O., Sokil, M., Slobodian, L., Hud, V. & Vovk, Yu. (2019). Resonant oscillation of vertical working part of conveyer-loader. *Bulletin of the Karaganda University. Series PHYSICS,* 2(94), 73–81.

9 Hevko, I.B., Dyachun, A.Ye., Hud, V.Z., Rohatynska, L.R. & Klendiy, V.M. (2015). Investigation of the stability of the torsorial vibrations of a screw conveyer under the influence of pulse forces. *INMATEH — Agricultural Engineering. Polytechnic University of Bucharest, Vol. 45, № 1,* 77–86.

10 Fernandez, J.W., Cleary, P.W. & McBride, W. (2011). Effect of screw design on hopper draw dawn by a horizontal screw feeder. *Seventh International Conference on CFD in the Minerals and Process Industries CSIRO, Melbourne, Australia 9–11 December*:1–6.

11 Roberts Alan, W. (1999). The influence of granular vortex motion on the volumetric performance of enclosed screw conveyors. *Power technology, 104(1)*, 56–67.

12 Sun, X.X., Meng, W.J. & Yuan, Y. (2017). Design method of a vertical screw conveyor based on Taylor-Couette-Poiseuille stable helical vortex. *Advances in mechanical engineering*. 9(7).

13 Schlesinger, D., & Papkov, A. (1997). Screw conveyor calculation based on actual material properties. *Powder Handling and Processing*. 9(4).

14 Zareiforoush, H., Komarizadeh, M.H. & Alizadeh, M.R. (2010). Effect of crop-screw parameters on rough rice grain damage in handling with a horizontal screw conveyor. *Journal of Food, Agriculture and Environment*, *8(3–4),* 494–499.

15 Owen, P.J., & Cleary, P.W. (2009). Prediction of screw conveyor performance using the Discrete Element Method (DEM). *Powder Technology*, *193(3),* 274–288.

16 Rogatinskyi, R.M., Gevko, I.B., & Diachun, A.E. (2014). *Nauchno-prikladnye osnovy sozdaniia vintovykh transportno-tekhnolohicheskikh mekhanizmov [Scientific and applied bases of creation of screw transport-technological mechanisms]*. Ternopil [in Ukrainian].

17 Lyashuk, O., Pyndus, T., Marunych, O. & Sokil, M. (2016). Longitudinal-angular oscillation of wheeled vehicles with nonlinear power characteristics of absorber system. *Vestnik Ternopolskoho natsionalnoho tekhnicheskoho universiteta — Bulletin of the Ternopil National Technical University*, *2 (83)*, 82–89 [in Ukrainian].

18 Sokil, B.I., & Sokil, M.B. (2017). Vynuzhdennye kolebaniia hibkikh trubchatykh tel, vdol kotorykh dvizhetsia sploshnoi potok sredy [Inhibited oscillations of flexible tubular bodies along which a continuous flow of medium moves]. *Vestnik Natsionalnoho universiteta «Lvovskaia politekhnika». Dinamika, prochnost i proektirovanie mashin i priladiv — Bulletin of the national university «Lviv Polytechnic» Dynamics, strength and design of machines and devices, 866*, 60–65 [in Ukrainian].

19 Rogatynskyi, R.M., Hevko, I.B., Liashuk, A.L., Hud, V.Z., Diachun, A.E., Melnychuk, A.L. & Slobodyan, L.M. (2019). *Perspektivnye vintovye konveiery: konstruktsii, raschet, issledovaniia [Prospective screw conveyors: structures, calculation, research]*. Ternopil: FOP «Palyanitsa» [in Ukrainian].

20 Hevko, B. Lyashuk, O., Sokil, M., Skyba, O., Marunych, O., & Shmatko, D. (2018). Dynamics of auger working body of a multifunctional conveyor. *Bulletin of the Karaganda University: Series Mathematics, 1*(89), 105–113.

21 Lyashuk, O., Sokil, M., Vovk, Y., Gupka, A. & Marunych, O. (2018). Torsional oscillations of an auger multifunctional conveyor's screw working body with consideration of the dynamics of a processed medium continuous flow. *Ukrainian Food Journal, 7(3)*, 499–510.

22 Hevko, I.B., Gud, V.Z., & Shust, I.M. (2018). Teleskopicheskii vintovoi konveier [Telescopic screw conveyor]. *Patent № 129581, Ukraine. Bulletin No. 21* [in Ukrainian].

ФИЗИКАНЫ ОҚЫТУ ӘДІСТЕМЕСІ
МЕТОДИКА ПРЕПОДАВАНИЯ ФИЗИКИ
METHODS OF TEACHING PHYSICS

DOI 10.31489/2020Ph2/127-135

ӘОЖ 378.147, 372.853

Ж.Т. Камбарова, А.К. Тусупбекова

Е.А. Бөкетов атындағы Қарағанды мемлекеттік университеті, Қазақстан
(E-mail: kambarova@bk.ru)

Студенттерге көптілді білім беруді жүзеге асыру аясында жаратылыстану-ғылыми пәндерді оқытудағы CLIL тәсілін қолдану ерекшеліктері

Тілдік пәндерді оқыту және шетел тілінде математикалық және жаратылыстану-ғылыми пәндерді оқыту арқылы *тілдік білім беру* — Қазақстан Республикасындағы көптілді білім беруді бағдарламасын практикалық іске асырудың негізгі тетігі болып табылады. Мақалада Е.А. Бөкетов атындағы Қарағанды мемлекеттік университетінің физика-техникалық факультетінде жаратылыстану-ғылыми пәндерді оқытуда CLIL технологиясын жүзеге асыру тәжірибесі ұсынылған. Жұмыста физика-техникалық факультетінің 5В011000-Физика білім беру бағдарламасы бойынша оқитын 4 курс студенттерін «Computer methods in Physics» және «Nuclear physics» атты мамандық бойынша таңдау пәндерін оқытуға «Content and language integrated learning» (CLIL) әдістемесінің әсері зерттелген. Мақалада CLIL технологиясын қолданудың артықшылықтары мен кемшіліктері зерделенген. CLIL әдісін іске асырудың мысалы ретінде тапсырмалар түрлері ұсынылған. Педагогикалық зерттеу барысында бақылаудың негізгі құралдары мен формалары зерттелген. Студенттерді бағалау процедурасы мен бағалау критерийлері ұсынылған. Оқыту үрдісінде CLIL әдістемесін қолдану білім алушыларда ағылшын тілін меңгеруге ынтасын жоғарылатады және өз кезегінде білім алушыларды әрі қарай білім алуға және алған білімдерін болашақ кәсіби салада қолдануға үйретеді. CLIL технологиясы студенттердің тек шетел тілін ғана емес, басқа да арнайы пәндерді оқуға ынталандырудың маңызды құралы болып табылады. Мақала соңында педагогикалық зерттеудің қорытындысы мен нәтижелері келтірілген.

Кілт сөздер: пәндік-тілдік интеграцияланған оқыту, CLIL технологиясы, әдіснама, көптілді білім беру, шетел тілді кәсіби-коммуникативтік құзыреттілік, бағалау критерийлері.

Кіріспе

CLIL (Content Language Integrated Learning) технологиясы немесе пәндік-тілдік интеграцияланған оқыту, яғни шетел тілінде пәнді оқыту соңғы онжылдықта қарқын алып, шетел елдерінің көптеген білім беру мекемелерінде кеңінен қолданылуда.

Соңғы жылдары шетел тілін оқытуда дәстүрлі грамматикалық-аударма әдіс-тәсілінің тиімділігі төмендегені байқалды, себебі мұндай әдістеменің беретін нәтижесі қоғамның заманауи қажеттіліктерін қанағаттандырмайды. Жоғары мектеп алдында экономиканы дамытудағы кілттік элементтер мен қозғаушы күші ретінде жоғары білікті мамандарды даярлау міндеті тұр. Бүгінгі жаһандану дәуірінде болашақ маман үшін өмір бойы өз білімін үнемі жандандыру қабілетіне ие болуы, сондай-ақ өзінің кәсіби ортасында өз білімдерімен алмасу мүмкіндігіне ие болу ерекше өзектілікке ие. Осыны болашақ маманның кәсіби шетел тілдік құзыретінсіз толыққанды жүзеге асыру мүмкін емес. Университетте тиімді кәсіби-бағытталған шетел тілдік даярлау үздіксіз білім беру үшін қажетті құзыреттіліктерді қалыптастыруға көмектеседі.

Шетелдік және отандық ғылыми әдебиеттерде пәндік-тілдік интеграцияланған оқытудың мәселелеріне арналған көптеген мақалалар бар [1-3]. Олардың басым бөлігі оқу сабақтарын жоспарлау және ұйымдастырудың, оқу материалдарды таңдау және бейімдеу, білім алушылардың білімін бақылаудың әдістемелік аспектілерін ашады. Алайда CLIL технологиясының әдістемелік құраушысына жеткіліксіз назар аударылған.

Әдістеме

CLIL технологиясы оқытудың үш негізгі мақсатына қол жеткізуге бағытталған:

– мазмұны (content) — оқытылатын пән бойынша жаңа білімді, іскерлікті және дағдыларды меңгеру процесі;

– байланыс (communication) — оқылатын шетел тілінің құралдарын жан-жақты пайдалану;

– танымдық дағдылар (cognition) — оқылатын пәнді және меңгерілетін тілді жақсы түсіну үшін білім алушылардың ойлау қабілеттіліктерін дамыту. Бұл мақсатқа қол жеткізуге аналитикалық және сыни ойлауға бағытталған тапсырмалар ықпал етеді.

Пәндік-тілдік интеграцияланған оқыту — шетел ғалымы Дэвид Маршпен [4] ұсынылған термин. Бұл термин басқа пәндерді оқыту үшін шетел тілін құрал ретінде қолдануды білдіреді. CLIL технологиясы шетел тілінде арнайы пәндерді оқытуды көздейді, сонымен қатар мұнда басты назар шетел тілді меңгеруден нақты пәндік облыста жаңа білім алуға аударылады. Яғни CLIL аясында шетел тілін меңгеру негізгі мақсат ретінде емес, арнайы пән бойынша жаңа ақпарат алу үшін оқыту жүргізіледі. Осылайша, екі жақты мақсатқа қол жеткізіледі — пәнді және кәсіби-бағытталған шетел тілін бір уақытта оқыту. Білім алушылардың бір уақытта кәсіби және шетел тілдік құзыреттіліктерін қалыптастыратын ерекше танымдық орта құрылады.

Пәндік-тілдік интеграцияланған сабақты жоспарлау классикалық практикалық сабаққа дайындалумен салыстырғанда әлдеқайда көп уақытты қажет етеді, себебі оқытушыға әрбір сабаққа екі жақты мақсаттарды қоюға тура келеді (пәндік мазмұнды және тілдік материалды меңгеруі бойынша). Сонымен бірге дайын оқу материалдарының қажетті мөлшері мен алуан түрлілігінің жоқтығына байланысты оқытушыға материалдарды іздеуге және педагогикалық бейімдеуге көп уақыт жұмсауға тура келеді.

Ағылшын тілі көптеген еуропалық жоғары оқу орындарында «басым» тіл ретінде кеңінен қолданылады. Осыған байланысты, пәндік-тілдік интеграцияланған оқыту саласындағы көптеген еуропалық маман-зерттеушілердің бұл әдістемені бірнеше пәндерді оқытудың бірегей тәсілі ретінде бөліп көрсетеді. Интеграцияланған оқыту саласындағы зерттеуші, профессор де Койл CLIL әдістемесінің үш моделін ажыратады [4]:

C1 моделі: Көптілді оқыту. Бұл жағдайда әртүрлі пәндерді оқыту кезінде әр жылдары бірнеше шетел тілі қолданылады. Мұндай оқыту үлгісі студентке толық курсты аяқтағаннан кейін бірнеше тілде кәсіби білім меңгеруге мүмкіндік береді.

C2 моделі: Пән және тілді қосымша интеграцияланған оқыту. Оқытудың бұл моделі — пәндерді бірігіп оқытуды көздейді, бұл жағдайда жоғары ретті ойлау процестерін қамтамасыз ету мақсатында тілді қолдану үшін білім мен іскерлікті дамытуға басты назар аударылады. Тілді оқыту арнайы салалармен ұштастырылып, осылайша болашақ мамандарды оқыту кезінде шетел тілі оқытушылары тарапынан қолдауды жүзеге асырады. Пәндік-тілдік интеграцияланған оқыту процесінде студенттер мамандық бойынша болашақта жұмыс істеу үшін шетел тілін қолдана алады.

C3 моделі: Тілдік қолдауды қамтитын пәндік курстар. Мамандықтарды оқыту бағдарламалары тек кәсіби дағдыларды дамыту тұрғысынан ғана емес, сонымен бірге және тілдік дағдыларды дамыту тұрғысынан құрастырылған. Мұндай модель бойынша пәндер оқытушылары да, тілдерді оқыту саласындағы мамандары да оқыту жүргізеді. Тіпті тілді нашар білетін студенттер оқу процесі барысында қолдау ала алады, бұл кезде оқытылатын пәнді де, тілді де меңгеруге мүмкіндік бар болады. Бұл модель бойынша әртүрлі тілдік деңгейі бар студенттер оқи алады.

С1 моделі тек нақты мамандандырылған жоғары оқу орындарында (мысалы, бизнес және басқару) іске асырылады, ал С2 және С3 модельдері білім беруде кең таралған болып табылады.

CLIL форматындағы сабақты жоспарламас бұрын, оқыту мақсаттары мен пәннің мазмұнын нақты анықтау қажет. Басты назар білім алушыға аударылады, ал оқытудың мақсаттары мен күтілетін нәтижелерін қалыптастыру кезінде студенттердің нақты, өлшенетін қажеттіліктерінен ескеруден бастау керек. Жоспарға оқытудың күтілетін нәтижелерін кіргізе отырып, оқытушы курсты нақты және бірыңғай көруге, топта жалпы түрде және әр студентке назар аударуға, нақты айтқанда,

қойылған нәтижелердің қол жетімділігін, яғни жұмыстың тиімділігін бақылауға көмектеседі. Студент үшін бұл, ең алдымен, оқуға деген саналы көзқарасты қалыптастыру, танымның белсенді процесіне тарту және өз білімі үшін жауапкершілікті қабылдау болып табылады [5].

Оқытушы алдында келесі есеп тұрады: сабақтың барысында шеберлік-сыныбын көрсетіп, коммуникация құралы ретінде шетел тілін қолдануына білім алушылардың қызығушылығын арттыру, жарытылыстану-ғылыми пәндер мен шетел тілінің интеграциясын максималды түрде тиімді ұйымдастыру. CLIL технологиясын қолдану арқылы сабақты оқытудың мазмұнына қарай әртүрлі тәсілмен құрастыруға болады.

CLIL технологиясын қолдануымен оқытуды ұйымдастыру үшін келесі ерекшеліктерді ескерген жөн:

– оқытылатын пән бойынша тапсырмалар ана тіліндегі бар білімдерден бір деңгейге төмен болуы керек;

– CLIL әдісін қолданылатын оқытушы өзінің кәсіби біліктілігін үнемі жоғарылатуы тиіс;

– оқу материалының формасы оқытылатын пәндермен көрнекілік, қол жетімділік, контекстік байланыс принциптеріне сәйкес болуы керек;

– бағалау критерийлері жетілдіруі тиіс.

Жұмыста авторлар ұсынған CLIL әдістемесі негіздерін қарастырған [6]. Мысал ретінде физика бойынша оқу құралдарын құрастырған кезде осы әдісті жүзеге асыру мүмкіндіктері мен құрылымы көрсетілді. Жаратылыстану-математика бағытында оқыту үшін оқу құралдары, ұқсас оқулықтар құрастыру қажеттілігі туралы айтылды.

CLIL технологиясы тек ағылшын тілінде сөйлеу дегенді білдірмейді. CLIL әдістемесін уақыт бойынша жүзеге асыру үшін үш негізгі моделі бар (1-кесте) [7].

1 - к е с т е

CLIL технологиясын уақыт бойынша жүзеге асыру модельдері

	Сабақтың барысындағы CLIL мақсаты	Уақыт аралығы	Мазмұны
«Жұмсақ» CLIL	Тілдік материалды кеңейту	Аптасына бір рет 50 минут	Ағылшын тілінде тек пәннің кейбір тақырыптары оқытылады.
«Қатты» CLIL	Модульдік оқыту	Семестрде 30 сағат	Ағылшын тілінде модульдер кешені оқытылады.
	Толық үңілу	Семестрде 40 сағат	Пәннің 90% дерлік ағылшын тілінде оқытылады.

CLIL әдістемесімен оқытылатын жаратылыстану-ғылыми пән бойынша интеграцияланған сабақтарда пайдаланылатын грамматикалық материал жалпы және кәсіби шетел тілі курстарына айтарлықтай мөлшерде сәйкес болуы керек. Студенттер ағылшын тілінің базалық грамматикасын меңгеруін, яғни сабақты және ырықсыз етістердің негізгі уақыт топтарын, сын есімді және үстеулердің салыстыру дәрежелерін, етістіктің жалқы емес формаларын және т.б. білуі тиіс.

Сонымен, бұл технология жақсы перспективаға ие екенін атап өтуге болады, бірақ оны кең оқытушылық практикаға енгізу үшін кейбір дәстүрлі концепцияларды және арнайы пәндер мен шетел тілін оқытуға көзқарасты қайта қарастыру қажет.

Алайда, CLIL тәсілін қолдануда келесі мәселелер бар:

– арнайы пәндер оқытушыларының тілдік дайындығының жеткіліксіздігі;

– жоғары мектеп үшін CLIL элементтерін қолданудың толық әдістемелік әзірлемесінің болмауы;

– тілдік емес ЖОО студенттерінің базалық тілдік дайындығының әлсіздігі;

– шетел тіліндегі оқу материалдарын қолдануымен оқытуда студенттер ынтасының төмен деңгейі;

– CLIL элементтерін пайдалануға деген оқытушылардың қызығушылығының төмен деңгейі.

Педагогикалық тәжірибе

Академик Е.А. Бөкетов атындағы Қарағанды мемлекеттік университетінде шетел тілдері мамандарды даярлаудың бүкіл бағыттарында, соның ішінде студент-физиктерге де оқытылады.

Төменде 5В011000-Физика мамандығы бойынша шетел тілінде жаратылыстану-ғылыми пәндерді оқытуда CLIL технологиясын жүзеге асыру тәжірибесі ұсынылған.

«Computer methods in Physics» және «Nuclear physics» таңдау бойынша пәндерді оқыту ФОК-400 п/я (11 студент, қазақ бөлімі) және ФОР-401 п/я (3 студент, орыс бөлімі) көптілді топтарында CLIL әдістемесін қолдануымен жүргізілді. Бұл екі пән ағылшын тілінде оқытылды. Ағылшын тілі лингвистикалық емес пәнді меңгеруге арналған құрал ретінде пайдаланылды, сондықтан қолданылған CLIL әдістемесі шетел тілдерін қарапайым стандартты оқытудан әлдеқайда күрделі. Пәндердің таңдауы болашақ мұғалімдерді даярлауда маңызды рөл атқаратын бейінді пәндер болуымен шартталған. Бұл пәндерді пәндік-тілдік интеграцияланған оқыту әдістемесінің көмегімен оқытудың негізгі міндеттері келесідей болады:

– жоғары деңгейдегі ойлау дағдыларын дамыту;

– ағылшын тілін меңгеру деңгейін арттыру.

«Computer methods in Physics» және «Nuclear physics» пәндерінің оқу бағдарламасы аясында ағылшын тілінде тапсырмалар мен жаттығулардың жүйесі құрастырылған. Жаттығулар жүйесі екі блоктан құрылады. Бірінші блок қысқа жауапты талап ететін жаттығулар (формулалардың, құбылыстардың және процестердің білуін тексеретін сұрақтар, терминдердің анықтамалары, көрнекі материалдарды талдауға негізделген жаттығулар және т.б.). Екінші блок толық жауапты талап ететін сұрақтар (ашық сұрақтардан құрылатын жаттығулар). Тапсырмалардың көпшілігі студенттердің ойлау дағдыларын дамытуға бағытталған, өз бетімен орындалатын жұмыстарға ерекше назар аударылады.

CLIL технологиясы көмегімен сабақты әртүрлі тәсілмен, яғни тақырып мазмұнына қарай құрастыруға болады. Оқытушыға сабақтарды жоспарлауда көмектесетін келесідей сатыларды бөліп көрсетуге болады:

Тақырып бойынша лексиканы таңдап, талқылауға қажетті анықталған грамматикалық құрылымдарды таңдау қажет. Сабақта қолданылатын әртүрлі жұмыс формаларын, оқыту тәсілдерін қолдану керек [8-10].

Төменде CLIL технологиясы аясында сабақ үлгісі және қолданылған тапсырмалар мысалдары келтірілген.

Танысу. Студенттерге ағылшын тілінде ашық сұрақтар арқылы тақырыпқа кіріспе жасау. Сонымен бірге көп жауабы бар сұрақтар қою, шын / ақиқат сұрақтарды қою және т.б.

Vocabulary. Мысалы, тақырыптың терминдерін үш тілдік сөздікпен таныстырып, кілттік сөздерінің синоним сөздерін ағылшын тілде беруді ұсыну. Кейін оқытушы терминдерге түсініктемелер беруі тиіс.

Question Loop activity. Бұл ойында топ студенттеріне арнайы карточкалар таратылады, карточканың бір бетінде студенттің басқа топтастарына қойылатын сұрағы, ал басқа бетінде өзгеше сұрақтың жауабы жазылады. Ойынның басында бір студент өз сұрағын оқи бастайды. Кейін бұл сұрақтың дұрыс жауабын өзінің карточкасында тапқан басқа топ студенті карточканы аударып, өз сұрағын оқи бастайды, сөйтіп ойын әрі қарай жалғасады. Осылайша, барлық топ студенттері өз сұрақтарын оқып, жауаптар анықталады. Кейін ойында тізбек аяқталып, цикл сұрақты бірінші оқыған студентке оралады.

«G*rab it*!». Бұл ойын топтық жұмыс үшін арналған. Мысалы, ойын үшін 4–5 студенттерден құрылатын 4 кіші топтар құрылады. Оқытушы алдын-ала сабақтың тақырыбы бойынша анықтамалары бар 4 мәтін және одан бөлек бұл мәтіндерде кездесетін терминдері жазылған карточкаларды дайындайды. Оқытушы студенттерге карточкалар (мысалы, әрбір топқа 12 термин) таратады. Топтардан бір-бірден спикерлерден таңдалады. Топтар кезек-кезекпен ойнайды. Спикер мәтінді дауыстап оқуды бастайды. Бұл кезде топтың студенттері мәтіннен естіген терминдерді таратылған карточкалардан жарыса тез тауып, оларды шап беріп ұстайды. Әрбір топ көшбасшысы көп карточкаларды жинаған студент болып саналады.

«True or false». Оқытушы студенттерге сабақ тақырыбы бойынша тұжырымдамалар жазылған кесте таратады. (кесте 2).

2 - к е с т е

«True or false» іс-әрекеттілік

№	THE STATEMENT	ANSWER (TRUE /FALSE)
1		
2		
...		

Студенттер берілген тұжырымдамалардың шын немесе жалған екенін анықтап, оған сәйкесті белгі жазу керек. Оқытушы студенттердің орындалған тапсырманың дұрыстығын тексеру үшін, олардан жауаптарды сұрап, сол жауаптардың дұрыстығын дәлелдейтін себеп не дәлелді ағылшын тілінде беруді сұрайды.

«Reading activity». Мәтінді сабақтың орталық ядросы ретінде қолдануға болады. Уақыттың шектеулі болуына байланысты бұл мәтіннің бір бөлігі болуы мүмкін. Оқытушы интерактивтік тақтада немесе арнайы карточкаларда жазылған сабақтың тақырыбы бойынша мәтінді береді. Мәтіннің ішінде кейбір бос орындар қалдырылады. Мәтіннің төменгі жағында бос орындарға қойылатын сөздер беріледі. Тапсырма бойынша студенттер бұл сөздерді мәтіндегі бос орындарға дұрыс сәйкестендіріп жазу керек.

Визуализация құралдарын қолдану (бейнероликтерді көру). Ең алдымен, мұнда бейтаныс лексикалық бірліктерді (сөздерді) жылдам түсінуді қамтамасыз ету үшін көрнекі құралдар ретінде қолданылатын нақты объектілер жатады. Жылдамдық пен оңайлылықтан басқа, затты көру мүмкіндігі осы ұғымды есте сақтауға оң әсер етеді және келесі сатыда осы терминологияны пайдалана отырып мүмкін болатын мәселелерді жояды.

Мультимедиа құралдары негізгі лексикамен алдын ала танысу үшін де пайдаланылуы мүмкін.

Сонымен қатар, мультимедиялық құралдарды дұрыс пайдалана білу олардың қолданылуын кеңейтуге және олардың көмегімен кез келген сұрақты топта талқылауды немесе пікірталасты ұйымдастыруға мүмкіндік береді. Мысалы, қысқа кіріспелі бейнероликті көруден кейін білім алушыларға тапсырмаларды беруге болады. Тапсырмалар мысалдары 3-кестеде келтірілген.

3 - к е с т е

Қысқа бейнероликтермен жұмыс істеу мысалы

Мақсаты	Тапсырма
– сабақтың тақырыбына қызығушылықты ояту; – пән бойынша білімді анықтау; – тіл бойынша білімді анықтау	Бейнероликті көріңіз. Бейнероликте көрсетілген затты немесе физикалық құбылыс (процесті) атаңыз. Анықтаманы айтыңыз.
– терминология және пәндік мазмұны бойынша; білімдерін бар / жоғын анықтау; – студенттерді мәтіннен ақпарат алуға дайындау	Ми шабуылы (топпен жұмыс). Тақтада студенттердің жауаптарынан алынған түсініктер картасын құрастыру.

Мысалы, студенттер сабақтың негізі ойы немесе тақырыбы туралы бейнеролик көреді (мысалы, YouTube каналынан). Бейнеролик кезінде студенттер түсінбеген сөздерді жазып алады, соңында олар оқытушыға сұрақтар қойып, сондай-ақ бейнероликтегі оқу ақпараты арқылы ой пікірлерін қорытындылайды.

«Domino game activity». Студенттер екі парақ жолақтарын бір-бірімен қосады. Әрбір парақ жолағында бір сөйлемнің бөлігі жазылады. Мағынаға ие сөйлемді алу мақсатында студенттер парақ жолақтарын бір-бірімен сәйкестендіріп қосу керек.

Интерактивті викторина. Оқытушы бірнеше жауап нұсқалары бар сұрақтардан құралатын викторина ойынды ұйымдастырады. Әрбір студенттер тобы дұрыс жауап таңдау үшін анықталған уақытқа ие болады. Сондықтан жауап беру уақытына және берген дұрыс жауаптарға байланысты топтар ұпайларды жинайды [11].

Кестелерді, сұлбаларды, алгоритмдерді, фреймдерді құру.

Студенттердің назарын белгілі бір грамматикалық формаға немесе функционалдық тілге қатысты фразаларға аудару үшін кестелер мен сұлбаларды қолдануға болады. Олар ақпаратты визуализациялауға және жүйелендіруге көмектеседі. Кесте нақты мысалдардан құрылуы тиіс, яғни студент сөйлемнің құрылымын түсіну және оны кейіннен басқа контексте қолдану үшін қажетті жалпылаулар берілуі тиіс. 4-кестеде мысал үшін ырықсыз етіс (Passive Voice) сұлба түрінде берілген.

4 - к е с т е

Осы шақтағы ырықсыз етіс

WHAT	(to be)	ACTION (V3)		WHOM/WHAT
diffusion	is	described	by	a second order differential equation
the nucleus	was	surrounded		7 more orbiting electrons
studies of nuclear spin	were	carried out		Franco Rasetti

Рефлексия және сабақ қорытындысын жасау.

Семестр соңында студенттерге топтық жұмыс ретінде жоба тапсырмасын орындауды ұсынуға болады. Студенттерге нақты тақырыптар бойынша мини-жоба дайындап, қорғауға ұсынылады. Ең соңғы сабақта студенттер өздерінің мини-жобаларына презентация жасайды.

Білім алушылардың қанағаттануы. Студенттердің қанағаттанушылығы емтихандар аяқталғаннан кейін семестр соңында сауалнаманың көмегімен бағаланды. Бұл сауалнама екі негізгі бөлімнен тұратын сұрақтардан құрылды. Сауалнаманың бірінші бөлімі ағылшын тілін меңгеруі туралы кейбір ақпарат алуға; ал екінші бөлімі студенттердің оқыту тәжірибесімен қанағаттануын бағалауға арналған. Жоғарыда аталған екі топтың бүкіл студенттері сауалнамаға қатысты. 5-кестеде екінші блокқа енгізілген маңызды сұрақтар бойынша алынған нәтижелер жинақталған.

5 - к е с т е

Студенттердің қанағаттану нәтижелері

Сұрақтар				
	Жеңіл	Қиын емес	Қиын	Өте қиын
Сіздің ойыңызша, ағылшын тілінде жүргізілген сабақтар қандай болды?	19%	76%	5 %	0 %
Курстардың мазмұнына қанағаттанасыз ба?	Иә, техникалық және ағылшын мазмұнымен	Тек техникалық мазмұнымен	Тек ағылшын мазмұнымен	Жоқ, техникалық және ағылшын мазмұнымен
	100%	0 %	0 %	0 %
Сіз ағылшын тілінде оқылатын басқа курстарына барғыңыз келе ме?	Ия	Жоқ	Білмеймін	
	80 %	20 %	0 %	

Кестеден көрінетіндей, студенттердің CLIL тәжірибесімен қанағаттануы оңтайлы деп санауға болады, себебі олардың 95% ағылшын тіліндегі сабақтары «жеңіл» (19%) немесе «қиын емес» (76%) деп жауап берді. Сонымен бірге студенттердің 100% сабақтардың техникалық және ағылшын мазмұнымен қанағаттанған. Сонымен қатар, 80% ағылшын тіліндегі басқа курстарына қатысуға қызығушылық танытты.

Студенттерді бағалау процедурасы мен бағалау критерийлері. Төмендегі келтірілгендердің әрқайсысы қорытынды бағаны алуға үлесін қосады:

1. *Сыныптағы студенттердің жұмысын бағалау (10%):* студенттер тиянақты, қызығушылық білдіреді және сабақтың барысында белсенділік танытады. Ал топтық жұмыста олар бірігіп, бір-біріне қолдау көрсетеді.

2. *Жұмыс дәптері (10%):* студенттер күнделікті тапсырмаларды орындайды, үйде жұмыстарын толық аяқтап, жалпылайды, қорытынды жасайды, сөздің дұрыс жазылуын ескереді.

3. *Зертханалық жұмыс (30%).* Бұл бөлім екі аспекті бойынша бағаланады: эксперимент (10 %) — орындалуы, нәтиже алуы, есеп беру (10%) — студенттер әрбір зертханалық жұмысты орындағаннан кейін есеп береді, есеп беруге зертханалық жұмыстың мақсаты, құрал-жабдықтары, орындалу тәртібі, нәтижелер мен бақылаулар, қорытынды мен графиктер кіреді, ауызша презентация жасау (10 %) — ақпаратты жинау, түсіндіру, грамматика, сөздік қор және сөйлеу.

4. *Минижоба қорғау*. (10%).

5. *Тестілеу* (40%). Әрбір сабақтың соңында тестілеу жүргізіледі. Бұл жағдайда тест сұрақтарына ғылыми сөздік енгізу керек. Тестілеу лексика-грамматикалық тест болып табылады, оған пәндік сала бойынша терминология жиынтығы, қолданылатын грамматика мен функционалдық тілді тексеруге арналған тапсырмалар және т.б. кіреді.

Ұсынылған пәндік-тілдік интеграцияланған оқыту нәтижелерін бағалау жүйесі CLIL оқытушының жұмысын жеңілдетуі мүмкін.

Педагогикалық экспериментті жүргізу келесі нәтижелерді көрсетті: CLIL технологиясы көмегімен жаратылыстану-ғылыми пәндерді оқыту барысында физика-техникалық факультеттің 4-курс студенттерінің шетел тілді кәсіби-коммуникативтік құзыреттілігінің қалыптасу деңгейін сөйлеу іс-әрекетінің барлық үш түрі (сөйлеу, тыңдалым және оқу) бойынша артты. Студенттер ағылшын тілінде терминологияны меңгеруде, тапсырмалармен жұмыс істеу барысында үлкен қызығушылық танытты, себебі бұл оларды пән бойынша білімдерді тереңдетуге ықпал тигізді.

Болашақ мұғалімдердің шетел тілді кәсіби-коммуникативті құзыреттілікті қалыптастыру заманауи шетел тілді білім берудің негізгі мақсаты болып табылады. Өйткені шетел тілді кәсіби-коммуникативті құзыреттілік мұғалімнің жалпы құзыреттілігінің маңызды құраушысы болып, өз кезекті болашақта мәдениет-аралық кәсіби өзара әрекеттесуге дайындайды.

CLIL технологиясы кез келген білім беру технологиясы сияқты артықшылықтар мен кемшіліктерге ие. Берілген технологияның оңтайлы сәті шетел тілді меңгеруге ынтасын арттыру болып табылады, бұл мақсатты бағытталған түрге айналады, яғни шетел тілі нақты есептер мен міндеттерді шешуде қолданылады. Берілген технологияны қолдану нәтижесінде студенттер кәсіби контекстіде шетел тілінде коммуникацияға қатысу үшін дайындыққа көп назар аударған. Сонда олар өздерінің салаларында көбірек сұранысқа ие болады.

Берілген CLIL технологиясын енгізу кезінде нақты қиындықтар туындауы мүмкін. Олардың біреуі — пәнді оқытатын оқытушының шетел тілін жеткілікті емес деңгейде білуі. Берілген мәселенің шешімі оқытушының шетел тілінің мұғалімімен бірігіп дайындалуы.

Қорытынды

Мақалада Е.А. Бөкетов атындағы Қарағанды мемлекеттік университетінің физика-техникалық факультетінде көптілді білім беру жобасын жүзеге асырудағы негізгі нәтижелер көрсетілген. Сонымен, мақалада CLIL технологиясы көмегімен ағылшын тілінде жаратылыстану-ғылыми пәндерді оқытуды ұйымдастыру ерекшеліктері қарастырылған. CLIL-технологиясының қолдануымен оқытудың әдіс-тәсілі жеткілікті тиімді болып табылады. Себебі оқытушы бүкіл оқыту талаптарын ескере отырып, өз бетімен тілдік контентін іріктеп, білім беру процесінің барлық қатысушыларының интеграциялау дәрежесін анықтайды. CLIL технологиясын қолдануымен жүргізілетін сабақтарда оқытушы мен студенттердің тиімді жұмысы студентте шетел тілді кәсіби — коммуникативті құзыреттіліктің қажетті деңгейін қалыптастыруға, жалпы ғылыми білімдер мен іскерліктерінің дамуына, болашақ мамандарды мәдениетаралық өзара әрекеттесуге даярлауға ықпал тигізеді.

Әдебиеттер тізімі

1 Marsh D. Content and Language Integrated Learning: The European Dimension — Actions, Trends and Foresight Potential / D. Marsh. — Cambridge: Cambridge University Press, 2002. — 552 p.

2 Pavón V. Examining teacher roles and competences in Content and Language Integrated Learning (CLIL) / V. Pavón, M. Ellison // Lingvarvmarena. — 2013. — №4. — C. 65–78.

3 Mehisto P. Uncovering CLIL: Content and Language Integrated Learning and Multilingual Education / P.Mehisto. — London: MacMillan Oxford, 2008. — 240 p.

4 Coyle D., Hood P., Marsh D. Content and Language Integrated Learning / D. Coyle, P. Hood, D. Marsh. — Cambridge: Cambridge University Press, 2010. — 184 p.

5 Белова Л.А. Подготовка будущих учителей к межкультурному профессиональному взаимодействию с использованием технологии CLIL / Л.А. Белова, М.Г. Заседателева, Е.Б. Быстрай, Т.В. Штыкова // Вестн. Челяб. гос. пед. ун-та. — 2018. — № 4. — С. 9–16.

6 Kuralbayeva, Zh.Sh. Application of CLIL teaching methods in the educational process of physics lessons / Zh.Sh. Kuralbayeva, A.S. Kudussov, A.Z. Beybitova // Bulletin of the University of Karaganda-Physics. — 2017. — №1(85). — P. 97–103.

7 Лебедева Е.А. Совершенствование иноязычной компетенции студентов-юристов / Е.А. Лебедева // Наука и образование: хозяйство и экономика, предпринимательство, право и управление. — 2011. — № 7 (13). — С. 49–52.

8 Сақыпова С.Е. «Газ заңдары» тақырыбын оқытуда инновациялық технологияларды қолдану әдістемесі / С.Е. Сақыпова, Р.И. Жұманова, Ж.Т. Камбарова // ҚарМУ хабаршысы. — Физика сериясы. — 2011. — №3 (63). — Б. 62–68.

9 Омаркұлов К.А. Геометриялық оптика тақырыбы бойынша компьютерлік зертханалық жұмыстарды өткізу әдістемесі / К.А. Омаркұлов, С.Е. Сакипова, Р.И. Жұманова, Ж.Т. Камбарова // Вестн. Караганд. ун-та. Сер. физика. — 2013. — №4 (72). — С. 88–95.

10 Мусабекова А.М. Оқушылардың функционалдық сауаттылығын дамытуға бағытталған физиканы оқытудағы инновациялық тәсілдер / А.М. Мусабекова, Р.И. Жұманова, Ж.Т. Камбарова // Вестн. Караганд. ун-та. Сер. Физика. — 2015. — №2 (78). — С. 92–98.

11 Moreno Concezzi. CLIL Teaching in Physics: Methodologies and Technological Innovations / New perspectives in Science Education: International Conference Proceedings (16-17 March 2017). — Florence: Pixel, 2017. — P. 285–289.

Ж.Т. Камбарова, А.К. Тусупбекова

Особенности использования CLIL подхода в обучении естественнонаучным дисциплинам в рамках реализации полиязычного образования студентов

Языковое образование через изучение языковых дисциплин и преподавание математических и естественнонаучных дисциплин на иностранном языке является основным механизмом практической реализации полиязычного образования в Республике Казахстан. В статье представлен опыт реализации CLIL технологии в обучении естественнонаучным дисциплинам на физико-техническом факультете Карагандинского государственного университета им. академика Е.А. Букетова. Исследовано влияние методики «Content and language integrated learning» (CLIL) на обучение студентов 4-го курса физико-технического факультета, обучающихся по образовательной программе 5В011000 — «Физика» при преподавании дисциплин по выбору по специальности «Computer methods in Physics» и «Nuclear physics». Обобщены преимущества и недостатки использования CLIL технологии. В качестве примера реализации CLIL методики приведены типы заданий. В ходе педагогического исследования изучены основные средства и формы контроля. Представлены процедура и критерии оценки студентов. В заключении статьи подведены итоги педагогического исследования и результаты. Применение методики CLIL в учебном процессе повышает мотивацию обучающихся к овладению английским языком и, в свою очередь, помогает обучающим при дальнейшем овладении знаниями и применении полученных знаний в будущей профессиональной сфере. Технология CLIL является важным инструментом для стимулирования студентов к изучению не только иностранного языка, но и других специальных дисциплин.

Ключевые слова: предметно-языковое интегрированное обучение, технология CLIL, методология, полиязычное образование, профессионально-коммуникативная компетентность, критерии оценки.

Zh.T. Kambarova, A.K. Tussupbekova

Features of using CLIL approach in teaching natural scientific disciplines in the framework of implementation of multilingual education of students

Language education through the study of language disciplines and the teaching of mathematical and natural scientific disciplines in a foreign language is the main mechanism for the practical implementation of multilingual education in The Republic of Kazakhstan. This article presents a experience of implementing CLIL technology in teaching natural scientific disciplines at the faculty of physics and technology of Karaganda State University named after academician Y.A. Buketov. The influence of the Content and language integrated learning (CLIL) method on the learning the «Computer methods in Physics» and «Nuclear physics» courses of choice by specialty by 4th-year students (the 5B011000-Physics educational program) of the faculty of physics and technology is studied in the work. The article summarizes the advantages and disadvantages of using CLIL technology. Types of tasks are given as an example of the implementation of the CLIL method. During the pedagogical study, the basic means and forms of control were examined.The procedure and criteria for evaluating students are presented. In conclusion of the article, the results of pedagogical research was summarized. Using of the CLIL methodology in the educational process increases the motivation of students to studying the English language and, in turn, helps students to

further master the knowledge and apply the acquired knowledge in the future professional field. CLIL technology is an important tool to stimulate students to learn not only a foreign language, but also other special courses.

Keywords: Content and language integrated learning, CLIL technology, methodology, multilingual teaching, foreign professional and communicative competence, criteria for evaluation.

References

1 Marsh, D. (2002). *Content and Language Integrated Learning: The European Dimension — Actions, Trends and Foresight Potential.* Cambridge: Cambridge University Press.

2 Pavón, V., & Ellison, M. (2013). Examining teacher roles and competences in Content and Language Integrated Learning (CLIL). *Lingvarvmarena, 4,* 65–78.

3 Mehisto, P. (2008). *Uncovering CLIL: Content and Language Integrated Learning and Multilingual Education.* London: MacMillan Oxford.

4 Coyle, D., Hood, P., & Marsh, D. (2010). *Content and Language Integrated Learning.* Cambridge: Cambridge University Press.

5 Belova, L.A., Zasedateleva, M.G., Bystray, Ye.B., & Shtykova, T.V. (2018). Podhotovka budushchikh uchitelei k mezhkulturnomu professionalnomu vzaimodeistviiu s ispolzovaniem tekhnolohii CLIL [Preparing future teachers for intercultural professional interaction using CLIL technology]. *Vestnik Cheliabinskoho hosudarstvennoho pedahohicheskoho universiteta — Bulletin of the Chelyabinsk State Pedagogical University, No. 4,* 9-16 [in Russian].

6 Kuralbayeva, Zh.Sh., Kudussov, A.S., & Beybitova, A.Z. (2017). Application of CLIL teaching methods in the educational process of physics lessons. *Bulletin of the University of Karaganda-Physics, 1(85),* 97–103.

7 Lebedeva, Ye.A. (2011). Sovershenstvovanie inoiazychnoi kompetentsii studentov-yuristov [Improving the foreign language competence of law students]. *Nauka i obrazovanie: khoziaistvo i ekonomika, predprinimatelstvo, pravo i upravlenie — Science and education: economy and economics; entrepreneurship; law and management, 7 (13),* 49–52 [in Russian].

8 Sakipova, S.E., Zhumanova, R.I. & Kambarova, Zh.T. (2011). «Haz zandary» taqyrybyn oqytuda innovatsiyaluq tekhnolohialardy qoldanu adistemesi [The methodology of application of innovative technologies at studying the theme «Gas Laws»]. *Vestnik Karahandinskoho universiteta. Seriia fizika — Bulletin of the University of Karaganda-Physics, 3 (63),* 62–68 [in Kazakh].

9 Omarkulov, K.A., Sakipova, S.E., Zhumanova, R.I., & Kambarova, Zh.T. (2013). Heometriialyq optika taqyryby boiynsha kompiuterlik zertkhanalyq zhumystardy otkizu adistemesi [Methodology of computer lab works on geometrical optics]. *Vestnik Karahandinskoho universiteta. Seriia fizika — Bulletin of the University of Karaganda-Physics, 4 (72),* 88–95 [in Kazakh].

10 Musabekova, A.M., Zhumanova, R.I, & Kambarova, Zh.T. (2015). Oqushylardyn funktsionaldyq sauattylyhin damytuga bagyttalgan fizikany oqytudagy innovatsiialyq tasilder [Innovative approaches to the teaching physics aimed to the development of functional literacy of pupils]. *Vestnik Karahandinskoho universiteta. Seriia fizika — Bulletin of the University of Karaganda-Physics, 2 (78),* 92–98 [in Kazakh].

11 Moreno Concezzi (2017). CLIL Teaching in Physics: Methodologies and Technological Innovations. *International Conference Proceedings: New perspectives in Science Education.* (pp. 285–289) Florence: Pixel.

DOI 10.31489/2020Ph2/136-142

УДК 621.383:537.311.33

Л.В. Чиркова, К.Т. Ермаганбетов, Л. Тезекбаева

Карагандинский государственный университет им. Е.А. Букетова, Казахстан
(E-mail: Tchlv_53@mail.ru)

Принципы синергетики в подготовке специалистов физико-технического профиля

В статье рассмотрены вопросы использования основных принципов синергетики в подготовке специалистов физико-технического профиля при изучении дисциплины «Физическая электроника». Работа основана на многолетнем опыте преподавания авторами названной дисциплины на кафедре радиофизики и электроники Карагандинского государственного университета им. академика Е.А. Букетова. Показано, что система «полупроводниковая структура + внешний источник электрической энергии» может рассматриваться как открытая неравновесная термодинамическая система, в которой получают развитие кооперативные процессы стихийной самоорганизации за счет постоянного обмена энергией и веществом. Проанализированы физические процессы в биполярных транзисторах в активном режиме работы. Путем качественного теоретического анализа установлено, что в рассматриваемой системе возникают взаимосодействующие самоорганизующиеся процессы, в результате которых происходит самопроизвольное понижение потенциального барьера в области эмиттерного и повышение аналогичного барьера в области коллекторного переходов; наблюдается самопроизвольная инжекция неосновных носителей заряда в базу, в результате чего происходит самопроизвольное увеличение концентрации неосновных носителей заряда в приграничном с переходом слое базы. Самопроизвольный перенос носителей заряда через базу к коллектору вызывает самопроизвольное понижение сопротивления коллекторного перехода до сопротивления прямосмещенного эмиттерного перехода и т.д. Все перечисленные выше процессы обусловливают самопроизвольное перераспределение напряжения источника питания, в результате чего мощность на выходе транзистора начинает превышать мощность на его входе, т.е. биполярный транзистор будет усиливать мощность.

Ключевые слова: синергетика, открытая система, полупроводниковая структура, биполярный транзистор, режимы работы, теоретический анализ, процессы самоорганизации.

Основными критериями учебной деятельности вузов являются качественная подготовка специалистов, их востребованность и конкурентоспособность на рынке труда. Стремительно меняющийся мир ставит перед государством, обществом и высшей школой задачи ее реформирования, создания современной индустрии образования. Проблема подготовки специалистов сегодня требует кардинально новой научно-педагогической основы, что определяет ее необходимость и актуальность.

Развитие современного образования можно определить как нелинейное, что связано в том числе и с социально-экономическими преобразованиями в стране. Требования общества к системе образования включают в себя несколько аспектов, основными из которых являются усиление экологической составляющей образовательных программ, реализация гуманитарного компонента в естественнонаучном и инженерном образовании, формирование современной естественнонаучной картины мира и ряд других. Все перечисленные аспекты находят свое отражение в рамках междисциплинарного научного направления — синергетики, которое базируется на результатах исследований в области нелинейной динамики, термодинамики необратимых процессов, статистической физики, физики лазеров, качественной теории дифференциальных уравнений и т.д. [1].

В течение довольно непродолжительного времени, прошедшего с момента своего возникновения, синергетика, как теория неравновесных процессов, превращается во всеобщую теорию развития, имеющую серьезные мировоззренческие последствия. Смысл и содержание этой новой интегральной науки состоит в том, что в открытых системах, обменивающихся с внешней средой энергией, веществом и информацией, возникают процессы стихийной самоорганизации. Они приводят к возникновению из физического хаоса устойчивых упорядоченных процессов и структур с новыми свойствами систем. Это общее определение справедливо для систем любой природы. Синергетика изучает конкретные принципы и механизмы самоструктурирования естественных и технических систем. То есть основное внимание она сосредотачивает на кооперативных, когерентных и самосогласованных процессах, происходящих в сложных нелинейных системах.

Вообще понятие системы является для синергетики объединяющим. При этом, помимо формирования общей системной концепции — самоорганизации, синергетика учитывает конкретное, например, физическое, содержание рассматриваемых явлений и процессов [2]. Среди множества определений понятие «система» многие исследователи выделяют как самое оптимальное определение, сформулированное П.К. Анохиным: «Системой можно назвать только такой комплекс избирательно вовлеченных компонентов, у которых взаимодействие и взаимоотношение приобретают характер взаимосодействия компонентов на получение фиксированного полезного результата» [2].

В настоящее время общепризнанными фундаментальными свойствами синергетических систем являются обязательный обмен с внешней средой (энергией, веществом, информацией) и непременное взаимосодействие, т.е. когерентность поведения между компонентами системы.

На современном этапе развития общества, в условиях усложнения производственных отношений, его технической и социальной инфраструктуры, решающим оказывается изменение отношения образовательных структур к подготовке специалистов в любой области. Это существенным образом зависит от организации целостного педагогического процесса, который заключается в создании новых организационных приемов, объединении научных направлений, инновационной деятельности, которые можно осуществить посредством внедрения синергетического подхода в образовании.

Использование синергетического подхода позволяет по-новому раскрыть научно-педагогическое знание, ориентированное на многомерность, многокомпонентность познаваемых процессов, обнаружение в них нераскрытых или недостаточно раскрытых состояний, признание большой роли случайности в их развитии [3].

Чаще всего под синергетикой понимается теория самоорганизации. В то же время необходимо отметить, что синергетика — более комплексная система, нежели самоорганизация. Так, Г.Хакен [1] определяет самоорганизующиеся системы как системы, обретающие присущие им структуры или функции без какого-то вмешательства извне. Самоорганизация имеет место исключительно в таких системах, которые обладают высоким уровнем сложности и достаточным количеством элементов, связи между которыми имеют не жесткий, а вероятностный характер. Отличительной особенностью процессов самоорганизации является нецеленаправленный, естественный, спонтанный характер. Эти процессы, хотя и протекают во взаимодействии системы с окружающей средой, остаются автономными, не зависящими от среды. Сложность открытых систем представляет широкие возможности для существования в них коллективных явлений.

Понятие открытых физических систем широко применяется в физике полупроводников и полупроводниковых приборов, составляющих основу современной электроники и микроэлектроники.

Полупроводниковые кристаллы являются сложными динамическими системами, в которых возможно возникновение электрических неустойчивостей (срыв тока, спонтанные колебания тока или напряжения, переключение и гистерезис в вольтамперной характеристике и т.д.) [4, 5]. Большинство подобных неустойчивостей можно рассматривать как самоорганизацию, возникающую в термодинамической неравновесной системе. Чаще всего электрические неустойчивости оказывают негативное влияние на характеристики полупроводниковых приборов, но в отдельных случаях используются специально. Например, для генерации СВЧ-излучения в диапазоне от 0,1 до 1000 Гц, для усиления в гигагерцевом диапазоне частот, где не могут быть использованы обычные транзисторы [6].

На основе многолетнего опыта преподавания дисциплины «Физическая электроника» на кафедре радиофизики и электроники Карагандинского государственного университета имени Е.А. Букетова авторы разработали концепцию синергетического рассмотрения основных физических процессов, протекающих в полупроводниковых структурах и приборах (таких как *p-n*- переход, туннельный диод, диод Ганна, лавинно-пролетный диод, некоторые многослойные полупроводниковые структуры), и электрических неустойчивостей в них. Во всех этих структурах и устройствах, как было показано авторами [7–10], имеют место процессы самоорганизации. Теоретические изыскания были подкреплены многочисленными констатирующими (проведение отдельных упражнений и заданий по отдельным темам дисциплины) и обучающими (проведение отдельных занятий) педагогическими экспериментами.

Представленная статья продолжает цикл публикаций авторов, посвященных рассмотрению процессов самоорганизации в полупроводниковых структурах и приборах.

В основу статьи легли результаты теоретического анализа процессов самоорганизации, происходящих в полупроводниковых приборах с двумя электронно-дырочными переходами на примере биполярных транзисторов, полученные одним из авторов при выполнении магистерской диссертации. В

ходе работы были рассмотрены процессы обмена с внешней средой и взаимосодействия в биполярном транзисторе в режиме усиления.

Как известно, существует четыре режима работы биполярного транзистора: активный, насыщения, отсечки и инверсный. В активном режиме эмиттерный переход включен в прямом, а коллекторный переход — в обратном направлении. В режиме насыщения и эмиттерный, и коллекторный переходы включены в прямом направлении. В режиме отсечки и эмиттерный, и коллекторный переходы включены в обратном направлении. В инверсном режиме коллекторный переход включен в прямом, а эмиттерный переход — в обратном направлении.

Рассмотрим физические процессы и участие носителей заряда в самоорганизующихся процессах, происходящие в биполярном транзисторе при различных режимах работы.

Режим усиления слабых сигналов. В режиме усиления источника энергии эмиттерный переход транзистора включен в прямом, а коллекторный переход — в обратном направлении.

Модель (*а*), энергетическая диаграмма (*б*) биполярного транзистора и схемы физических процессов, происходящих в нем, показаны на рисунке 1.

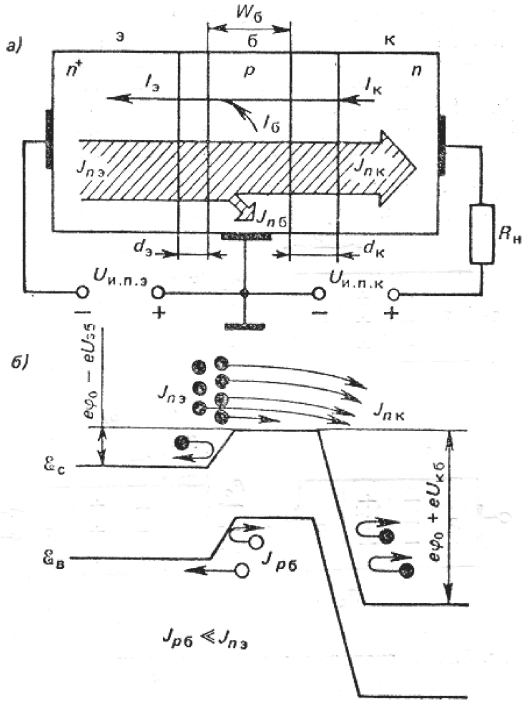

Рисунок 1. Модель (*а*), энергетическая диаграмма (*б*) биполярного транзистора $n^+ - p - n$ и схемы физических процессов, происходящих в нем [11]

На рисунке 1 даны следующие обозначения: $I_э, I_б, I_k$ — эмиттерный, базовый, коллекторный токи; $J_{nэ}$, $J_{nб}$, J_{nk}, $J_{nб}$ — диффузионные составляющие токов; $U_{ипэ}, U_{ипк}$ — источники питания; $q\varphi_0$, $qU_{эб}$, $qU_{кб}$ — высота потенциального барьера в равновесном состоянии, *самопроизвольное уменьшение* и *увеличение* высоты потенциального барьера, соответственно, эмиттерного и коллекторного переходов. Электроны обозначены темными кругами, дырки — светлыми кругами.

Если биполярный транзистор, состоящий из полупроводников *n*- и *p*-типов с носителями заряда (электронами и дырками) и внешних источников $U_{ипэ}$и $U_{ипк}$, считать как единую термодинамическую систему «биполярный транзистор + источники энергии», то она удовлетворяет всем требованиям синергетической науки:

– система состоит из многих элементов: носители заряда в полупроводниках, полупроводники *n*- и *p*-типов, источники энергии $U_{ипэ}, U_{ипк}$;

– элементы системы между собой обмениваются энергией и электронами, т.е. система находится в неравновесном состоянии;

– носители заряда на пути свободного пробега *самопроизвольно увеличивают* свою энергию за счет мощности внешних источников энергии и при столкновении с дефектами кристаллической ре-

шетки полностью отдают энергию кристаллу. Температура кристалла растет. Нагретый кристалл избыток тепловой энергии *самопроизвольно отдает* окружающей среде. Следовательно, система «биполярный транзистор + источники энергии» является открытой, неравновесной термодинамической системой.

Рассмотрим физические процессы и процессы самоорганизации, происходящие в биполярном транзисторе в режиме усиления. Функционирование биполярного транзистора в режиме усиления основано на *самопроизвольном* изменении сопротивления обратносмещенного коллекторного *p-n*-перехода при *самопроизвольной инжекции* неосновных носителей заряда.

Сопротивление обратносмещенного коллекторного *p-n*-перехода очень велико — несколько мегаом и более. Отметим одно важное обстоятельство. *Обратносмещенный p-n-переход* (рис. 2, *а*) *оказывает сопротивление только потокам* ***основных носителей заряда***, неосновные носители заряда проходят его, «*самопроизвольно скатываются* с потенциального барьера», практически не встречая сопротивления (рис. 2, *б*). Следовательно, при достаточно высоком уровне инжекции можно значительно увеличить ток в обратносмещенном *p-n*-переходе и тем самым снизить его сопротивление.

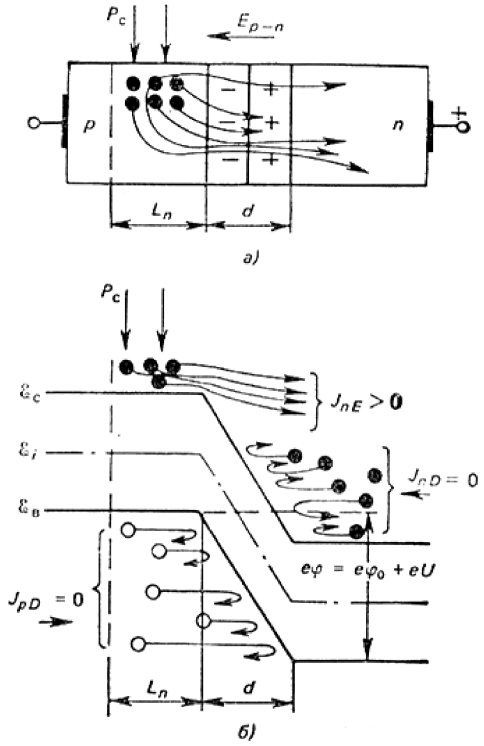

Рисунок 2. Схема инжекции электронов в *p*-область (*а*) и на энергетической диаграмме (*б*) [11]

При приложении прямого смещения к эмиттерному переходу дырки *самопроизвольно инжектируют* в *n*-слой, электроны *самопроизвольно инжектируют* в *p*-слой. Ток через эмиттерный переход должен определяться суммой потоков, *самопроизвольно инжектируемых* электронов и дырок. Биполярные транзисторы изготавливают так, чтобы концентрация электронов в эмиттере значительно превышала концентрацию дырок в базе. В этом случае малым потоком дырок, *самопроизвольно инжектируемых* из базы в эмиттер, можно пренебречь и считать, что при прямом смещении весь ток эмиттера определяется только потоком *самопроизвольно* инжектированных электронов:

$$|J_{n\text{э}}| \sim I_{n\text{э}} \approx I_{\text{э}}. \quad (1)$$

С целью уменьшения потерь на рекомбинацию инжектированных в базу электронов эмиттерный и коллекторный переходы располагают на расстоянии, меньшим диффузионной длины носителей заряда: $W_{\text{б}} \ll L_n$.

При прямом смещении эмиттерного перехода поток *самопроизвольно инжектированных* в базу электронов, практически без потерь на рекомбинацию (база тонкая и концентрация дырок мала), доходит до коллектора, поэтому $J_{n\text{э}} \approx J_{nk}$, или $I_{\text{э}} \approx I_k$. В результате ток коллектора *самопроизвольно*

повышается от очень малого значения обратного тока I_{k0} до $I_к \approx I_э$. По этой причине ток в обратносмещенном коллекторном переходе *самопроизвольно сравнивается* с током в прямосмещенном эмиттерном переходе.

Увеличение тока в обратносмещенном коллекторном переходе при неизменном напряжении источника питания $U_{ипк}$ физически означает, что сопротивление коллекторного перехода *самопроизвольно уменьшилось* и стало сравнимым с сопротивлением эмиттерного перехода. Следовательно, в результате инжекции неосновных носителей заряда происходит *самопроизвольное изменение* сопротивления коллекторного перехода.

Сопротивление обратносмещенного коллекторного перехода *самопроизвольно снижается* пропорционально *самопроизвольному возрастанию* тока инжекции. В результате инжекции ток коллектора может возрасти на 4-5 порядков, сопротивление его при этом соответственно на 4-5 порядков *самопроизвольно снизится*.

Сопротивление нагрузки R_k в цепи коллектора обычно носит постоянный характер и составляет около 1 МОм. Поскольку сопротивление коллектора *самопроизвольно уменьшается* и *становится* значительно меньшим сопротивления нагрузки, падением напряжения на коллекторе можно пренебречь и считать, что все напряжение источника питания $U_{ипк}$ будет сосредоточено на нагрузке: $U_{ипк} \approx I_э R_н$.

Падение напряжения на эмиттере равно: $U_{эб} = U_{вх} = I_э R_э$. Сопротивление нагрузки $R_н$ значительно превышает величину сопротивления $R_э$ прямосмещенного эмиттерного перехода. Поэтому при сравнимых токах эмиттера и коллектора будет выполняться соотношение $U_{вых} \gg U_{вх}$. Выделяемая на нагрузке мощность $P_{вых} \approx U_{вых} I_э$, а мощность, потребляемая в эмиттерной цепи, $P_{вх} = U_{вх} I_э$. Так как $U_{вых} \gg U_{вх}$, то $P_{вых} \gg P_{вх}$.

Таким образом, биполярный транзистор является усилительным прибором, так как усиливает мощность.

Из приведенного выше анализа работы транзистора в режиме усиления можно сделать следующие выводы:

Система «биполярный транзистор + источники энергии $U_{ипэ}$и $U_{ипк}$» является открытой, неравновесной термодинамической системой, удовлетворяющей всем требованиям синергетики.

В рассматриваемой системе возникают следующие самоорганизующиеся процессы:

– в зависимости от особенностей взаимодействий источников энергий и биполярного транзистора потенциальный барьер эмиттерного перехода *самопроизвольно понижается*, а потенциальный барьер коллекторного перехода *самопроизвольно повышается*;

– при приложении смещения в прямом направлении самопроизвольно возникает инжекция неосновных носителей заряда в базу, что приводит к самопроизвольному увеличению концентрации неосновных носителей заряда в приграничном переходом слое базы;

– самопроизвольный рост концентрации неосновных носителей заряда в приграничном с переходом слое базы приводит к самопроизвольному переносу неосновных носителей заряда по базе от эмиттера к коллектору;

– самопроизвольный перенос носителей заряда через базу к коллектору вызывает самопроизвольное понижение сопротивления коллекторного перехода до сопротивления прямосмещенного эмиттерного перехода;

– *самопроизвольное уменьшение* сопротивление коллекторного перехода приводит *самопроизвольному перераспределению* напряжения источника питания $U_{ипк}$ и в результате все напряжение источника питания $U_{ипк}$ будет *самопроизвольно* сосредоточиваться на нагрузке;

– это в результате приводит к *самопроизвольному перераспределению* напряжения источника питания, $U_{ипк}$ мощность на выходе $P_{вых} \approx U_{вых} I_э$ станет больше мощности на входе $P_{вх} = U_{вх} I_э$, $P_{вых} \gg P_{вх}$, т.е. биполярный транзистор будет усиливать мощность.

Таким образом, в полупроводниковой структуре с двумя электронно-дырочными переходами и, соответственно, в биполярном транзисторе имеют место взаимосодействующие самоорганизующиеся процессы, которые сопровождаются самопроизвольным перераспределением напряжения источника питания транзистора, в результате чего мощность на выходе транзистора начинает превышать мощность на его входе, т.е. биполярный транзистор усиливает мощность входного сигнала.

Список литературы

1 Хакен Г. Синергетика: пер. с англ. / Г.Хакен. — М.: Мир, 1980. — 405 с.

2 Колесников А.А. Прикладная синергетика: проблемы и перспективы / Системный анализ и прикладная синергетика: сб. науч. тр. VIII Всерос. науч. конф. (18–20 сентября 2017 г.). — Н. Архыз: Изд-во ТРТУ, 2017. — С. 7–17.

3 Пелюхова Е.Б. Синергетика в физических процессах: самоорганизация физических систем: учеб. пос. / Е.Б. Пелюхова, Э.Е. Фрадкин. — СПб.; М.; Краснодар: Лань, 2011. — 320 с.

4 Шелль Э. Самоорганизация в полупроводниках: пер. с англ. / Э. Шелль. — М.: Мир, 1991. — 460 с.

5 Бонч-Бруевич В.Л. Доменная электрическая неустойчивость в полупроводниках / В.Л. Бонч-Бруевич, И.П. Звягин, А.Г. Миронов. — М.: Наука, 1972. — 415 с.

6 Усыченко В.Г. Электронная синергетика. Физические основы самоорганизации и эволюции материи: курс лекций / В.Г. Усыченко. — СПб.: Лань, 2010. — 235 с.

7 Ermaganbetov K.T. Electronic mechanisms of instability in semiconductor structures / K.T. Ermaganbetov, L.V. Chirkova, H.T. Arinova // Вестн. Караганд. ун-та. Сер. Физика. — 2015. — № 4 (80). — С. 4–11.

8 Ermaganbetov K.T. Nonlinear phenomena and instability in semiconductors / K.T. Ermaganbetov, L.V. Chirkova, E.V. Skubnevsky, H.T.Arinova // Вестн. Караганд. ун-та. Сер. Физика. — 2016. — № 1(81). — С. 39–45.

9 Ermaganbetov K.T. Physical processes in the Gunn diode and the energy balance / K.T. Ermaganbetov, L.V. Chirkova, E.V. Skubnevsky, H.T. Arinova, A.Omirbek // Вестн. Караганд. ун-та. Сер. Физика. — 2017. — № 1(85). — С. 15–21.

10 Ermaganbetov K.T. Current instability phenomena in a tunnel diode and electron self-organization processes / K.T. Yermaganbetov, L.V.Chirkova, K.M. Makhanov, K.S. Rozhkova, H.T. Arinova, A. Kurmash // Вестн. Караганд. ун-та. Сер. Физика. — 2019. — № 2(94). — С. 8–14.

11 Пасынков В.В. Полупроводниковые приборы: учеб. пос. / В.В. Пасынков, Л.К. Чиркин. — М.: Высш. шк., 1987. — 479 с.

Л.В. Чиркова, Қ.Т. Ермағанбетов, Л. Тезекбаева

Физика-техника мамандығы бойынша мамандарды дайындауда синергетика ілімінің ұстанымдары

Мақалада «Физикалық электроника» пәнін оқу кезінде физика-техникалық бейіндегі мамандарды даярлауда синергетиканың негізгі қағидаларын қолдану мәселелері қарастырылған. Жұмыс Е.А. Қарағанды мемлекеттік университетінің радиофизика және электроника кафедрасында аталған пән бойынша көп жылдық білім беру тәжірибесіне негізделген. «Жартылай өткізгіштік құрылым + электр энергиясының сыртқы көзі» жүйесін энергия мен затпен тұрақты алмасу есебінен стихиялық өзін-өзі ұйымдастырудың кооперативтік процестері дамитын ашық тепе-тең емес термодинамикалық жүйе ретінде қарастырылуы мүмкін. Қосөрісті транзисторлардағы белсенді жұмыс режиміндегі физикалық процестер талданған. Сапалы теориялық талдау арқылы қарастырылып отырған жүйеде өзара ықпал ететін өзін-өзі ұйымдастыру процестері пайда болады, нәтижесінде эмиттерлік саласындағы әлеуметтік кедергінің өздігінен төмендеуі және коллекторлық өту саласындағы ұқсас бартердің артуы орын алады; негізгі есе заряд тасығыштардың базаға өздігінен инжекциясы байқалады, соның нәтижесінде база қабатының ауысуымен шекара мамандығы заряд тасығыштарда негізгі емес заряд тасығыштардың шоғырлануының өздігінен артуы орын алады. Заряд тасығыштарды база арқылы коллекторға өздігінен көшіру коллекторлық өту кедергісінің тікелей ығыстырылған эмитенттік өту және т.б. кедергісіне дейін өздігінен төмендеуін тудырады. Жоғарыда аталған барлық процестер қорек көзі кернеуінің өздігінен қайта таралуына себепші болады, соның нәтижесінде транзистор шығысындағы қуат оның кірісіндегі қуаттан асып түседі, яғни биполярлы транзистор қуатты күшейтеді.

Кілт сөздер: синергетика, ашық жүйе, шалаөткізгіш құрылым, қосөрісті транзистор, жұмыс күйі, өздігінен жүретін үдерістер.

L.V. Chirkova, K.T.Yermaganbetov, L. Tezekbaeva

Principles of synergetics in training of specialists physical and technical profile

The article discusses the use of the basic principles of synergetics in the training of physicists in the study of the discipline «Physical Electronics». The work is based on many years of experience in teaching the discipline at the Department of Radiophysics and Electronics of Karaganda State University named after E.A. Buketova. It is shown that the system «semiconductor structure + external source of electrical energy» can be considered as an open nonequilibrium thermodynamic system in which cooperative processes of spontaneous self-organization due to the constant exchange of energy and matter develop. The physical processes in bipolar transistors in the active mode of operation are analyzed. By means of a qualitative theoreti-

cal analysis, it was established that the system under consideration interacts with self-organizing processes that result in spontaneous lowering of the potential barrier in the emitter region and an increase in similar barter in the region of collector junctions; spontaneous injection of minority charge carriers into the base is observed, resulting in a spontaneous increase in the concentration of minority charge carriers in the base layer adjacent to the transition. Spontaneous transfer of charge carriers through the base to the collector causes a spontaneous decrease in the collector junction resistance to the resistance of a forward-biased emitter junction, etc. All of the above processes determine the spontaneous redistribution of the voltage of the power source, as a result of which the power at the output of the transistor begins to exceed the power at its input, i.e. A bipolar transistor will amplify the power.

Keywords: synergetics, open system, semiconductor structure, bipolar transistor, operating modes, theoretical analysis, self-organization processes.

References

1 Haken, G. (1980). *Sinerhetika [Synergetics]*. Moscow: Nauka [in Russian].

2 Kolesnikov, A.A. (2017). Prikladnaia sinerhetika: problemy i perspektivy [Applied synergetics: problems and prospects]. Collection of works System analysis and applied synergetics `17: *VIII Vserossiiskaiia nauchnaia konferentsiia (18-20 sentiabria 2017 hoda) — VIII All-Russian Scientific Conference* (p. 7–17). New Arkhyz: Publishing House of TRTU [in Russian].

3 Pelyukhova, E.B. & Fradkin, E.E. (2011). *Sinerhetika v fizicheskikh protsessakh: samoorhanizatsiia fizicheskikh sistem [Synergetics in physical processes: self-organization of physical systems]*. Saint Petersburg – Moscow – Krasnodar: Lan [in Russian].

4 Shell, Je. (1991). *Samoorhanizatsiia v poluprovodnikakh [Self-organization in semiconductors]*. Moscow: Mir [in Russian].

5 Bonch-Bruevich, V.L., Zviagin, I.P., & Mironov, A.G. (1972). *Domennaia elektricheskaia neustoichivost v poluprovodnikakh [Domain electric instability in semiconductors]*. Moscow: Nauka [in Russian].

6 Usychenko V.G. (2010) *Elektronnaia sinerhetika. Fizicheskie osnovy samoorhanizatsii i evoliutsii materii [Electronic Synergetics. Physical foundations of self-organization and evolution of matter]*. Saint Petersburg: Lan [in Russian].

7 Ermaganbetov, K.T., Chirkova, L.V. & Arinova, H.T. (2015). Electronic mechanisms of instability in semiconductor structures. *Vestnik Karahandinskoho universiteta. Seriia Fizika — Bulletin of the University of Karaganda-Physics, 4(80),* 4–11 [in Russian].

8 Ermaganbetov, K.T., Chirkova, L.V., Skubnevsky, E.V. & Arinova, H.T. (2016). Nonlinear phenomena and instability in semiconductors. *Vestnik Karahandinskoho universiteta. Seriia Fizika — Bulletin of the University of Karaganda-Physics, 1(81),* 39–45 [in Russian].

9 Yermaganbetov, K.T., Chirkova, L.V., Skubnevsky, E.V., Makhanov, K.M., Arinova, H.T.& Omirbek, A. (2017). Physical processes in the Gunn diode and the energy balance. *Vestnik Karahandinskoho universiteta. Seriia Fizika — Bulletin of the University of Karaganda-Physics, 1(85),* 15–21 [in Rusiian].

10 Yermaganbetov, K.T., Chirkova, L.V., Makhanov, K.M.,Rozhkova, K.S., Arinova, H.T. & Kurmash, A. (2019). Current instability phenomena in a tunnel diode and electron self-organization processes. *Vestnik Karahandinskoho universiteta. Seriia Fizika — Bulletin of the University of Karaganda-Physics, 2(94),* 8–14 [in Rusiian].

11 Pasynkov, V.V. & Chirkin, L.K. (1987). *Poluprovodnikovye pribory [Semiconductor devices]*. Moscow: Vysshaia shkola [in Russian].

DOI 10.31489/2020Ph2/143-149

УДК 53.072.13

К.М. Маханов[1], Л.В. Чиркова[1], Б.А. Касымбаева[2], М.С. Бейсенбекова[2], Н.К. Әсет[1]

[1]Карагандинский государственный университет им. Е.А. Букетова, Казахстан;
[2]АО «НИШ ХБН», Караганда, Казахстан
(E-mail: makanov@inbox.ru)

Междисциплинарная связь физики, схемотехники и программирования

В статье представлены результаты разработки электронного устройства на основе цифровых компонентов, проведенной совместно с учащимися школ и студентами. Целью данной работы являлись проектирование и разработка электронного устройства на основе 32-битных микроконтроллеров серии STM32. Для проектирования и разработки электронной части устройства была использована интегрированная среда разработки Altium Designer. С применением языка высокого уровня C++ разработана управляющая программа в отладочной среде Keil v.5. В качестве центрального управляющего процессора использован микроконтроллер серии STM32F030K6T6. Разработаны электрическая схема и печатная плата прибора. В качестве сенсорного элемента использован высокочувствительный датчик газа TGS 2610 производства фирмы «Figaro» (Япония). Для передачи SMS применен модуль SIM800A. В процессе выполнения работы учащиеся самостоятельно изготовили электрические платы с использованием метода облучения ультрафиолетовой лампой специального фоторезиста. Практически все компоненты были расставлены и распаяны школьниками самостоятельно. Совместно со студентами была разработана управляющая программа для микроконтроллера. Для изготовления корпуса устройства была задействована среда «КОМПАС». Распечатка корпуса осуществлялась на 3D-принтере. Проведены калибровка прибора и ее тестовые испытания. По результатам предварительных тестовых испытаний устройства установлено, что датчик газа реагирует на наличие газа в течение первых 20 с от времени начала утечки. Ложных срабатываний устройства не зафиксировано. Показано значение основ физики, информатики и математики в процессе проектирования цифровых устройств и приборов.

Ключевые слова: датчик газа, дополнительное образование, микроконтроллер STM32, программирование, прибор, электрическая схема, печатная плата, модуль передатчика.

Введение

При обучении школьников и учащихся основам разработки современных электронных и робототехнических устройств важно дать знания по таким направлениям, как радиоэлектроника, механика, и программирование. Знакомство с данными направлениями в рамках общеобразовательных дисциплин, таких как физика, математика и информатика, учащиеся начинают с 6–7 классов. Однако следует отметить, что, как бы хорошо не были усвоены знания, умения и навыки по данным дисциплинам, они не позволят учащимся самостоятельно и в полной мере создавать цифровые электронные устройства, роботов, писать полноценные управляющие программы.

Для того, чтобы уметь создавать цифровые электронные и робототехнические устройства и писать программы, учащимся необходимы дополнительные, углубленные междисциплинарные знания по таким направлениям, как программируемая микроэлектроника [1], робототехническая технология [2] и т.д. Процесс обучения должен быть организован соответствующим образом. В первую очередь, учащиеся должны быть заинтересованы и увлечены идеей проектирования и разработки собственных устройств. Во-вторых, у них должно быть достаточно свободного времени для дополнительных занятий по электронике и программированию. Немаловажную роль играет наличие соответствующего оборудования и программного обеспечения.

В процессе обучения ученики должны научиться определять функциональные задачи и технические характеристики как электронных, так и механических компонентов. Овладеть навыками разработки электронных схем и печатных плат. Научиться разрабатывать алгоритмы и псевдокоды, для последующего воплощения в реальную программу. Уметь самостоятельно разрабатывать и писать программные блоки на одном из языков высокого уровня.

Как видим, разработка самодельных цифровых и робототехнических устройств требует более углубленных знаний и практических навыков по таким дисциплинам, как физика, математика, информатика.

Теоретические знания из курса физики и математики необходимы при расчетах электронных узлов и блоков разрабатываемого устройства. При расчете электронных компонентов проявляются навыки практического применения физических законов и математики.

Таким образом, можно отметить, что освоение основ микроэлектроники и программирования требует от учеников, наряду с изучением физики, математики и информатики, рассмотрения взаимосвязей между этими дисциплинами.

В основе всех современных разработок лежит микроэлектронная технология, представленная программируемыми микроконтроллерами, или в более сложных устройствах — микропроцессорами. В школьной образовательной программе в основном используют различные готовые конструкторы Lego [3; 5] и отладочные платформы Arduino [4].

Наш опыт работы со школьниками позволяет утверждать, что обучение на основе отдельных микроконтроллеров более эффективно по сравнению с обучением при помощи конструкторов в области информатики и электроники. На протяжении двух лет авторами данной статьи ведется работа с учениками старших классов по разработке электронных устройств на основе микроконтроллеров STM32.

Целью данной работы являются проектирование и разработка электронных устройств на основе программируемой микроконтроллерной техники. Для достижения поставленной цели были рассмотрены и решены следующие задачи:

– ведение дополнительных занятий с учениками по углубленному изучению основ полупроводниковой микроэлектроники;

– ведение дополнительных занятий по углубленному изучению языка программирования C++;

– ведение дополнительных занятий по изучению микроконтроллерной техники;

– проектирование и разработка как минимум одного электронного устройства, основанного на цифровом интерфейсе.

В дополнительном обучении принимали участие школьники 10–11 классов. Предварительно ученики были поделены на группы по два человека. Каждая пара выбрала себе направление, в рамках которого планировалось ведение разработок.

Результаты и их обсуждение

В статье представлены результаты проектирования и разработки электронного устройства, предназначенного для обнаружения утечки бытового газа.

На рисунке 1 изображена структурная схема разработанного прибора. Прибор состоит из датчика газа; управляющего микроконтроллера STM32F030K6T6 [5; 26]; GSM/GPS-модуля SIM800A (передатчика); светового и звукового индикаторов; микросхемы контроля заряда и *Li-Pol* аккумуляторной батарейки.

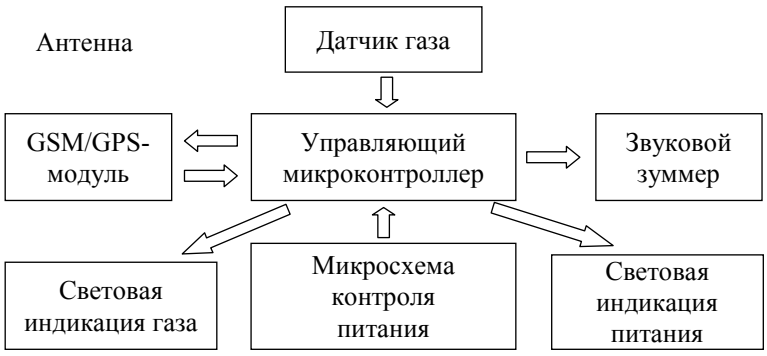

Рисунок 1. Структурная схема прибора

Прибор с датчиком газа, управляющим микроконтроллером и GSM/GPS-модулем составляет единую конструкцию прибора для контроля утечки газа.

Датчик газа, управляющий микроконтроллер и GSM/GPS-модуль для SMS-сигналов располагаются на одной общей плате. При изменении состояния датчика газа (наличие газа в окружающей среде) сигнал передается в управляющий микроконтроллер. В свою очередь, управляющий микроконтроллер на программном уровне анализирует уровень сигнала на входах. При «обнаружении» сенсором наличия газа на внешнем корпусе устройства загорается световой индикатор (светодиод) и включается звуковой

индикатор. По мере повышения концентрации газа частота звука возрастает, до момента превышения заданного порогового значения концентрации газа в помещении. При превышении порогового значения газа, которое задается на программном уровне, выполняется код программы, осуществляющий посылку управляющего сигнала на SIM-карту GSM/GPS-модуля. В свою очередь, GSM/GPS-модуль формирует и отправляет SMS-сообщение с заданным текстом. Сообщение одновременно может быть отправлено на несколько телефонных номеров. Перечень номеров предварительно «записывается» непосредственно в программу управления микроконтроллером.

Управляющая программа для микроконтроллера разработана на языке C++, с использованием среды разработки Keil v.5. Алгоритм работы программы и, в целом, устройства реализуется в следующем порядке:

– управляющий микроконтроллер с частотой не менее одного раза в 0,5 с. «опрашивает» состояние двух входов, один из которых связан с датчиком газа, второй — с микросхемой контроля заряда аккумуляторной батареи;

– при изменении состояния входа, связанного с датчиком газа, микроконтроллер активирует код программы, который отвечает за посылку сигнала на GSM/GPS-модуль;

– при изменении состояния входа, связанного с микросхемой контроля аккумуляторной зарядки, управляющий микроконтроллер активирует код программы, который также формирует посылку сигнала на GSM-модуль.

Ниже представлена часть программы, в которой отражены основные управляющие команды для включения, запуска и активации GSM-модуля, реализованного с применением структуры *While* и вложенной структуры выбора *if/else*.

```
void SendSMS (char* text)
{
uart.WriteString («AT+CMGS=\»+77009667591\»\r»);
int ch = uart.ReadByte ();
        while((ch!= '>') && (ch!= -1))
ch = uart.ReadByte ();
        if(ch == '>')

void MainTask ()
{ char str [100];
Enable ();
uart.WriteString («AT\r»);
ReadSrting (str,100);
uart.WriteString («ATE0\r»);
ReadSrting (str,100);
uart.WriteString («AT+CMGF=1\r»);
ReadSrting (str,100);
uart.WriteString («AT+CSCS=\»GSM\»\r»);
ReadSrting (str,100);
HAL_ADCEx_Calibration_Start (&hadc);
        while (! strstr(str,»+CREG: 0,1»))
SendSMS («POWER ON»);
ReadSrting (str,100);
        { if (! sms_sended)
{ SendSMS («GAS!»);
ReadSrting (str,100);
sms_sended = true; }
}
        else
        { if (sms_sended)
{
SendSMS («NO GAS OK»);
ReadSrting (str,100);
sms_sended = false;
```

При включении прибора автоматически осуществляются первичная активация SIM-карты, подключение модуля к системе GPS и обмен данными между микроконтроллером и модулем передатчика.

Электрическая схема и плата устройства спроектированы в среде Altium Designer. На рисунке 2 представлены схемы подключения микроконтроллера к внешней периферии (а) и печатной платы (б).

(а) (б)

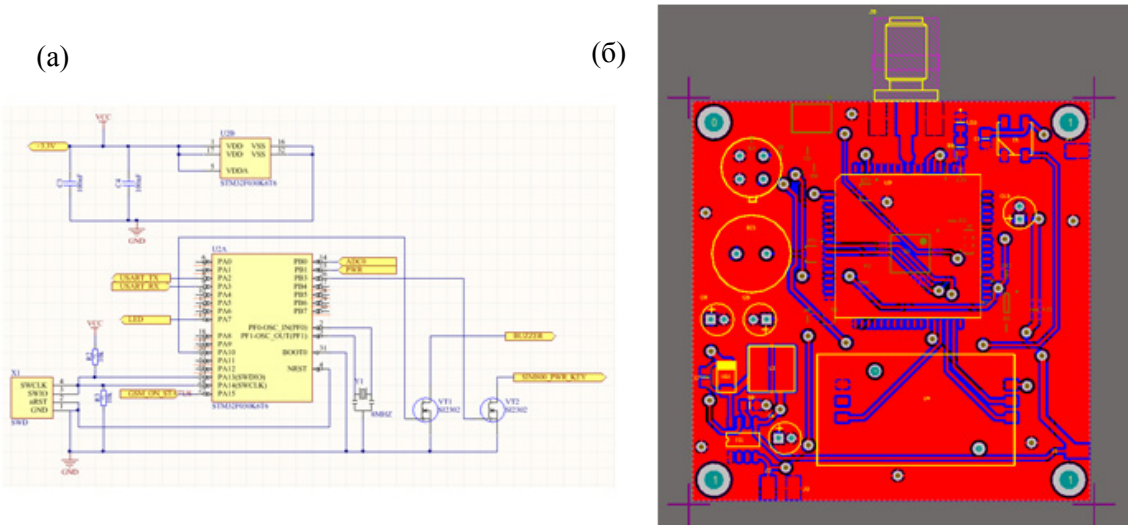

Рисунок 2. Схемы подключения микроконтроллера к внешней периферии (а) и печатной платы (б)

Использованный нами STM32F030K6T6 32-битный микроконтроллер относится к первой линейке микроконтроллеров STM32. Выбор наиболее упрощенной версии микроконтроллера обусловлен простотой его изучения и программирования учащимися.

В качестве сенсора газа использован продукт фирмы FIGARO ENGINEERING, это полупроводниковый датчик на основе пленок оксида олова, сопротивление которых в чистом воздухе очень высоко [6].

Изготовление платы осуществлялось путем облучения ультрафиолетовой лампой специального фоторезиста через фотонегатив схемы, распечатанный на лазерном принтере. Травление платы происходило в растворе перекиси водорода и лимонной кислоты.

После изготовления печатной платы, лужения и очистки поверхности была проведена работа по распайке компонентов. Данная работа была выполнена совместно со школьниками. Все компоненты, за исключением микроконтроллера и модуля передатчика, были расставлены и распаяны школьниками самостоятельно. Для пайки использовали маломощную паяльную станцию, оснащенную функцией термовоздушной обдувки. Корпус для прибора был разработан в среде «КОМПАС» и распечатан на 3D-принтере.

Тестовые испытания прибора на количество отказов по срабатыванию и ложных срабатываний показали положительные результаты. Тестирование на количество отказов проводилось следующим образом: на расстоянии двух метров от датчика, в течение двух секунд распыляли с маленького баллончика газ (пропан). Затем для ускорения распространения паров газа в окружающей среде включали вентилятор.

Во всех случаях срабатывали световая и звуковая индикации устройства. Параллельно на выбранный телефонный номер приходили сообщения «***GAS!***». Тестовые испытания проводились в течение 2–3 дней, так как после каждого распыления газа требовалось на 1–2 ч проветривать помещение. В отсутствии газа на тот же телефонный номер приходили сообщения об отсутствии газа «***NO GAS OK***».

На рисунке 3 представлено созданное совместно с учащимися устройство.

Рисунок 3. Внешний вид разработанного устройства

Ложных срабатываний прибора не зафиксировано. При проведении данных испытаний «опасения» были связаны не с самим датчиком, а с разработанной программой. Следовало убедиться в том, что в самой программе нет ошибок, которые приводили бы к ложной активации прибора и посылкам сообщений.

Заключение

В ходе выполнения работы была разработана схема устройства, предназначенного для обнаружения паров бытового газа в окружающей среде. В качестве основного сенсорного элемента использован высокочувствительный датчик TGS-2610. Осуществлено проектирование печатной платы устройства с трассировкой проводников и разводкой электронных компонентов. Для проектирования схемы платы устройства были задействованы возможности среды Altium Designer. Для разработки управляющей программы был использован язык высокого уровня C++. Обмен передаваемых команд между микроконтроллером и модулем SIM800A осуществлялся посредством AT-команд.

В качестве конечного продукта нами был собран прототип устройства, оснащенный сенсором газа, управляющим микроконтроллером, модулем передачи данных, звуковым индикатором и аккумуляторной батареей. Функциональные возможности устройства проверены в ходе предварительных тестовых испытаний. Тестовые испытания устройства показали положительные результаты: во всех случаях включалась звуковая сигнализация, и устройство осуществляло посылку SMS-сообщения. При этом случаев ложного срабатывания устройства не было зафиксировано.

Также следует отметить, что учащиеся, выполняя поставленные задачи, получили более глубокие знания в области цифровой техники и программирования микроконтроллеров.

Список литературы

1 Жукова Е.А. Hi-Tech и Hi-Hume: новые требования к подготовке профессионала / Е.А. Жукова // Вестн. Том. гос. пед. ун-та. — 2005. — Вып. 5, № 49. — С. 70–72.

2 Борисова Т.С. Формирование инновационного поведения молодежи институтами социального воспитания / Т.С. Борисова, С.Б. Куликов // Вестн. Том. гос. пед. ун-та. — 2012. — Вып. 8, № 123. — С. 47–50.

3 Никитина Т.В. Образовательная робототехника как направление инженерно-технического творчества школьников: учеб. пос. / Т.В. Никитина. — Челябинск: Изд-во Челяб. гос. пед. ун-та, 2014. — 169 с.

4 Гайсина И.Р. Развитие робототехники в школе / Педагогическое мастерство (II): материалы Междунар. заоч. науч. конф. (декабрь 2012 года). — М.: Буки-Веди, 2012. — С. 105–107.

5 Торгаев С.Н. Практическое руководство по программированию STM-микроконтроллеров: учеб. пос. / С.Н. Торгаев, М.В. Тригуб, И.С Мусоров. — Томск: ТПУ, 2015. — 111 с.

6 Игнатьева Н. Датчики газа фирмы «Figaro» / Н. Игнатьева // Электроника. Наука. Техника. Бизнес. — 2005. — № 2. — С. 34–37.

К.М. Маханов, Л.В. Чиркова, Б.А. Касымбаева, М.С. Бейсенбекова, Н.К. Әсет

Физика, сұлбатехника және программалаудың пәнаралық байланысы

Мақалада мектеп оқушылары және студенттермен бірлесіп жүзеге асырылған цифрлық компоненттерге негізделген электрондық құрылғыны жасау нәтижелері келтірілген. Бұл жұмыстың мақсаты STM32 сериялы 32-биттік микроконтроллер негізінде электрондық құрылғыны жобалау және жасау болып табылады. Құрылғының электрондық бөлігін жобалау және әзірлеу үшін Altium Designer интеграцияланған әзірлеу ортасы қолданылған. Keil v.5 әзірлеу ортасында, жоғары деңгейлі C ++ тілін қолдану арқылы басқару бағдарламасы жасалған. Орталық басқару процессоры ретінде STM32F030K6T6 сериялы микроконтроллер пайдаланылған. Электр тізбегі және құрылғының электрлік тақтасы әзірленген. Сенсорлы элемент ретінде Figaro (Жапония) фирмасында өндірілген сезімталдығы өте жоғары TGS 2610 газ датчигі қолданылған. SMS жіберу үшін SIM800A модулі пайдаланылған. Жұмысты орындау барысында студенттер ультракүлгін сәулемен арнайы фоторезистті сәулелендіру әдісін қолдана отырып, электрлік тақталарды өз бетінше жасаған. Іс жүзінде барлық компоненттерді оқушылар өздері реттеп, дәнекерлеген. Микроконтроллерді басқару бағдарламасы студенттермен бірге әзірленген. Құрылғының корпусын жасау үшін «КОМПАС» ортасы қолданылған. Корпустың өзі 3D-принтерде басылып шығарылған. Құрылғының жұмыстық дәлдігі реттеліп оның сынақ тестілері жүргізілген. Құрылғыны алдын-ала сынау нәтижелері бойынша, газ датчигі ағып кету басталған сәттен бастап алғашқы 20 секунд ішінде газдың болуын сезіп, сәйкесінше хабарлама жіберетіні анықталған және өз еркімен қосылып хабарламаны жіберуі байқалмады. Сандық құрылғылар мен аспаптарды жобалау процесінде физика, информатика және математика негіздерінің маңыздылығы көрсетілген.

Кілт сөздер: газ датчигі, қосымша білім беру, STM32 микроконтроллері, бағдарламалау, аспап, электр сұлбасы, баспа тақтасы, таратқыш модулі.

K.M. Makhanov, L.V. Chirkova, B.A. Kassymbayeva, M.S. Beissenbekova, N.K. Aset

Interdisciplinary communication of physics, schemes and programming

The article presents the results of the development of an electronic device based on digital components, carried out jointly with schoolchildren and students. The aim of this work was the design and development of an electronic device based on 32-bit microcontrollers of the STM32 series. For the design and development of the electronic part of the device, the integrated development environment Altium Designer was used. Using a high-level C ++ language, a control program was developed in the Keil v.5 debugging environment. The microcontroller of the STM32F030K6T6 series was used as the central control processor. The electrical circuit and the circuit board of the device are developed. A highly sensitive gas sensor TGS 2610, manufactured by Figaro (Japan), was used as a sensor element. For SMS transmission, the SIM800A module was used. In the process of doing the work, students independently made electric boards using the method of irradiation of a special photoresist with a UV lamp. Practically all the components were arranged and soldered by the students on their own. Together with the students, a control program for the microcontroller was developed. To manufacture the case of the device, the «KOMPAS» environment was used. The case was printed on a 3D — printer. Calibrated the device and its test tests. According to the results of preliminary test tests of the device, it was found that the gas sensor responds to the presence of gas during the first 20 seconds from the time the leak started. False positives of the device are not fixed. The importance of the foundations of physics, computer science and mathematics in the process of designing digital devices and instruments is shown.

Keywords: gas sensor, additional education, STM32 microcontroller, programming, device, electrical circuit, printed circuit board, transmitter module.

References

1 Zhukova, E.A. (2005). Hi-Tech i Hi-Hume: novye trebovaniia k podhotovke professionala [New professional training requirements]. *Vestnik Tomskoho hosudarstvennoho pedahohicheskoho universiteta — Bulletin of Tomsk State Pedagogical University, V 5, 49,* 70–72 [in Russian].

2 Borisova, T.S., & Kulikov, S.B. (2012). Formirovanie innovatsionnoho povedeniia molodezhi institutami sotsialnoho vospitaniia [Formation of innovative behavior of youth by institutions of social education]. *Vestnik Tomskoho hosudarstvennoho pedahohicheskoho universiteta — Bulletin of Tomsk State Pedagogical University, V 8, 123*, 47–50 [in Russian].

3 Nikitina, T.V. (2014). *Obrazovatelnaia robototekhnika kak napravlenie inzhenerno-tekhnicheskoho tvorchestva shkolnikov [Educational robotics as a direction of engineering and technical creativity of schoolchildren]*. Chelyabinsk: Izdatelstvo Cheliabinskoho hosudarstvennoho pedahohicheskoho universiteta [in Russian].

4 Gaisina, I.R. (2012). Razvitie robototekhniki v shkole [Robotics development at school]. Pedahohicheskoe masterstvo (II): *Mezhdunarodnaia zaochnaia nauchnaia konferentsiia (dekab 2012 hoda) — International Correspondence Scientific Conference.* (p. 105–107). Moscow: Buki Vedi [in Russian].

5 Torgaev, S.N., Trigub, M.V., & Musorov, I.S. (2015). *Prakticheskoe rukovodstvo po prohrammirovaniiu STM-mikrokontrollerov [Practical Guide to Programming STM Microcontrollers]*. Tomsk: TPU [in Russian].

6 Ignateva, N. (2005). Datchiki haza firmy «Fiharo» [Figaro gas sensors]. *Elektronika. Nauka. Tekhnika. Biznes — Electronics. The science. Equipment. Business, 2,* 34–37 [in Russian].

АВТОРЛАР ТУРАЛЫ МӘЛІМЕТТЕР
СВЕДЕНИЯ ОБ АВТОРАХ
INFORMATION ABOUT AUTHORS

Aimukhanov, A.K. — Professor, Ye.A. Buketov Karaganda State University, Kazakhstan.

Alibiyev, D.B. — Candidate of physical and mathematical sciences, Associate Professor of applied mathematics and informatics Department, Ye.A. Buketov Karaganda State University, Kazakhstan.

Anishchenko, Yu.V. — PhD, Associate Professor, Tomsk Polytechnic University, School of Non-Destructive Testing, Tomsk, Russia.

Aset, N.K. — Student of the Department «Radiophysics and electronics», Faculty of Physics and Technology, Ye.A. Buketov Karaganda State University, Kazakhstan.

Beisenbekova, M.S. — Physics Teacher, Nazarbayev Intellectual School, Karaganda, Kazakhstan.

Bekturganov, Zh.S. — Doctor of chemical sciences, Professor, Ye.A. Buketov Karaganda State University, Kazakhstan.

Bespalko, A.A. — Doctor of technical sciences, Leading Researcher, Problem Research Laboratory of Electronics, Dielectrics and Semiconductors, Research School of High Energy Process Physics, Tomsk Polytechnic University, Russia.

Chirkova, L.V. — Candidate of technical sciences, Docent, Ye.A. Buketov Karaganda State University, Kazakhstan.

Dalskaya, G.Yu. — Ph.D, Associate Professor, MIREA – Russian Technological University, Moscow, Russia.

Dzhanabekova, R.Kh. — Junior research fellow, Scientific Center for Nanotechnology and Functional Nanomaterials, Ye.A. Buketov Karaganda State University, Kazakhstan.

Gavrilin, A.N. — PhD, Associate Professor, National Research Tomsk Polytechnic University, School of Advanced Manufacturing Technologies, Tomsk, Russia.

Gevko, E. — Candidate of technical sciences, Associate Professor, Associate Professor at the Department of Biomedical Systems, Ternopil Ivan Puluj National Technical University, Ukraine.

Golosov, D.A. — Ph.D., Leading Research Scientist, Belarusian State University of Informatics and Radioelectronics, Minsk, Republic Belarus.

Guselnikov, M.E. — PhD, Associate Professor, Tomsk Polytechnic University, School of Non-Destructive Testing, Tomsk, Russia.

Gyngazov, A.S. — Head of testing laboratory Joint-stock company «Sibkabel», Tomsk, Russia.

Hevko, I. — Doctor of technical sciences, Professor, Professor of the Department of Management and Administration, Ternopil Ivan Puluj National Technical University, Ukraine.

Hraniak, V.F. — PhD of technical science, Associate Professor of Department Theoretical Electrical Engineering and Electrical Measurements, Vinnitsa National Technical University, Vinnitsa, Ukraine.

Hud, V. — Candidate of technical sciences, Associate Professor, Associate Professor at the Department of Automobiles, Ternopil Ivan Puluj National Technical University, Ukraine.

Ibrayev, N.Kh. — Doctor of physico-mathematical sciences, Professor, Director of the Institute of Molecular Nanophotonics, Ye.A. Buketov Karaganda State University, Kazakhstan.

Kakimzhanov, D.N. — Master student, D. Serikbaev East Kazakhstan State Technical University, Ust-Kamenogorsk, Kazakhstan.

Kambarova, Zh.T. — PhD, Docent of Department of Physics and Nanotechnology, Faculty of Physics and Technology, Ye.A. Buketov Karaganda State University, Kazakhstan.

Kantai, N. — Doctoral student of D. Serikbaev East Kazakhstan State Technical University, Ust-Kamenogorsk, Kazakhstan.

Karabekova, D.Zh. — PhD, Associate Professor, Ye.A. Buketov Karaganda State University, Kazakhstan.

Kashkanov, A.A. — Candidate of technical sciences, Associate Professor, Doctoral Student, Kharkiv National Automobile and Road University, Kharkiv, Ukraine.

Kashkanov, V.A. — Candidate of technical sciences, Associate Professor, Associate Professor Vinnytsia National Technical University, Vinnytsia, Ukraine.

Kassenov, B.K. — Doctor of chemical sciences, Professor, Head of laboratory, Abishev Chemical-Metallurgical Institute, laboratory of thermochemical processes, Kazakhstan.

Kassenova, Sh.B. — Doctor of chemical sciences, Professor, Chief researcher, Abishev Chemical–Metallurgical Institute, laboratory of thermochemical processes, Kazakhstan.

Kassymbayeva, B.A. — Head of the Department of physics, Nazarbayev Intellectual School, Karaganda, Kazakhstan.

Katsyv, S.Sh. — PhD of technical science, Associate Professor of Department Theoretical Electrical Engineering and Electrical Measurements, Vinnitsa National Technical University, Vinnitsa, Ukraine.

Kazhikenova, A.Sh. — Candidate of Technical Sciences, Associate Professor of mathematics and informatics teaching technique Department, Ye.A. Buketov Karaganda state university, Kazakhstan.

Kenesbekov, A.B. — Doctoral Student, D. Serikbaev East Kazakhstan State Technical University, Ust-Kamenogorsk, Kazakhstan.

Kenzhegulov, B. — Doctor of technical sciences, Professor, Kh. Dosmukhamedov Atyrau State University, Kazakhstan.

Khassenov, A.K. — PhD, Associate Professor, Ye.A. Buketov Karaganda State University, Kazakhstan.

Khorsov, P.N. — PhD, Junior Researcher, Problem Research Laboratory of Electronics, Dielectrics and Semiconductors, Research School of High Energy Process Physics, Tomsk Polytechnic University, Russia.

Kim, M.S. — 3rd year student of the Faculty of Physics and Technology, Ye.A. Buketov Karaganda State University, Kazakhstan.

Kowalevski, P. — PhD, Assistant Professor, Wroclaw University of Science and Technology, Poland.

Kozhanova, R.S. — Junior researcher, Sarsen Amanzholov East Kazakhstan State University, Ust-Kamenogorsk, Kazakhstan.

Kuanyshbekov, E.E. — Master of technical sciences, lead engineer, Abishev Chemical-Metallurgical Institute, laboratory of thermochemical processes, Kazakhstan.

Kucheruk, V.Yu. — Doctor of science (Engineering), Professor, Head of the Department, Vinnytsia National Technical University, Vinnytsia, Ukraine.

Kukharchuk, V.V. — Doctor of technical science, Professor, Head of Department Theoretical Electrical Engineering and Electrical Measurements, Vinnitsa National Technical University, Vinnitsa, Ukraine.

Kultan Jaroslav — PhD, Dr. Ing., Katedra aplikovanej informatiky FHI EU v Bratislave, Ekonomická univerzita v Bratislave UMP, Centrum štúdií východnej a juhovýchodnej Európy.

Kuvshinov, K.A. — Chief Lecturer, National Research Tomsk Polytechnic University, School of Advanced Manufacturing Technologies, Tomsk, Russia.

Kylyshkanov, M.K. — Doctor of physical and mathematical sciences, Professor, Head of the scientific center by science and projects, Joint-stock company «Ulbinsky metallurgical plant» Ust-Kamenogorsk, Kazakhstan.

Laas, R.A. — Engineer at the Problem Research Laboratory of Electronics, Dielectrics and Semiconductors, Research School of High Energy Process Physics, Tomsk Polytechnic University, Russia.

Luchnikov, P.A. — Research Scientist, MIREA – Russian Technological University, Moscow, Russia.

Lyashuk, O. — Doctor of technical sciences, Professor, Professor at the Department of Automobiles, Ternopil Ivan Puluj National Technical University, Ukraine.

Makhanov, K.M. — Candidate of physical and mathematical sciences, Associate Professor of the Department of «Radiophysics and electronics», Faculty of Physics and Technology, Ye.A. Buketov Karaganda State University, Kazakhstan.

Maulet M. — Doctoral Student, Sarsen Amanzholov East Kazakhstan State University, Ust-Kamenogorsk, Kazakhstan.

Moyzes, B.B. — PhD, Associate Professor, National Research Tomsk Polytechnic University, School of Non-Destructive Testing, Tomsk, Russia.

Nizhegorodov, A.I. — Dr. Sc., Professor, Irkutsk National Research Technical University, Department of Construction and Road-Making Machines and Hydraulic Systems, Irkutsk, Russia.

Popova, N.A. — Candidate of technical sciences, Senior Researcher of Tomsk State Architecture and Building University, Tomsk, Russia.

Rakhadilov, B.K. — PhD, Senior Researcher of the Research Center «Surface Engineering and Tribology», S. Amanzholov East Kazakhstan State University, Ust-Kamenogorsk, Kazakhstan.

Rogachev, A.V. — Dr.Sc., Professor, Head of Department, Francisk Skorina Gomel State University, Gomel, Republic Belarus.

Rotshtein, A.P. — Doctor of science (Engineering), Professor, Professor Jerusalem College of Technology, Machon Lev, Jerusalem, Israel.

Rudenkov, A.S. — PhD, Leading Research Scientist, Francisk Skorina Gomel State University, Gomel, Republic Belarus.

Sadykova, A.E. — Master, Engineer, Scientific center for fundamental nanotechnologies and nanomaterials, Ye.A. Buketov Karaganda State University, Kazakhstan.

Sagintayeva, Z.I. — Candidate of chemical sciences, Associate Professor, Abishev Chemical-Metallurgical Institute, laboratory of thermochemical processes, Lead researcher, Kazakhstan.

Seliverstova, E.V. — Senior researcher, PhD Physics, Institute of molecular nanophotonics, Ye.A. Buketov Karaganda State University, Kazakhstan.

Shust, I. — Graduate Student, Department of Automobiles, Ternopil Ivan Puluj National Technical University, Ukraine.

Sokol, M. — Doctor of education, Professor, Foreign Languages Department, I. Horbachevsky Ternopil National Medical University, Ukraine.

Surzhikov, A.P. — Doctor of physics PhD, professor, Head of the department — head of the department as a department of Control and Diagnostics, School of Non-Destructive Testing and Safety Engineering, Principal Researcher, Problem Research Laboratory of Electronics, Dielectrics and Semiconductors, Research School of High-Energy Process Physics, Tomsk Polytechnic University, Russia.

Tabiyeva, Y.Y. — Junior Researcher of the Research Center «Surface Engineering and Tribology» S. Amanzholov East Kazakhstan State University, PhD student D. Serikbayev East Kazakhstan State Technical University, Ust-Kamenogorsk, Kazakhstan.

Tezekbaeva, L. — Master student, Ye.A. Buketov Karaganda State University, Kazakhstan.

Tussupbekova, A.K. — PhD, Head of the Department of «Radiophysics and electronics», Faculty of Physics and Technology, Ye.A. Buketov Karaganda State University.

Uazyrkhanova, G.K. — PhD, Deputy Dean Of the School of information technology and intelligent systems D. Serikbayev East Kazakhstan State Technical University, Ust-Kamenogorsk, Kazakhstan.

Vtorushina, A.N. — PhD, Associate Professor, National Research Tomsk Polytechnic University, School of Non-Destructive Testing, Tomsk, Russia.

Wojciech Wieleba — Doctor of Engineering, Professor, Wroclaw University of Science and Technology, Poland.

Yermaganbetov, K.T. — Candidate of physical and mathematical sciences, Docent, Ye.A. Buketov Karaganda State University, Kazakhstan.

Zavadski, S.M. — Ph.D, Head of Department, Belarusian State University of Informatics and Radioelectronics, Minsk, Republic Belarus.

Zeinidenov, A.K. — PhD, Associate Professor, Dean of the Faculty of Physics and Technology, Ye.A. Buketov Karaganda State University, Kazakhstan.

Zhumabekov, A.Zh. — 3rd year PhD student, Ye.A. Buketov Karaganda State University, Kazakhstan.

Zhurerova, L.G. — PhD, Senior Lecturer, D. Serikbayev East Kazakhstan State Technical University, Ust-Kamenogorsk, Kazakhstan.